

BONNER METEOROLOGISCHE ABHANDLUNGEN

Heft 68 (2015) (ISSN 0006-7156)

Herausgeber: Andreas Hense

Pablo A. Saavedra Garfias

**RETRIEVAL OF CLOUD AND RAINWATER FROM
GROUND-BASED PASSIVE MICROWAVE OBSERVATIONS
WITH THE MULTI-FREQUENCY DUAL-POLARIZED
RADIOMETER ADMIRARI**

BONNER METEOROLOGISCHE ABHANDLUNGEN

Heft 68 (2015) (ISSN 0006-7156)

Herausgeber: Andreas Hense

Pablo A. Saavedra Garfias

**RETRIEVAL OF CLOUD AND RAINWATER FROM
GROUND-BASED PASSIVE MICROWAVE OBSERVATIONS
WITH THE MULTI-FREQUENCY DUAL-POLARIZED
RADIOMETER ADMIRARI**

Retrieval of cloud and rainwater from ground-based
passive microwave observations with the
multi-frequency dual-polarized radiometer
ADMIRARI

DISSERTATION
ZUR
ERLANGUNG DES DOKTORGRADES (DR. RER. NAT.)
DER
MATHEMATISCH-NATURWISSENSCHAFTLICHEN FAKULTÄT
DER
RHEINISCHEN FRIEDRICH-WILHELMS-UNIVERSITÄT BONN

vorgelegt von
Pablo A. Saavedra Garfias
aus
Bolivien

Bonn, September 2014

Diese Arbeit ist die ungekürzte Fassung einer der Mathematisch-Naturwissenschaftlichen Fakultät der Rheinischen Friedrich-Wilhelms-Universität Bonn im Jahr 2014 vorgelegten Dissertation von Pablo A. Saavedra Garfias aus Bolivien.

This paper is the unabridged version of a dissertation thesis submitted by Pablo A. Saavedra Garfias born in Bolivien to the Faculty of Mathematical and Natural Sciences of the Rheinische Friedrich-Wilhelms-Universität Bonn in 2014.

Anschrift des Verfassers:

Address of the author:

Pablo A. Saavedra Garfias
Meteorologisches Institut der
Universität Bonn
Auf dem Hügel 20
D-53121 Bonn

1. Gutachter: Prof. Dr. Clemens Simmer, Rheinische Friedrich-Wilhelms-Universität Bonn
2. Gutachter: Priv-Doz. Dr. Alessandro Battaglia, Leicester University, UK

Tag der Promotion: 18. Dezember 2014
Erscheinungsjahr: 2015

Contents

Abstract	XI
Zusammenfassung	XIII
1. Introduction	1
2. Radiative Transfer in Precipitating Clouds	9
2.1. Microwave Radiative Transfer Formulation	9
2.2. Polarized RTE	11
2.2.1. Intensity Formalism	12
2.3. Vector Radiative Transfer Equation	13
2.4. Interaction Parameters	14
2.4.1. Gaseous Absorption	14
2.4.2. Scattering and Absorption by Hydrometeors	16
2.4.3. Boundary Conditions	19
2.5. Solution of the Radiative Transfer Equation	21
2.5.1. Plane-Parallel Radiative Transfer	22
2.5.2. Monte Carlo Methods	25
3. Microwave Radiometry	27
3.1. Passive Microwave Radiometer	27
3.1.1. Dual Polarized Radiometer ADMIRARI	30
3.1.2. Radiometer's Performance	41
3.2. Co-located Ancillary Instruments	52
3.2.1. Micro Rain Radar	53
3.2.2. Cloud Lidar	61
4. Retrieval Methods of Precipitating Clouds	69
4.1. Retrieval Approach by Czekala	69
4.2. Bayesian Approach	73
4.3. The Forward Model	75
4.4. Description of the Retrieval Technique	86
4.4.1. Non-precipitating LWP Retrievals	96
5. Observations of Precipitating Clouds	101
5.1. The COPS Field Campaign	101
5.2. CBAUW Measurements	105
6. Retrieval Results	107
6.1. Mid-Latitude Rain Regime Retrieval	107
6.2. Long-term Statistical Analysis	111

7. Discussion on LWP Partition	117
7.1. Observed Cloud/Rain Partition	117
7.2. Effects on the Retrievals Due to the Geometry of Observation	119
8. Validation for Rain Water Content	123
8.1. Retrievals by Two Active Sensors	123
8.1.1. MRR Approach	123
8.1.2. Dual-Polarization Approach	124
9. Conclusions	127
Appendix	131
Table of appendices	133
A. Rain Liquid Water Path Retrieved by Two Independent Method	135
A.1. Introduction	135
A.2. Rain LWP retrieval from pure MRR data	135
A.2.1. Results for R_LWP as a function of DSD	137
A.3. The ZPHI Method Applied to RHI observations	139
A.3.1. Instrumentation and strategy	140
A.3.2. ZPHI application for LWC retrievals	140
A.3.3. Results for rain liquid water content	142
A.4. Conclusions	144
B. Publications	147
Acronyms	149
List of Symbols	153
List of Constants	155
Bibliography	157
Acknowledgements	167

List of Figures and Tables

List of Figures

1.1.	Convective cloud <i>Cumulonimbus-lenticularis</i> developing before precipitation during the GPM/CHUVA field campaign in Brazil. (<i>photo credits: P. Saavedra</i>)	2
1.2.	The relationship between cloud and precipitation water in UMORA (left) and GPROF (right). Note how GPROF partitions more water as precipitation and less as cloud, compared to UMORA's empirical partition represented by the black line. The colors in each plot represent the number of observations (Extracted from Hilburn, K. and Wentz, F. (2008)).	3
2.1.	Assumed geometry for the remote sensing of the atmosphere. The specific intensity is the radiant energy flowing at each point in the medium per unit area normal to the flux, per unit solid angle, in a frequency interval dv . The variation of intensity with position is governed by the radiative transfer equation.	10
2.2.	Atmospheric extinction in the microwave spectrum for a cloudy atmosphere. The red dotted line indicates the contribution by O_2 , the green dashed line is the water vapour and the blue dotted-dashed line indicates the contribution by Liquid Water Content (LWC) of 0.2 g m^{-3} . While the black solid line is the result of adding all components. The frequency bands normally used by conventional radiometers are show by A and B. (Extracted from Pospichal, B., 2009)	15
2.3.	Ratio of scattering to absorption cross-section microwave spectrum for water droplets of radius r . Typical droplet size ranges are indicated for clouds with and without rain. (Extracted from Hewison, T.J. (2006) adapted from Janssen, M. A., 1993).	16
3.1.	Simplified schematic for a total power radiometer. The output voltage V , as given by this simple circuit, is proportional to the received signal power.	28
3.2.	Radiometer ADMIRARI at its standard operational configuration. Mounted on a transportable trailer. Note the ancillary instrumentation: on the left a cloud-lidar and on the right a MRR. (<i>photo credit: P. Saavedra</i>).	30
3.3.	Module picture and receiver layout (3.3(a) <i>photo credit: RPG GmbH</i> , 3.3(b)) from (Rose, T. and Czekala, H., 2007).	32
3.4.	Calibration of antenna temperature using a cold and hot load. 3.4(a) linear approximation, 3.4(b) non-linearity scheme including the injection of noise temperature T_n	35
3.5.	ADMIRARI set-up for Liquid Nitrogen calibration 3.5(a), with the cold target positioned below the antenna 3.5(b). (<i>photo credit: P. Saavedra</i>)	38

3.6. Boxplot for calibration coefficients obtained after long term operation from August 2007 to June 2011. The lowest/highest border of the boxplot indicated the 25th and 75th quantile, the middle red-line in box indicates the median, and the red crosses are outliers.	40
3.7. ADMIRARI historical first data set as shown in the TB-PD space for the three frequencies, from left to right 10.7, 21.0 and 36.5 GHz. Every point represents the average of a data sub-set grouped in a bin of 5 K, the error bar is the standard deviation. The lower row indicates de number of data at every TB bin in the abscissa.	44
3.8. Example from July 19th, 2009 of a sky-tipping calibration with optical thickness as a function of airmass. From top to bottom 10.7, 21.0, 36.5 GHz vertical polarization, with respective test criteria correlation coefficient r^2 and χ^2 . The black line is the linear regression fit.	45
3.9. Brightness temperature time series for two consecutive days, top: Feb. 13th and bottom: Feb. 14th 2009. There were two successful calibrations at 06:00 UTC the first day and at 18:00 UTC the second. Note the drop on TB at 10.7GHz (blue line) after the second calibration.	46
3.10. Brightness temperatures for the 10.7 and 36.5 GHz frequencies. Measurements are indicated by the coloured distribution pixels with the colour representing the number of observations. Simulations are indicated by the crosses and diamonds (Extracted from Battaglia, A., Saavedra, P., Simmer, C., and Rose, T. (2009)).	48
3.11. Two elevation scan over obstacles to block the radiometer FOV till 25° . The scan was performed form 0 to 90° elevation, with 1° step and 5 samples per angle to smooth down noise.	49
3.12. Studies performed at the CSU-CHILL facility together with Manuel Vega from NASA Goddard, to find out the origin of interference by Ka-band radars.	51
3.13. New ADMIRARI's band-pass filter for the 36.5 GHz module (plot courtesy from RPG).	52
3.14. Reflectivity profiles as observed by MRR in slant mode. Example profiles for the three reflectivity calculations i.e. (red) METEK standard output, (blue) from METEK spectrum, (green) from RAW data. Note that undefined values are indicated with 0 dBz (red circles) for clarity.	57
3.15. Corresponding spectral power for the noise level estimation shown in figure 3.16(b), note that below the 5th and at 8th range the spectrum presents bi-modal distribution.	57
3.16. (a): Three reflectivity profiles calculated with and without noise. (b): Two noise levels considered	59
3.17. Spectrum from two MRR: slant 30° elevation (left) and vertical (middle), and their corresponding vertical normalized reflectivity profiles (right) for two different events on 20 September 2010, 09:59UTC convective rain (top) and on 21th September 2010, 08:19UTC stratiform rain (bottom)	60
3.18. Time series of cloud lidar's backscattering coefficient profiles β in logarithm scale as observed at 30° elevation angle for (top) Vaisala ct25k and (middle) CBM80 mounted at ADMIRARI. The bottom panel is the error of the cloud base range in % relative to the Vaisala ct25k measurement.	64

3.19.	Backscattering factor average over range for the Vaisala ct25k versus CBM80 in logarithm scale. Blue circles profile average below cloud top (CT), light-green pluses average below cloud base (CB). Red line is the best fit for blue circles and red dashed line the standard deviation for the best fit.	65
3.20.	Typical ADMIRARI measurement dataset for slant observations with reflectivity profiles (top), Ceilometer Backscattering and cloud base (second), TB and PD (bottom) for three frequencies.	67
4.1.	The TB-PD space at 30° elevation angle composed by different combinations of cloud and rain LWP indicated by dash-dotted-blue and dash-red iso-lines respectively. The total LWP is indicated by the green dotted iso-line. The three ADMIRARI frequencies are represented with the 21.0GHz on top and on the bottom the 10.7 and 36.5GHz from left to right correspondently.	70
4.2.	Same as figure 4.1 but including precipitation measurements from March 23rd, 2010. Note that at every frequency the highest (TB,PD) data point suggests a different cloud/rain LWP partition.	72
4.3.	Simplified scheme for the cloud box model. Radiances are computed for the observation point RAD. The hydrometeor atmospheric profile from a Cloud Resolving Model are illustrated by the red, blue and green lines for rain, cloud and ice respectively. Outside the gray box contains only atmospheric gases. . .	76
4.4.	Example of the four hydrometeor profiles (cloud, rain, graupel, and snow) extracted from a Cloud Resolving Model and adopted in the 3 – D radiative transfer simulations (Extracted from Battaglia, A., Saavedra, P., Rose, T., and Simmer, C. (2010)).	77
4.5.	Shapes of drops falling in stagnant air calculated by the procedure in (Pruppacher, H. and Pitter, R., 1971). The number indicates the equi-volume sphere radius. (Extracted from Sokamura, S. and Oguchi, T. (2010))	77
4.6.	Effect of the emissivity assumption on the down-welling brightness temperature (top) and polarization difference (bottom) for the three ADMIRARI frequencies. The differences on TBs and PDs computed for emissivities of 0.8, 0.9 and 1.0 are compared to the assumed emissivity of 0.9.	79
4.7.	Scatter plots in the TB-PD space for the comparison between SPA RT4 and Monte-Carlo computations to highlight 3-D scattering effects. The geometry of the simulations is the one illustrated in figure 4.3 with an elevation angle of 30° , $L_x = L_y = 4\text{km}$ and $P_x = [-3.5, -3.0, -2.5, \dots, 3.5]\text{km}$. About 3000 profiles with freezing level ranging from 2 to 4km are considered in this example (Extracted form Battaglia, A., Saavedra, P., Rose, T., and Simmer, C. (2010)). .	80
4.8.	Top panel: extinction cross section per unit volume in $[\text{mm}^2\text{mm}^{-3}]$ as a function of the raindrop equi-volume diameter for the three ADMIRARI frequencies. Raindrops up to 9mm diameter are considered. Bottom: vertical polarization extinction coefficient as a function of the rain LWC in gm^{-3} for three different Drop Size Distribution (DSD)s as indicated in the legend. The line's thickness accounts for the assumed variability in the coefficient b in equation 4.79 from 0.5 to 0.7 (Extracted form Battaglia, A., Saavedra, P., Rose, T., and Simmer, C. (2010)).	82

4.9.	Parameter $\Delta\xi$ as defined in equation 4.81 evaluated at 30° elevation angle for 10.7GHz (top) and 36.5GHz (bottom) for three different DSD as a function of rain LWC. Curves plotted with the same style correspond to different b values: 0.5, 0.6 and 0.7 from the top to bottom (Extracted form Battaglia, A., Saavedra, P., Rose, T., and Simmer, C. (2010)).	84
4.10.	Simulation study for sensitivity of PDs (top panels) to the DSD and the assumed raindrops axial ratio. The equilibrium axial ratio of b=0.6 and the Marshall-Palmer DSD is used as a reference. The overall effect in the TB-PD space is shown in the bottom panels (Extracted from Battaglia, A., Saavedra, P., Morales, C., and Simmer, C. (2011))	85
4.11.	Synthetic measurements selected to test the retrieval technique. Top: Radar attenuated reflectivity, middle: Brightness Temperature and bottom: Polarization Difference at the three ADMIRARI frequencies.	87
4.12.	Scatter plot for retrieval versus true values for cloud (first row), rain (middle row) and water vapour (bottom row). The columns correspond to three different elements of the covariance matrix for Brightness temperatures (TBs) (from left to right: 1.0, 1.75 and 2.50K) and Polarization Differences (PDs) (from left to right: 0.8, 1.5 and 2.0K). The blue crosses correspond to the minimum distance method and the red-points to the Bayesian retrievals, the black-dashed line indicates the 1:1 relation.	88
4.13.	Scatter plot for retrieval versus true values for cloud (first row), rain (middle row) and water vapour (bottom row). The first column corresponds to pure-radiometer (RAD) and radar combined technique (RADMRR), the second column corresponds to the combination of only two frequencies.	90
4.14.	Absolute errors box-plots for cloud, rain and water vapour obtained from the retrieval sensitivity study. The approaches RAD, RADMRR, 10&21, 10&36 and 21&36 are enumerated from 1 to 5 correspondingly. The red mark indicates the median, the first and third quartiles are the bottom and top box's edges and the blue-crosses depicts the outliers.	92
4.15.	Relative error ($\frac{LWP_{true}-LWP_{ret}}{LWP_{true}}$) for cloud versus rain for: (a) RAD and (b) RADMRR. The color modulates the cloud component, and the square marker size modulates the rain component as it is shown in the inner coloured table. The distribution of relative errors for cloud and rain are shown in the right and top panels respectively.	94
4.16.	Relative entropy (a quantity indicative of the information content added by the measurement in the sensitivity study) as a function of rain Liquid Water Path (LWP) (left panel) and cloud LWP (right panel).	95
4.17.	Cloud and rain profiles for the 660 samples retrieval sensitivity study: a) True cloud lwc in logarithm scale, c) the cloud lwc retrieved using the NSI approach, e) NSI approach for cloud but including the Micro Rain Radar (MRR) geometrical constrain. The second column's panels b), d) and f) same as the first column but for the rain lwc.	97
4.18.	Retrieval performance based on the comparison between the true and the retrieved LWP. Results from the tree-frequencies 10.7, 21.0 and 36.5 GHz (red squares), and two-frequencies 21.0 and 36.5 GHz (blue circles) approaches. The black dashed line represents the one to one line.	99

4.19.	Relative errors as a function of minimum LWP. The dot-circle represents the median, the 25th (75th) quantile are the lower (upper) box limit. The whiskers corresponds to $\pm 2.7\sigma$ and the red crosses are outliers.	100
4.20.	Same as figure 4.18 but using Bayesian technique. Results from the tree-frequencies 10.7, 21.0 and 36.5 GHz (red squares), and two-frequencies 21.0 and 36.5 GHz (blue circles) approaches. The black dashed line represents the one to one line.	100
5.1.	Precipitation regime and temperature registered during the whole COPS campaign.	102
5.2.	Examples of measurements for 18/9/2007. From top to bottom: gauge rain rate and 2 meter temperature, 10.7, 21.0 and 36.5 GHz brightness temperature and polarization difference. Grey intervals indicate rainy periods as sensed by the gauge at the Atmospheric Radiation Measurement (ARM) site.	103
5.3.	Distribution of occurrences for long term measurements (TB, PD) in rainy conditions for the whole COPS campaign. The three ADMIRARI frequencies are shown (10.7GHz top, 21.0GHz center, 36.5GHz bottom).	104
6.1.	Measurements from 10 November 2008, at 30° elevation angle and fixed azimuth. Top panel: MRR slant path reflectivity in dBZ, the estimated freezing level is shown in dashed black line; second panel: brightness temperatures for the three frequencies; third, fourth and bottom panels: polarization difference at 36, 21 and 10GHz respectively. Gray areas indicate rainy periods flagged by the rain sensor.	108
6.2.	Retrieval results for the case illustrated in Figure 6.1. Top panel: quality index (QI); second panel: integrated water vapour; third panel: cloud LWP; bottom panel: rain LWP. The gray area in the top panel indicates precipitation sensed by the rain sensor; colored areas shade the one-standard-deviation interval for the retrieved quantities.	109
6.3.	Time series of (a) 2 m temperature and (b) rain amount accumulated at ten minute intervals from a rain gauge at CESAR; (c) retrieved IWV, (d) C_LWP and (e) R_LWP, from 23 August to 12 November 2008. Only rainy periods are shown.	112
6.4.	Histograms of (a) quality index QI, retrieved (b) IWV, (c) C_LWP and (d) R_LWP from 23 August to 12 November 2008. Statistics for pure cloud (class 1: gray area), radiometer inside the rain cell (class 2: solid black line) and outside the rain cell (class 3: red line-dot columns) are presented separately as described in the text.	114
7.1.	Retrieved partition for Cloud and Rain LWP during the whole observation period (class 2). The color bar indicates the number of observations in logarithmic scale.	118
7.2.	Cloud versus Rain LWP distribution for vertical (top) and slant (bottom) retrievals.	120
7.3.	Quantile-Quantile plot for the rain/cloud ratio to compare the distribution of columnar (x-axis) versus slant (y-axis) retrievals.	122

8.1.	Independent retrievals for Rain LWP as observed by ADMIRARI and a X-band Radar. The vertical errorbars indicate the Bayesian 2σ , while the horizontal errorbars represent the variance of radar observations along the radiometer's FOV. The black-dashed line represents a 1:1 relationship, the solid red line the median of the distribution of the point-to-point difference, while the upper and lower dashed-dotted-red lines holds the 90% of the data.	125
A.1.	Distribution of Rain LWP retrieved by ADMIRARI versus the estimation from MRR by using equation A.10, for $N_0 = 1.4, 4.0, 8.0$ and $32.0 \times 10^3 \text{ m}^{-3} \text{ mm}^{-1}$ at a) thunderstorm, b) heavy-rain, c) M-P and d) Light-rain respectively. The black-dashed-line indicates the 1:1 relation, the color-bar indicates the number of repetitions. (Extracted from Saavedra, P., Battaglia, A., and Simmer, C. (2012b))	138
A.2.	ADMIRARI time series of Brightness Temperatures and Polarization Difference at 10.7 (blue), 21.0 (green) and 36.5 (red) GHz. Case study from June 20th, 2013. Gray area represent rain periods.	140
A.3.	JuXPoI radar reflectivity RHI scans at same ADMIRARI's azimuth. Red cone at 3.8km represents the instantaneous radiometer FOV.	141
A.4.	Φ_{dp} range profile for different elevation angles. The red circle denotes the bottom of the bright-band i.e. the maximum range for the integration.	143
A.5.	X-band specific attenuation for RHI sequences. The red cone at 3.8km represents the instantaneous radiometer FOV.	143
A.6.	Liquid water content for RHI sequences. Red cone represent the instantaneous radiometer's FOV.	144
A.7.	Scatter plot for LWP as retrieved from ADMIRARI versus the ZPHI algorithm from RHI radar data. Note that ADMIRARI's retrievals are shown with error-bars corresponding to 2σ . The black-dashed line represent a 1:1 relation. The data as well as RMSE and BIAS corresponds to slant 30° elevation angle. (Extracted from Saavedra, P., Battaglia, A., Ryzhkov, A., and Simmer, C. (2013))	145

List of Tables

3.1. ADMIRARI calibration variables (Gain G [mVK^{-1}], system temperature T_{sys} [K] and noise injector temperature T_n [K]) after long term operation, from August 2007 to June 2011. Note that only sky tipping calibration which has been flagged as successful are taken into account, the number of successful cases are indicated in the last row together with the percent relative to a total of 1310 attempts.	41
3.2. Main specifications for the microwave radiometer ADMIRARI (*) feature is independently estimated from Radiometer Physics GmbH (RPG).	42
3.3. Main Features of the MRR radar used aside the radiometer ADMIRARI	58
3.4. Main features of the CBM80 cloud-lidar used aside the radiometer ADMIRARI	63
3.5. Coefficients for the three dataset of average β after fitting a linear relationship. All coefficients must be multiplied by a factor $\times 10^{-4} \text{sr}^{-1} \text{km}^{-1}$	66
4.1. Bias and Root Mean Square Error (RMSE) for integrated water vapour (Integrated Water Vapour (IWV)), cloud (Cloud Liquid Water Path (C_LWP)) and rain (Rain Liquid Water Path (R_LWP)) liquid water path, resulting from the retrieval sensitivity study normalized to zenith observations. The last column correspond to retrievals obtained by the minimum distance method (eq. 4.78). The last row indicates the Bias and RMSE for retrievals of total LWP below 450gm^{-2}	89
4.2. RMSE for integrated water vapour (IWV [kgm^{-2}]), cloud (C_LWP [gm^{-2}]) and rain (R_LWP [gm^{-2}]) liquid water path, resulting from the retrieval sensitivity study normalized to zenith observations. Every row corresponds to one DSD assumed: Thunderstorm (TS), Heavy-rain (HR), Marshall-Palmer (MP) and Light-rain (LR). The last row indicates the RMSE for retrievals of total LWP [gm^{-2}] below 450gm^{-2}	91
6.1. Mean of the standard deviation for the retrieved variables according to three classifications: 1) non-precipitating clouds, 2) radiometer inside the rain cloud, and 3) radiometer outside the rain cloud. The last two rows indicate the mean QI and the number of observations for every class.	113
8.1. Results for R_LWP Radiometer-MRR comparison assuming four different intercept parameter for an exponential DSD: Light rain (L-R), Marshall-Palmer (M-P), Heavy rain (H-R) and Thunderstorm (TH-S). Results normalized to zenith.	124
8.2. Results for the radar-radiometer comparison as a function of the minimum rain LWP considered. Values are normalized to zenith.	126
A.1. Coefficients c and d in equation A.15 for different temperatures.	142

Abstract

A ground-breaking new-concept multi-wavelength dual-polarized passive microwave radiometer ADMIRARI (ADvanced MICrowave RAdiometer for Rain Identification) has been developed to perform observations of atmospheric precipitating clouds. The radiometer is suited to be operated in rainy conditions, fully steerable in elevation and azimuth angle and comprises of six independent channels measuring brightness temperatures in horizontal and vertical polarization at 10.7, 21.0 and 36.5 GHz. The passive sensor has been enriched with two ancillary active sensors, i.e. a micro rain radar (MRR) and a cloud-Lidar, thus range resolving capability is also achieved.

An inversion algorithm has been implemented to retrieve simultaneously cloud and rain liquid water paths and total water vapour from ADMIRARI's measurements. A long-term data set of linearly polarized brightness temperatures has been collected from field experiments. The slant path integrated values are retrieved via a Bayesian inversion approach based on many atmospheric states by a numerical weather prediction model which build up *a-priori* probability density function of rainfall profiles. Detailed three-dimensional radiative transfer calculations, which account for the presence of non-spherical particles in preferential orientation, simulate the down-welling brightness temperatures and establish the similarity of radiative signatures and thus the probability that a given profile is actually observed. Long-term measurements demonstrate that the observed brightness temperatures and polarization differences can be well interpreted and reproduced by the simulations.

The quality of the inversion algorithm is evaluated by a simulation-based sensitivity study applied to rainy cases. In a pure radiometric retrieval approach the study indicates an absolute errors characterized by RMSE of 235.3 and 129.1 g m^{-2} for cloud and rain liquid water path respectively, and 1.89 kg m^{-2} for water vapour. Biases are found to be -19.3 g m^{-2} for cloud, 43.3 for rain, and 0.17 kg m^{-2} for water vapour. The retrievals are improved when extra information from the MRR is used.

The inversion algorithm has been applied to long-term measurements from precipitating clouds, with results showing -for the zenith-normalized retrievals- an average statistical error of 1.54 kg m^{-2} , 144 g m^{-2} and 52 g m^{-2} for water vapour, cloud and rain liquid water path respectively. Based on these results, long-term estimated distributions of cloud/rain water partitioning for Mid-latitude precipitating clouds are presented for the first time as obtained by a ground-based radiometer. Finally for a case study the rain water path retrieval has been validated by a distinct instrument using an independent method. A systematic error of 68 g m^{-2} (overestimation by ADMIRARI) is found, with a statistical error of 192 g m^{-2} .

Zusammenfassung

Ein innovatives neues Konzept, Multi-Wellenlängen, dualpolarisierten, passive Mikrowellenradiometer wurde entwickelt, um Beobachtungen des atmosphärischen Wolken und Niederschlag zuführen.

Das Radiometer ist in Elevation und Azimut-Winkel voll steuerbar und besteht aus sechs unabhängigen Kanälen, die die Strahlungstemperaturen in horizontaler und vertikaler Polarisation bei den Frequenzen 10,7GHz, 21,0GHz und 36,5GHz messen. Der passive Sensor ist mit zwei Neben aktive Sensoren bereichert gewesen, nämlich ein Mikro Regen Radar (MRR) und Wolken-Lidar, damit sind atmosphärischen Profilen zusätzlich beobachten.

Mittels der Entwicklung einer Inversionsalgorithmus, nämlich Bayes-technik, die Gesamtwolkenwassergehalt, Gesamtregenwassergehalt und die Gesamtwasserdampf Retrievals aus den Radiometersmessungen gleichzeitig gerechnet haben. Eine langfristige Datenbank ist von linear polarisierten Strahlungstemperaturen aus Feldexperimenten gesammelt gewesen.

Der Inversionsalgorithmus nutzt viele atmosphärische Erkenntnisse aus einer numerischen Wettervorhersagemodell, um eine Wahrscheinlichkeitsdichtefunktion der Regenprofile vor zu bauen. Die Strahlungstemperaturen wurden durch detaillierte dreidimensionale Strahlungstransportrechnungen simuliert. Die Simulationen des Niederschlages sind als abgeplatteten Regentropfen mit horizontale Vorzugsausrichtung bearbeitet. Deshalb die Wahrscheinlichkeit, die ein gegebener Atmosphärenprofil tatsächlich beobachtete ist, liegt auf der Ähnlichkeit der Strahlungs Signaturen mit den Messungen.

Die Qualität des Inversionsalgorithmus ist durch eine simulationsbasierte Sensitivitätsstudie an Regenfällen angewendet bewertet. Die Studie zeigt eine mittlere absolute Fehler gekennzeichnet durch RMSE von 235,3 und 129,1 g m^{-2} für Cloud- bzw. Regen Gesamtflüssigwassergehalt, sowie 1.89 kg m^{-2} für Wasserdampf. Biases haben typische Werte von -19,3 g m^{-2} für Cloud, 43,3 g m^{-2} für Regen, und 0,17 kg m^{-2} für Wasserdampf. Die Ungewißheiten sind reduziert, wenn Information aus dem Zusatzgerät MRR verwendet ist.

Die Inversionsalgorithmus hat auf eine langfristige Niederschlagsmessungen angewendet. Davon die durchschnittlich statistische Unbestimmtheit, die für den Zenit normalisiert sind, haben Werte von 1.54 kg m^{-2} , 144 g m^{-2} und 52 g m^{-2} für Wasserdampf, Wolkenflüssigwassergehalt und Regenflüssigwassergehalt. Zum ersten Mal aus einen Bodengebundenen Radiometer abgeleitet, ist die Verteilung der Partition Cloud/Regen Flüssigwassergehalt für Mittel-Geografische Breite Niederschlagsregimes vorgestellt.

Schließlich, die Retrievals des Regen Flüssigwasserinhalts mittels einem verschiedenem Instrument und mit Hilfe eines unabhängigen Methode validiert gewesen ist. Für einen Fallbeispiel, die Validierung hat ergeben eine systematische Unbestimmtheit von 68 g m^{-2} (Überschätzung von ADMIRARI), mit einer statistischer Unbestimmtheit von 192 g m^{-2} .

1. Introduction

One of the most familiar images that we have when looking at the sky is certainly the blue canvas embellished by regular or irregular patterns of clouds, which constitutes one of the most beautiful visible expressions we experience (figure 1.1). This is certainly one of the reasons, why clouds have been under observation since ancient times; the other reason is their direct relation with current and approaching weather. Clouds represent atmospheric water in its liquid or solid state. Numerous methods have been developed to categorize, and quantify clouds. Methods range from the simple classifications of cloud types and determination of cloud cover, to the estimation of cloud base, cloud vertical structure and their liquid or frozen water content. Besides their relevance for weather, clouds have a strong effect on Earth's energy balance, since they reduce the incoming solar radiation due to their relatively high albedo and warm the atmosphere and surface due to long-wave emission (Salby, M. L., 1996).

Clouds are the precursor and generator of precipitation, which is one of the most important components of the Earth's hydrological cycle and constitutes the link to the Earth's energy cycle by its irreversible release of latent heat. The water cycle is an important concern for our society since it relates to the availability of fresh water resources which affects almost every environmental issue on Earth. Precipitation may yield hazardous conditions for the people, for instance solid precipitation as snow can cause tough conditions during winter and disrupt aerial and ground transportations. Extreme intense or persisting liquid precipitation may produce floods affecting people's life and economies.

Expected changes of intensity and spatial distribution of precipitation due to climate change may pose serious risks (Wentz, F., Ricciardulli, L., Hilburn, K., and Mears, C., 2007). Past changes in precipitation are thought to have profoundly affected past human societies, and projected increases in the total area affected by drought or flood risk associated with increased frequency of heavy precipitation events are expected to exert an adverse effect on agriculture, water resources, human health and infrastructure (Allan, R. and Soden, B., 2007, and reference therein).

The impact of global warming on the hydrological cycle has become an important issue. Climate models suggest that the amount of water in the atmosphere will increase with warming at a rate of $\sim 7 \text{ \%K}^{-1}$. This might suggest that precipitation from convective systems will increase at a similar rate (Allan, R. and Soden, B., 2007). However, those same climate models predict that global precipitation will increase at a much slower rate to 1 to 3 \%K^{-1} . This is in contrast with satellite observations which suggest that models underestimate the observed global precipitation response which is found to be $\sim 6 \text{ \%K}^{-1}$ over the past two decades (Wentz, F., Ricciardulli, L., Hilburn, K., and Mears, C., 2007).

Nevertheless climate precipitation estimates are the products from a variety of satellites which have a number of issues affecting their use for the study of climate variations. These include the combination of multiple sensors with discontinuity in datasets, differences in calibration methods, and methodologies to estimate precipitation. Moreover climatological values of precipitation over ocean are still a matter of discussion specially over middle and high latitude, as well as polar latitude precipitation estimates over land are subject for further examination



Figure 1.1.: Convective cloud *Cumulonimbus-lenticularis* developing before precipitation during the GPM/CHUVA field campaign in Brazil. (photo credits: P. Saavedra)

and validation (Adler, R. et al., 2003).

For that reason the requirements for reliable precipitation databases to permit its assimilation in global climate and [Numerical Weather Prediction \(NWP\)](#) models, analysis and model verification, as well as validation of satellite observations (Marzano, F. and Visconti, G., 2002, pp. 107-108). Hence, the achievement of accurate global measurements of precipitation amounts and its distribution must be a priority for the scientific community.

Clouds, primarily determined by their total liquid water content, are currently parametrized or directly modelled in both [NWP](#) and general circulation models (GCMs). A prognostic approach that contains an explicit calculation of cloud water content involving the formation and evaporation of clouds and precipitation was first proposed by Sundqvist, H., 1978; Sundqvist, H., Berge, E., and Kristjánsson, J. E., 1989 for large-scale models. Following this work, an increasing number of GCM and NWP models have included a prognostic equation for the mass of cloud water and/or ice to parametrize the cloud processes (Zhao, Q. and Carr, F., 1995, and references therein)

Quantitative precipitation forecasting has been one of the weakest aspects of [NWP](#) models. One reason for the slow progress in precipitation forecasts is the simple treatment of condensation and precipitation processes (Zhao, Q. and Carr, F., 1995) in most operational models. In recent years, many [NWP](#) models have become quite sophisticated in their advanced treatment of boundary layer processes and radiation amongst others. However, the representation of precipitation processes is not yet implemented to the same degree of refinement. Although reasonable precipitation forecasts are produced by the simple precipitation schemes, one may argue that the fact that they neglect the conversion process of precipitation from cloud water and cloud ice can lead to some significant errors in the model thermodynamics and hydrological fields since clouds are the primary link connecting moisture and precipitation in the hydrological cycle of the atmosphere.

Although quite complex and challenging, the use of observational data to evaluate and

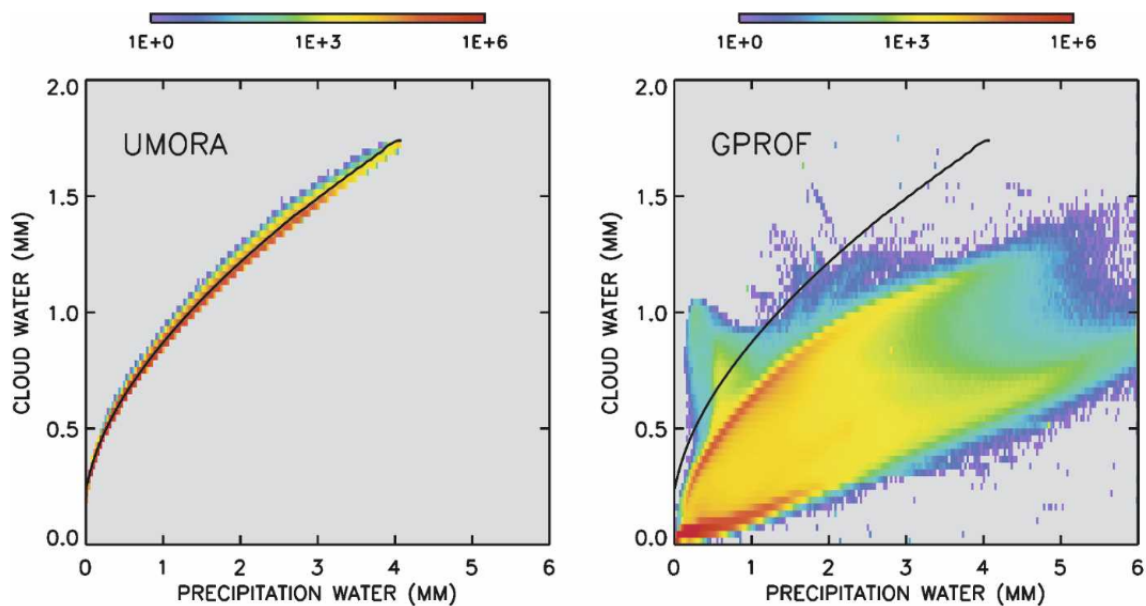


Figure 1.2.: The relationship between cloud and precipitation water in UMORA (left) and GPROF (right). Note how GPROF partitions more water as precipitation and less as cloud, compared to UMORA’s empirical partition represented by the black line. The colors in each plot represent the number of observations (Extracted from Hilburn, K. and Wentz, F. (2008)).

improve model forecasts, parametrization schemes, and satellite retrieval algorithms is fundamental to further success (Randall, D. et al., 2003). In particular simultaneous observations of cloud and rain LWC might provide paramount information to modellers and satellite rainfall retrieval algorithms, which usually assume a cloud/rain partitioning based on empirical relationships (Hilburn, K. and Wentz, F., 2008; Lebsock, M., L’Ecuyer, T., and Stephens, G., 2011; O’Dell, C., Wentz, F., and Bennartz, R., 2008; Wentz, F. and Spencer, R., 1998). For that reason providing methods for continuous and accurate atmospheric observations of hydrometeor content resolved in its components e.g. cloud, rain, and ice is a major requirement for the modelling and meteorological satellite community.

Motivation

Few studies have been performed in order to estimate the cloud and rain LWP simultaneously i.e. the partition of the total LWP in its cloud and rain components, which plays an important role in cloud modelling as well as in space-based retrievals algorithms where empirical assumptions are required (Hilburn, K. and Wentz, F., 2008; Lebsock, M., L’Ecuyer, T., and Stephens, G., 2011; Wentz, F. and Spencer, R., 1998). Such empirical assumptions lead to considerable disagreements between retrieval methods as it is highlighted in figure 1.2 which compares the Unified Microwave Ocean Retrieval Algorithm (UMORA) by Hilburn, K. and Wentz, F. (2008) with the version 6 Goddard Profiling Algorithm (GPROF) by Kummerow, C., Hong, Y., et al. (2001).

O’Dell, C., Wentz, F., and Bennartz, R. (2008) identify assumptions regarding the partitioning of cloud and rain water as a major source for systematic errors in the retrieval algorithms

from space-borne instruments (mostly for passive microwave instruments over ocean). They conclude that the usefulness of microwave based retrievals of cloud and rain water as well as derived climatologies can be hampered by those systematic errors. Therefore the simultaneous measurement of the rain and cloud component of the water content of precipitating clouds is required. For ground-based observations Matrosov, S. (2009b, paragraph 3) also emphasizes that until recently precipitating clouds studies were hampered to a significant degree by the lack of joint simultaneous retrievals of the cloud and rainfall parameters.

Some studies have already addressed this problem by the common analysis of weather radar data and microwave radiometers from ground (Matrosov, S., 2009a,b), and from space e.g. using CloudSat and MODIS (Lebsock, M., L'Ecuyer, T., and Stephens, G., 2011). Despite the difficulties that involve the observation and posterior retrievals of rain/cloud LWP, the benefits for doing so range from validation of Numerical Weather Prediction models, understanding the cloud/precipitation micro-physical properties and validation of space-borne retrievals. In order to fill the gap of such observations the challenge to study the rain and cloud partition by means of ground-based radiometry becomes a priority. This problem has prompted the development of a novel ground-based multi-frequency dual-polarized microwave radiometer.

State-of-the-art

Nowadays cloud and rain liquid water content measurements can be obtained for instance from aircraft *in situ* measurements, but such data are available only for special intensive observational periods, and they are very limited in terms of spatial and temporal resolution, not to mention that they are excessively expensive to collect. Since several years, ground-based microwave radiometric remote sensing of the atmospheric thermal emission has been largely employed as a useful tool for meteorological observations and forecasting, satellite validation, climate studies, and monitoring soil moisture among others. Clouds are semi-transparent to microwave radiation; this feature offers a method to estimate remotely the cloud water content in the atmosphere.

Another important feature of sensing the atmosphere with microwave radiometers is the fact that with careful design, radiometers can be operated in a long-term unattended mode under almost all weather conditions. In the past decade, synergistic observations were widely used to retrieve the vertically integrated cloud liquid content also known as C_LWP (e.g. Crewell, S., Czekala, H., et al. (2001), Crewell, S. and Löhnert, U. (2003), Gaussiat, N., Hogan, R., and Illingworth, A. (2007), Liljegren, J., Clothiaux, E., Mace, G., Kato, S., and Dong, X. (2001), Löhnert, U. and Crewell, S. (2003), Mätzler, C. and Morland, J. (2009), and Rose, T., Crewell, S., Löhnert, U., and Simmer, C. (2009)).

Microwave observations can also be used to estimate profiles of temperature, water vapour and, some even adventure to cloud liquid water profiling (e.g. Crewell, S., Czekala, H., et al., 2001; Knupp, K. et al., 2009), with a temporal resolution of 1-5 min up to a height of 10 km. Nevertheless, Crewell, S., Ebell, K., Loehnert, U., and Turner, D., 2009 concludes that the profiling of cloud water without additional information from active instruments can only be performed in very limited situations, where the clouds have large liquid water contents and observations at higher frequencies are available, in this case limited information is gained but on the other hand the uncertainties in the retrieval of liquid water cloud can range from 30 to 100%.

Rain comprises the most of the world's precipitation and it is normally quantified by the rain rate. Rain rates are typically measured directly from rain gauge networks, disdrometers

or indirectly derived from backscattered signals from ground and space-borne radars. In the past decades numerous passive and active remote sensing methods have been developed for its quantification, using ground and airborne/satellite-based approaches.

Mostly active systems are utilized from the airborne perspective with only few approaches to use passive radiometers. Meneghini, R. (2005) presented the theoretical basis for a technique to estimate rain and DSD by airborne radiometry. According to that study multiple brightness temperature measurements at X-band (8.2-12.4 GHz) can be used to estimate rainfall rate once a correction for cloud water attenuation is performed. Exploiting the closely relation between brightness temperature and the Path Integrated Attenuation (PIA) for frequencies up to about 12 GHz, two path attenuation measurements yield two parameters of an assumed DSD function. Then rain rate is estimated by expressing the DSD parameters as a function of the differential PIA, once the rain parameters are estimated the cloud liquid water can in principle be recovered. This theoretical study assumes a stratiform storm model, low to moderate wind speeds over ocean, a constant vertical rain rate column, etc. A serious problem of this technique is that for moderate and heavy rain rates, the cloud water attenuation is a very small fraction of the total with the consequence that estimates of integrated cloud water are generally unreliable.

For regional and global scales, satellite-based techniques for precipitation observation play an important role. Since 1978 the Special Sensor Microwave Imager (SSM/I), a four-frequency passive microwave space-borne radiometer is successfully estimating precipitation over ocean including total water vapour and also near-surface wind speed. The Tropical Rainfall Measurement Mission (TRMM) launched in 1997 became the first satellite with passive and active systems dedicated to rainfall observation; it is still in orbit and operating, exceeding its life-time expectations. TRMM carries a Microwave Imager, a Precipitation Radar, Visible and Infrared Scanner, Cloud and Earth Radiant Energy Sensor, and a Lighting Imaging Sensor. TRMM's partial coverage of the globe (ranging from 36° North to 36° South latitude) and its relatively infrequent sampling (i.e. passing over a location once a day) limit the understanding of a complete role of precipitation in the hydrological cycle in a global scale. TRMM is also limited concerning the estimation of frozen precipitation and light rainfall, leaving therefore a large gap in global rainfall observation (<http://trmm.gsfc.nasa.gov>). Recently, the Global Precipitation Measurement (GPM) core satellite has been put in orbit and became TRMM successor with a dual-frequency radar on board, and expanding the observations coverage to $\pm 63^\circ$ latitude as well as expanding the capabilities to measure solid and light precipitation (Hou, A. et al., 2014).

Space-based rainfall observations, however, need to be validated with ground-based observations in order to assess whether satellite products meet their stated accuracy requirements and objectives. Thus ground-based instruments and methods to retrieve rain parameters are required.

The increasing use of ground-based multi-frequency passive microwave radiometers for the observation of atmospheric parameters has fostered the exploitation of such instruments for retrieving rainfall rates from ground. Among the difficulties faced in that effort, the impact of water layers on the receiving antenna has become a major problem for ground-based radiometry for rainfall. The presence of rain drops on the radiometer antenna may cause absorption losses and produce hardly predictable signals. Moreover, their presence within the sensed volume tends to break the applicability of the Rayleigh approximation making the signal interpretation in terms of liquid water contents utterly difficult. In the latter situation, a specific liquid water path (hereafter LWP) with a significant rain component produces much higher

TBs than a pure cloud water component. In the presence of rain, LWP retrieval is affected by a strong increase in RMSE and bias errors which can easily exceed 0.1 kg m^{-2} even for total LWP-values below 1 kg m^{-2} (e.g. Löhnert, U. and Crewell, S., 2003). In order to avoid the wetting problem hardware solutions have been undertaken, e. g. the installation of a hydrophobic radome coating, styrofoam windows, or a water-repellent film in conjunction with a rain cover for shielding during low elevation angle observations (see Battaglia, A., Saavedra, P., Simmer, C., and Rose, T., 2009; Crewell, S., Czekala, H., et al., 2001; Marzano, F. S., Cimini, D., and Ware, R., 2005b; Mätzler, C. and Morland, J., 2009, respectively).

Czekala, H. and Simmer, C. (1998) first predicted the possibility to exploit the PD in brightness temperatures, $PD = TB_V - TB_H$, produced by oblate raindrops to distinguish cloud water from rain water in ground-based microwave brightness temperature measurements at vertical TB_V and horizontal TB_H polarization. The signal is explained by the fact that large rain drops have non-spherical shapes and tend to be flattened horizontally. Such particles produce negative PD the amplitude of which mainly depends on the radiometer frequency, the distribution of hydrometeors, and the observation slant angle. They also demonstrate that spherical raindrop shapes totally fail to explain the observations. Czekala, H., Crewell, S., Simmer, C., and Thiele, A., 2001 provided one of the first proofs of the predicted polarization signal and Czekala, H., Crewell, S., Hornbostel, A., et al., 2001b proposed a first simplified retrieval methodology based on the extra information given by the polarization difference to separate the total liquid water path into its two components, i.e. rain and cloud LWP. The authors show that if the polarization difference is not considered then cloud LWP can be largely overestimated.

Inversion algorithms for ground-based radiometer retrieval of surface rain-rates were presented by Marzano, F. S., Cimini, D., Ciotti, P., and Ware, R., 2005a; Marzano, F. S., Cimini, D., and Ware, R., 2005b; Marzano, F. and Visconti, G., 2002 with measurements from standard non-polarized microwave radiometers. In an even more ambitious approach Knupp, K. et al., 2009 showed the potential of microwave radiometers for profiling temperature within precipitating cloud systems up to mid-tropospheric levels.

Radar systems have largely been utilized to observe the weather, however depending on the wavelength radar based retrievals are usually developed either to estimate rainfall or non-precipitating clouds. Centimeter wavelength radars (weather radars) that are traditionally used for rain rate estimation, are typically not sensitive to cloud droplets. On the other hand, millimetre wavelength radars (cloud radars) are often used for remote sensing of non-precipitating clouds, suffering significant signal attenuation in rainfall (Matrosov, S., 2009b). Recently dual-frequency radar systems have shown some interesting features and potential to estimate cloud liquid water profiles for vertical observations of stratocumulus clouds (Hogan, R., Gaussiat, N., and Illingworth, A., 2005). But radar based retrieval techniques suffer from the fact that rain masks the backscatter signal from clouds along the observation volume. Thus multi-frequency passive radiometers have an advantage over active instruments not only from the point of view of reliable measurements but also in terms of cost and long term maintenance.

—
The spinal column of the present work is the introduction of the **ADvanced Microwave Radiometer for Rain Identification (ADMIRARI)**, its potential for novel observations and required retrieval techniques for deriving precipitating cloud parameters.

Battaglia, A., Saavedra, P., Rose, T., and Simmer, C. (2010) and Battaglia, A., Saavedra, P., Simmer, C., and Rose, T. (2009) and Saavedra, P., Battaglia, A., and Simmer, C. (2012b)

have already published results for a variety of case studies, which document the capability of the new instrument to assess continuously and simultaneously the [C_LWP](#), [R_LWP](#), and [IWV](#) during rain.

The present document is structured in six chapters: Chapter [2](#) provides an introduction to terminology and general concepts for the Radiative Transfer problem for precipitating cloud. Chapter [3](#) introduces the remote sensing instrumentation used in the present work, namely the passive radiometer ADMIRARI and a set of ancillary active sensors. The inversion method adopted for the retrieval of precipitating cloud parameters with a detailed sensitivity study are presented in chapter [4](#). In chapter [6](#) the measurements from specific field campaigns and mainly the results from the retrieval scheme applied to those measurements are presented. Finally in chapter [9](#) relevant conclusions are summarized along with discussion on the envisaged future work.

2. Radiative Transfer in Precipitating Clouds

Abstract

In this chapter fundamental concepts on radiative transfer for the microwave region of the spectrum are introduced. The mathematical formalism for the radiative processes occurring in an absorbing/emitting and scattering medium are treated as well as key definitions like brightness temperature are presented. An in-depth treatment of radiative transfer is beyond the scope of this chapter, rather general concepts are found in order to support the next chapters related to forward modelling for retrieving precipitating parameters.

2.1. Microwave Radiative Transfer Formulation

The key variable for describing the radiation field is the spectral radiance, which is directly measured by radiometers. To describe the spatial and angular dependence of such variable it is necessary to solve the [Radiative Transfer Equation \(RTE\)](#). This equation describes the modification of the radiation intensity due to emission and extinction as it travels throughout a medium, in this case the atmosphere. The extinction is responsible of the reduction of radiation due to two processes, absorption and scattering.

In a simplified approach of the theory, an starting point is the description of the radiation field in terms of the specific intensity I_ν , that is the instantaneous radiation power which passes through each point of the medium per unit of area dA , per unit of frequency interval $d\nu$, and at a given direction per unit of solid angle $d\Omega$ (figure 2.1). The variation of I_ν through an infinitesimal distance ds along the direction of propagation is obtained by considering the sources and sinks of the radiation in an infinitesimal volume element along the line. This is expressed as a differential form of the radiative transfer equation

$$\frac{dI_\nu}{ds} = -I_\nu \alpha + S \quad (2.1)$$

in this simplified case α represents only the absorption coefficient ¹, e.g. the loss of energy. Then S represent the source or gain of energy into the propagation direction.

Generally the scattering into and from other directions can lead to both losses and gains to the intensity and can be taken into account in the terms S and α . When scattering is neglected, as in the above case, the source term S express only the locally generated contribution to the radiation due to emission, and the coefficient α , which has a contribution only from absorption, becomes a characteristic of the medium that describes a true loss of energy from the radiation field into the medium. Under the assumption of local thermodynamic equilibrium (the local kinetic temperature is equal to the temperature of the radiation field given by Planck law) and absence of scattering, the strict requirement of balance between the energy absorption and emitted by the volume element into consideration leads to the Kirchoff's law

¹Generally α is the extinction coefficient which includes absorption and scattering

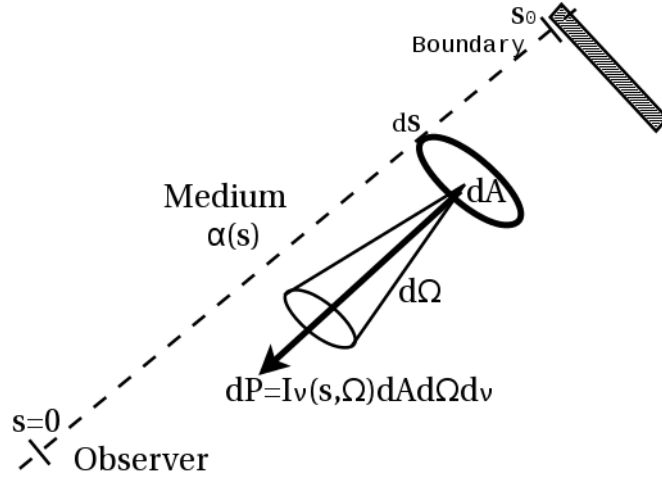


Figure 2.1.: Assumed geometry for the remote sensing of the atmosphere. The specific intensity is the radiant energy flowing at each point in the medium per unit area normal to the flux, per unit solid angle, in a frequency interval dv . The variation of intensity with position is governed by the radiative transfer equation.

for the source term,

$$S = \alpha B_\nu(T) \quad (2.2)$$

with $B_\nu(T)$ being the Planck's function,

$$B_\nu(T) = \frac{2h\nu^3}{c^2} \frac{1}{e^{h\nu/k_B T} - 1} \quad (2.3)$$

whit $c = 2.997925 \times 10^8 \text{ m s}^{-1}$ the speed of light in vacuum, $h = 6.62606957 \times 10^{-34} \text{ m}^2 \text{ kg s}^{-1}$ the Planck's constant, $k_B = 1.3806488 \times 10^{-23} \text{ m}^2 \text{ kg s}^{-2} \text{ K}^{-1}$ the Boltzman's constant, and ν represents the frequency. The factor 2 in the numerator accounts for both polarizations. $B_\nu(T)$ is also know as the surface brightness of a black-body emitter as viewed through free space in the solid angle element that produces a flow of energy equivalent to I_ν .

With the assumption in equation 2.2 and the neglecting of scattering in the absorption coefficient α , all terms in equation 2.1 depend only on the intensity along the path of propagation. Thus, by substituting S and $B_\nu(T)$, the transfer equation becomes a standard differential equation for which the complete solution is readily obtained as

$$I_\nu(0) = I_\nu(s_0) e^{-\tau(s_0)} + \int_0^{s_0} B_\nu(T) e^{-\tau(s)} \alpha ds \quad (2.4)$$

where τ is the optical thickness and is defined as

$$\tau(s) = \int_0^s \alpha(\xi) d\xi \quad (2.5)$$

with the integration extending from an observation point $s = 0$ through the medium along the path of propagation and ends at some boundary $s = s_0$ where the intensity has a value of $I_\nu(s_0)$ and direction towards the observation point (figure 2.1).

In case of thermal radiation it is common practice to translate the specific intensity $I_\nu(s)$ into **Brightness temperature (TB)**. According to Planck's law a black-body² emits an intensity $B_\nu(T)$ given by 2.3, however natural media rarely fits into the black-body definition, meaning that they emit less radiation. The brightness temperature **TB** is defined as the temperature at which the black-body emission $B_\nu(T_B)$ matches the measured intensity I_ν , i.e. $I_\nu = B_\nu(T_B)$. By inverting Planck's function (equation 2.3) for a measured intensity one obtains the corresponding brightness temperature

$$T_B = B_\nu^{-1}(I_\nu) \quad (2.6)$$

In microwave radiometry a common used approximation is given by the Rayleigh-Jeans approximation

$$B_\nu = \frac{2k_B T \nu^2}{c^2}, \quad (2.7)$$

accurate enough in cases where $h\nu \ll k_B T$, condition valid in almost the whole microwave region with typical temperatures in the lower atmosphere (Janssen, M. A., 1993, section 1.2.2).

By using the brightness temperature definition, equation 2.4 can be rewritten as

$$T_B(\nu) = T_{B0}(\nu) e^{-\tau(s_0)} + \int_0^{s_0} T(s) e^{-\tau(s)} \alpha ds \quad (2.8)$$

with the background brightness temperature T_{B0} derived from the general boundary condition as $T_{B0} = \lambda^2/2k_B I_\nu(s_0)$.

2.2. Polarized RTE

The definition of a polarized electromagnetic wave is described by the time dependent electric field $\vec{E}(t)$, with respect to a right-handed Cartesian coordinate system as a reference frame, having its origin inside the particle (laboratory coordinate system). The field components can be projected to two perpendicular vectors in the plane orthogonal to the direction of propagation:

$$\vec{E}(t) = \vec{E}_h(t) + \vec{E}_v(t) = E_h(t)\hat{e}_h + E_v(t)\hat{e}_v \quad (2.9)$$

The direction of propagation of a transverse electromagnetic wave is specified by the unit vector \hat{s} , the unit vectors \hat{e}_h and \hat{e}_v must fulfil the condition of orthogonality, such that $\hat{s} = \hat{e}_h \times \hat{e}_v$. The subscripts are relative to the local frame of reference when considering a scattering process for the wave. The field \vec{E} might have any polarization state, however is generally defined as elliptically polarized and the components h and v are chosen for decomposition of the electromagnetic wave into orthogonal components.

The elliptically polarized wave with circular frequency $\omega = 2\pi\nu$ can be expressed with four constants for the amplitudes and phases

$$\begin{aligned} a_h &= a_{0h} \sin(\omega t - \varepsilon_h) \\ a_v &= a_{0v} \sin(\omega t - \varepsilon_v) \end{aligned} \quad (2.10)$$

²A black-body is defined as idealized absorber with an emissivity of $\varepsilon=1$

These equations give the real numbers that define the amplitude within the local (h,v) system. The complex electric field components of an electromagnetic wave travelling in a specific direction z can also be written as

$$\begin{aligned} E_h &= a_{0h} e^{-i\delta_h} e^{-kz+i\omega t} \\ E_v &= a_{0v} e^{-i\delta_v} e^{-kz+i\omega t} \end{aligned} \quad (2.11)$$

with the phase lag $\delta = \varepsilon_h - \varepsilon_v$ between both components of the wave. It is obvious that the two amplitudes and a phase difference are sufficient to describe the state of polarization for an arbitrary elliptical wave (Czekala, H., 1999, chapter 2).

2.2.1. Intensity Formalism

Polarimetric optical instruments cannot measure the electric field associated with a beam of light but rather measure some quantities that are quadratic combinations of the electric field components. Therefore it is convenient to introduce the so-called Stokes parameters of the monochromatic orthogonal electromagnetic wave defined in the previous section, thus the Stokes vector $\vec{I} = (I, Q, U, V)^T$ are defined by the field components (Mishchenko, M., Hovenier, J., and Travis, L., 2000):

$$\begin{pmatrix} I \\ Q \\ U \\ V \end{pmatrix} = \begin{pmatrix} 1 & 1 & 0 & 0 \\ 1 & -1 & 0 & 0 \\ 0 & 0 & -1 & -1 \\ 0 & 0 & i & -i \end{pmatrix} \begin{pmatrix} E_h E_h^* \\ E_v E_v^* \\ E_h^* E_v \\ E_h E_v^* \end{pmatrix} \quad (2.12)$$

The vector \vec{I} can also be expressed with the real amplitudes (a_{0h} and a_{0v}) and the phase difference δ in the more suitable way as

$$\vec{I} = \begin{pmatrix} I \\ Q \\ U \\ V \end{pmatrix} = \begin{pmatrix} a_{0h}^2 + a_{0v}^2 \\ a_{0h}^2 - a_{0v}^2 \\ -2a_{0h}a_{0v}\cos\delta \\ 2a_{0h}a_{0v}\sin\delta \end{pmatrix} \quad (2.13)$$

The first Stoke parameter I gives the total intensity while Q indicates the degree of linear polarization. The plane of polarization (with respect to the frame of reference \hat{e}_h and \hat{e}_v) is described by the parameter U according to

$$\tan(2\chi) = \frac{U}{Q} \quad (2.14)$$

being χ the angle between the unit vector \hat{e}_h and the longest axis of the ellipse. Moreover the ellipticity, that is, the ratio of the minor to major axis of the ellipse, is given by

$$\tan(2\beta) = -\frac{V}{\sqrt{Q^2 + U^2}} \quad (2.15)$$

the sign of V specifies the handedness of polarization: the polarization is left-handed for positive V and right-handed for negative V .

As follow from the definition of the Stokes parameters, for an elementary monochromatic plane or spherical electromagnetic wave, the total intensity obeys the relation

$$I^2 \equiv Q^2 + U^2 + V^2 \quad (2.16)$$

However, light beams that are commonly measured are incoherent mixtures of many elementary plane waves. Since there are no permanent phase relations between these elementary waves, the Stoke parameters obey the fundamental property of additivity i.e. the Stoke parameters for the mixture are sums of the respective Stoke parameters of the elementary waves (Mishchenko, M., Hovenier, J., and Travis, L., 2000). In this case the identity before is replaces by the inequality

$$I^2 \geq Q^2 + U^2 + V^2 \quad (2.17)$$

Moreover the Stokes parameters polarization can be characterised as

$$\begin{aligned} Q^2 + U^2 + V^2 &= I^2 && \text{fully polarized} \\ Q^2 + U^2 + V^2 &\leq I^2 && \text{partially polarized} \\ Q = U = V &= 0 && \text{totally un-polarized} \end{aligned} \quad (2.18)$$

The degree of polarization p is defined by the ratio

$$p = \frac{\sqrt{Q^2 + U^2 + V^2}}{I} \leq 1 \quad (2.19)$$

and is equal to unity for fully polarized light. The state of polarization is fully described by means the three parameters (Q, U, V) , which makes the Stokes vector the ideal concept for the representation of polarized electromagnetic waves in a combination with the transfer equation. Sums and differences of Stokes vectors are justified by the fact that does not exist a well-defined phase relation between single waves originating from thermal emission on the macroscopic scale.

2.3. Vector Radiative Transfer Equation

The radiative transfer equation for polarized light uses the Stokes vector instead of the scalar intensity (equation 2.4). Since the components of the Stokes vector are intensities themselves then scalar intensities are exchanged with vectors of intensities, the parameters describing loss, gain and redistribution are modified to account for the vectorial nature of the radiation. In the presence of mixture of independent scatterers, for which the incoherent addition property of Stokes parameter is valid, the differential change of the Stokes vector, in a point of the space \vec{r} and direction of intensity propagation given by the unit vector \hat{s} , is described by the differential vector radiative transfer equation (Battaglia, A. and Mantovani, S., 2005; Janssen, M. A., 1993, pp. 91-92)

$$\begin{aligned} \hat{s} \cdot \nabla \vec{I}_V(\vec{r}, \hat{s}) &= -\alpha_{eV}(\vec{r}, \hat{s}) \cdot \vec{I}_V(\vec{r}, \hat{s}) + \vec{\alpha}_{aV}(\vec{r}, -\hat{s}) B_V(T) \\ &+ \int_{4\pi} \mathbf{Z}_V(\vec{r}, \hat{s}, \hat{s}') \cdot \vec{I}_V(\vec{r}, \hat{s}') d\Omega' \end{aligned} \quad (2.20)$$

where α_{eV} is the extinction matrix, $\vec{\alpha}_{aV}$ is the absorption vector, \mathbf{Z}_V is the four-by-four phase matrix. All these quantities can be calculated from the complex amplitude scattering function

\vec{I}_v (equation 2.13). The extinction matrix, absorption vector, and phase matrix describe the macroscopic interaction of the radiation field with absorbing and scattering gases and particles. The spectral intensity function $B_v(T)$ is the energy density emitted by a black-body (for one of two orthogonal modes) at thermodynamic temperature T .

The scattering phase matrix \mathbf{Z}_v and the extinction matrix $\alpha_{e,v}$ are non-diagonal and thereupon all their components are coupled. The emission source is a vector with four different and non-zero emission coefficients, one for each Stokes component. Moreover, the extinction, emission, and scattering matrices do not only depend on polarization but also on the specific direction. In case of scattering two directions in space have to be taken into account, namely the incoming and the outgoing beam.

The differential RTE (equation 2.20) is a phenomenological relation based on the detailed balancing of energy flux at each point in space and each frequency, and assumes that all scattered fields are incoherent. Macroscopic wave-interference phenomena, such as propagation path bending in an atmosphere with an inhomogeneous refractive index, coherent superposition of scattered waves near medium discontinuities, or multiple-coherent scattering are not modelled (Janssen, M. A., 1993, section 3.1).

2.4. Interaction Parameters

The numerical quantities which determine how much of the radiation within the atmosphere is emitted, scattered, and absorbed are called interaction parameters since they describe the interaction processes of electromagnetic waves with matter. For the ensemble of atmospheric constituents the interaction parameters are calculated with regard to the corresponding different physical processes that are involved. These processes are not the same for liquid, solid, and gaseous matter. The total quantities at every location of the medium then are calculated by adding the results for all constituents.

2.4.1. Gaseous Absorption

For the propagation of microwave radiation through the atmosphere, the assumption of constant intensity I_v throughout the path does not hold. Even if clear sky conditions are assumed, atmospheric gases like water vapour (H_2O) and molecular oxygen (O_2) are responsible of significant absorption. Due to their small particle sizes of these gases, scattering at microwave will be negligible. The absorption by nitrogen (N_2 , the most abundant gas in the atmosphere) is small compared to H_2O and O_2 , but becomes significant at high altitudes.

The absorption by the molecules is related to transitions between rotational and vibrational resonance states. They occur at specific frequencies characteristic for each molecule and their intensity is dependent on environmental parameters like temperature and density.

An example of the absorption spectrum for frequencies below 100GHz is shown in figure 2.2 (when scattering is dismissed the extinction coefficient is equal to absorption α in equation 2.1). In the lower microwave region (below 40GHz), a weakly absorbing, pressure-broadened water vapour line at 22.235GHz is dominant (figure 2.2). Moving to higher frequencies a window region with highest transmittance at around 31.4GHz is followed by a strong oxygen absorption complex around 60GHz caused by magnetic dipole transitions resulting in a complete opaque atmosphere. The decrease in transmittance towards the center of the complex

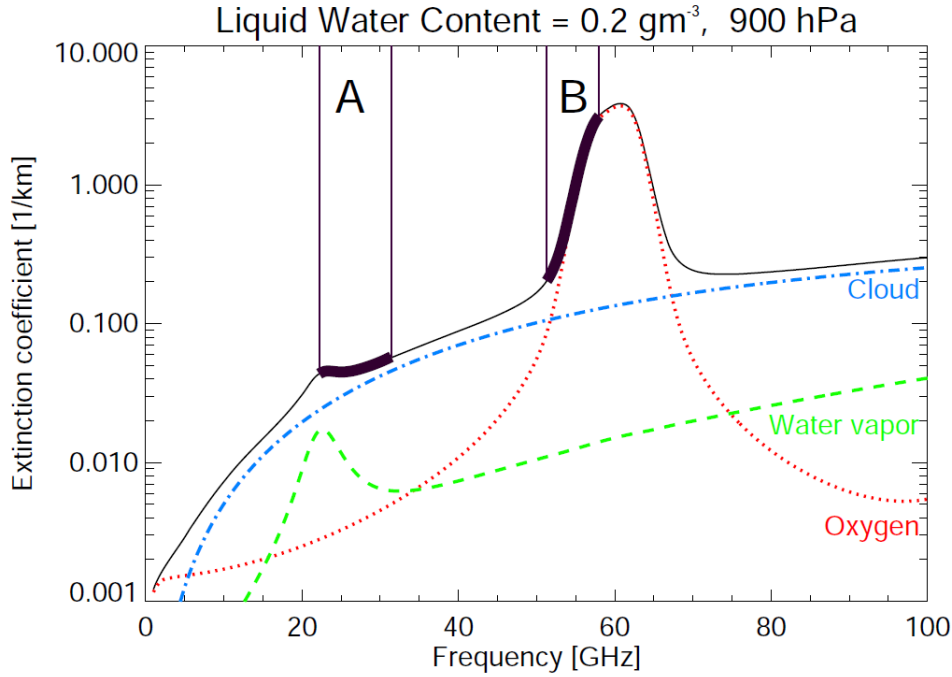


Figure 2.2.: Atmospheric extinction in the microwave spectrum for a cloudy atmosphere. The red dotted line indicates the contribution by O_2 , the green dashed line is the water vapour and the blue dotted-dashed line indicates the contribution by LWC of 0.2 gm^{-3} . While the black solid line is the result of adding all components. The frequency bands normally used by conventional radiometers are show by A and B. (Extracted from Pospichal, B., 2009)

is often used for temperature profiling of the atmosphere (Janssen, M. A., 1993; Löhnert, U., 2002).

The optical thickness $\tau(s)$ of a medium (equation 2.5) is defined as the integrated absorption coefficient over the ray path of light propagation through the medium. The corresponding transmission is given by the ratio of attenuated intensity to incident intensity as

$$T = \frac{I(s)}{I_0} = \exp(-\tau(s)) \quad (2.21)$$

The resonant frequencies produce a total optical thickness between 1 and 100 for a typical path of 10km, and therefore a total transmission close to zero. The resonant regions are separated by transparent regions with optical thickness below 0.1 enabling the remote sensing of the lower atmosphere and surface conditions by space-borne instruments.

The absorption model by (Liebe, H. J., Hufford, G. A., and Cotton, M. G., 1993) applied in this study considers contributions by water vapour, oxygen, and nitrogen. However in the higher microwave region narrow absorption lines by traces gases (mainly ozone O_3) become relevant.

For surface observations the optical thickness due to water vapour and oxygen is high enough for a saturation of the observed temperature. At higher altitudes the line spectrum caused by a large number of trace gases become relevant and must be included by absorption models specially for observations from space or observations in very cold and dry atmosphere, especially at high altitudes.

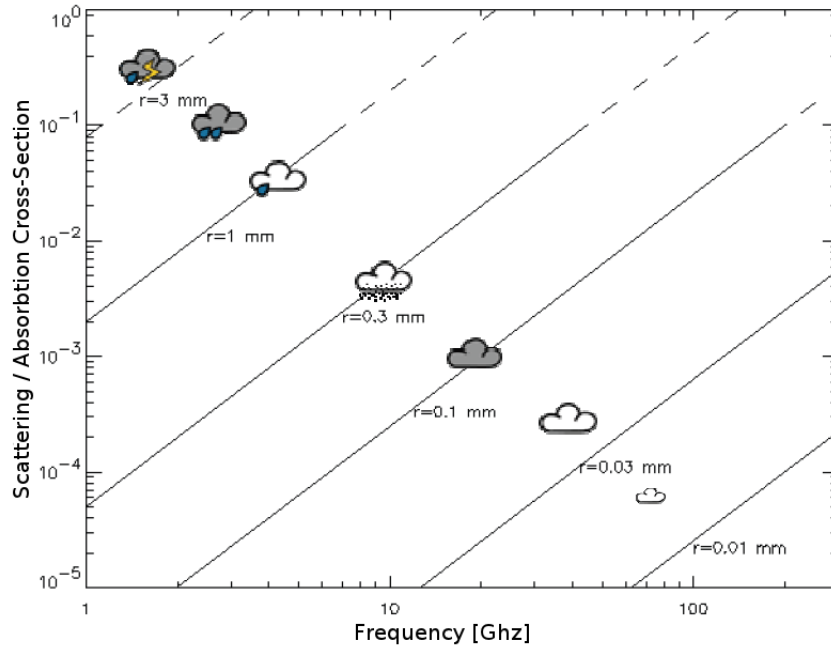


Figure 2.3.: Ratio of scattering to absorption cross-section microwave spectrum for water droplets of radius r . Typical droplet size ranges are indicated for clouds with and without rain. (Extracted from Hewison, T.J. (2006) adapted from Janssen, M. A., 1993).

2.4.2. Scattering and Absorption by Hydrometeors

The interaction of the radiation field with hydrometeors is based on the scattering and absorption of coherent electromagnetic waves propagating in a poly-dispersion of liquid and ice dielectric particles. The size distribution and phase of hydrometeors vary widely, depending on the particular precipitation regime or cloud type (e.g. cumulus cloud, cumulus-nimbus, dissipating stage rain cell, cirrus anvil or stratiform cirrus) as well as the ambient temperature, geographical location, and season. For purposes of microwave radiative transfer modelling, hydrometeors can be categorized into the following:

- 1.) Liquid droplets of radius less than $\sim 50 \mu\text{m}$, commonly assigned to non-precipitating cumulus and stratus clouds, fog and haze.
- 2.) Liquid precipitation, with radius ranging from $\sim 50 \mu\text{m}$ to $\sim 5 \text{mm}$. Presenting a horizontally oblate shapes due to viscous forces.
- 3.) Frozen particles of dimensions $\sim 1 \text{mm}$ or less, having a needle-, plate-, or dendrite-shape.
- 4.) Frozen large particles, with sizes ranging from 1mm to $\sim 10 \text{mm}$, (e.g., snow, hail, or graupel). Commonly comprised of a combination of liquid and ice, mixed with regions of air.

Liquid hydrometeors of radius less than $\sim 50 \mu\text{m}$ absorb microwave radiation significantly, but scatter very little (figure 2.3). The absorption coefficient $\tilde{\alpha}_{av}$ (clouds), for a distribution of particles in the radius range till $\sim 50 \mu\text{m}$ can be calculated using the optical extinction theorem

(Janssen, M. A., 1993, p. 93)

$$\alpha_{av}^{\text{cloud}} = 6\pi \times 10^{-2} \nu \text{LWC} \frac{\Im\{\epsilon_w\}}{|\epsilon_w + 2|^2} \quad (2.22)$$

which is proportional to the **Liquid Water Content (LWC)**, where ν is the frequency, and ϵ_w is the relative dielectric constant of cloud liquid water. Thus, in an atmosphere composed by small cloud droplets only absorption and emission occurs.

For large liquid or frozen hydrometeors (e.g., rain, snow, hail, and cirrus ice), microwave scattering can be strongly significant, specially at high frequencies (see middle- to upper-left sector in figure 2.3). Furthermore, the absorption and scattering are dependent on the particle size distribution and particle shape, in addition to total water density. In case of stratiform and convective precipitation cells, the approximation made in equation 2.22 is not applicable for microwave frequencies below 30GHz. In that case the precipitation cells can be modelled by sparse distribution of electrically large liquid-, ice-, or mixed-phase spheres. For this type of precipitation the typical hydrometeor separations are in the order of ~ 1 cm for a large cloud drop of radius $\sim 50 \mu\text{m}$, and ~ 10 cm for rain drops of radius ~ 1 mm (Rodgers, C. D., 2000). Thus, at frequencies below 30GHz ($\lambda \sim 1$ cm), hydrometeors can be considered to scatter and absorb independently due to electrically large inter-separation distances.

Viscous forces shape raindrops with an oblate shape as they fall, with the minor axis in the direction of relative airflow. Nevertheless, the axial-ratio depends on the equivolumetric diameter D_e according to equation 4.79 (Matrosov, S., Clark, K., Martner, B., and Tokay, A., 2002), with $D_e > 0.05$ cm.

For small drops, surface tension dominates over hydrodynamic forces and the drop shapes are nearly spherical (see figure 4.5). Drops as large as 4 mm in diameter exhibit axial ratios of ~ 0.8 , and those larger than 8 mm are hydrodynamically unstable, and tend to break-up into small drops (Rodgers, C. D., 2000, figure 10.5). Therefore, the assumption of spherical raindrops will be compromised by drop-shape variations when the diameters are larger than ~ 3 mm.

2.4.2.1. Scattering and Absorption by Sparse Distribution of Particles

Scattering and absorption by sparse particle distribution is based on the field radiated by a single particle excited by an incident plane wave of a given amplitude and polarization. The scattering function matrix $\mathbf{S}(\theta_s, \phi_s, \theta_i, \phi_i)$ describes the amplitude and polarization of the scattered wave along any direction at a distance r far from the scatterer:

$$\begin{bmatrix} E_{hs}(r, \theta_s, \phi_s) \\ E_{vs}(r, \theta_s, \phi_s) \end{bmatrix} = \frac{\exp(-ik_0 r)}{r} \mathbf{S}(\theta_s, \phi_s, \theta_i, \phi_i) \cdot \begin{bmatrix} E_{hi}(0, \theta_i, \phi_i) \\ E_{vi}(0, \theta_i, \phi_i) \end{bmatrix} \quad (2.23)$$

where E_i and E_s are the complex electric fields of the incident and scattered waves respectively, and $k_0 = 2\pi/\lambda$ the wave number. It is assumed a spherical coordinate system with the origin at the center of the scatterer and with the z-axis in the vertical direction. In terms of the vertical and horizontal polarization \mathbf{S} might be expressed as

$$\mathbf{S} = \begin{bmatrix} f_{vv}(\theta_s, \phi_s, \theta_i, \phi_i) & f_{vh}(\theta_s, \phi_s, \theta_i, \phi_i) \\ f_{hv}(\theta_s, \phi_s, \theta_i, \phi_i) & f_{hh}(\theta_s, \phi_s, \theta_i, \phi_i) \end{bmatrix} \quad (2.24)$$

2. Radiative Transfer in Precipitating Clouds

The Stokes vector of the incident and scattered radiation fields (\vec{I}_i and \vec{I}_s) can be found from the electric fields \vec{E}_i and \vec{E}_s . The Stokes' matrix σ describes the resulting relationship between the incident and the scattered Stokes' vectors according to

$$\vec{I}_s = \frac{1}{r^2} \sigma(\theta_s, \phi_s, \theta_i, \phi_i) \cdot \vec{I}_i \quad (2.25)$$

and

$$\sigma(\theta_s, \phi_s, \theta_i, \phi_i) = \begin{bmatrix} |f_{vv}|^2 & |f_{vh}|^2 \\ |f_{hv}|^2 & |f_{hh}|^2 \\ 2\Re\{f_{vv}f_{hv}^*\} & 2\Re\{f_{vh}f_{hh}^*\} \\ 2\Im\{f_{vv}f_{hv}^*\} & 2\Im\{f_{vh}f_{hh}^*\} \\ \Re\{f_{vh}f_{vv}^*\} & \Im\{f_{vv}f_{vh}^*\} \\ \Re\{f_{hh}f_{hv}^*\} & \Im\{f_{hv}f_{hh}^*\} \\ \Re\{f_{vv}f_{hh}^* + f_{vh}f_{hv}^*\} & -\Im\{f_{vv}f_{hh}^* - f_{vh}f_{hv}^*\} \\ \Im\{f_{vv}f_{hh}^* + f_{vh}f_{hv}^*\} & \Re\{f_{vv}f_{hh}^* - f_{vh}f_{hv}^*\} \end{bmatrix} \quad (2.26)$$

with $\Re\{\cdot\}$ and $\Im\{\cdot\}$ indicating the real and imaginary part, respectively, of the complex number within curved-brackets.

The phase matrix is subsequently computed by averaging over an ensemble of particles of varying geometry, orientation, and dielectric constitution

$$\mathbf{Z}(\theta_s, \phi_s, \theta_i, \phi_i) = n_0 \sum_{particles} \sigma(\theta_s, \phi_s, \theta_i, \phi_i) \quad (2.27)$$

where n_0 is the total particle density, and each particle is assumed to scatter incoherently.

From the scattering function, the frequency dependent extinction matrix $\alpha_{e\nu}$ can be calculated under Foldy's effective field approximation Janssen, M. A., 1993, and references therein by

$$\alpha_e(\theta_i, \phi_i) = \begin{bmatrix} -2\Re\{M_{vv}\} & 0 & -\Re\{M_{vh}\} \\ 0 & -2\Re\{M_{hh}\} & -\Re\{M_{hv}\} \\ -2\Re\{M_{hv}\} & -2\Re\{M_{vh}\} & -(\Re\{M_{vv}\} + \Re\{M_{hh}\}) \\ 2\Im\{M_{hv}\} & -2\Im\{M_{vh}\} & -(\Im\{M_{vv}\} - \Im\{M_{hh}\}) \\ -\Im\{M_{vh}\} & \Im\{M_{hv}\} & \\ (\Im\{M_{vv}\} - \Im\{M_{hh}\}) & & \\ -(\Re\{M_{vv}\} + \Re\{M_{hh}\}) & & \end{bmatrix} + \alpha_a^{gases} I \quad (2.28)$$

where $M_{xx} = (i2\pi n_0/k_0) \langle f_{xx}(\theta, \phi; \theta, \phi) \rangle$, and $\langle \cdot \rangle$ denotes the expectation operator. The total gaseous absorption coefficient α_a^{gases} is a sum of the background absorption due to all of the constituent molecules

$$\alpha_a^{gases} = \sum_j \alpha_{a;j}, \quad j \in \{\text{molecules}\}$$

and I is the identity matrix. The diagonal elements of α_e are the attenuation rates of the coherent part of the wave, and are consistent with the optical extinction theorem (Janssen, M. A., 1993, p. 97).

From the phase matrix \mathbf{Z} and extinction matrix α_{ev} , the absorption vector $\vec{\alpha}_{av}$ for the particles is computed as

$$\vec{\alpha}_a(\theta_i, \phi_i) = \begin{bmatrix} \alpha_{e11}(\theta_i, \phi_i) - \int_{4\pi} [Z_{11}(\theta_s, \phi_s; \theta_i, \phi_i) + Z_{21}(\theta_s, \phi_s; \theta_i, \phi_i)] d\Omega'_s \\ \alpha_{e22}(\theta_i, \phi_i) - \int_{4\pi} [Z_{12}(\theta_s, \phi_s; \theta_i, \phi_i) + Z_{22}(\theta_s, \phi_s; \theta_i, \phi_i)] d\Omega'_s \\ 2(\alpha_{e13}(\theta_i, \phi_i) + \alpha_{e23}(\theta_i, \phi_i) - \int_{4\pi} [Z_{13}(\theta_s, \phi_s; \theta_i, \phi_i) + Z_{23}(\theta_s, \phi_s; \theta_i, \phi_i)] d\Omega'_s) \\ 2(-\alpha_{e14}(\theta_i, \phi_i) - \alpha_{e24}(\theta_i, \phi_i) + \int_{4\pi} [Z_{14}(\theta_s, \phi_s; \theta_i, \phi_i) + Z_{24}(\theta_s, \phi_s; \theta_i, \phi_i)] d\Omega'_s) \end{bmatrix} \quad (2.29)$$

For decoupled third and fourth components of the Stokes vector the absorption, extinction, and scattering matrices reduce to the following simple forms

$$\begin{aligned} \alpha_e(\theta_i, \phi_i) &= \begin{bmatrix} -2\Re\{M_{vv}\} & 0 \\ 0 & -2\Re\{M_{hh}\} \end{bmatrix}, \\ \mathbf{Z}(\theta_s, \phi_s; \theta_i, \phi_i) &= \begin{bmatrix} |f_{vv}|^2 & |f_{vh}|^2 \\ |f_{hv}|^2 & |f_{hh}|^2 \end{bmatrix}, \\ \vec{\alpha}_a(\theta_i, \phi_i) &= \begin{bmatrix} \alpha_{e11}(\theta_i, \phi_i) - \int_{4\pi} [Z_{11}(\theta_s, \phi_s; \theta_i, \phi_i) + Z_{21}(\theta_s, \phi_s; \theta_i, \phi_i)] d\Omega'_s \\ \alpha_{e22}(\theta_i, \phi_i) - \int_{4\pi} [Z_{12}(\theta_s, \phi_s; \theta_i, \phi_i) + Z_{22}(\theta_s, \phi_s; \theta_i, \phi_i)] d\Omega'_s \end{bmatrix} \end{aligned} \quad (2.30)$$

In case of spherical (axial ratio equal 1) or non-spherical particles randomly oriented within an ensemble, the absorption and scattering cross sections and therefore the extinction cross section do not depend either on direction or polarization. Thus, they can be represented by simple scalar numbers designated as efficiencies, defined for spherical particles with radius r as

$$Q_a = \frac{\sigma_a}{\pi r^2}, \quad \text{absorption} \quad (2.31)$$

$$Q_e = \frac{\sigma_e}{\pi r^2}, \quad \text{extinction} \quad (2.32)$$

which are the radiative cross sections divided by their geometric cross sections. Thereby, the extinction efficiency is a measure of how effective a particle can block a beam of light in relation to its geometric size $2\pi r^2$. In the optical limit for large particles (compared with the wavelength) the extinction efficiency tends towards 2, thus the fraction of light, which is prevented from propagating forward with the same direction is twice the geometric size of the particle.

2.4.3. Boundary Conditions

In order to solve the vectorize RTE in the atmosphere, appropriate upper and lower boundary conditions are required in terms of reflection, scattering, and absorption of the microwave radiation.

Upper boundary

The upper boundary condition is straightforward obtained by assuming a background temperature at all incident angles of $\text{TB}_{\text{cmb}} = 2.73\text{K}$. The effect of the sun, a source with a brightness temperature above 6000 K, can be neglected in most instances for the following reason: The enormous intensity of the sun is only emitted within a very narrow angular interval. The width of the sun disk is approximately 0.5° , so even an antenna in up-looking geometry with a larger

beam width will only receive a diminished signal by averaging the sharp peak of the sun over the whole antenna pattern.

A radiometer with a 6° beam-width (see chapter 3) implies an approximately factor of 12 in angular resolution compared to the sun's peak. Therefore it will average the signal of the sun over an angular pattern which is larger than hundred times, thus leading to a reduction of the sun signal by a factor of ≈ 140 .

Surface

Reflection and absorption of microwave radiation at land surfaces cannot be calculated with sufficient accuracy for the remote sensing of rain at low frequencies, especially in the presence of canopy layers above the soil. Only in case of calm water surfaces there exists a quite accurate treatment of surface reflection.

The boundary conditions for the Vectorize RTE may be written as

$$\vec{I}^+(z_0) = \vec{\psi} B_v(T_0) + (1 - f_d) \mathbf{R}_s \vec{I}_m^- + \frac{f_d}{\pi} \left(\mathbf{R}_d \vec{I}_c^- + \int_0^{2\pi} \mathbf{R}_d \vec{I}^- \cos(\theta) d\varphi' \right), \quad (2.33)$$

$$\vec{I}^o(z_1) = \vec{I}_{ba}^o + \vec{I}_c^o \delta(\vartheta - \vartheta') \delta(\varphi - \varphi'), \quad (2.34)$$

where the superscripts +, -, and O represent radiation moving from the lower boundary at $z = z_0$ towards the domain, from the domain toward the lower boundary, and from outside the upper boundary at $z = z_1$ toward the domain, respectively. The vectors \vec{I}_{ba} and \vec{I}_c denote background and collimated radiation, respectively, \vec{I}_m^- is the Stokes vector in the direction mirroring that of \vec{I}^+ , and $\delta(\cdot)$ is the Dirac delta function. The symbol f_d is set to 1 for the case of diffuse reflection and is set to 0 for the case of specular reflection. The symbol $\vec{\psi}$ denotes the emission vector, $B_v(T_0)$ is the Planck black-body radiance (eq. 2.3) for the surface at temperature T_0 , and the symbols \mathbf{R}_s and \mathbf{R}_d are the bidirectional reflectance matrices for specular and diffuse reflection, respectively. Finally, $\cos(\theta)$ is the cosine of the angle between the propagation direction and the normal to the boundary under consideration. The equation 2.34 states that radiation transmitted from outside the boundary at $z = z_1$ is due to background and collimated radiation. Equation 2.33 states that the Stokes vector for radiation leaving the surface $z = z_0$ is due to emission plus contributions from secondary and diffusely reflected radiation (Mishchenko, M., Hovenier, J., and Travis, L., 2000).

The interaction of electromagnetic radiation with a plane boundary between two dielectric media might be described by either a Lambertian or Fresnel reflection.

A Lambertian, or diffuse, surface is an idealized surface that is "perfectly" rough and therefore emits and reflects equally in all directions. For such a surface, in which the reflected radiation is unpolarized, the bidirectional reflection matrix is given by

$$\mathbf{R}_d = \begin{bmatrix} \rho_{z0} & 0 & 0 & 0 \\ 0 & 0 & 0 & 0 \\ 0 & 0 & 0 & 0 \\ 0 & 0 & 0 & 0 \end{bmatrix}, \quad (2.35)$$

where ρ_{z0} is the hemispherical reflectance at the boundary. The emission vector for a Lamber-

tian surface is given by

$$\vec{\psi} = \begin{bmatrix} \psi_{z0} \\ 0 \\ 0 \\ 0 \end{bmatrix}, \quad (2.36)$$

where ψ_{z0} is the unpolarized hemispherical emittance of the boundary.

A Fresnel, or specular, surface is an idealized surface that is "perfectly" smooth, in which surface the reflected radiation is polarized and angle dependent. The bidirectional reflection matrix is given by

$$\mathbf{R}_s = \begin{bmatrix} \frac{1}{2}(|R_v|^2 + |R_h|^2) & \frac{1}{2}(|R_v|^2 - |R_h|^2) & 0 & 0 \\ \frac{1}{2}(|R_v|^2 - |R_h|^2) & \frac{1}{2}(|R_v|^2 + |R_h|^2) & 0 & 0 \\ 0 & 0 & \Re e(R_v R_h^*) & \Im m(R_v R_h^*) \\ 0 & 0 & -\Im m(R_v R_h^*) & \Re e(R_v R_h^*) \end{bmatrix}, \quad (2.37)$$

where the vertical and horizontal reflection coefficients are given by the Fresnel relations

$$R_v(\mu) = \frac{n^2 \mu - \sqrt{n^2 + \mu^2 - 1}}{n^2 \mu + \sqrt{n^2 + \mu^2 - 1}},$$

and

$$R_h(\mu) = \frac{\mu - \sqrt{n^2 + \mu^2 - 1}}{\mu + \sqrt{n^2 + \mu^2 - 1}},$$

where μ is the cosine of the incident angle, and n the surface refractive index of either water or ice. The radiation emissivity by a purely specular reflecting surface is also polarized and angle dependent, and the emission vector is given by

$$\vec{\psi} = \begin{bmatrix} 1 - \frac{1}{2}(|R_v|^2 + |R_h|^2) \\ -\frac{1}{2}(|R_v|^2 - |R_h|^2) \\ 0 \\ 0 \end{bmatrix}, \quad (2.38)$$

The emission vector $\vec{\psi}$ is used in equation 2.33 with $f_d = 1$ for case of a diffuse reflecting boundary (Lambertian) and $f_d = 0$ in case of a specular reflecting boundary (Fresnel).

2.5. Solution of the Radiative Transfer Equation

Remote sensing techniques requires the solution of the three-dimensional fully polarized RTE (equation 2.20) with boundary conditions. Equation 2.20 can be solved analytically only in cases where no scattering is considered e.g. cloudless atmosphere, but the presence of scattering prevents this solution.

In the Vectorized RTE the scattering process is described by the phase matrix depending on the incoming and outgoing direction, i.e. (θ_i, ϕ_i) and (θ_s, ϕ_s) . Together with the three positions in space, 2.20 is a seven dimensional set of equations. Because of the mixing between the component intensities of the Stokes vector by scattering and extinction, this set of four integro-differential equations is coupled. The problem can be simplified by making assumptions on the atmosphere, shape and orientation of the scattering particles for most of applications.

Prior to any numerical integration algorithm, the [Vectorized Radiative Transfer Equation \(VRTE\)](#) needs to be discretized, namely all continuous variables (such as position and angle of propagation direction) are approximated by a set of discrete values. Provided that the solving algorithm itself is not approximative, the resulting solution will converge to the true solution when the discretization is made fine enough. After the selection of a suitable discretization mechanism, three major tasks have to be performed (Czekala, H., 1999):

- definition of the geophysical environment in terms of atmospheric profiles of temperature, humidity, pressure, hydrometeor content, and hydrometeor size distributions,
- calculation of corresponding optical properties (interaction parameters), and
- solution of the [VRTE](#) by a numerical algorithm (integration schemes, successive order of scattering or Monte Carlo methods).

Numerical methods for the solution of the 3D [RTE](#) are categorized in two main classes: deterministic (or explicit) and statistical (or Monte Carlo) methods. Explicit methods represent the radiation field in some discrete fashion, and the elements of the field are iteratively adjusted until agreement with the RTE is achieved. After the iterations –once solved the whole radiance field– the desired radiative quantities are calculated from the radiation field elements. On the other hand, Monte Carlo methods estimate the desired radiative quantities statistically with some level of confidence the depends on the number of photons trajectories simulated and the variance of the estimate. Moreover the implicit dynamics of the radiative transfer, captured as order of scatter and photon path-length decomposition, can be obtained naturally by Monte Carlo methods.

The following sections highlights general features of explicit and statistically 3D radiative transfer solutions methods.

2.5.1. Plane-Parallel Radiative Transfer

One of the most common discrete method consists on assuming the concept of plane-parallel radiative transfer. Under this assumption the [VRTE](#) (equation 2.20) can be reformulated by performing a variable change of the infinitesimal ds to $d\tau = \alpha_{ev} \cdot d\hat{s}$, and $\mu = \cos(\theta)$, furthermore a transformation of the laboratory coordinates to match the incident and scatter plane with the z axis i.e. $\phi_s = 0$ and $\phi_i = 0$. Thus a monochromatic plane-parallel polarized radiative transfer equation with randomly oriented particles can be formulated as (Evans, K. and Stephens, G., 1991)

$$\begin{aligned} \mu \frac{d\vec{I}(\tau, \mu_s, \phi_s)}{d\tau} = & -\vec{I}(\tau, \mu_s, \phi_s) + (1 - \tilde{\omega})B_v(T) \begin{bmatrix} 1 \\ 0 \\ 0 \\ 0 \end{bmatrix} \\ & + \frac{\tilde{\omega}}{4\pi} \int_0^1 \int_{-1}^1 \mathbf{M}(\mu_s, \phi_s; \mu_i, \phi_i) \times \vec{I}(\tau, \mu_i, \phi_i) d\mu_i d\phi_i \\ & + \frac{F_0}{\mu_0} \frac{\tilde{\omega}}{4\pi} \exp(-\tau/\mu_0) \mathbf{M}(\mu_s, \phi_s; \mu_0, \phi_0) \times \begin{bmatrix} 1 \\ 0 \\ 0 \\ 0 \end{bmatrix}, \end{aligned} \quad (2.39)$$

where \vec{I} is the radiance field expressed as four-vector of the Stokes parameters (I, Q, U, V) in direction (μ_s, ϕ_s) at optical depth τ . \mathbf{M} is the 4×4 scattering (Mueller) matrix proportional to the phase matrix $\mathbf{Z}(\theta_s, \phi_s = 0; \theta_i, \phi_i = 0)$ (see equation 2.40) (Mishchenko, M., Hovenier, J., and Travis, L., 2000); $\tilde{\omega}$ the single scattering albedo, μ the cosine of the zenith angle and ϕ the azimuth angle. For the coordinate system under consideration ν is positive for downwards direction and τ increases downward (Evans, K. and Stephens, G., 1991).

The first term on the right hand side of equation 2.39 is the sink due to attenuation, the second and fourth terms are sources of diffuse radiation with the unpolarized thermal emission and a "pseudo-source" respectively, with $B_\nu(T)$ the Planck black-bode function and F_0 the unpolarized solar flux at the top of the atmosphere. While the third term is the source due to light scattered into the direction of propagation Marshak, A. and Davis, A., 2005, pp. 244-245.

The polarized transformation from the phase matrix \mathbf{Z} to the scattering matrix \mathbf{M} is expressed mathematically by (Evans, K. and Stephens, G., 1991)

$$\mathbf{M}(\mu_s, \phi_s; \mu_i, \phi_i) = \mathbf{L}(\eta_2 - \pi) \times \mathbf{Z}(\cos(\Theta)) \times \mathbf{L}(\eta_1) \quad (2.40)$$

For the Stokes basis, the polarization rotation matrix is

$$\mathbf{L}(\eta) = \begin{bmatrix} 1 & 0 & 0 & 0 \\ 0 & \cos(2\eta) & -\sin(2\eta) & 0 \\ 0 & \sin(2\eta) & \cos(2\eta) & 0 \\ 0 & 0 & 0 & 1 \end{bmatrix}, \quad (2.41)$$

where the rotation angle η with sub-indexes 1 and 2 are the angle between scattering plane and the meridional plane containing the incoming ray (θ_i, ϕ_i) , and the outgoing ray (θ_s, ϕ_s) , respectively.

The usual way to discretize the angular variables in plane-parallel RTE is to expand in a Fourier series in azimuth angle and use discrete angles in zenith. The Fourier series in azimuth converts the radiance from $\vec{I}(\tau, \mu, \phi)$ to $\vec{I}_m(\tau, \mu)$:

$$\vec{I}(\tau, \mu_s, \phi_s) = \sum_{m=0}^M \vec{I}_m(\tau, \mu_s) \cos[m(\phi_0 - \phi_s)] \quad (2.42)$$

If the scattering phase function is only a function of the scattering angle Θ_s , for randomly oriented particles with a plane of symmetry the 4-by-4 phase matrix can be expressed in terms of a Legendre series

$$\mathbf{M}(\cos(\Theta_s)) = \sum_{l=0}^N \chi_l \mathcal{P}_l(\cos(\Theta_s)), \quad (2.43)$$

where χ_l are the $N + 1$ Legendre coefficients and \mathcal{P}_l are the Legendre polynomials. Using the Legendre series representation for the phase function allows to calculate the Fourier transformation of the phase matrix with the addition theorem of spherical harmonics, the phase matrix is determined by (Marshak, A. and Davis, A., 2005, derivation details at pp. 244-245)

$$\mathbf{M}_{m_j j'}^{\pm \pm} = \sum_{l=m}^{N_\mu} (2 - \delta_{0m}) \frac{(l-m)!}{(l+m)!} \chi_l \mathcal{P}_l^m(\pm \mu_j) \mathcal{P}_l^m(\mu_{j'}), \quad (2.44)$$

where δ_{mm} is a Kronecker-delta symbol. The pluses representing downward radiance ($\mu > 0$), and the minuses representing upward radiance ($\mu < 0$).

2. Radiative Transfer in Precipitating Clouds

The next step is to discretize the cosine of the zenith angle μ , so the whole scattering integral becomes summation. By using Gaussian quadrature approximation the integrals are substituted by summations as

$$\int_{-1}^1 f(\mu) d\mu \approx \sum_{j=1}^{N_\mu} w_j f(\mu_j),$$

where μ_j are the discrete ordinates and w_j are the quadrature weights. Then, the discretized RTE results in:

$$\pm \mu_j \frac{dI_{mj}^\pm(\tau)}{d\tau} = I_{mj}^\pm(\tau) - \frac{\tilde{\omega}}{2} \sum_{j'=1}^{N_\mu} w_{j'} \left[\mathbf{M}_{mj'j'}^{\pm+} I_{mj'}^+ + \mathbf{M}_{mj'j'}^{\pm-} I_{mj'}^- \right] + S(\pm \mu_j) \quad (2.45)$$

where the radiance is a vector $I_{mj}^\pm(\tau) = I_m(\tau, \pm \mu)$, the phase matrix is given by equation 2.44, and the S is the discrete source term.

The plane-parallel RTE is now discretized in angle so that the radiance is a vector at each optical thickness, $\vec{I}^\pm(\tau)$, and the RTE results in an ordinary differential matrix equation

$$\mathbf{U} \frac{d}{d\tau} \begin{bmatrix} \vec{I}^+ \\ \vec{I}^- \end{bmatrix} = \begin{bmatrix} \vec{I}^+ \\ \vec{I}^- \end{bmatrix} - \begin{bmatrix} \mathbf{M}^{++} & \mathbf{M}^{+-} \\ \mathbf{M}^{-+} & \mathbf{M}^{--} \end{bmatrix} \begin{bmatrix} \vec{I}^+ \\ \vec{I}^- \end{bmatrix} - \begin{bmatrix} \vec{S}^+ \\ \vec{S}^- \end{bmatrix}, \quad (2.46)$$

with all matrices having $N_\mu \times N_\mu$ entries; where \mathbf{U} is a diagonal matrix with $\pm \mu_j$ entries, \mathbf{M} is the discrete ordinates phase matrix (including $\tilde{\omega}/2$ and weights w_j), and \vec{S} is the source vector.

The equation 2.46 is a discrete system in the angular variables, however the optical thickness needs to be discretized too, which can be done by means of a uniform grid and the derivative in the matrix RTE expressed with a finite difference. Thereafter resulting in an algebraic system to solve with radiance vector $\vec{I}_m(\tau_k, \mu_j)$ of length $N_\tau \times N_\mu$ for each Fourier azimuthal mode m .

The more commonly used methods are the doubling-adding method and the eigen-matrix method. The key concept behind the doubling and adding method is the interaction principle, which expresses the linear interaction of radiation with a medium. The radiation emerging from a layer (\vec{I}_0^- and \vec{I}_1^+) is related to the radiation incident upon the layer (\vec{I}_0^+ and \vec{I}_1^-) together with the radiation generated within the layer (using here the same signs nomenclature as Evans, K. and Stephens, G., 1991 i.e. \uparrow [-] and \downarrow [+]). With the formulation in terms of radiance vector, the interaction principle is given by

$$\begin{aligned} \vec{I}_1^- &= \mathbf{T}^+ \times \vec{I}_0^+ + \mathbf{R}^+ \times \vec{I}_1^- + \vec{S}^+, \\ \vec{I}_0^- &= \mathbf{T}^- \times \vec{I}_1^- + \mathbf{R}^- \times \vec{I}_0^+ + \vec{S}^-, \end{aligned} \quad (2.47)$$

where \mathbf{T} is the transmission matrix, \mathbf{R} the reflection matrix, and \vec{S} the source vector.

When the layer in question is the whole atmosphere (together with the surface), computing \mathbf{T} , \mathbf{R} and \vec{S} amounts to solve the radiative transfer equation. On the other hand, relating \mathbf{T} , \mathbf{R} and \vec{S} for an infinitesimal layer to the single scattering information into a form suitable for applying the interaction principle and, second, using the doubling and adding method to compute the properties of the whole atmosphere from the local -infinitesimal layer- properties. For the present work the [Radiative Transfer, version 4 \(RT4\)](#) code for radiative transfer numerical solution developed by Evans, K. and Stephens, G., 1991 is used.

2.5.2. Monte Carlo Methods

The previous section has described a method to solve the vector radiative transfer equation (2.20), by considering a plane-parallel horizontally homogeneous one-dimensional atmosphere, a numerical method commonly used to study cloudy or precipitating atmospheres (e.g. Czekala, H. and Simmer, C., 1998; Evans, K. and Stephens, G., 1991). However more complicated scenarios requires to treat the RTE as fully polarized 3D approach, which has lead to the development of Monte Carlo methods to solve the radiative transfer equation.

The Monte Carlo methods (or statistical modelling) are techniques for constructing probabilistic models of real processes to estimate certain average properties, e.g. mathematical expressions, variances and covariances. The main points of the Monte Carlo method are: 1st, generation of random numbers r_{rn} uniformly distributed between [0,1]; 2nd, simulation of random values with more complicated distribution functions with the help of r_{rn} ; 3th, calculation of the quantities of interest for the simulated process via realizations of random values obtained in the 2nd step.

Monte Carlo methods are know for generally being easier to implement than other computational methods. In fact in the Monte Carlo methods the photons are followed as they propagate through the medium. Therefore it is possible a simple understanding of their interaction with the medium itself and the computation of quantities like the mean number of scattering events, the weighting functions for a 3D geometry, and the relative contribution of photons coming from the surface. Problems such as the definition of a physically realistic boundary condition disappear once a model for the surface is defined. Furthermore, Monte Carlo methods seems to be particularly suited to solve both the 3D geometry problem and the radiative equation for the full Stokes vector. A disadvantage of this numerical methods are a lower accuracy and the fact that they are expensive in terms of computational time (Battaglia, A. and Mantovani, S., 2005).

To illustrate the method, it can be considered a simple example to simulate radiative transfer along a line where a photon can fly only forward or backward. In a medium interval of 0 to h ($[0,h]$) with a photon mean-free-path equal to ℓ , thus the optical thickness is $\tau = h/\ell$. When a photon encounters a particle, the probability of absorption is $1 - \tilde{\omega}$. Upon each scattering, photons either continue forward or turn backward. The asymmetry parameter g gives the probability $p = (1 + g)/2$ that a photon goes forward and the probability $1 - p = (1 - g)/2$ that it turns backward. For simplicity reasons a total of N_p photons is used, these N_p photons cannot scatter more than N_s times, after N_s scatterings the photon is called "lost". If the photon is not absorbed at the collision, its direction (forward with $\mu_s = +1$ or backward $\mu_s = -1$) is simulated using the probability p defined by the asymmetry factor g . Finally, reflectance, transmittance and absorptance are estimated by averaging the number of outcome photons.

In cases when it is studied the photon's probability to exit in a small solid angles, the task might become computationally very expensive without sacrificing spatial or angular resolution, or both. The alternative then is a "weighted" method based on the solution of the RTE. One of them which uses the direct RTE is called forward Monte Carlo or "local estimation"; the other uses the adjoint radiative transfer process and is called the backward Monte Carlo. In contrast to forward Monte Carlo where photons travel as they do in the real atmosphere, in backward Monte Carlo they start at the detector and follow in the time-reverse direction along the photon path (Marshak, A. and Davis, A., 2005, pp. 261-272).

The limit is that backward Monte Carlo schemes cannot, by design, deal with photons changing polarization state. This is because when a photon is started and drawn back the

initial polarization state is unknown: the first collision is the last in the temporal physical sequence. To overcome with this problem, (Liu, Q. and Simmer, C., 1996) developed the so called "backward-forward" scheme that allows for the treatment of polarized radiation, but requires that the extinction matrix be diagonal. In a backward or even backward-forward Monte Carlo scheme, the fact that the probability distribution function that governs the photon path do not depend on the polarization state of the radiation, makes it not very useful in the case of polarized radiative transfer with oriented non-spherical particles. Only pure forward Monte Carlo schemes are able to completely describe the polarization effects of preferentially oriented particles. With this aim, different forward Monte Carlo codes have been developed. Battaglia, A. and Mantovani, S., 2005 developed a direct plane parallel polarized code for oriented symmetric particles and extended it to a fully polarized version, completely biased and within a 3D framework. There the Monte Carlo model is considered as a 3D grid in which the photons can travel in every direction, by crossing the external boundaries of the cloud. A precipitation scheme with determined area is described by a finite cloudy region with an underlying surface (modelled as Lamberian or Fresnel) embedded in a background 1D atmosphere. The Monte Carlo reproduces the brightness temperature vector, derived from the 4D Stokes vector, as measured by a radiometer looking at some selected viewing angle (θ_v, ϕ_v) with a footprint coincident with the receiving grid (Battaglia, A. and Mantovani, S., 2005, figure 1).

In the present work, a full 3D Monte Carlo simulations code (Battaglia, A., Davis, C., Emde, C., and Simmer, C., 2007) is being used to simulate 3D features for the brightness temperatures at vertical and horizontal polarization by non-spherical hydrometeors with preferential orientation.

3. Microwave Radiometry

Abstract

This chapter introduces the passive microwave radiometer as a main instrument to be used in order to estimate precipitating cloud parameters. Along the properties of the radiometer, some important issues are discussed to better understand and improve the performance of the radiometer. Moreover two active sensors are introduced as ancillary instrumentations to sense rain and cloud which provides additional information with range resolving capabilities. The chapter widely discusses the adequateness of these active instruments to be operated alike the radiometer in scan mode, e.g. elevation angles others than zenith.

3.1. Passive Microwave Radiometer

In general terms a radiometer is a radio receiver device used for measuring the electromagnetic radiation average power of radiant flux in a well defined frequency range. Historically the term radiometer generally refers to an infrared radiation detector, however nowadays there is a large variety of detectors working on a wide range of electromagnetic wavelength. Thus a microwave radiometer operates in the microwave region, which generally spans the range from about 3GHz to 300GHz, although there is no wide acceptance of an exact range, or an upper frequency limit (Janssen, M. A., 1993).

In general terms natural radio emission from the cosmic microwave background, discrete astronomical sources, the Earth's atmosphere, etc. behaves like random noise that has very similar behaviour as a noise generated by a warm resistor or by receiver electronics. A so called square-law detector is an element to produce an output voltage proportional to the square of the input noise power. It has been found convenient to describe the noise power in units of temperature in accordance with the relationship 3.52 as explained in section 3.1.1.1.

The figure 3.1 illustrates the common features of most microwave radiometers with the specific example of a total power radiometer. This comprises of an antenna which is used to receive the incident **Radio-Frequency (RF)** signal within a certain range of frequencies. Thus the antenna has the purpose to couple the RF into a transmission line like a wave-guide which carries the signal to and from the other elements of the radiometer. In figure 3.1 the mixer combines the RF with a constant frequency signal generated by a local oscillator (LO). The output of the mixer are signals at variety of frequencies. One of these frequencies is the difference between the RF and LO denominated intermediate-frequency (IF), this has the property that its power is proportional to the power of RF signal, that under the condition that the RF signal is much weaker than the LO signal. The reason why the signal is down-converted to IF is mainly technical, since traditionally microwave frequencies are difficult to deal directly with, whereas there is a variety of techniques to work with the low IF frequency (Janssen, M. A., 1993).

The following elements in figure 3.1 are an amplifier for the IF signal and a filter to exclude the spurious frequencies produced by the mixing. The power of the IF signal is measured

by a non-linear element named square-law detector that produces an output voltage which is proportional to the input power. The net IF power measured by the square-law detector comprises of two components, namely: one that represents the amplified signal power and is proportional to the antenna temperature T_a , and a second component the system noise equivalent temperature T_{sys} which describes the noise power added to the receiver signal by the various circuits within the receiver ¹. The radiometric brightness temperature T_R is then composed of

$$T_R = T_a + T_{sys} \quad (3.48)$$

with T_a representing mainly the contribution from the atmospheric emission T_{atm} , which is of particular interest, and other sources like for instance the cosmic microwave background radiation $T_{cmb} = 2.73\text{K}$ among others. Therefore T_{sys} must be calibrated on the same scale as the antenna temperature.

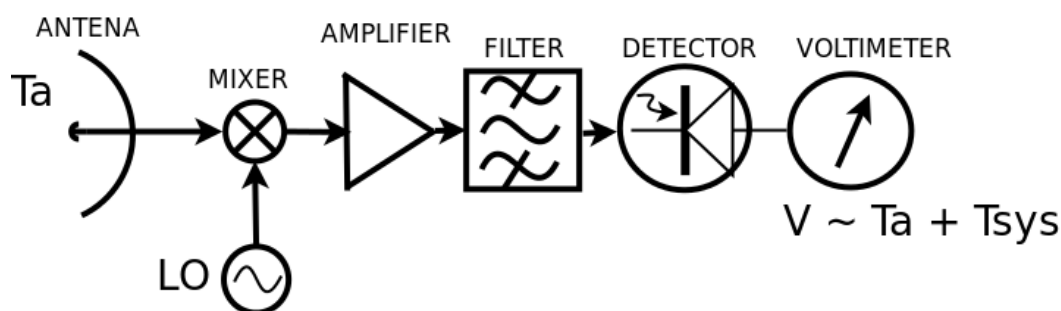


Figure 3.1.: Simplified schematic for a total power radiometer. The output voltage V , as given by this simple circuit, is proportional to the received signal power.

The output signal in scheme 3.1 includes some unwanted rapid variations that can be suppressed by calculating the arithmetic mean of the detector output voltage over some time. This integration reduces importantly the receiver output fluctuation. If the integration is made over a time τ the independent samples of the total noise power is $N = 2\tau\Delta\nu$, each of which has a RMSE error of $\Delta T_R = (2/N)^{1/2}T_R$. In terms of band-width $\Delta\nu$ and integration time τ ,

$$\Delta T_R \approx \frac{T_R}{\sqrt{\tau\Delta\nu}} \quad (3.49)$$

this is called the ideal radiometer equation for a total power receiver.

The ideal radiometer equation suggests that the sensitivity improves as $\tau^{1/2}$ continuously. However, in practice systematic errors set a floor to the noise level that can be reached. A second source of fluctuations which occurs at the receiver output are attributable to receiver gain instabilities. The following example helps to see its significance: if it is considered a system with $T_R=1000\text{K}$, $\Delta\nu=400\text{MHz}$, and $\tau=1$ second in equation 3.49, a RMS value for the amplitude of statistical noise fluctuation at the receiver output of the order of 0.05 K is obtained. This would be the case if the receiver were absolutely gain stable. Unfortunately even the best receivers exhibit instabilities of the order of 1% during a time period required for most signal measurements. Thus a receiver with gain changes of the order of 1% would provide an output fluctuation of 10 K. Hence, the receiver's noise measurement sensitivity would be driven by the variation of the gain rather than the level of statistical noise fluctuation.

¹Note that some literature instead of system noise temperature uses the terminology of receiver temperature.

Note that the output voltage of a total power receiver is directly proportional to the overall gain of the receiver:

$$P_v = GkT_R$$

If G is not perfectly constant, the change in output $\Delta P_v = \Delta GkT_R$ caused by a gain fluctuation ΔG produces a false signal

$$\Delta T_G = T_R \left(\frac{\Delta G}{G} \right)$$

that is indistinguishable from a comparable change ΔT in the system noise temperature produced by a source. Since receiver gain fluctuations and noise fluctuations are independent random processes, their variances add, and the total receiver output fluctuation becomes:

$$\Delta T^2 = \Delta T_R^2 + \Delta T_G^2$$

Thus, the practical total power radiometer equation is:

$$\Delta T \approx T_R \left[\frac{1}{\tau \Delta \nu} + \left(\frac{\Delta G}{G} \right)^2 \right]^{1/2} \quad (3.50)$$

Clearly, gain fluctuations will significantly degrade the sensitivity unless

$$\left(\frac{\Delta G}{G} \right) \ll \frac{1}{\sqrt{\tau \Delta \nu}}$$

Continuing with the example above, the 10.7GHz receiver used in this work has a beam-width $\Delta \nu$ of 400MHz and normally has an integration time of $\tau = 1$ second, so the fractional gain fluctuation on that time scales has to satisfy

$$\frac{\Delta G}{G} \ll 0.5 \times 10^{-4}$$

this, however, is difficult to achieve in practice. The solution to this problem was provided by Dicke, R., 1946 with a method to minimize the effects of gain fluctuations. The method efficiently switches magnetically the receiver inputs with an absorber target of well know physical temperature. This method is called Dicke-switching, named after its inventor Robert Henry Dicke.

To this point the basic concepts of a radiometer has been described, however in case of modern radiometers some features need to be adjusted. Unfortunately, many external sources around 100MHz exist, like strong radio transmitters, mobile phone stations, data transfer links, etc. That is the reason why receivers with intermediate frequency band (IF) are prompt to suffer from interference. For instance, direct detection radiometers do not have any mixers or active sources (local oscillators) which down-convert the reception frequency band (e.g. 22-32GHz) to a low frequency band. Therefore direct detection radiometers are totally immune to interference in there low frequency bands (IF). Direct detections receivers with their advantages require a signal filtering and detection at the high reception frequencies. State of the art technology developed over the last 7-10 years has made this receiver technology feasible (Rose, T. and Czekala, H., 2007).



Figure 3.2.: Radiometer ADMIRARI at its standard operational configuration. Mounted on a transportable trailer. Note the ancillary instrumentation: on the left a cloud-lidar and on the right a MRR. (photo credit: P. Saavedra).

3.1.1. Dual Polarized Radiometer ADMIRARI

The **AD**vanced **MI**crowave **RA**diometer for **R**ain Identification ADMIRARI (see picture in Fig. 3.2), manufactured by **RPG**, has been designed to investigate rain processes. The main instrument characteristics are summarized in Tab. 3.2. Additional information can also be found at the ADMIRARI home page <http://www2.meteo.uni-bonn.de/admirari>.

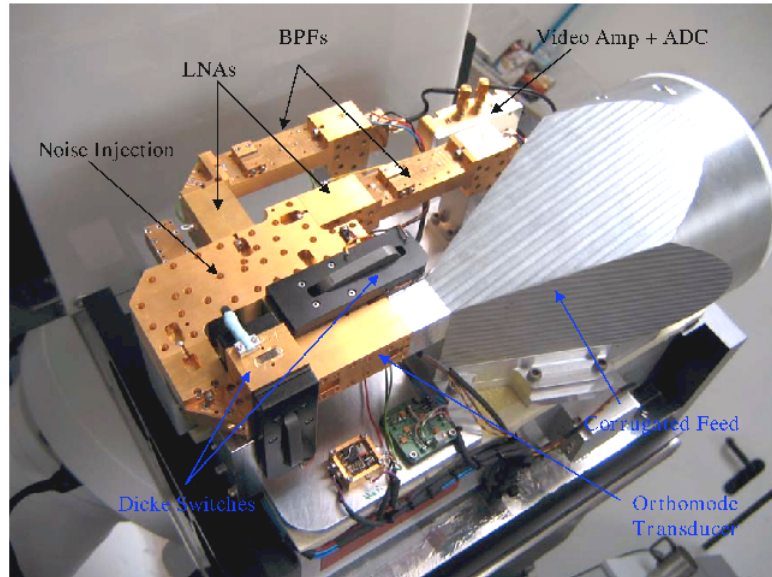
As exposed in the next section 7, the standard atmospheric parameters, which can be derived from ADMIRARI observations, are the cloud liquid water path (C_LWP), the rain liquid water path (R_LWP), and the integrated water vapour (IWV). For this purpose the radiometer comprises in total six channels covering three frequencies (10.7, 21.0 and 36.5 GHz) and horizontal and vertical (H and V) polarizations. These frequencies have been selected based on different considerations:

- The use of a multi-frequency approach allows a better discrimination of different rain rate classes. For instance, the sensitivity to small amounts of R_LWP is significantly better at the higher frequency (see figures 2-3 in (Czekala, H., Crewell, S., Hornbostel, A., et al., 2001b)) while high amounts are better monitored at the lower frequency.
- The radiometer must produce the usual dual-channel IWV - LWP product for no-rain conditions. Therefore one frequency (21.0 GHz, with weighting function almost independent of height- has been selected within the weak 22 GHz water vapour absorption line and the other (36.5 GHz) in the window region between this line and the oxygen line complex around 60 GHz.
- The three ADMIRARI frequencies mirror those which are/will be present in many space-borne radiometers (e.g. TMI at TRMM, SSM/I, and GMI at GPM). Thus this set-up

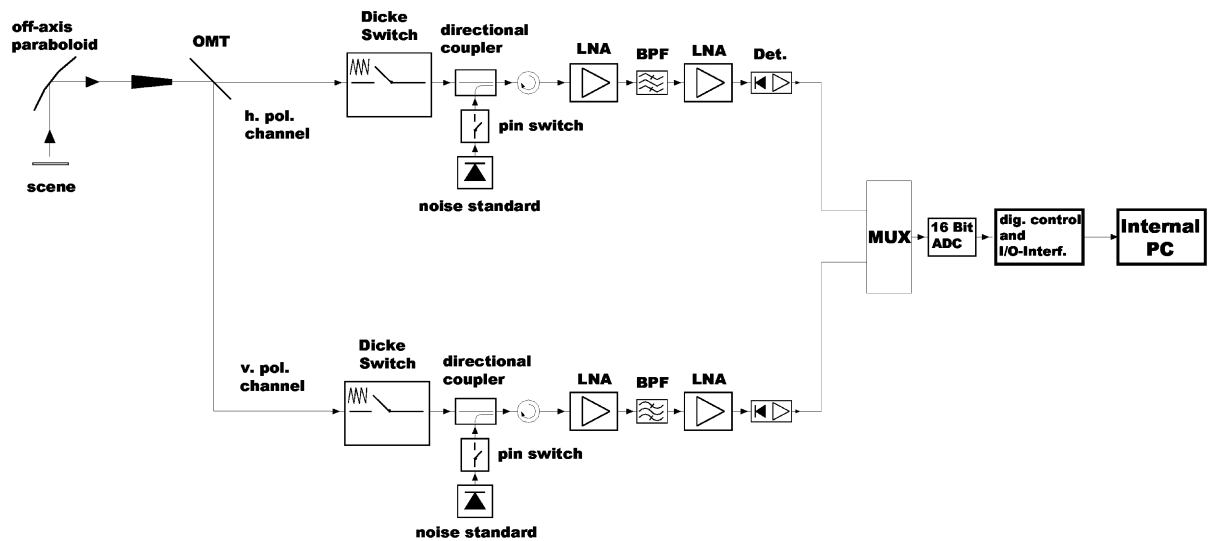
offers an important contribution to the ground-based observations which can be used to validate passive microwave space-borne rain-rate retrieval algorithms.

The general radiometer configuration is illustrated in figure 3.3(b) and the hardware inner receiver module is pictured in figure 3.3(a). The system is a direct receiver radiometer. For each frequency module has a corrugated feed horn as a optimal choice to achieve minimum reflection losses and compactness at the same time. This solution offers a wide band-width, low cross polarization level and a rotationally symmetric beam, meeting thereon the optical requirement. The receiver optics consists of a corrugated feed horn with an aperture lens (only at 10.7 GHz the beam is formed by a combination of a corrugated feed horn and an off-axis parabola antenna, see the white parabola reflector in the center of ADMIRARI picture in figure 3.2) which achieves an antenna beam-width of approximately 6° at [Half-Power Beamwidth \(HPBW\)](#). The aperture lenses and the 10.7 GHz parabola antenna are coated by a water repellent film to avoid the sticking of raindrops on them; they are also equipped with a shield which is effective in protecting the lenses and the parabola antenna from rain when the radiometer is measuring at low elevation angles (typically 20 to 40 degrees). These angles are favourably affecting the polarization signal as well and have been selected for normal operation. Depending on the precipitation type it has for instance noticed that only in few cases the antennas have experienced wetting, for situations with strong wind blowing toward the radiometer viewing direction. On the other hand, during solid precipitation when the wind is blowing towards the radiometer, accumulation of snow on the antennas radome has been an issue which degrades the measurements for long periods until either the snow is melted or removed manually. In absence of “adverse” wind, observations with elevation angles up to 60 degrees are generally not affected by antenna wetting. In order to undoubtedly confirm the antennas dryness during operation, lately antenna monitoring video-cameras have been installed, which helped for instance flagging events affected by the above mentioned snow problem.

The corrugated feed horns offer a low cross polarization level and a rotationally symmetric beam pattern. The Ortho Mode Transducer splits the signal into the V and H polarization components. The ADMIRARI receivers are designed to achieve a high thermal and electrical stability, a compact layout with a minimum of connectors and thermally drifting components, an integrated radio-frequency design, low power consumption and weight. The receivers are based on the direct detection technique (thus no mixers and local oscillators are needed, leading to reduced sensitivity to interfering external signals at down-converted frequencies). As illustrated in the bottom panel of figure 3.3(b) a Dicke Switch is a fundamental component of the system, its function is to periodically switch the receiver inputs to an internal black body with fixed TB (Dicke, R., 1946). In combination with the built-in noise injection system, the radiometer automatically performs a continuous calibration of all relevant drift parameters like gain and system noise temperature. The Dicke switches are wide bandwidth Y-junction Circulators where one port is terminated by absorber material. By inverting the magnetic field direction, the isolator function of this device is also reverted. When the radiometer is “looking” to the sky, its input is isolated from all signals coming from the receiver input (e.g. the noise power reflected from the noise injection system). When the Dicke switch is in the ON state, the receiver input is isolated from signals coming from the sky. This set-up continuously determines the gain and system noise temperature of the radiometer. The Dicke Switch is followed by a directional coupler which allows for the injection of a precision noise signal generated by an on/off switching calibrated noise source. This noise signal is used to determine



(a) Picture of on the inner radiometer component, the 21.0GHz module with the antenna horn-feed and the components in the scheme below.



(b) Schematic of the receiver layout, the orthomode is splitted the H and V signal which are directly detected in two different receiver chains.

Figure 3.3.: Module picture and receiver layout (3.3(a) photo credit: RPG GmbH, 3.3(b)) from (Rose, T. and Czekala, H., 2007).

system non-linearities and system gain drifts during measurements by the “four point” method (Rose, T. and Czekala, H. (2007), figure. 9). A 40 dB low noise amplifier (LNA) boosts the input signal before it is filtered by a wave-guide bandpass filter with bandwidth 200 MHz and again boosted by another 20 dB amplifier. Each of the six channels has its own detector diode, which allows for a parallel detection and integration. The detector outputs are finally amplified by an ultra-low drift operational amplifier chain, AD converted and transmitted to the internal radiometer PC for each of the three frequency modules.

In order to fulfil the requirement of low maintenance regarding absolute calibrations, the receivers are integrated together with their feeds and lenses and are thermally insulated to achieve a high thermal stability with an accuracy of < 0.05 K over the whole operating temperature range (-30 to $+40^\circ$ C see table 3.2). The system achieves a full internal calibration by using the internal Dicke Switch calibration targets (absolute standards) in combination with the built-in noise injection systems (one for each frequency module) which is used to calibrate the gain drifts. Noise diodes are secondary standards; they are calibrated by sky tipping procedures, which can be manually performed during clear sky conditions. A radiometer accuracy of the order of 0.5 K RMS @ 1.0 s integration time is achieved with an absolute system stability of 1.0 K. The system is fully steerable both in azimuth (0 to 360°) and in zenith (-90 to 90°) with azimuthal speed and elevation speed approximately equal to 5° s^{-1} and 3° s^{-1} , respectively. In order to allow easy transportation to campaign sites the whole system is mounted on a trailer (see mounted platform in figure 3.2).

3.1.1.1. Radiometer Calibration

As any other measuring system calibration errors can be attributed as the major source for inaccuracies, therefore the radiometer’s receiver output voltage must be calibrated in units of antenna temperature. In this matter a calibration procedure is required to find: a gain coefficient G to convert from voltage to temperatures, and an offset T_{sys} which accounts for power generated within the receiver itself.

The standard calibration procedure consist in providing two absolute calibration targets to the radiometer input. These targets are assumed to be ideal targets that means their radiometric temperatures are equal to their physical temperature. This assumption is valid with reasonable accuracy as long as proper absorber materials are chosen for the frequency bands in use and barometric pressure corrections are applied to liquid coolants in the determination of their boiling temperature (Rose, T. and Czekala, H., 2007).

In figure 3.4(b) a simplified scheme to determine the radiometer calibration coefficient and offset at the same time by observing black-body emitters at two different temperatures, for instance enclosing the antenna’s **Field of View (FOV)** with a temperature controlled targets (or loads) at each of two temperatures, T_{cold} and T_{hot} . A practical approximation is that the radiometer response (voltages) is linear with respect to temperature (figure 3.4(a)), then the antenna temperature can be determined for a target at unknown temperature as

$$TB = G(V - V_0)$$

where V_0 is the voltage offset due to the receiver temperature and the radiometer calibration constant (slope of the linear response) is determined as

$$G = \frac{T_{\text{hot}} - T_{\text{cold}}}{V_{\text{hot}} - V_{\text{cold}}}$$

where the voltages V_{hot} and V_{cold} are the measured output voltages for the respective T_{hot} and T_{cold} targets (Janssen, M. A., 1993).

System Non-Linearity Correction Accurate noise injection measurements have shown that the assumption of linear system response is not valid in general (Rose, T. and Czekala, H., 2007, and reference therein). Calibration errors of 1-2K have been observed at brightness temperatures in between the two calibration target temperatures. This system non-linear behaviour is mainly caused by detector diodes needed for total power detection. Even in the well defined square law operating regime (input power < -30 dBm) the detector diode is not an ideal element with perfect linearity. The noise injection calibration algorithm implemented in all [RPG](#) radiometers corrects for these non-linearity effects.

The system non-linearity is modelled by the following formula:

$$V = GP^\alpha, \quad 0.9 \leq \alpha < 1.0 \quad (3.51)$$

where V is the detector voltage, G is the receiver gain coefficient, α is a non-linearity factor and P is the total noise power that is related to the radiometric brightness temperature T_R through the Planck's radiation law:

$$P(T_R) \approx \frac{1}{\exp(\frac{h\nu}{k_B T_R} - 1)} \quad (3.52)$$

Note that the proportionality factor, incorporated in G , gives units of power to the right hand side which is a-dimensional. T_R is the sum of the system noise temperature T_{sys} and the antenna temperature T_a (scheme 3.1), $h = 6.62606957 \times 10^{-34} \text{ m}^2 \text{ kg s}^{-1}$ being the Planck's constant, ν the frequency and $k_B = 1.3806488 \times 10^{-23} \text{ m}^2 \text{ kg s}^{-2} \text{ K}^{-1}$ the Boltzmann constant.

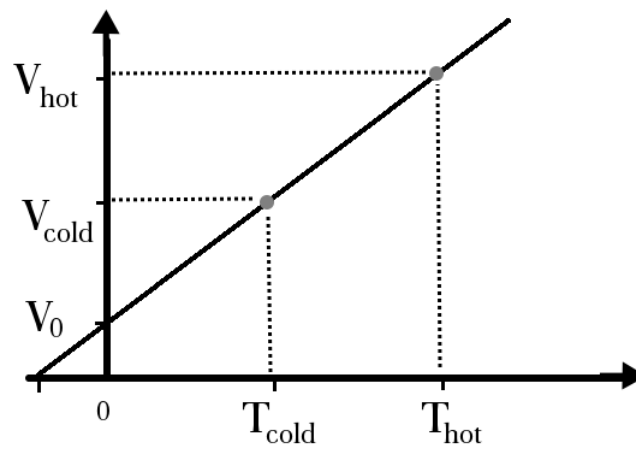
The problem is how to determine G , α and T_{sys} experimentally (three unknowns cannot be calculated from a measurement on two standards). The introduction of an additional noise injection of temperature T_n becomes a solution to generate four temperature points which leads to four independent equations with four unknowns (G , α , T_{sys} and T_n). The procedure is illustrated in figure 3.4(b) with the two targets obtained by [Liquid Nitrogen \(LN2\)](#) or sky tip calibration as explained in the following sections. The initial calibration is performed with absolute standards and leads to the voltages V_{cold} and V_{hot} . By injection of additional noise V_{n1} and V_{n2} are measured. For example V_{n1} is given by

$$V_{n1} = G[P(T_{\text{sys}}) + P(T_{\text{cold}}) + P(T_n)]^\alpha \quad (3.53)$$

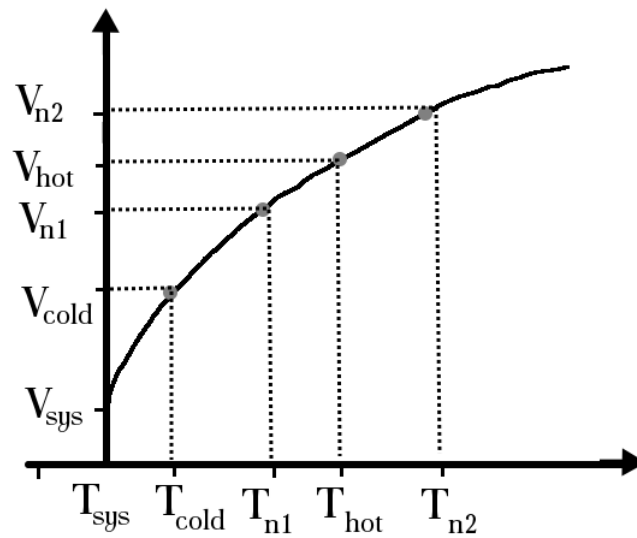
where T_{cold} is the radiometric temperature of the cold target. The evaluation of the additional equations for V_{cold} , V_{hot} and V_{n2} results in the determination of T_{sys} , G , α and T_n (Rose, T. and Czekala, H., 2007). It is important to notice that it is assumed T_n being constant during the measurement of V_{cold} , V_{n1} , V_{hot} and V_{n2} .

After finishing the procedure the radiometer is calibrated. With the four point calibration method also the noise diode equivalent temperature T_n is determined. Assuming a high radiometric stability of the noise injection temperature, successive calibrations can use this secondary standard (together with the built-in ambient temperature target) to recalibrate T_{sys} and G (considering α to be constant) without the need for liquid nitrogen.

In the following subsections different calibration procedures that are used by standard and dual-polarized radiometers alike ADMIRARI are presented along with general remarks.



(a) Linear response



(b) Non-linear response

Figure 3.4.: Calibration of antenna temperature using a cold and hot load. 3.4(a) linear approximation, 3.4(b) non-linearity scheme including the injection of noise temperature T_n

The Internal Dicke Switch Calibration Target

In case of ADMIRARI the Dicke switch target (see figure 3.3(a) and 3.3(b)) is one of the instrument's key components. The switch magnetically terminates the receiver inputs with an absorber target of well known physical temperature (ON position). This absorber serves as a load with same brightness temperature as the physical temperature, thus equivalent to a quasi-optical target (of the same temperature) when positioned in front of the receiver. The Dicke switch is located behind the feed horn and cannot calibrate changes in the feed horn brightness temperature. It is therefore essential to thermally stabilize the feed horn and lens of each receiver to keep this contribution constant. The switches are operated once per second and are used to adjust drifts in the system noise temperature. For that purpose it is of key importance to measure the Dicke switch physical temperature as accurate as possible. The main advantage of using a Dicke switch instead of a quasi-optical target for absolute calibration is that this calibration can be performed frequently (the calibration is alternated with measurement in a period of one second) while the radiometers are continuously pointing to the scene i.e. not necessary to move physically the radiometer towards any specific target.

The switches work in combination with the built-in noise injection system which is used to calibrate gain drifts. In contrast to the Dicke switches (which are absolute standards), noise diodes are secondary standards that have to be calibrated by a hot/cold calibration with liquid nitrogen or by a tip curve calibration on the clear sky as it will be presented in the next sections (Rose, T. and Czekala, H., 2007).

External Liquid Nitrogen Cooled Calibration Target

Another absolute calibration standard which is used with ADMIRARI is the liquid nitrogen cooled target (see figure 3.5(a)). This procedure is only used for absolute calibrations, which is mainly performed after long-term measurements, transportation or changes of hardware or antenna configuration like alignment, beam-width, etc. To perform this test the pedestal's elevation axis is tilted down to -90° elevation and the target is located underneath the receiver antenna of the module which is being calibrated. The calibration is repeated for each module separately. This standard - together with the internal Dicke switch target - is used for the absolute calibration procedure. The cooled load is stored within a 40 mm thick polystyrene container (see light-green container in figure 3.5(b)) with approximately 25 litres of liquid nitrogen needed for one filling. The whole radiometer must be covered to protect the container from wind blowing which can create pressure gradients that yields evaporation of LN2 at the calibration container, see for instance in figure 3.5(b) the LN2 evaporation being blown by some breeze before the calibration is performed.

The boiling temperature of the liquid nitrogen and thus the physical temperature of the cold load depends on the barometric pressure P . The radiometer's pressure sensor is read during absolute calibration to determine the corrected boiling temperature T_c according to the Clausius-Clapeyron equation (Rose, T. and Czekala, H., 2007):

$$T_c = \frac{T_0}{1 - T_0 \left(\frac{R}{\Delta H}\right) \ln\left(\frac{P}{P_0}\right)} \quad (3.54)$$

$T_0 = 77.25$ K is the boiling temperature at 1013.25 hPa, $\Delta H = 199.1$ kJ kg⁻¹ is the latent heat of nitrogen and $R = 8.3144621$ JK⁻¹ mol⁻¹ the universal gas constant. The calibration error due

to microwave reflections at the LN2/air interface is automatically corrected by the calibration software running in the internal radiometer PC. Despite covering the whole radiometer it is also recommended to wrap a cloth around the cold load and the radiometer's module during absolute calibration to avoid the formation of condensed water above the liquid surface (caused by wind etc.).

Sky Tipping Calibration

The sky tipping calibration method is convenient since it does not need any external apparatus or material like LN2 or cold/warm targets. For the sky tipping calibration the only one requirement is to have a homogeneous, stratified atmosphere with water vapour homogeneity. This procedure is suitable for low frequencies at which the atmosphere must be highly transparent and fulfil a further requirement that the earth's atmosphere optical thickness (or opacity τ) is very low.

The sky tipping calibration method uses measurements of optical thickness, derived from measurements of brightness temperature, as a function of airmass to estimate a calibration factor. The atmospheric airmass m_A is defined as the ratio of the optical thickness at the direction θ and at zenith i.e. $\theta_z=90^\circ$ elevation.

$$m_A = \frac{\tau(\theta)}{\tau_z} \quad (3.55)$$

In a plane stratified atmosphere, the equation 3.55 can be used to estimate a calibration factor if the relationship between airmass m_A and the observation angle θ is known (Han, Y. and Westwater, E. R., 2000). In a simplified case, e.g. no gradient of refractive index that can cause rays bending, the airmass can be calculated as

$$m_A = \frac{1}{\sin(\theta)}$$

This calibration method requires the measurement of the opacities for at least two observational angles θ_1 and θ_2 whose corresponding measurements are converted to optical thickness $\tau_v(\theta_1)$ and $\tau_v(\theta_2)$ by using

$$\tau_v(\theta) = \ln \left(\frac{T_{mr,v}(\theta) - TB_{cmb}}{T_{mr,v}(\theta) - TB_v(\theta)} \right) \quad (3.56)$$

where $TB_{cmb} = 2.73K$ is the cosmic background temperature and TB is the brightness temperature, v indicates the frequency dependence for all variables, and T_{mr} at direction θ , defined as

$$T_{mr,v} = \frac{\int_0^\infty T_v e^{-\tau_v(\theta)} d\tau_v(\theta)}{1 - e^{-\tau_v(\infty,\theta)}} \quad (3.57)$$

The mean radiating temperature T_{mr} plays an important role in the determination of optical thickness from TBs. Therefore uncertainties in T_{mr} may cause significant calibration errors when large airmasses are used (Han, Y. and Westwater, E. R., 2000). T_{mr} was traditionally determined from radiosonde data and its uncertainties can be reduced by separating the T_{mr} in climatological seasons. The RPG build-in sky tipping algorithm however, claims to achieve sufficient accuracy by relating T_{mr} with a quadratic equation of the surface temperature measured directly by the radiometer (Rose, T. and Czekala, H., 2007).



Figure 3.5.: ADMIRARI set-up for Liquid Nitrogen calibration 3.5(a), with the cold target positioned below the antenna 3.5(b). (photo credit: P. Saavedra)

To reduce measurement uncertainties, the calibration is often taken at several elevation angles, thus a set of values for airmass versus optical thickness can be collected to form a straight line. Thereon a least-square technique is applied to extrapolate the adjusted line to zero airmass. At that point the detector reading V_{sys} corresponds to a radiometric temperature which equals to the system noise temperature plus $T_{\text{B}_{\text{cmb}}} = 2.73\text{K}$, i.e. $V_{\text{sys}} = G(T_{\text{sys}} + 2.73)$. The proportionality factor (gain) G can be calculated when a second detector voltage is measured with the radiometer pointing to the ambient target with known radiometric temperature (Rose, T. and Czekala, H., 2007, section 4.3).

The radiometer typically scans the atmosphere from zenith to around 19° in elevation and stores the corresponding detector readings for each frequency and angle. The path length for a given elevation angle θ is m_A times the zenith path length (defined as one “air mass”), thus the corresponding optical thickness should also be multiplied by this factor.

Although the sky tipping is considered to be an accurate absolute calibration method, calibration errors may be caused due to violation of the assumptions needed to apply the theory above mentioned. Among those calibration errors can be listed the radiometer antenna pattern, antenna beam width, system random noise, radiometer pointing error, the uncertainty on estimation of T_{mr} and uncertainties in the relationship between airmass and the elevation angle (equation 3.55) normally affected by non-stratified atmosphere, air temperature gradients and earth’s curvature (Han, Y. and Westwater, E. R., 2000). The sky tipping calibrates the system noise temperature and the gain factor for each frequency without using a LN2 cold load and can be performed several times as long as the atmospheric conditions favour it.

The causes of error for the sky tipping method, finding for instance that the horizontal inhomogeneity of the water vapour and temperature fields may cause significant uncertainties. The conversion from brightness temperature into optical thickness with the estimation of T_{mr} are also source of uncertainties, becoming larger when the brightness temperature is larger, that is the reason the sky tipping is not recommendable to perform at higher frequencies which sense larger optical depths. Neglecting the earth curvature may cause a 0.1° of calibration error. The antenna beam-width of, for instance, 6° may cause a 0.5K calibration error. The estimation of mean radiating temperature by means of climatological approximation results in errors up to 0.5K. Pointing angle errors of about 2° might lead to calibrations errors of 1K, which can be reduced however if the tipping data is collected at both sides e.g. scanning in elevation at two azimuth angles separated by 180° (Han, Y. and Westwater, E. R., 2000).

Moreover the invisible inhomogeneity of the water vapour distribution can question the applicability of this method. In order to minimize that inhomogeneous effect the built-in sky tipping algorithm applies a quality criteria to detect those atmospheric conditions that do not satisfy some calibration requirements. Two types of criteria are used, namely the linear correlation coefficient of the sky-tip curve and the χ^2 -test. The correlation coefficient acts as indication of how well a linear curve is adjusted to the optical thickness as a function of the airmass, important to mention is that the linear correlation coefficient is not sensitive to the noise of the optical thickness samples caused by clouds. The χ^2 -test criteria measures the variance of the measured optical thickness samples relative to the expected straight line.

The stability of the sky tipping method for calibration of gain G , system temperature T_{sys} and noise injector temperature T_n are shown in figure 3.6. The figure present a set of box-plots that depicts the distribution of calibration variables in a long term radiometer operation for the time span from August 2007 to June 2011. During that period, the radiometer has been performing 1310 sky tipping calibration. Figure 3.6 and table 3.1 are results based on the statistics of only calibrations flagged as successful according to the correlation coefficient and

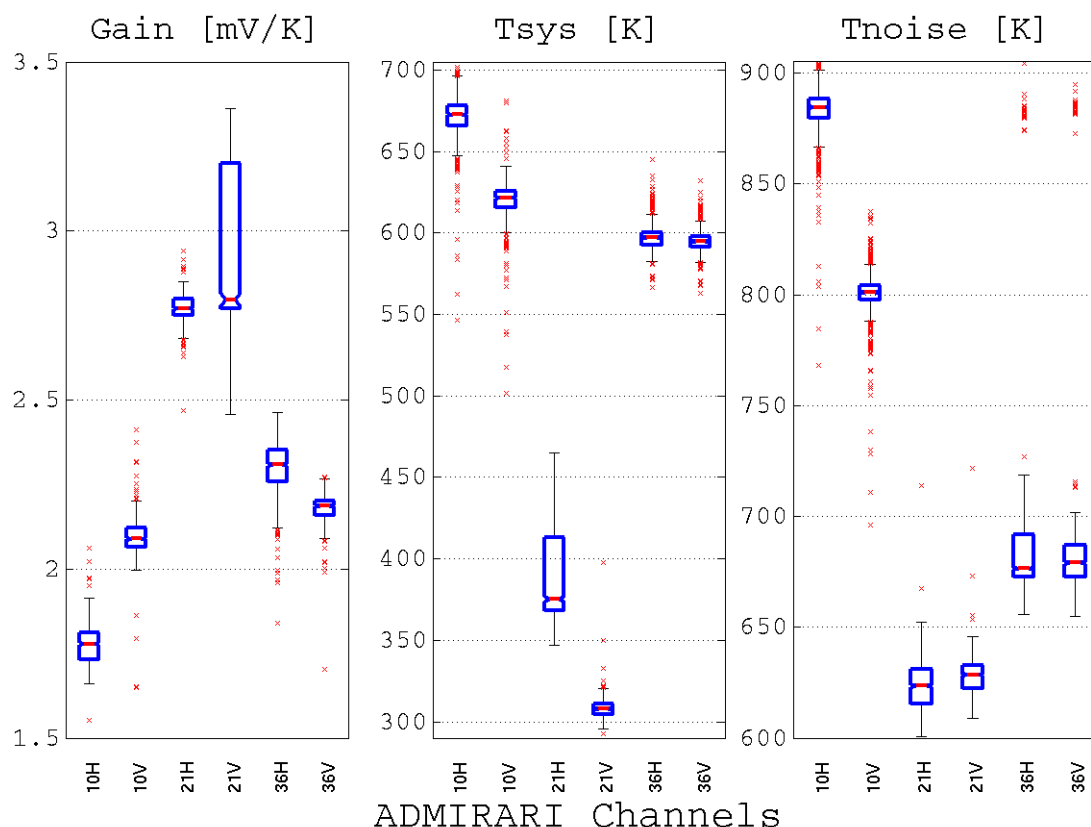


Figure 3.6.: Boxplot for calibration coefficients obtained after long term operation from August 2007 to June 2011. The lowest/highest border of the boxplot indicated the 25th and 75th quantile, the middle red-line in box indicates the median, and the red crosses are outliers.

χ^2 -test criteria.

For the 10.7 GHz channels, the distribution of calibration variables are very narrow and extended equally around the median making alike a normal distribution with very few outliers mainly for gain and T_{sys} , while the temperature noise injector is the one with slightly sparser outliers for this channels. Similar behaviour can be observed for the 36.5GHz channels with a excellent performance for the calibration of T_{sys} and gain, while the T_n at this channel presents high values around 880 K, producing a large standard deviation ($\sim 7\%$) both at vertical and horizontal polarization, this mainly happens due to LN2 calibration after changes of internal measurement parameters or hardware adjustments.

For the case of 21.0 GHz channels, the box-plots show a different pattern with a very good performance for the T_n with almost no outliers. The T_{sys} (vertical polarization) and gain (horizontal polarization) have a very narrow distribution as a result of a good long-term performance. However the same is not mirrored by T_{sys} (horizontal) nor the gain (vertical), with the latter showing a large tail toward higher values ranging from $\sim 2.7 \text{ mVK}^{-1}$ (median) to 3.3 mVK^{-1} (75th quantile) corresponding to the vertical channel. In case of T_{sys} horizontal channel, a largely spread towards high values is found. Observing at the time series it has been seen that the gain at 21.0 K (vertical channel) has suffered a drop of $\sim 0.6 \text{ mVK}^{-1}$ on January 22nd, 2009. After that date the gain at vertical and horizontal became approximately the same magnitudes. The same drop is observed for the system temperature but at horizontal

Table 3.1.: ADMIRARI calibration variables (Gain G [mVK^{-1}], system temperature T_{sys} [K] and noise injector temperature T_n [K]) after long term operation, from August 2007 to June 2011. Note that only sky tipping calibration which has been flagged as successful are taken into account, the number of successful cases are indicated in the last row together with the percent relative to a total of 1310 attempts.

	10.7 GHz		21.0 GHz		36.5 GHz	
	H	V	H	V	H	V
G	1.78 ± 0.06	2.01 ± 0.37	2.77 ± 0.05	2.92 ± 0.23	2.29 ± 0.08	2.18 ± 0.04
T_{sys}	670.3 ± 17.0	624.7 ± 28.8	384.1 ± 22.0	308.2 ± 7.5	598.5 ± 17.2	595.7 ± 15.9
T_n	881.7 ± 15.1	800.1 ± 13.8	623.8 ± 10.6	628.3 ± 8.5	693.3 ± 50.3	691.6 ± 50.6
No.	592 (45%)	592 (45%)	355 (27%)	355 (27%)	384 (29%)	384 (29%)

channel. That is an effect of a hardware upgrade on January 22th, 2009 for the 21.0K horizontal channel after a malfunction of an internal amplifier. Thus the extension of the 75th quantile in gain and T_{sys} are the result of mixing two databases before and after January 22th, 2009 and not the result of poor calibration performance.

3.1.2. Radiometer's Performance

During the radiometer ADMIRARI operations, issues related to the system specifications which had direct effect on the reliability of the measurements and the performance of the system itself. In this section some of those issues along with their solutions will be discussed.

Bias on polarization

After collecting the first set of measurements, the data has been sorted in the TB-PD space giving a first glance on the performance of the radiometer during precipitation. Figure 3.7 highlights the expected behaviour for precipitation observations in the TB-PD space, with data collected along almost two months during precipitation and the radiometer performing [Plane Position Indicator \(PPI\)](#) scans. The data was grouped in bins of 5 K for TBs and plotted against the mean PD together with its standard deviation depicted as error bar.

Although the main feature of the data in figure 3.7 is the experimental confirmation of theoretical studies by Czekala, H., Crewell, S., Simmer, C., and Thiele, A. (2001) regarding the polarization effect of precipitating clouds and its uneven effect at different frequencies, the plots also reveal some hints to understand the quality of these first measurements. First it was evident from the lowest TB bins (e.g. mostly data at rain culmination with most of the antenna FOV sensing clear/cloudy sky) that there was an intrinsic difference on the TBs at vertical and horizontal polarization, thereon a bias on PD at all the frequencies was found. Those biases for this particular data set comprise of $\sim +1$ K at 10.7 GHz, ~ -1 K at 21.0 GHz and ~ -0.6 K at 36.5 GHz. Nevertheless larger biases have been found with subsequent observations.

The variance for TBs < 10 K are very small (error bars) meaning that all points laying at the lowest TB bins present a systematic bias at every frequency which must be subtracted from all the data. The origin of the PD bias can be attributed to the fact that at every frequency the vertical and horizontal channel receive independently, therefore they have different coefficients and calibration drifts in either channels that result in systematic bias. A bias observed even after successful sky-tipping calibration lead to the improvement of the calibration procedure

3. Microwave Radiometry

Table 3.2.: Main specifications for the microwave radiometer ADMIRARI
 (*) feature is independently estimated from [RPG](#).

Radiometer receiver	
Frequency	Module 1: 10.7 GHz Module 2: 21.0 GHz Module 3: 36.5 GHz
Channels	6 (Vertical and Horizontal each frequency)
System noise temperature	<900 K all receivers
Radiometer's resolution	0.5 K RMS 1.0 second integration time
Channel bandwidth	Module 1: 450 MHz (*) Module 2: 400 MHz Module 3: 250 MHz (*)
Absolute system stability	1.0 K
Radiometric Range	0 to 350 K
Receiver and antenna thermal stabilization	accuracy < 0.05 K
Integration time	≥ 1 sec
Optical resolution (Half Power Beam Width)	6.11° 6.09° 6.10°
Sidelobe level	Module 1: < -35 dBc Module 2: < -40 dBc Module 3: < -45 dBc
Operation temperature	-30° to +45° C
Radiometer pedestal	
Angular range	elevation: -90 to 90° , azimuth: 0 to 360°
Pointing speed	elevation: 3° /sec , azimuth: 5° /sec (see text)
Pointing resolution	0.5°
Operation temperature	-30° to +63° C
Weight (*)	Module 1: 20.7 kg Module 2: 31.0 kg Module 3: 23 kg Pedestal: 140 kg

by assuming no polarization sources at zenith ($\theta_z=90^\circ$ elevation). Thereon the radiometer software imposes a zero polarization difference at that elevation and adjust the calibration coefficients to achieve bias free PD.

To sense the polarization produced by a dichroic media, the radiometer's channels (vertical and horizontal) must have independence, i.e. receiver, dicke-switch, noise injector, etc. Nevertheless it has been found that in case of sky-tipping calibration the vertical and horizontal channels cannot be treated independently after a calibration procedure has finished. Thus if the calibration of vertical (horizontal) channel at a specific frequency has been successful and the corresponding horizontal (vertical) channel has not succeed then both channels must be flagged as unsuccessful calibration and vice-versa. In other words, a calibration must be designed as successful only if both channel calibrations have succeeded after the sky-tipping procedure. It must be noted that it is not the same case for channels at different frequencies, meaning that if the calibration in one frequency is successful it does not mean that the other frequencies may also be successful, so that they can be treated independently. This condition was added in the internal calibration algorithm by [RPG](#) as a consequence of the results obtained in the present work.

Despite of PD bias, figure 3.7 also shows some outliers at 10.7 and 36.5 GHz like some point at TB=150 K at 10.7 GHz or some data (~ 30 points) with positive PD=1 K and TB lower than 60 K at 36.5 GHz. These non-physically points are related to antenna wetting, since the radiometer ADMIRARI at its first stage did not have any shelter to protect against rainfall (see the shelters above the blue antenna radome and the reflector in the middle of figure 3.2), rather it had only the hydrophobic coating on the radome to avoid water accumulation. That configuration did not work properly and was prone to antenna wetting which was the motivation to add the shelters that protect properly against wetting until elevation angles of 60° .

The error bars in figure 3.7 (top panels) are basically expressing the variability in rain water content and drop size distribution along the observational path.

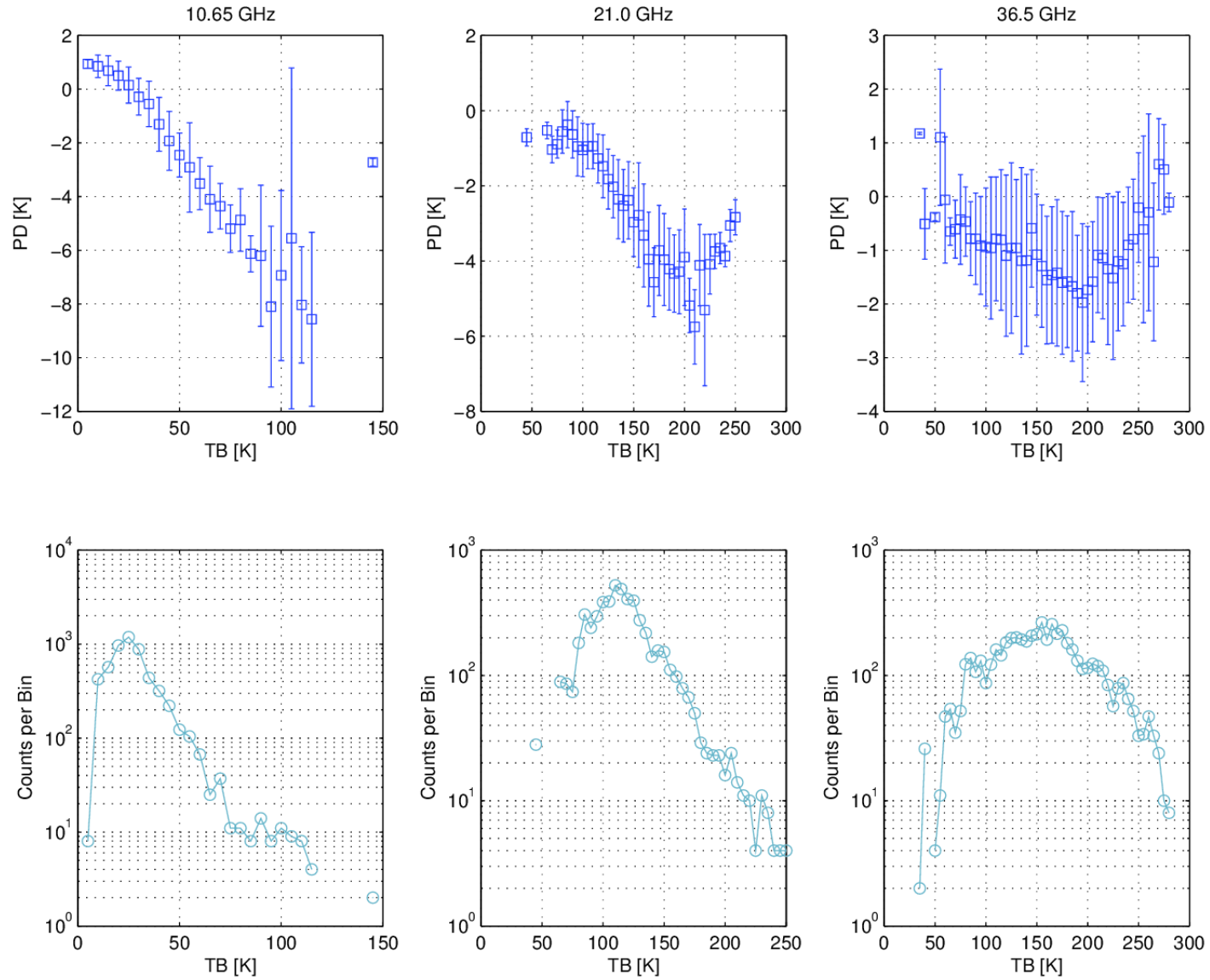


Figure 3.7.: ADMIRARI historical first data set as shown in the TB-PD space for the three frequencies, from left to right 10.7, 21.0 and 36.5 GHz. Every point represents the average of a data sub-set grouped in a bin of 5 K, the error bar is the standard deviation. The lower row indicates de number of data at every TB bin in the abscissa.

Non-linearity at 10.7GHz sky-tipping curve

As mentioned in section 3.1.1.1, the sky-tipping calibration is considered one of the most accurate absolute calibration method. Nonetheless an important issue occurs to the 10.7GHz channels, namely the tipping curve does not fit a linear relationship but rather it resembles a *quadratic-like* dependence of the optical thickness as a function of the airmass. To illustrate this, figure 3.8 shows the result of a successful sky-tipping calibration where the higher frequencies (21.0 blue squares and 36.5GHz red diamonds) show a practically perfect linear adjustment. The black line represents the linear regression best fit to the points, and the parameters to test the results of the calibration are also shown e.g. the correlation coefficient and the χ^2 -test. Normally as a criterion to accept a sky-tipping as a successful, the parameters must fulfil the conditions $r^2 > 0.9995$ and for $\chi^2 < 1.2$ which is why this particular example was flagged as success.

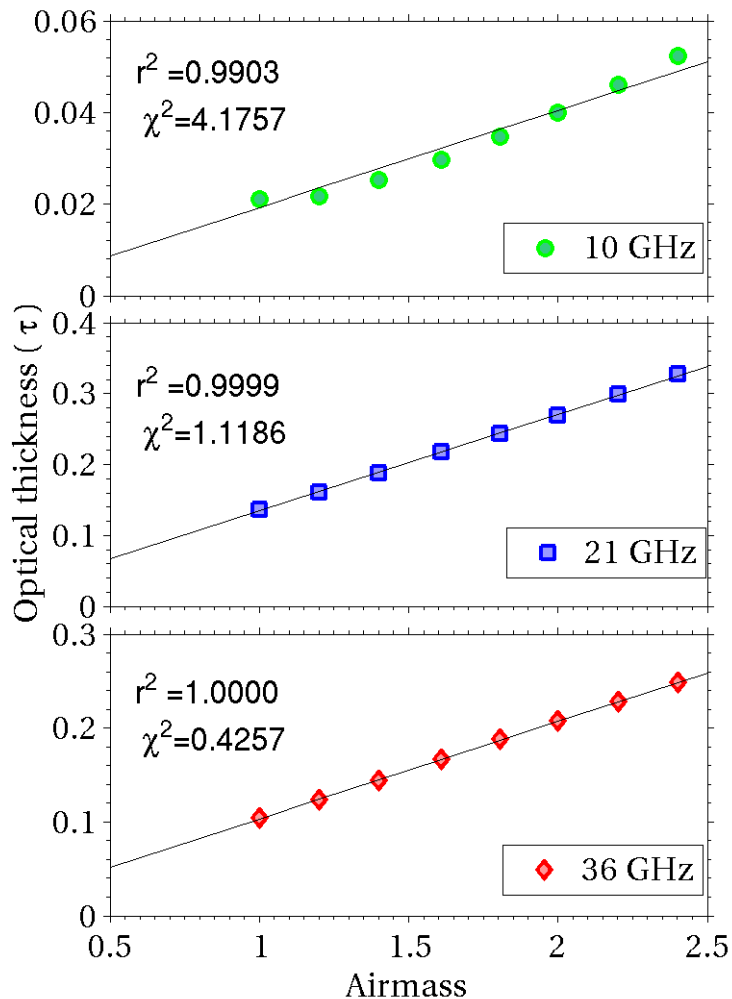


Figure 3.8.: Example from July 19th, 2009 of a sky-tipping calibration with optical thickness as a function of airmass. From top to bottom 10.7, 21.0, 36.5GHz vertical polarization, with respective test criteria correlation coefficient r^2 and χ^2 . The black line is the linear regression fit.

However by looking at the results for the 10.7GHz channels, it is clearly seen that the points do not fit a line and have a bending pattern at low airmass values, namely below 1.5. The same behaviour is observed also when looking at the antenna voltages instead of optical thickness τ , indicating that the issue is not an artefact of how the τ is estimated. The origin of this non-linearity is argued to be due to the fact that at low airmass (high elevation angles) the atmosphere is too transparent and does not produce significant change on opacity any more. Another possible explanation is that the antenna side-lobes might produce this effect but there is not a clear explanation for this phenomenon so far. This, however, limits the validity of linear regression and thereon jeopardizes the reliability of the calibrated variables as for instance T_{sys} .

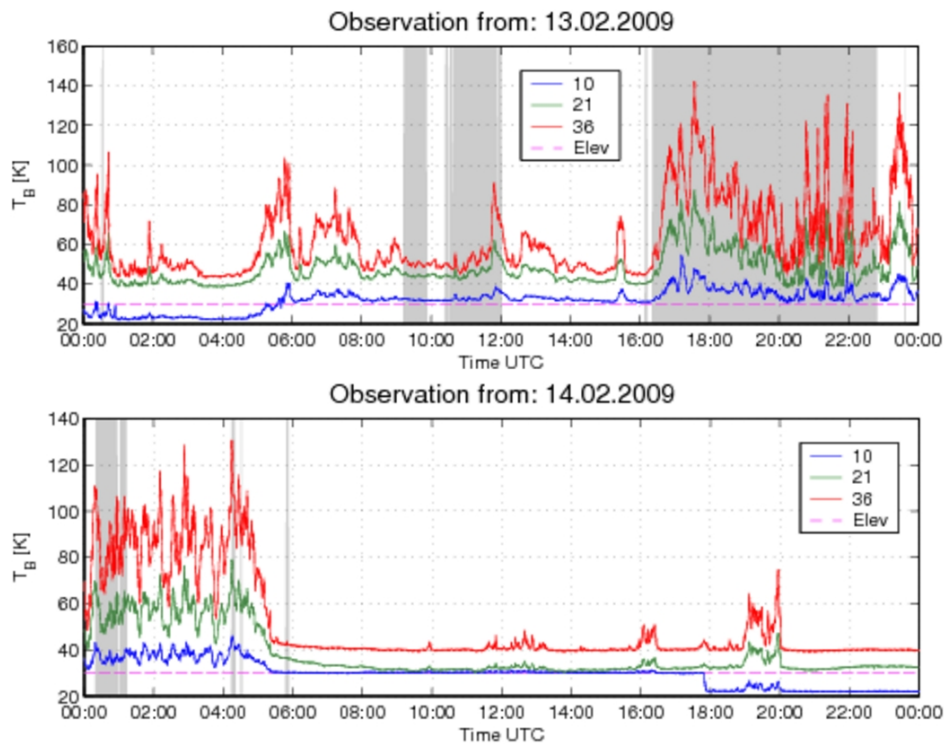


Figure 3.9.: Brightness temperature time series for two consecutive days, top: Feb. 13th and bottom: Feb. 14th 2009. There were two successful calibrations at 06:00 UTC the first day and at 18:00 UTC the second. Note the drop on TB at 10.7GHz (blue line) after the second calibration.

The low airmass bending pattern is not a peculiarity of the example shown in figure 3.8 but rather a common behaviour at that frequency and it was also observed at 15 GHz radiometers (RPG personal communication). Obviously the regression tries to fit a line which represents better the whole set of points, leading to a low correlation coefficient and poor χ^2 . For that reason, at the beginning of operations the 10.7GHz was never flagged as successful since the same criterion was used for all frequencies. After reporting this issue, a modification in the software has made possible to set-up the test criterion separately for every frequency, therefore the test parameters were adjusted such as a fitting as shown in figure 3.8 top panel can be considered a successful calibration. That modification however led to another issue which allowed the 10.7 GHz channels to be successfully calibrated in almost any sky conditions,

with even worse consequences for the reliability of the measurements. To highlight the latter, figure 3.9 shows a good example about the effects produced when being less strict with the sky-tipping curve test parameter (r^2 and χ^2).

The case in figure 3.9 depicts measurements where the sky-tipping procedure was scheduled at 6:00 and 18:00 every day. The first day in figure 3.9, at 6:00 UTC, the calibration failed for 21.0 and 36.5 GHz because the sky was cloudy (see high TBs at that time), but for the 10.7 GHz the calibration was successful and the calibration parameters inappropriately adjusted. This caused a significant bias on TB's base line of approximately +10 K. At 18:00 UTC the calibration was not performed at all since rain was detected by the rain sensor (gray area in figure 3.9). The next successful calibration for the 10.7 GHz was the day after at 18:00 UTC with the sky not overcast but some cloud still present around. This time the sky-tipping has changed again the calibration parameters and produced a drop on TB's base line till approximately 21 K for the 10.7 GHz (see figure 3.9 bottom panel after 18:00 UTC).

After reporting this kind of incidents with the sky-tipping method at 10.7 GHz the radiometer constructor RPG decided to dismiss the two lowest airmass points in the linear regression calculation. By doing so, the regression test parameters can again be set up in such a way that only a very linear distribution of optical thickness and airmass is assumed as successful. Moreover the company has decided to include an extra constrain, by including an extra point at zero airmass (top of the atmosphere) corresponding to an optical thickness equal zero. Although the company did not report any technical details regarding the feasibility of that assumption, the actual software includes this constrain.

Antenna misalignment

Long term observations have been compared with state-of-the-art radiative transfer simulation for precipitating clouds. The comparisons has shown good agreement in TB-TB space (see 4.3 for details). While the simulations fit properly well into the measurements field, for the couple of frequencies 21.0 and 36.5 GHz, the same was not observed in case of the 10.7 GHz where the model results cannot capture the variability shown by measurement (figure 3.10). That mismatch has been already reported by Battaglia, A., Saavedra, P., Simmer, C., and Rose, T. (2009, section IV) giving as possible explanation the fact that this channel differs from the others for the use of an off-axis parabola antenna and arguing that this might produce biases due to different calibration procedures. Another possible reason was that the model did not consider any melting particles; however this should affect all frequencies with a relative higher effect at the lowest frequency 10.7 GHz.

Later studies have discovered that the 10.7 GHz channels present a significant difference when sensing hot targets like for instance trees, buildings or the sun. This difference were mainly related to the pointing direction towards the hot targets, with the 10.7 GHz showing a clear misalignment with respect to the other channels. In figure 3.11 the results of a elevation scan from 0 to 90° is presented, the scan was performed with a step of 1° and 5 samples per angle in order to reduce variations. The radiometer scanned over a building located about 30 meters distance with some trees at the top and with clear sky as a background. The top panel of figure 3.11 (a), are the brightness temperatures for all frequencies with a clear mismatch shown by the TB at 10.7 GHz, while the TB corresponding to the other frequencies match each other until the radiometer starts to drive out of the hot target (building) at ~18° elevation. That is even better highlighted when the polarization difference is seen for the same scan as it is shown in figure 3.10 (b), where the peak of polarization for the higher frequencies match

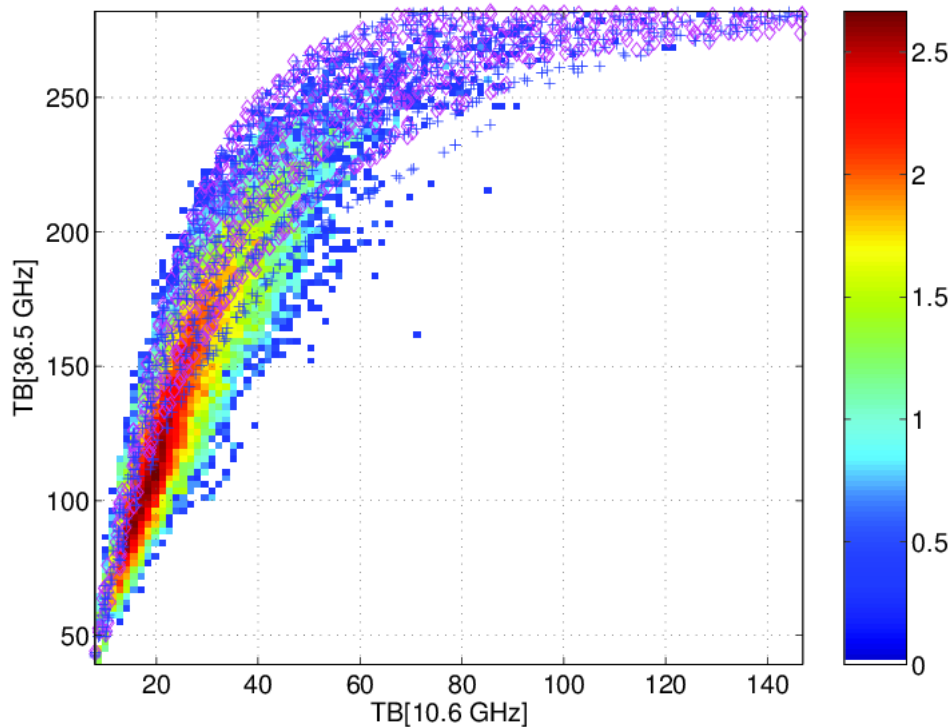
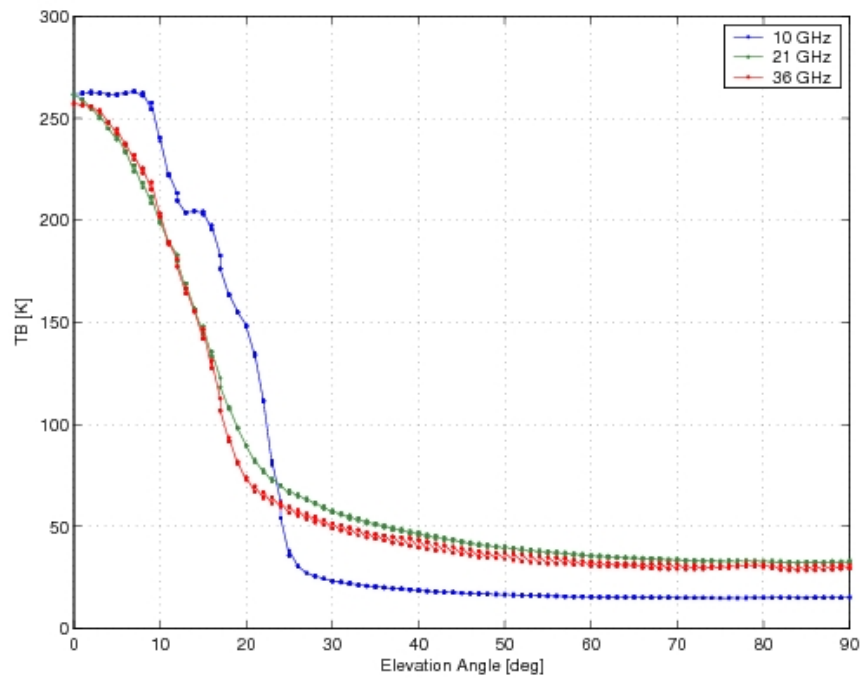


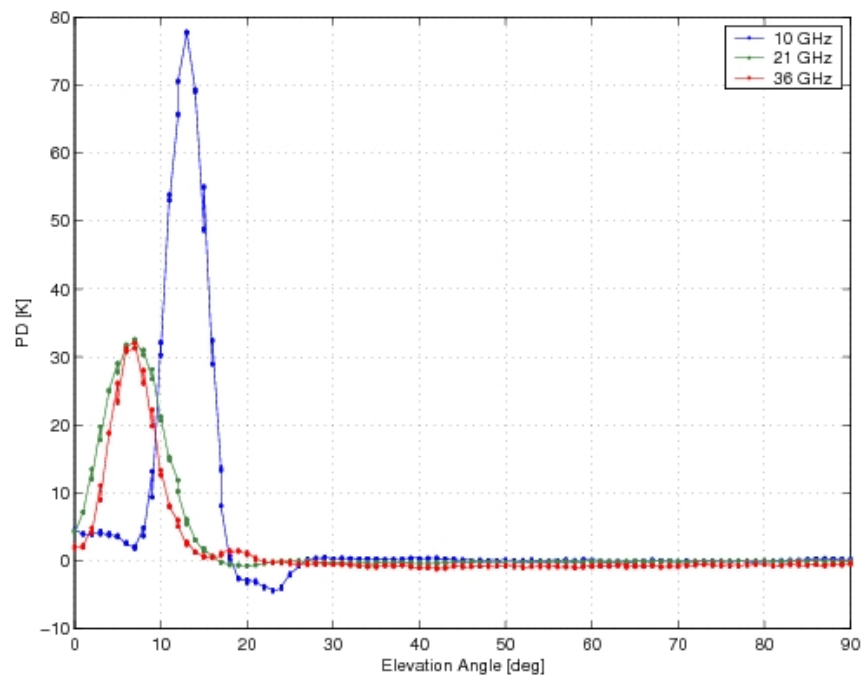
Figure 3.10.: Brightness temperatures for the 10.7 and 36.5 GHz frequencies. Measurements are indicated by the coloured distribution pixels with the colour representing the number of observations. Simulations are indicated by the crosses and diamonds (Extracted from Battaglia, A., Saavedra, P., Simmer, C., and Rose, T. (2009)).

at the same angle but the same is not case for the 10.7 GHz with a peak at $\sim 14^\circ$ elevation. In addition the higher frequencies reach already the clear sky ($PD=0K$) at approximately 21° elevation while the 10.7 GHz still senses some polarization from the top of the trees and just reach zero polarization from 27° elevation up. That was the indication of a clear misalignment between the 10.7 GHz channels with respect to the others.

Posterior studies by scans over the sun in elevation and azimuth have determined that the misalignment was at about 7° in elevation while in azimuth the difference between all channels were below 1° . The origin of misalignment was the off-axis parabola reflector (on the top-middle in picture 3.2 surrounded by black absorber) which was not installed properly to fulfil alignment with the whole system. The manufacturer corrected the misalignment. Thereafter, as a good practice, a scan over the sun has been performed every time the radiometer has been transported/installed to different locations with adjustments needed in every set-up. Moreover, with the antenna alignment correction, posterior measurements have shown a good agreement with the simulations, being therefore the 7° in elevation mismatch the main origin of the discrepancy shown in figure 3.10 among model and observations at 10.7 GHz.



(a) Brightness temperatures



(b) Polarization difference

Figure 3.11.: Two elevation scan over obstacles to block the radiometer FOV till 25°. The scan was performed from 0 to 90° elevation, with 1° step and 5 samples per angle to smooth down noise.

Antenna beam-width

Figure 3.11 (b) also gives a hint on another issue, namely the antenna beam-width. Observing the angular distribution along the scan, for the 21.0 and 36.5 GHz channels, it turned out that the 21.0 GHz channels had a larger antenna beam-width of approximately 3° larger than the 36.5 GHz. The original instrument specification required a 5° beam-width for all channels. However an inspection with scans alike figure 3.11 and sun overpasses have determined that the actual antenna beam were around 6, 8.5, 6° for 10.7, 21.0 and 36.5 GHz respectively. Later the radiometer constructor RPG had agreed in those numbers and corrected the hardware of the 21.0 GHz module by changing an improved lens which is coupled to the antenna feed horn. After this correction the actual antennas beam-width are all around 6° as it is summarized in table 3.2.

Antenna band-width

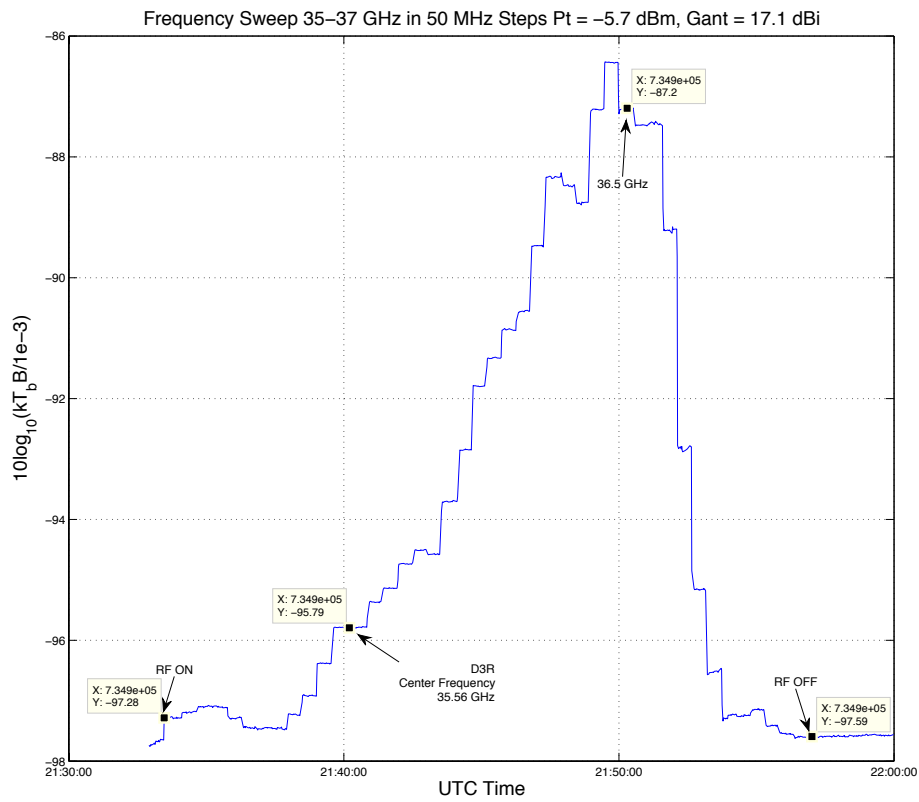
Recently, the radiometer ADMIRARI has performed co-located measurements with Ka-band cloud [Radio Detection And Rangings \(RADARs\)](#), e.g. the NASA's [Dual-frequency, Dual-polarization, Doppler Radar. Web site \(D3R\)](#) and the [Ka-band Scanning ARM Cloud Radar. Web site \(KASACR\)](#) during field campaigns at the [ARM](#) facility in Oklahoma, U.S.A and at [Environment Canada \(EC\)](#) near Ontario, Canada (Saavedra, P., Battaglia, A., and Simmer, C., 2012a). Those measurements revealed another issue: the 36.5 GHz channel suffers of strong interference by the Ka-band radars not only when targets are present within the common instruments' [FOV](#) but also during target free cases presumably due to clutter or radar side-lobe effects.

That interference was particularly unexpected since Ka-band cloud radars operate in a frequency around 35.5 GHz while the ADMIRARI's nominal frequency is 36.5 GHz with a band-width of 400 MHz.

In order to figure out the origin of interference, ADMIRARI was deployed to Colorado State University's CHILL (CSU – CHILL) radar facility to make some band-width testing. At the facility a non-invasive frequency respond test has been performed by Manuel Vega from NASA Goddard Space Flight Center, who is also engineer responsible for the [D3R](#).

Figure 3.12 illustrates the test performed in order to understand the origin of interference. The picture in 3.12(b) shows the experimental set-up, with the transmitter antenna horn in front and the radiometer in the back located approximately 10 meters distance. Neither the radiometer nor the transmitter were pointing in straight line rather in a slant configuration, this in order to avoid saturation on the radiometer's receiver and undesired signal from the ground due to the transmitter side-lobes. The transmitter worked with a very low power of -5.7 dBm (~ 0.27 mW), with antenna gain of 17.1 dBi and the frequency span was in the range from 35 to 37 GHz and changed in steps of 50 MHz, the test was performed with horizontal polarization. Although during the test the sky was mostly cloudy and the transmitter set-up at a low power, this was enough to clearly exceeds the natural emission by the cloudy atmosphere.

In figure 3.12(a) the test's result is summarized in a time series frequency response plot. The arrows labelled with RF ON and RF OFF indicates where the transmitter were powered on and off respectively, i.e. before and after these points the plot shows only the natural atmospheric emission. It is also indicated the [D3R](#) Ka transmission frequency and the nominal ADMIRARI frequency. As a result of the test, the following conclusions can be mentioned:



(a) Non-invasive frequency response test for the 36.5GHz ADMIRARI's channel.



(b) Experimental set-up.

Figure 3.12.: Studies performed at the CSU-CHILL facility together with Manuel Vega from NASA Goddard, to find out the origin of interference by Ka-band radars.

3. Microwave Radiometry

- The band-width is not symmetric around the central frequency, rather it is skewed towards the lower part and has a sharp drop-off in the higher part.
- It is clear that the stop-band rejection on the bandpass filter of the ADMIRARI is not enough to completely reject the D3R Ka-band frequency.
- Apparently the ADMIRARI central frequency is not at 35.6GHz but 35.0GHz, although this is difficult to establish by this method unless a coupled radiometer antenna-transmitter test is performed.

The experiment performed was not ideal to characterize the frequency response of the 36.5 GHz ADMIRARI frequency. However it was good enough to identify the origin of interference since up to that point it was not clear if the interference was due to radiometer/radar receiver/transmitter frequency misspecification. After this issue was reported to the radiometer's constructor RPG, a new bandpass filter was ordered to fulfil the original specifications and mainly to avoid interference in future synergistic measurements between cloud radars and ADMIRARI.

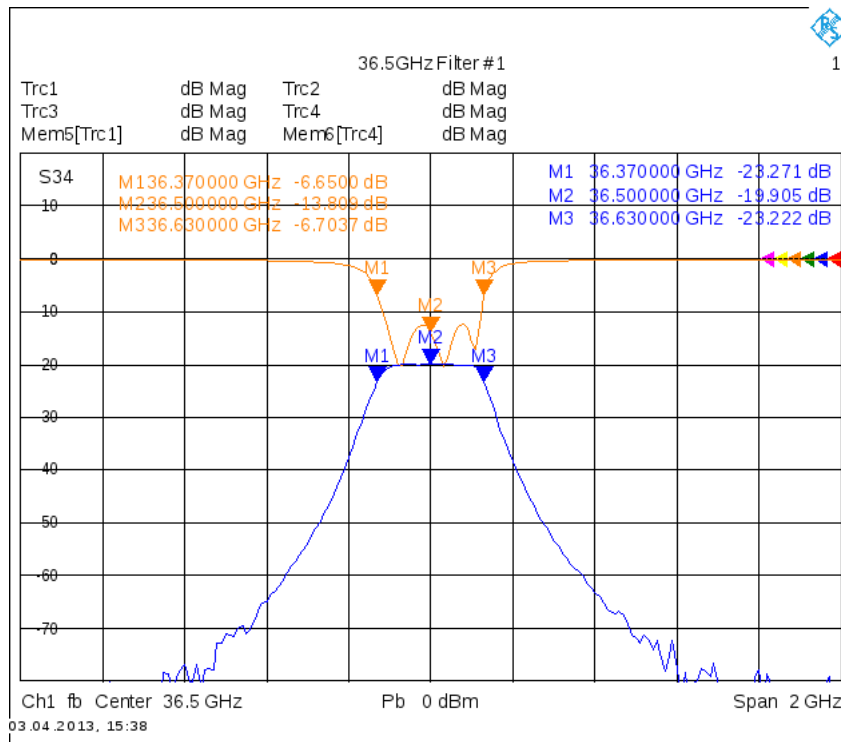


Figure 3.13.: New ADMIRARI's band-pass filter for the 36.5 GHz module (plot courtesy from RPG).

3.2. Co-located Ancillary Instruments

The radiometer ADMIRARI is a standalone instrument whose radiometric signal is affected by the hydrometeors and gases contained in the atmosphere (see chapter 4, section 4.2) along the observational column. As a result the radiometer has no range capabilities, making the inversion of atmospheric states from the measurements an ill-posed problem. Therefore the more

constrained the atmospheric states are the better the inversion is likely to be. For that reason, the ideal observational scenario includes multiple sensors in synergy; in order to achieve this goal the radiometer has been equipped with two active sensors with range resolution capabilities to have an insight into the hydrometeor profile.

The need of avoiding stress to the ADMIRARI's positioner mechanics, light and small active sensors was an imperative requirement. The next subsections present the features and performances of those active instruments and how they have been incorporated into the passive observations.

3.2.1. Micro Rain Radar

3.2.1.1. General description

The [Meteorologische Messtechnik GmbH \(METEK\)](#)'s [MRR](#) is a compact [Frequency Modulated-Continues Wave \(FM-CW\) RADAR](#) system that takes advantage from the measured vertical profiles of spectral radar echo from falling hydrometeors, for estimating [DSD](#). The number of concentration for rain drops at each drop-diameter bin is estimated from the backscatter signal corresponding to each frequency bin, to do so a relationship between terminal falling velocity and drop size is being used ([METEK-GmbH, 2010](#)).

Therefore, the estimation of drop size distribution from the [MRR](#) power spectrum is the most important procedure for the subsequent derivation of rain parameters. Hence the [DSD](#) is used to derive various integral rain parameters, namely reflectivity, rain rate, liquid water content and characteristic falling velocity following:

$$\begin{aligned} \text{Reflectivity: } Z &= \int_0^{\infty} N(D) D^6 dD \\ \text{Liquid water: } LWC &= \rho_w \frac{\pi}{6} \int_0^{\infty} N(D) D^3 dD \\ \text{Rain rate: } RR &= \frac{\pi}{6} \int_0^{\infty} N(D) v(D) D^3 dD \end{aligned} \quad (3.58)$$

The raw spectral power received by the radar is given by

$$f(n,i)\Delta f = \frac{10^{20} TF(i)}{C^2 \Delta h} \eta(n,i) \Delta f \quad (3.59)$$

where,

- i ranges from 1 to 32 and denotes the range index,
- n ranges from 0 to 63 and denotes the spectrum bin,
- $\eta(n,i)$ the backscattering cross section per volume [m^{-1}],
- $TF(i)$ the system's specific transfer function and depends on the hardware,
- C the calibration constant, also specific for the hardware,
- Δh the range resolution in meters,
- Δf 30.52 Hz the frequency resolution of the 2nd Fourier Transform.

The term $\eta(n,i)\Delta f$ is derived from the raw spectra $f(n,i)\Delta f$ given the factory determined calibration constant and transfer function which are stored in the system firmware.

The [MRR](#) spectral raw data (as recorded by the system and denoted as $F_n(n,i)$) is related with the backscattering cross section following:

$$F_n(n,i) = 10 \log_{10}(\eta(n,i)) \quad (3.60)$$

Nevertheless, the signal corresponding to the spectral backscattering cross section η , as it is primary recorded by the instrument, includes the signal noise i.e. antenna noise, electronic

noise. Thus the software has an internal procedure to estimate the noise level for every single spectrum at every range and subtract it from the spectral backscattering in order to avoid inaccuracies in further computations due to systematic inclusion of noise spectral signal. Therefore, the estimation of antenna spectral noise and the correction to $F_n(n, i)$ must be done before the application of equations 3.59 and 3.60. The procedure to correct the spectral noise is presented in detail by (METEK-GmbH, 2010, section 15). The MRR software produces a set of data files which include the one minute average and the instantaneous 10 seconds products (e.g. Z, DSD, LWC, RR, all calculated after its internal signal processor). Additionally and optionally it is possible to archive the lowest data type level, the 10 seconds time resolution Raw data file which is composed by only $F_n(n, i)$ including the noise system.

To estimate DSD from $\eta(n, i)$ an empirical relation between terminal fall velocity and drop diameter is used (METEK-GmbH, 2010). The number of drops per volume and diameter $N(D_n)$ is obtained by dividing the spectral backscattering cross section $\eta(n, i)$ with the backscattering cross section $\sigma(D_n)$ of a rain drop with specific diameter D_n ,

$$N(D_n, i) = \frac{\eta(n, i)}{\sigma(D_n, i)} \quad (3.61)$$

For drop diameters small compared to the wavelength λ (Rayleigh approximation) $\sigma(D_n, i)$ could be expressed analytically

$$\sigma_\lambda(D_n, i) = \frac{\pi^5}{\lambda^4} |K|^2 D_n^6 \quad (3.62)$$

with $K = \frac{m^2-1}{m^2+1}$, where m is the complex refractive index of water and depends on temperature, D_n the drop diameter corresponding to the n^{th} bin of the spectrum and λ is the radar wavelength [m]. For water (ice) $|K|^2$ has a value of about 0.92 (0.18) for 24.1 GHz. Since the MRR's wavelength is not larger enough compared to most naturally occurring rain drop diameters, the Rayleigh approximation does not yield accurate results, therefore the MRR estimations are done by using σ calculated according to MIE theory.

Since the spectral reflectivity is stored in discrete bins, the analytical integrals in equations 3.58 must be numerically integrated and be replaced with summation, for instance the reflectivity becomes

$$Z(i) = \sum_{n=1}^{Nbin} N(D_n, i) \sigma(D_n, i) \quad (3.63)$$

and likewise for all expressions in 3.58. It is important to note that although the MRR spectrum has 63 bins, the software selects different spectral integration intervals depending on the range (METEK-GmbH, 2010, figure 7), this due to some electronic coupling between the spectrum in one range and the next one, see for instance the lowest and highest bins in figure 3.15.

The MRR software calculates the rain drop size distribution for each rain gate (thereby the index i in equation 3.61) resolved in discrete steps that are equidistant in the Doppler velocity domain.

The MRR operates in a nominal frequency of 24.1 GHz (see table 3.3) which gives a high sensitivity to small rain drops. On the other hand, it is strongly attenuated by moderate to intense rain. Moreover at 24GHz the attenuation due to water vapour is not negligible (0.2 dB km⁻¹ for 10 mm water vapour column). Therefore the equation 4.80 is corrected for

attenuation assuming that in the first range the attenuation is negligible and for the subsequent ranges is described by the following recursive relation

$$N(D_n, i+1) = N_{att}(N_n, i+1) \exp[\Delta h \sum_{k=1}^i \kappa(N(D_n, k))] \quad (3.64)$$

with N_{att} the DSD from equation 3.61 and the extinction coefficient κ given by

$$\kappa(i) = \sum_{n=1}^{Nbin} N(D_n, i) \sigma_e(D_n, i) \quad (3.65)$$

with σ_e being the single particle extinction coefficient of a drop with diameter D_n and calculated according to MIE theory.

Note that the MRR has been conceived to operate as a vertical pointing instrument, but in the previous description the range bins have not been referred to as altitude bins. This was done intentionally since in the present work the MRR was operating alike ADMIRARI in scan mode i.e. measuring slant rather than vertical configuration. Therefore the application of an empirical relationship between terminal fall velocity and drop diameter cannot be used any longer because in slant configuration the Doppler velocity is affected by horizontal wind component along the line of sight i.e. equation 3.61 no longer applies. For that reason, the DSD estimation and thereafter the calculation of radar parameters cannot be used in slant configuration in addition to other issues related with the software's signal processing method. The next subsection explains how the signal processing has been adapted in order to operate the MRR in slant mode.

3.2.1.2. MRR in Slant Configuration

When the MRR was installed to ADMIRARI's pedestal it was clear that the products from METEK were not meaningful in slant configuration due to uncertainty of the wind velocity's vertical component on the DSD. Therefore the reflectivity was calculated from the spectral backscattering cross section $\eta(n, i)$ which is recorded by the system in intervals of 10 seconds and is corrected from the system noise level by the METEK internal signal processor. In order to obtain the reflectivity from the spectral reflectivity without using the METEK DSD estimation, $N(n, i)$ must be replaced in equation 3.58 by the ratio in 3.61, therefore the reflectivity Z is expressed in terms of η and σ . When using the relationship between the backscattering cross section and drop diameter 3.62, the radar reflectivity factor is given by

$$Z_e = \frac{\lambda^4}{\pi^5 |K|^2} \sum_{n=1}^{63} \eta(n, i) \quad (3.66)$$

where the derivative of the spectral frequency is used instead of the drop size $\eta(D_n)dD_n = \eta(f_n)df$ and the integral has been replaced by a summation over all spectral bins $\int g(f)df = \sum g_n$.

However, the application of equation 3.66 has produced non-physical values mainly during convective rain. As a reference large hail thunderstorm might produce reflectivity about 50 to 55 dBZ in radars at 5.64 GHz (C-band); for the MRR's frequency that kind of precipitation should attenuate the signal considerably therefore less reflectivity values are expected to be observed. Nonetheless values way above 60 dBZ has been obtained. The reason for that is

mainly due to the METEK firmware processing for the spectral backscattering η which uses the method by Hildebran, P. and Sekhon, R., 1974. The method determines the noise level in Doppler spectra but the METEK signal processing does not take into consideration issues related with spectrum aliasing and wind vertical component, rather it assumes that the Doppler spectra comes purely from falling drops. Tridon, F., Van Baelen, J., and Pointin, Y. (2011) have already shown that the MRR measured spectra can suffer from aliasing errors that affects the DSD, which need to be corrected adequately in order to obtain further retrievals based on the DSD.

In case of scanning mode the shift introduced by the combined effect of vertical and horizontal winds, projected to the slant observational angle, augments even more the aliasing issue. Hence the METEK signal processing misstates the MRR spectrum and therefore the estimated DSD results are meaningless. In order to avoid this issue, the post-processing spectrum by METEK firmware must be avoided since it does not take into account aliasing and its noise level is estimated assuming that the spectrum has a mono-modal distribution.

Fortunately the MRR's software has the option for recording the RAW data files. The RAW data has the advantage that the spectrum presents no pre-processing, meaning no information is lost and aliasing can be identified and properly processed. Moreover the RAW data includes the system noise which can be subtracted once a procedure to estimate the noise level is developed.

The RAW data file contains only $F_n(n, i)$ sorted in 63 spectrum bins and 32 range gates, hence reflectivity (thereafter denoted as Z_raw) is calculated using the equation 3.59 with the spectral backscattering cross section $\eta(n, i)$ obtained by inverting equation 3.60 with $F_n(n, i)$ as independent variable.

The improvement in reflectivity calculation is clearly highlighted in figure 3.14 where three profiles are compared, namely: the standard output by METEK (red circles), the calculated from the post-processing $\eta(n, i)$ (blue crosses), and the calculated from primitive RAW data (green squares). Note that the latest still includes the noise floor of the radar receiver.

A procedure to estimate the noise level has been implemented based on the method by Hildebran, P. and Sekhon, R. and following the steps as in METEK-GmbH, (section 1.5.2). This method, as a first step, computes the spectrum mean \overline{NL}_1 , then identifies the highest peak which is afterwards removed to calculate a new spectrum mean \overline{NL}_2 . If the condition $|\overline{NL}_2 - \overline{NL}_1| < \varepsilon$ is fulfilled then the remaining spectrum peaks are considered noise. In case the condition fails then the highest peak (from the two next to the latest removed) is removed and a new mean is computed. That procedure is repeated n-times till the condition is fulfilled and the last mean \overline{NL}_n is considered the spectrum noise level. This is applied at every range gate.

The method described above fails in cases when: 1st) spectrum folding yields a bimodal shape which is the case at ranges number 2 to 4 in the $F_n(n, i)$ example in figure 3.15, 2nd) all 63 spectrum bins are filled with signal as happens in figure 3.15 at ranges number 1, 2, 7, 8 where no bins are free of signal from which a noise level might be estimated. The first case was solved by unfolding the spectrum i.e. making it continuous at the borders. The second case was solved by using a long-term range resolved noise average $\overline{NL}_a(r)$ obtained from several clear sky observation, thus whenever the method estimates a high noise level as an artefact, then it is replaced by $\overline{NL}_a(r)$ for the corresponding range r .

The effect on reflectivity calculation of the above issues (cases 1 and 2) are summarized in figure 3.16(a) where three reflectivity profiles are shown, namely the one without any noise correction (green line), the one which considers 1st case (red circles), and the one which con-

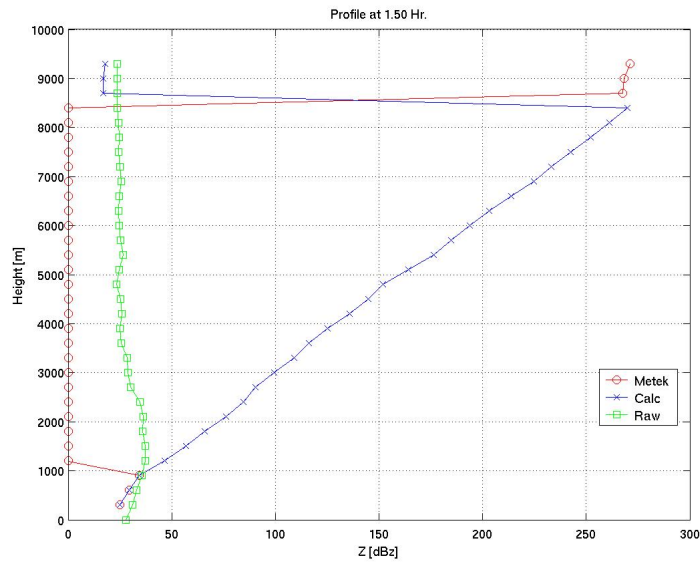


Figure 3.14.: Reflectivity profiles as observed by MRR in slant mode. Example profiles for the three reflectivity calculations i.e. (red) METEK standard output, (blue) from METEK spectrum, (green) from RAW data. Note that undefined values are indicated with 0 dBz (red circles) for clarity.

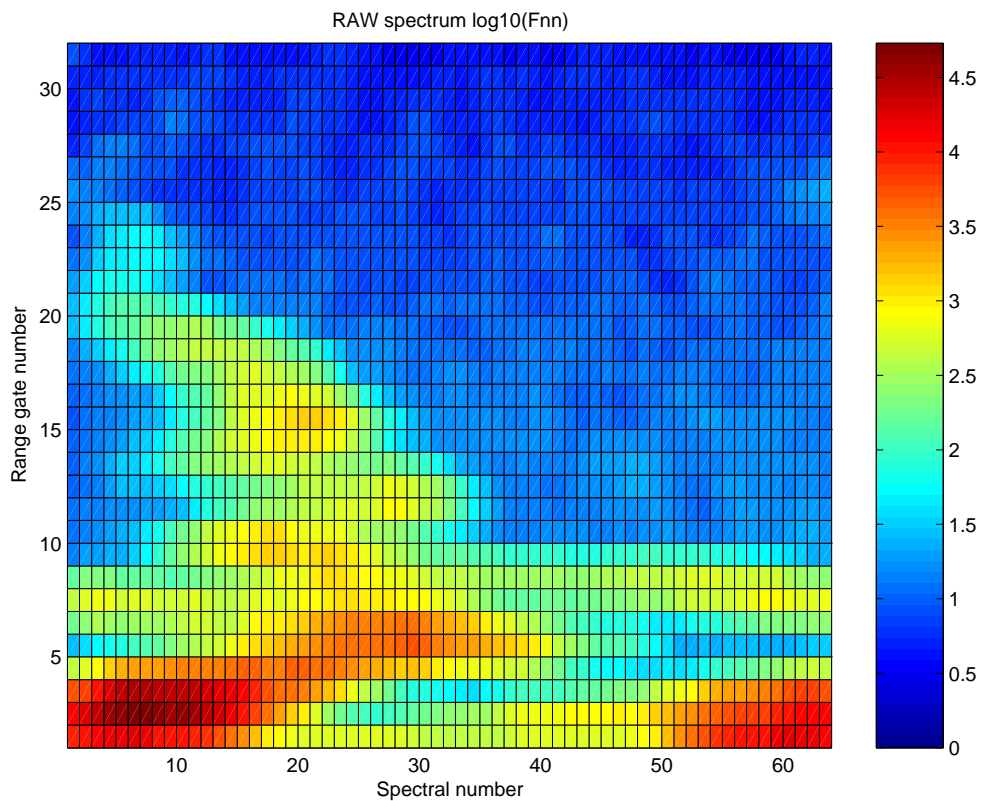


Figure 3.15.: Corresponding spectral power for the noise level estimation shown in figure 3.16(b), note that below the 5th and at 8th range the spectrum presents bi-modal distribution.

siders 2nd case (blue squares). Both cases produce an overestimation of the noise level (figure 3.16(b), red diamonds) which leads to an underestimation on reflectivity (figure 3.16(a)). Such is the case where the whole spectrum is either filled by signal (figure 3.15, ranges number 7 and 8) or bimodal is observed (for instance ranges 1 to 4 in figures 3.15 and 3.16(b)). As a consequence, the noise estimation algorithm developed here is based on the Hildebran, P. and Sekhon, R. method with spectrum unfolding procedure, combined with a long-term clear sky noise level $\overline{NL}_a(r)$ only if cases like in figure 3.16(b) (ranges 1 to 4, 7 and 8) miscalculates the noise floor.

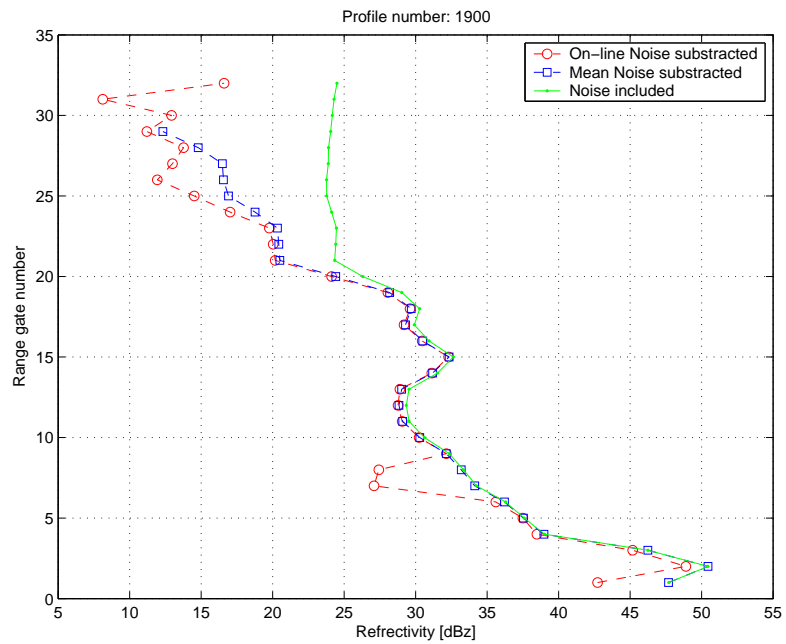
As a test to the validity of the algorithm, two nearby MRRs have been operated, one mounted at ADMIRARI in slant configuration and another (~ 5 meters away) vertically pointing. Figure 3.17 shows the different spectrum shapes for convective (top) and stratiform rain (bottom). Note how different the spectrum distribution is for the vertical and slant; similarly the vertical normalized reflectivity profiles are very different in case of convective rain (top row) due to the highly horizontal variability expected in presence of small rain convective cells. On the other hand, for stratiform rain the Z_e profiles match quite well regardless the different observational geometry. Nonetheless the methodology developed in the present study only allows to compute the reflectivity rather than the other standard MRR products like LWC, rain rate and wind speed.

Finally, it is important to mention that the present study is not only useful for cases where the MRR is operating in slant configuration but also when convective rain causes a wide variability of Doppler velocities which are mirrored in the MRR's spectral power (alike the study by Tridon, F., Van Baelen, J., and Pointin, Y., 2011). Moreover the present algorithm has been utilized by Kneifel, S., Maahn, M., Peters, G., and Simmer, C., 2011 to calculate vertical reflectivity profiles for snow observations, and thereafter has fostered the development of an algorithm to improve the MRR sensitivity for snow observations at vertical pointing MRR (Maahn, M. and Kollias, P., 2012).

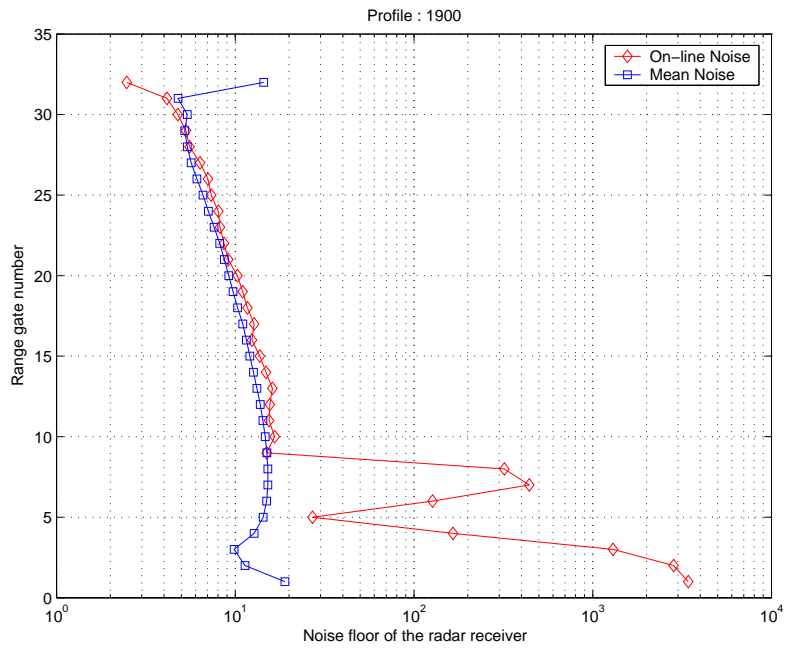
The software developed for the adaptation of the MRR in slant configuration is written in FORTRAN 95 and it is available, as well as a report with detailed description of the method) at <http://www.meteo.uni-bonn.de/mitarbeiter/pablo-saavedra-garfias>.

Table 3.3.: Main Features of the MRR radar used aside the radiometer ADMIRARI

Transmitter	
Type	FM-CW
Output Power	50 mW
Modulation	1.5 - 15 MHz
Frequency	24.230 GHz
Antenna Beam-width	1.5° (3dB)
Gain	40.1 dBi
Receiver	
Polarization	single
System Specifications	
Antenna diameter	60 cm
System power consumption	25 W



(a) Noise included (green), on-line noise (red) and mean noise method (blue)



(b) Noise level from RAW spectrum: mean noise $\overline{NL}_a(r)$ (blue), on-line noise estimator (red)

Figure 3.16.: (a): Three reflectivity profiles calculated with and without noise. (b): Two noise levels considered

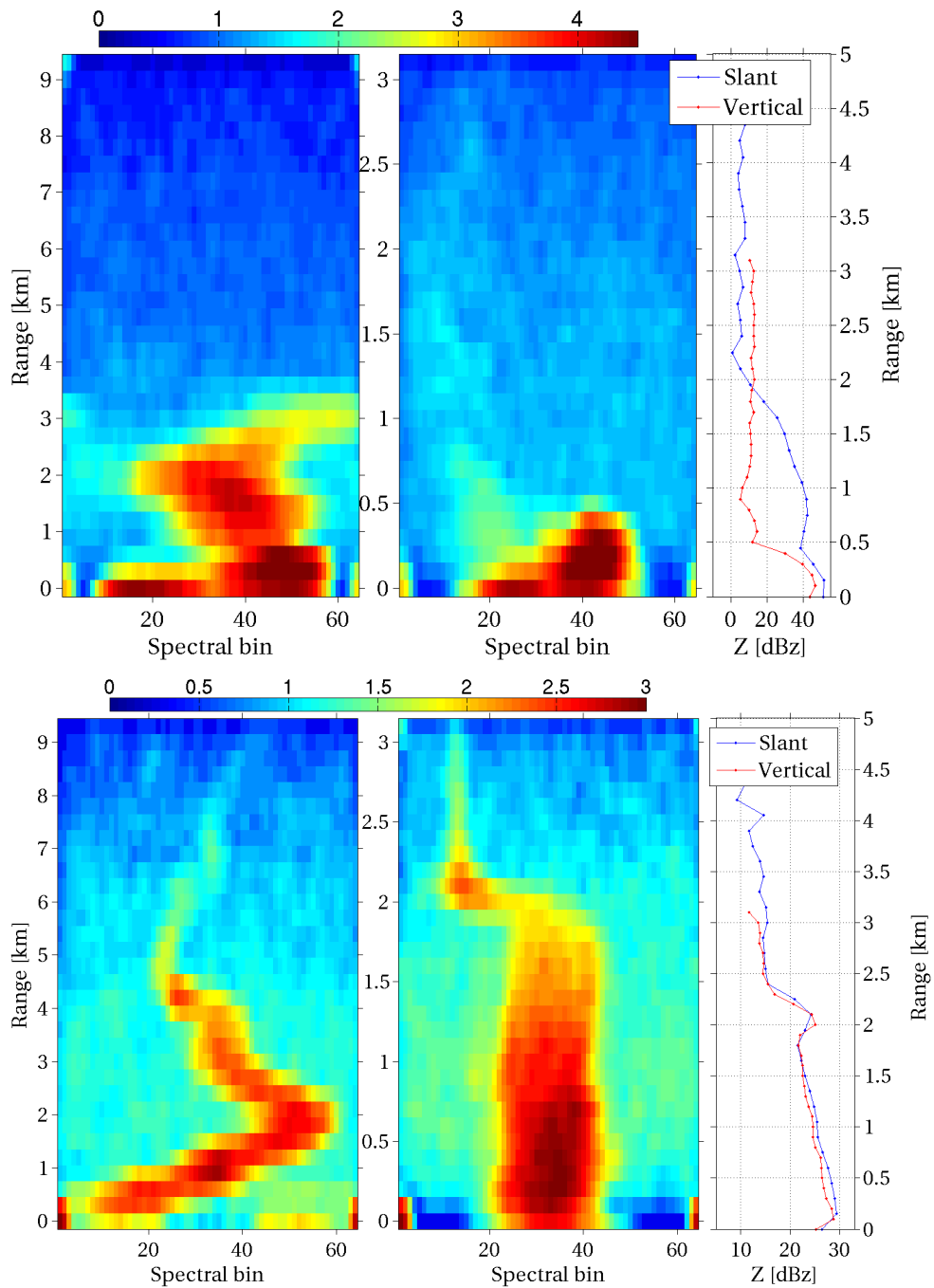


Figure 3.17.: Spectrum from two MRR: slant 30° elevation (left) and vertical (middle), and their corresponding vertical normalized reflectivity profiles (right) for two different events on 20 September 2010, 09:59UTC convective rain (top) and on 21th September 2010, 08:19UTC stratiform rain (bottom)

3.2.2. Cloud Lidar

The radiometer senses the radiative emission by all atmospheric components along the observing column, but an exact location of these components cannot be obtained with only the radiometric signature. Similar to the MRR's reflectivity profile which is a good indicator for the location and structure of the rain layer, a **Light Detection And Ranging (LIDAR)** might be useful to determine the position of the cloud layer. Although **LIDAR** and **RADAR** share similar detection principles, large differences exist in the physical processes and the system hardware, due to vast frequency difference of the radiation used by these instruments.

A **LIDAR** system is based on the principle of sending out a nano-second laser pulse in a certain direction (normally vertical) and measuring the time of the returned reflections. The amplitude of the reflected light, i.e. the backscattered signal caused by fog, haze, mist, aerosols, dust, precipitation and clouds is measured as a function of time while the laser beam traverse the medium. This signal then is processed to determine the location of the targets. Since the speed of light is constant, the time delay between the sending of the nanosecond pulse laser and the detection of its backscattering signal is calculated through the equation

$$\Delta s_{ld}(t) = \frac{\Delta t \times c}{2}$$

where $c = 2.997925 \times 10^8 \text{ ms}^{-1}$ is the speed of light in the medium, t is the time-of-light, and the factor 2 accounts for the round-trip of the photons travelled.

In general terms, the power received by a **LIDAR** from a given range s can be expressed by the following expression (Weitkamp, C., 2004)

$$P(s) = K G(s) \beta(s) T(s) \quad (3.67)$$

where the factor K is the **LIDAR** system calibration constant, $G(s)$ describes the measurement geometry; those two factors depend only on the **LIDAR** system. The factor K is a function of the system average power, the temporal laser pulse length, the aperture of the receiver optics and the system efficiency. The geometric factor $G(s)$ takes into account the laser beam receiver's overlapping field-of-view including the quadratic decrease with the distance (s^{-2} factor).

On the other hand $\beta(s)$, the backscatter coefficient, and $T(s)$ the transmittance factor are strictly dependent on the atmospheric state.

The backscatter coefficient in units of $\text{m}^{-1} \text{sr}^{-1}$ at a range s can be expressed as

$$\beta(s, \lambda) = \sum_i N_i(s) \frac{d\sigma_{sca;i}(\pi, \lambda)}{d\Omega}$$

where the sum is extended over all scatters within the backscattering volume. $N_i(s)$ is the concentration of atmospheric scatters and the $d\sigma_{sca;i}(\pi, \lambda)/d\Omega$ the particles' differential scattering cross section for the backward direction.

The last factor in equation 3.67 considers the fraction of laser radiation beam that is transmitted through the medium towards the target and back to the receiver. This transmission term assumes values between 0 and 1 following a specific form of the Lambert-Beer-Bouguer law applied to **LIDAR** (Weitkamp, C., 2004, pp. 6-11)

$$T(s, \lambda) = \exp \left[-2 \int_0^s \alpha(r, \lambda) dr \right]$$

In a similar way as the backscatter coefficient $\beta(s, \lambda)$, the extinction coefficient $\alpha(s, \lambda)$ is expressed as the product of number concentration and extinction cross section $\sigma_{ext,i}$ for each kind of scatterer i , with the extinction cross section given by the contribution of scattering and absorption cross sections i.e. $\sigma_{ext,i} = \sigma_{sca,i} + \sigma_{abs,i}$

When expanding the components of the equation 3.67, the LIDAR equation is depicted in its more common form as

$$P(s, \lambda) = P_0 \frac{c\tau}{2} A\eta \frac{O(s)}{s^2} \beta(s, \lambda) \exp \left[-2 \int_0^s \alpha(r, \lambda) dr \right] + P_{bg} \quad (3.68)$$

with P_{bg} is the expected contribution due to background photon sources (e.g. sun, moon, stars scattered light), detector and circuit shot noise.

The basic set-up of a LIDAR consists, alike a RADAR, of a transmitter, a receiver and the data acquisition and control system. The transmitter provides the laser pulses according to some parameters which determine the kind of laser (e.g wavelength, bandwidth, pulse duration time, pulse energy, repetition rate, divergence angle, etc.). On the other hand the receiver collects and detects returned photon signals, consisting usually of telescopes, filters, collimating optics, photon detectors, etc. LIDARs had originally the transmitter and receiver located in different places (bistatic configuration), nowadays modern LIDARs have the transmitter and the receiver at the same place (monostatic configuration) i.e. single-ended system. Moreover monostatic systems have either coaxial or biaxial arrangement.

A particular feature of LIDARs is the operation at wavelengths which are strongly attenuated by cloud droplets. Therefore LIDARs are well suited to measure the cloud base altitude and in some cases even cloud thickness. LIDARs specially designed to measure cloud bases are usually named Cloud-ceiling LIDAR or Ceilometer². A ceilometer not only provides an estimated altitude from a cloud layer, but the backscatter factor can also be obtained from some precipitation as long as the laser beam is not completely attenuated e.g. snowfall, drizzle or virga. An example is shown in figure 3.18 where two LIDARs were installed at 30° slant configuration at the Meteorological Institute, University of Bonn (MIUB)'s roof. In addition a MRR and a cloud LIDAR give complementary information on the presence/absence of rain and/or cloud layers (see figure 3.20). Therefore the utilization of a ceilometer, aside the radiometer antennas with similar steerable capabilities, may contribute significantly to the constrain of the observed scenario. Hence the motivation to include a ceilometer as an ancillary instrument for ADMIRARI.

The ADMIRARI's instrumentation was lately improved with a CBM80 ceilometer manufactured by Björn Eliasson Ingenjörfima AB (www.eliasson.com), this ceilometer has been chosen based on some considerations, i.e. the system needed to be light-weighted and small enough to be attached to the radiometer's pedestal and still have the basic capabilities as most of ceilometers. Not many system could fulfil this condition, but the Eliasson ceilometer has been found the most adequate. Nevertheless, the trade-off is the diminishing of some lidar's features like power, maximum range, optical field of view, polarization, etc. The main features of the Eliasson's CBM80 ceilometer are shown at table 3.4.

Unfortunately the CBM80 ceilometer does not report a backscatter factor β but only a normalized factor (from 000 to FFF hexadecimal). For that reason, a calibration factor must be determined by inter-comparison with other commercial systems. The Vaisala ceilometer model

²From the Latin Cealum which means heaven and the Greek metron meaning measure

Table 3.4.: Main features of the CBM80 cloud-lidar used aside the radiometer ADMIRARI

Transmitter	
Type	Laser, fibre attached CVD
Pulse Power	50 W
Pulse length	100 ns
Pulse Frequency	400 - 1000 Hz
Wavelength	905.2 \pm 5 nm
Divergence	2.8 mrad
Receiver	
Detector	Silicon Avalanche photo diode
Operating Voltage	345 V
Interference Filter	Centered at 906.7 nm
50% band-pass	7 nm
Transitivity	80% typical
Responsivity @ 1060 nm	18 A/W
Viewing angle	2 mrad
System Specifications	
Laser security	Class 1M according to IEC60825
Ambient temperature	-40 to +50° C
Max. Range	7600 m
Range Resolution	10 m till 1.6 km, 30 m afterwards
Time Resolution	15 or 30 sec
Weight	15 kg

ct25k was chosen as a reference to pursue an inter-comparison due to its availability at [MIUB](#) and mainly its matching wavelength i.e. 905 nm. However the ct25k has also unmatched features relative to the CBM80, namely: the time resolution, range resolution (30.48 m), normalization factor (0000 to FFFF hexadecimal), pulse peak power (16 W), beam divergence (± 0.75) and receiver's FOV (1.32 mrad) ([VAISALA, 1999](#)).

In figure [3.18](#) a case study for observations of the two co-located ceilometers is depicted. The backscattering coefficient (Vaisala ct25k) and the dimensionless backscattering factor (ADMIRARI's CBM80) have been collected at fixed slant 30° elevation. Both are shown with the same colour scale for comparison purposes.

Two features are clearly highlighted: first the CBM80 exhibits higher backscattering values at the cloud layer (overestimation), and second it lacks of sensitivity below the cloud base where aerosols are located. The first might be attributed to multiple scattering, it is known that multiple scattering yields an increase in backscattering and apparent reduction in attenuation. Multiple scattering occurs when the photons scattered by a cloud particle go through subsequent scattering events and reach the receiver afterwards ([O'Connor, E., Illingworth, A., and Hogan, R., 2004](#)). A multiple scattering factor, introduced by [Platt, C., 1973](#), varies between 0.5 and 1 depending on the telescope FOV, the wavelength of the radiation and the size of the particles the radiation encounters. A multiple scattering factor of 1 is the single scattering limit, where all the scattered photons are lost except for those directly backscattered to the

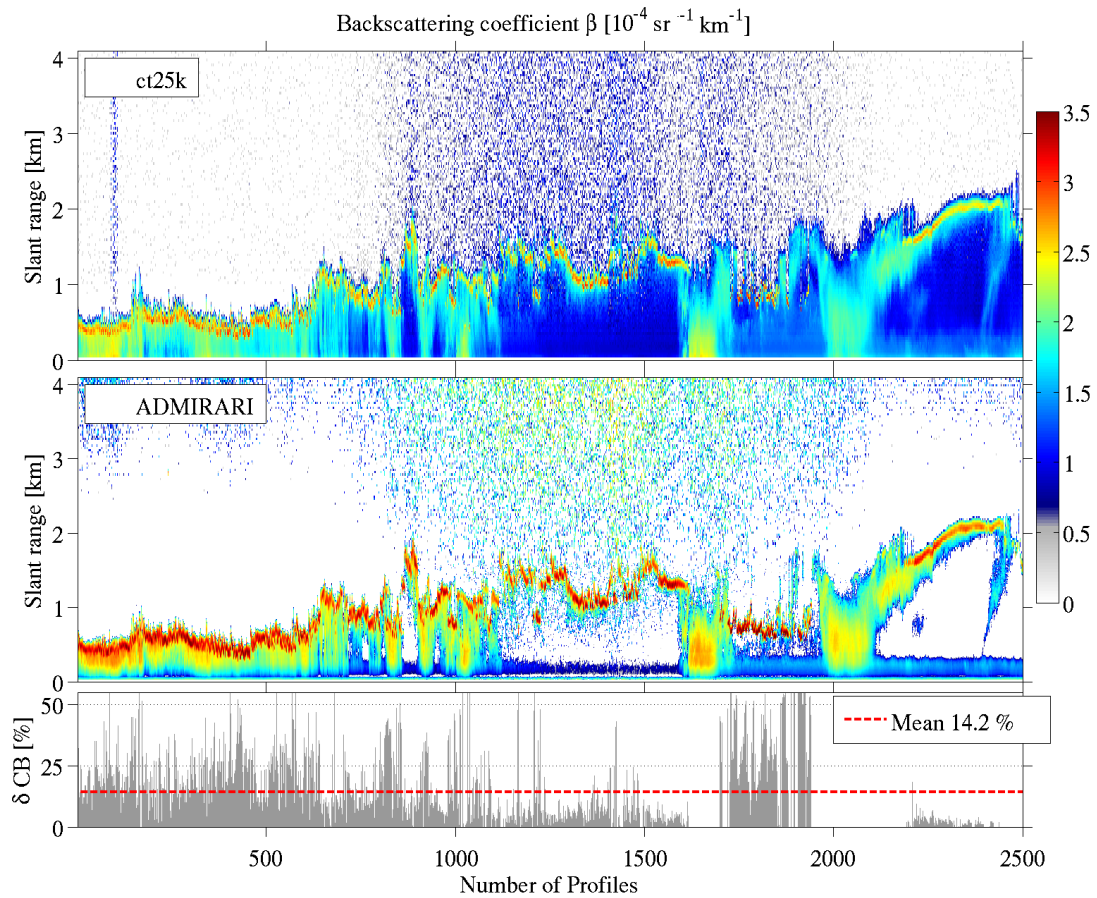


Figure 3.18.: Time series of cloud lidar’s backscattering coefficient profiles β in logarithm scale as observed at 30° elevation angle for (top) Vaisala ct25k and (middle) CBM80 mounted at ADMIRARI. The bottom panel is the error of the cloud base range in % relative to the Vaisala ct25k measurement.

instrument. The value of 0.5 is the wide FOV limit, where narrowly forward scattered photons remain within the telescope FOV.

For instance O’Connor, E., Illingworth, A., and Hogan, R., 2004, and references therein have found a multiple scattering factor of 0.83 ± 0.09 at 1 km and 0.73 ± 0.06 at 4 km for a Vaisala ceilometer alike the ct25k (ct75k), for stratocumulus with absence of drizzle. Hence, the larger CBM80 receiver’s FOV of 2mrad compared to the 1.32mrad for the Vaisala ct25k, suggest that the CBM80 is more prone to multiple scattering effect, thereof increasing in backscattering.

The detected cloud base range are compared as relative error on the bottom of figure 3.18. A mean of 14.2% for this specific case is found. Note that the relative error was calculated only when both instruments have detected a cloud base. The differences between cloud bases tend to be larger when the ceilometers have echoes from below the cloud base (case from 1st to 1000th profiles), and when broken clouds are detected (1700 to 1950th profiles). The lowest errors are found when the signature below cloud base is less than $1.5 \times 10^{-4} \text{sr}^{-1} \text{km}^{-1}$ for ct25k and undetectable for CBM80 (profiles from 2100 to 2500). It is important to remark that the ct25k has an internal zenith angle reader which allows an accurate adjustment, on the other hand the CBM80 needed to be adjusted manually and therefore some misalignment

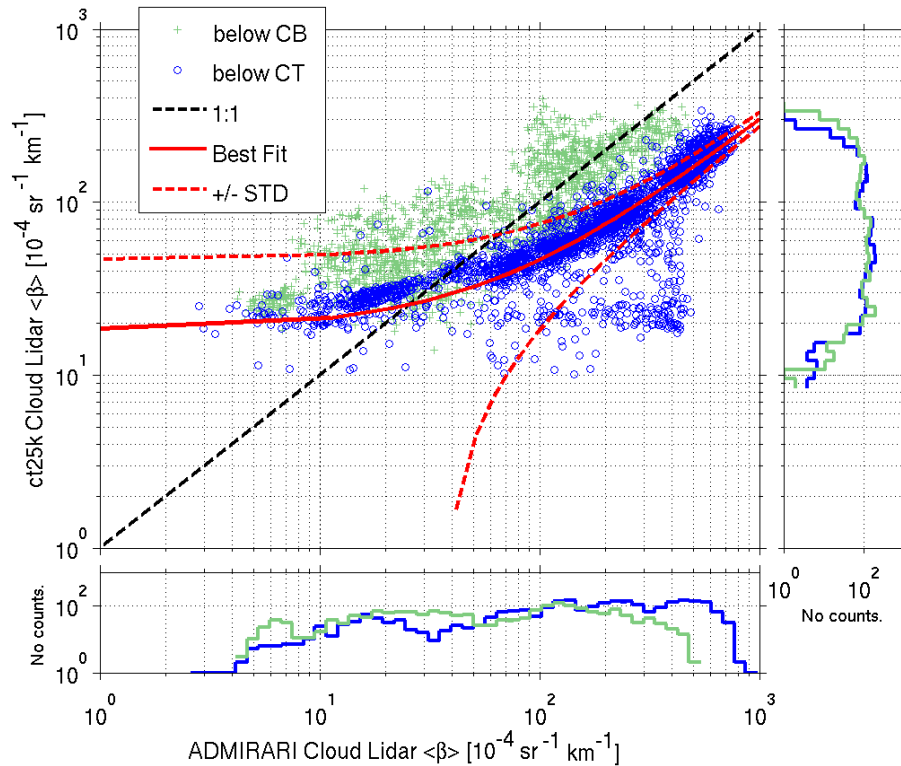


Figure 3.19.: Backscattering factor average over range for the Vaisala ct25k versus CBM80 in logarithm scale. Blue circles profile average below cloud top (CT), light-green pluses average below cloud base (CB). Red line is the best fit for blue circles and red dashed line the standard deviation for the best fit.

might also driving errors in this comparison.

Since the time and range resolution of the ct25k ceilometer is different to the CBM80, a direct point-to-point comparison was not possible. Instead profiles with coincident time has been selected and three datasets produced by averaging β over the ranges: 1st from 60m to cloud top (CT), 2nd to cloud base (CB) and 3th from cloud base to cloud top (CP) of the detected cloud layer. Two things need to be noticed: first the ranges below 60m were dismissed to avoid near field effects; second, the denomination for cloud top e.g CT indicates the range where the signal is completely attenuated in the cloud layer rather than the physical cloud top.

In figure 3.19 two of the datasets are depicted, CB as light-green-pluses and CT as blue circles. The CT has a linear pattern with smaller slope compared to the 1:1 black-dashed line showing an overestimation for larger backscattering values. On the other hand the CB is scattered and largely distributed around the 1:1 line. The CP dataset (not shown) is distributed on a cluster mostly below the 1:1 line and does not present any linear pattern. Therefore the data has been fitted to a first order polynomial $\beta(X) = a_0 + a_1X$ with the corresponding coefficients listed in table 3.5 and X being the corresponding dimensionless backscattering value from the CBM80 cloud lidar.

In figure 3.19 the linear fit for CT is exhibit (red line) together with the standard deviation of the predicted value (red-dashed-lines). It has been found that the coefficients for CT does

$\langle \beta \rangle$	a_0	a_1
CT	18.2151	0.2820
CB	45.8525	0.5848
CP	53.4704	0.1670

Table 3.5.: Coefficients for the three dataset of average β after fitting a linear relationship. All coefficients must be multiplied by a factor $\times 10^{-4} \text{ sr}^{-1} \text{ km}^{-1}$.

also fit properly the backscattering below the cloud base mainly in cases when precipitation is observed, but for the above cloud base it still tends to produce an overestimation. On the contrary, the CBM80 lack of sensitivity for the aerosols layer (e.g. $X \sim 0$ in profiles from 1100 to 1600 in figure 3.18) yields a large bias when either CT or CB coefficients are applied. Therefore the CBM80 ceilometer can be calibrated by using the CT and CB coefficients only when precipitation is sensed up to the cloud base.

The CBM80 cloud lidar has been added on lately to the ADMIRARI radiometer ancillary instruments suit, therefore it is used only in recent retrievals mainly to obtain the cloud base and to flag cases when the radiometer FOV is free of cloud. Hence bias are identified during cases of cloudless observations (Saavedra, P., Battaglia, A., and Simmer, C., 2012a, retrievals for GCPEX). For future studies it is recommended to attempt the auto-calibration approach presented by O'Connor, E., Illingworth, A., and Hogan, R., 2004 to have a calibrated backscattering coefficients β and thereupon use it in a more quantitatively way to better characterize precipitating variables.

3.2.2.1. ADMIRARI Instrumentation State-of-the-Art

The final ADMIRARI instrumentation set-up gives an holistic view on the rain-cloud precipitation system, with the MRR providing a rain reflectivity profile, the cloud-lidar showing the cloud base during no-rain cases as well as during light rain, and the ADMIRARI radiometer with brightness temperatures and polarization difference at three frequencies.

Figure 3.20 shows a typical example of a synergistic measurement with the three instruments. The case depicts a mostly cloudy day and some precipitation until 10:00 UTC, with high clouds before the rain starts and low clouds afterwards. Note the strong backscattering signal from the cloud-lidar at the cloud base during dry periods, while for some rainy spans the signal is fainter away. In general however the cloud-lidar signal is completely attenuated at moderate to strong rainfall. At figure 3.20 can also be seen that the radiometer only sense polarization during the rainy period while no polarization is observed when only clouds are present. Interesting is the observation at 02:24 UTC when a small precipitating cell is located at $\sim 2 \text{ km}$ slant, which produce a slightly polarized 36.5 GHz signature ($\sim -2 \text{ K}$). This is interesting signal is sensed from above the 0° C iso-term meaning it is precipitation in its ice phase, which is also corroborated by the lidar backscattering which is not strongly attenuated as in the case when liquid water is observed (for instance from 00:00 to 02:00 UTC). During the main rainy span, the polarization difference at 36.5 GHz dominates those at the other frequencies, which suggests that the rain was mainly comprised by small rain drops sizes. A slight drop on water vapour is also sensed by the 21.0 GHz which has a base line of $\sim 60 \text{ K}$ in brightness temperature at the beginning of the day and less than 50 K after the rain span.

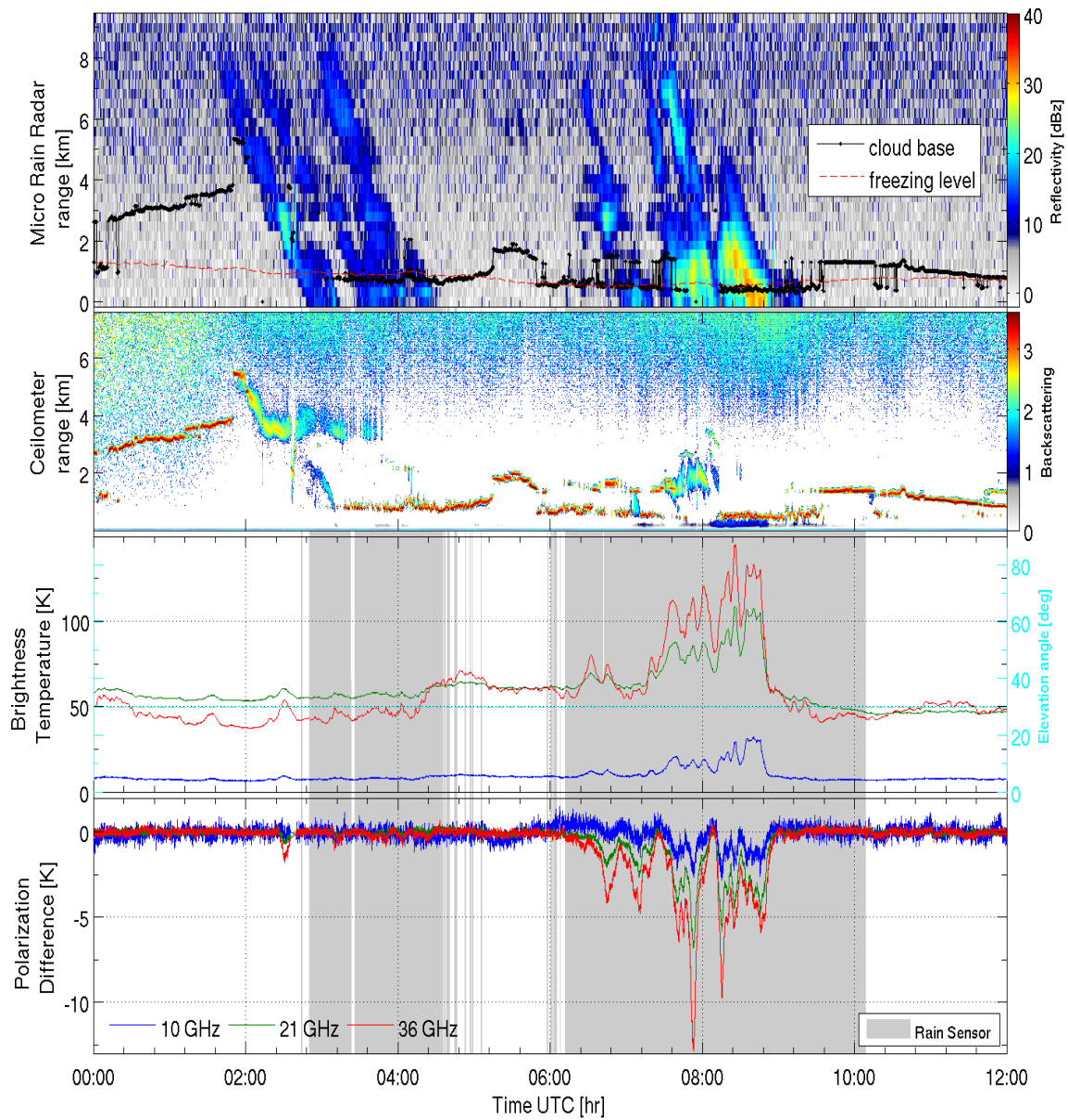


Figure 3.20.: Typical ADMIRARI measurement dataset for slant observations with reflectivity profiles (top), Ceilometer Backscattering and cloud base (second), TB and PD (bottom) for three frequencies.

4. Retrieval Methods of Precipitating Clouds

Abstract

An inversion method for retrieving atmospheric parameter is here discussed and applied to the problem of simultaneously retrieve integrated cloud, rain liquid water and water vapour. First the fundamental idea for retrieving cloud and rain water content by means of dual-polarized observation is presented as it was suggested by Czekala, H., Crewell, S., Simmer, C., and Thiele, A., 2001, then the Bayesian technique is introduced and applied to the ADMIRARI configuration. The forward modelling necessary to build a synthetic measurement database, for the retrieval, is described. Finally a sensitivity study assesses the performance of the retrieval technique. Based on synthetic measurements, the different retrieval approaches, e.g. pure-radiometer and combined radiometer-radar, are characterized by their respective accuracies.

4.1. Retrieval Approach by Czekala

A theoretical method to distinguish rain and cloud liquid water path (LWP) by exploiting the polarization difference has been presented by Czekala, H., Crewell, S., Simmer, C., and Thiele, A. (2001) who has proposed a simple retrieval approach in order to disentangle the total liquid water path (Total LWP i.e. Rain plus Cloud (T_LWP)) in its rain and cloud components. The fundamental retrieval idea was illustrated in a rain/cloud iso-lines diagram of the TB-PD space for a frequency of 19 GHz at 30.7° elevation angle (Czekala, H., Crewell, S., Simmer, C., and Thiele, A., 2001, Figure 2 and 3). Figure 4.1 is a reproduction of that idea for the three ADMIRARI frequencies in the TB-PD space, with the panel for the 21.0 GHz highlighting the proposed (Czekala, H., Crewell, S., Hornbostel, A., et al., 2001b) retrieval procedure.

Figure 4.1 are obtained from performing radiative transfer computations by the fast RT4 code for the three ADMIRARI frequencies and for 30° elevation angle, based on a 1 – D cloud resolving model hydrometeor profile (see figure 4.4). By preserving the profile's vertical shape, the amplitude of the cloud and rain water content profiles are modified in order to produce the different combinations of C_LWP (dashed-dotted blue lines) and R_LWP (dashed red lines) in a range of values from 0.0 to 5.0 kg m⁻². Pure cloud conditions are indicated by the uppermost horizontal dashed red line (no rain fraction). The increase in C_LWP from 0.0 to 5.0 kg m⁻² leads to an increase in the corresponding TBs, but no polarization is produced. Pure rain conditions (in the absence of cloud) produce the lowest limit of the PD signal (indicated by the lowest dash-dotted blue line). Then a combination of rain and cloud by increasing the R_LWP produces a shift on the horizontal line of pure cloud towards negative PDs.

The advantage of the PD additional information in the partitioning of LWP is obvious. Following the example at figure 4.1 in the top panel for 21.0 GHz, the vertical and horizontal dashed-back lines indicate a TB of 155 K and a PD of -3.2 K respectively. The brightness temperature of 155 K can be obtained from 0.8 kg m⁻² total liquid water path when assuming a composition of pure rain without clouds (retrieval case (1), pinpointed by a red arrow in Figure 4.1) or from 3.1 kg m⁻² of C_LWP when assuming a pure cloud contribution (retrieval case

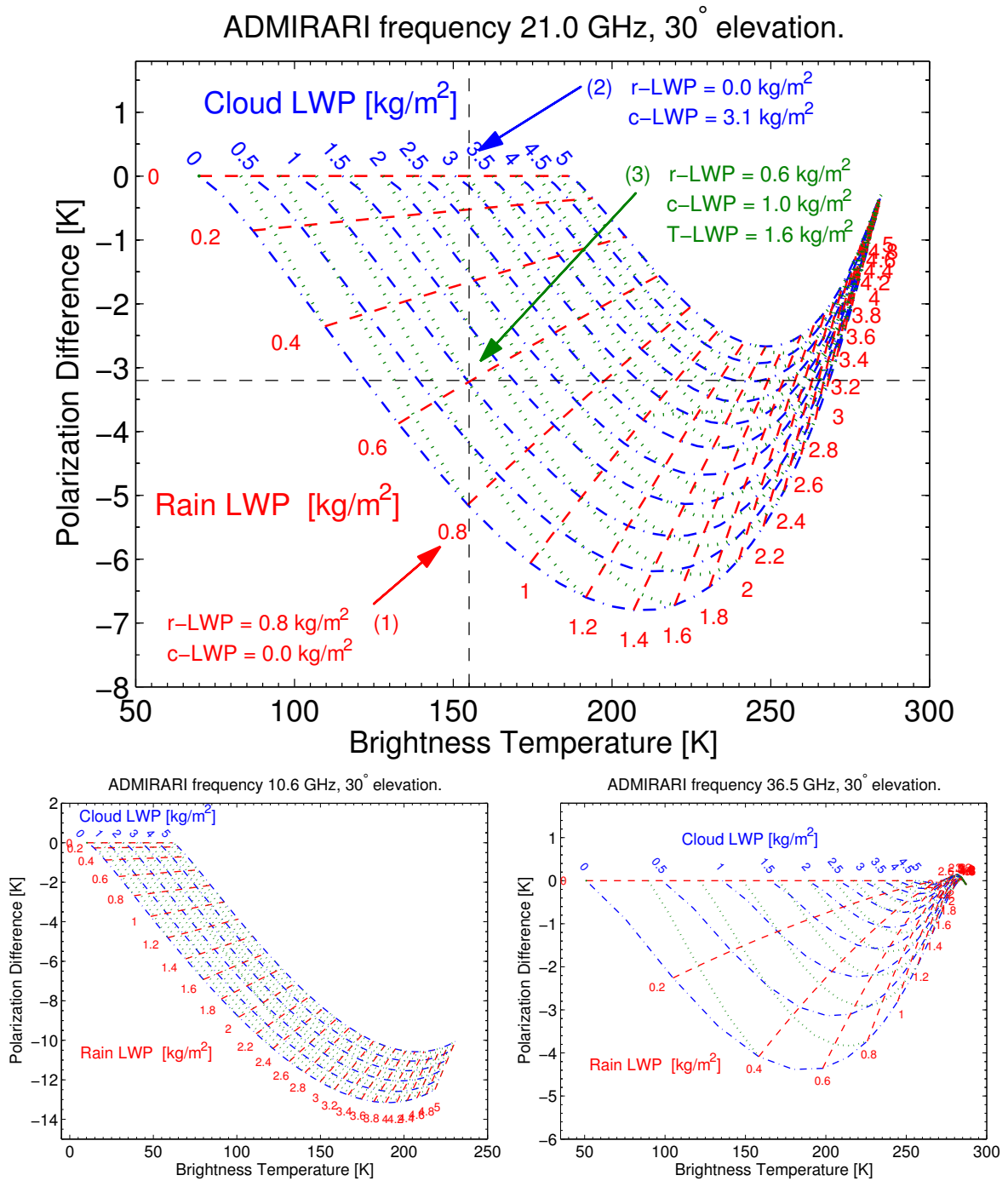


Figure 4.1.: The TB-PD space at 30° elevation angle composed by different combinations of cloud and rain LWP indicated by dash-dotted-blue and dash-red iso-lines respectively. The total LWP is indicated by the green dotted iso-line. The three ADMIRARI frequencies are represented with the 21.0GHz on top and on the bottom the 10.7 and 36.5GHz from left to right correspondently.

(2), blue arrow). These numbers give a good estimate about the uncertainty in LWP retrieval in the presence of raining clouds with unknown cloud fraction when only TB measurements are available. On the other hand, when the supplementary PD information is used (retrieval case (3), green arrow in Figure 4.1), a total LWP of 1.6 kg m^{-2} is estimated. Furthermore, it is feasible to separate the total LWP in cloud (1.0 kg m^{-2}) and rain (0.6 kg m^{-2}) liquid water path.

In addition Figure 4.1 highlights the advantage to use a multi-frequency approach, with the 10.7 GHz more appropriate to resolve large rain water contents and the 36.5 GHz being sensitive mainly to lower rain water contents since this frequency becomes saturated for R_LWP larger than 0.6 kg m^{-2} , where no rain/cloud distinction can be achieved.

Nevertheless, the retrieval approach proposed by Czekala, H., Crewell, S., Hornbostel, A., et al. (2001b) origins some contradictions when the retrieval is attempted for every frequency separately. For instance, figure 4.2 shows a set of few measurements superimposed to the TB-PD iso-line curves. Then it is observed that the point with highest polarization difference (-9 K) and highest brightness temperature (100 K) at 10.7 GHz can be retrieved as 0.5 kg m^{-2} cloud and 2.1 kg m^{-2} rain. In case of the 21 GHz is utilized, the same point can be retrieved as 2.0 kg m^{-2} cloud and 1.8 kg m^{-2} rain. On the other hand if the same measurement is retrieved by using the 36.5 GHz then different values for cloud and rain might be obtained i.e. 3 kg m^{-2} and 1.2 kg m^{-2} respectively. Since the 36.5 GHz is almost saturated for this case the retrieval is certainly unreliable at this frequency.

The previously discussed issue has fostered the development of an alternative retrieval approach taking into account the uneven effect introduced by the multi-frequency measurements rather than the one proposed by Czekala, H., Crewell, S., Hornbostel, A., et al. (2001b) which was based on a single frequency approach. In the next section the method adopted for a simultaneous retrieval of rain, cloud LWP and integrated water vapour is presented.

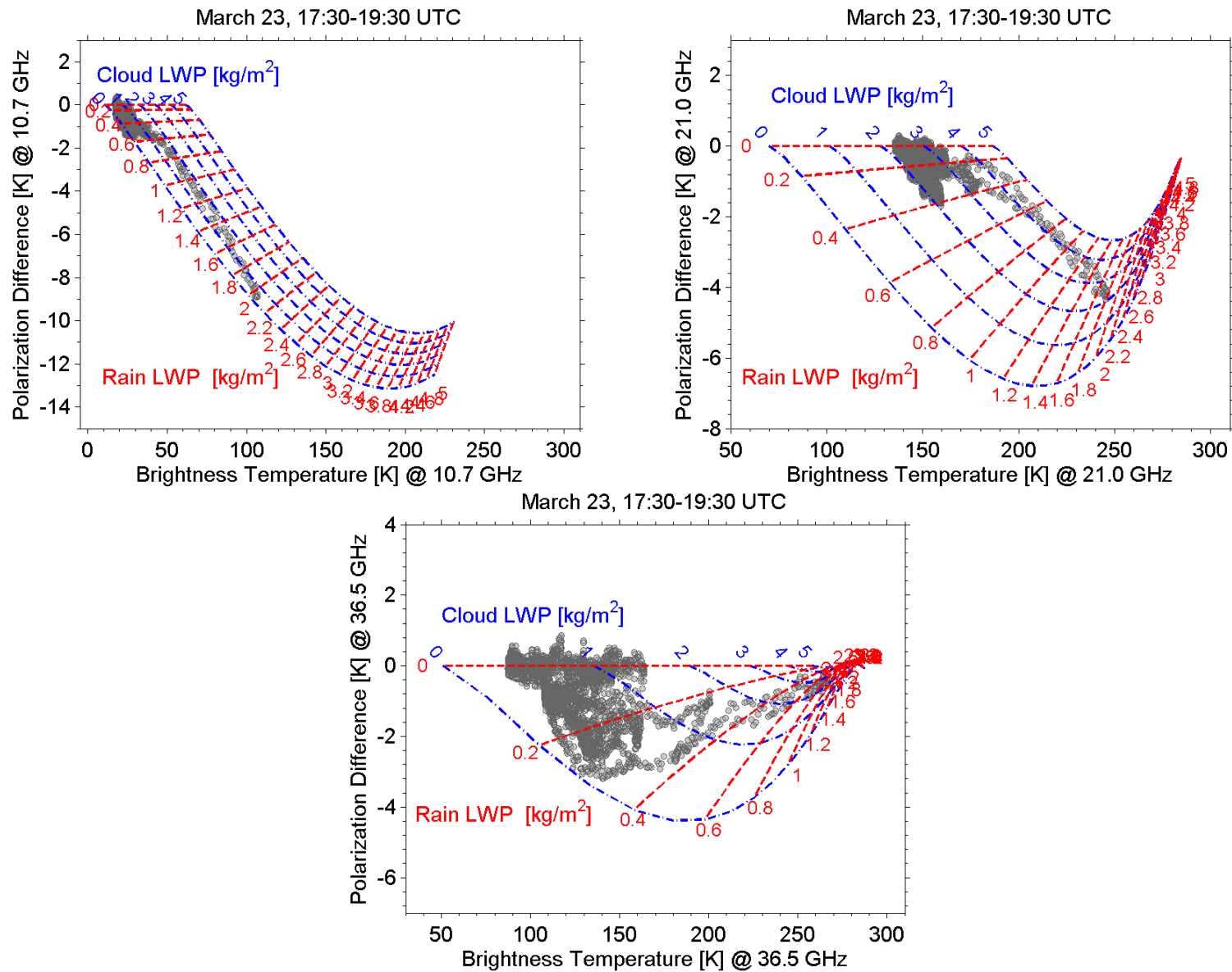


Figure 4.2.: Same as figure 4.1 but including precipitation measurements from March 23rd, 2010. Note that at every frequency the highest (TB,PD) data point suggests a different cloud/rain LWP partition.

4.2. Bayesian Approach

Bayesian theory is a general approach for solving inverse problems, i.e. the estimation of the true state of the atmosphere from indirect observations given *a priori* information on the expected atmospheric state. In our application the measurement vector \vec{y}_O contains spectral brightness temperatures and related polarization differences, which are assumed to be affected by random errors described by an error covariance matrix \mathcal{O} . The atmospheric state vector \vec{x} contains the profiles of all parameters (e.g. water vapour, temperature, cloud liquid water, rain water, DSDs, ...), which affect the measurement vector. Bayesian theory states that the inverse problem can be related to the forward problem through a set of measurements and prior knowledge about the probability of the state vector by (see e.g. (Marzano, F. S., Mugnai, A., et al., 1999; McFarlane, S., Evans, F., and Ackerman, A., 2002))

$$P_{post}(\vec{x}|\vec{y}_O) = \frac{p_f(\vec{y}_O|\vec{x}) p_{pr}(\vec{x})}{\int p_f(\vec{y}_O|\vec{x}) p_{pr}(\vec{x}) d\vec{x}}, \quad (4.69)$$

with $P_{post}(\vec{x}|\vec{y}_O)$ the conditional probability of the state vector \vec{x} given the observations \vec{y}_O , $p_{pr}(\vec{x})$ the *a priori* probability of the state vector \vec{x} before the measurement is made, and $p_f(\vec{y}_O|\vec{x})$ the conditional (or forward) probability of the measurement \vec{y}_O given the state vector \vec{x} .

The probability $p_f(\vec{y}_O|\vec{x})$ can be modelled from the distribution of observations close to the simulated synthetic observation $\vec{y}_S(\vec{x})$, with the width of the distribution governed by the measurement and the model errors. If these errors can be assumed to be Gaussian and uncorrelated, then the probability of observational deviations may be expressed as

$$p_f(\vec{y}_O|\vec{x} = \vec{x}_{true}) \propto P([\vec{y}_O - \vec{y}_S(\vec{x})]),$$

with

$$P([\vec{y}_O - \vec{y}_S(\vec{x})]) \propto \exp\left\{-\frac{1}{2}([\vec{y}_O - \vec{y}_S(\vec{x})]^T \mathcal{C}^{-1} [\vec{y}_O - \vec{y}_S(\vec{x})])\right\} \quad (4.70)$$

where \mathcal{C} is the error covariance matrix of the simulation error plus the instrument noise i.e. $\mathcal{O} + \mathcal{S}$. For simplification we denote the residuals as

$$[\vec{y}_O - \vec{y}_S(\vec{x})]^T \mathcal{C}^{-1} [\vec{y}_O - \vec{y}_S(\vec{x})] = \delta^2. \quad (4.71)$$

When substituting Eqs. (4.70) and (4.71) into (4.69) the posterior PDF may be rewritten as

$$P_{post}(\vec{x}|\vec{y}_O) = \frac{\exp(-\frac{1}{2} \delta^2) p_{pr}(\vec{x})}{\int \exp(-\frac{1}{2} \delta^2) p_{pr}(\vec{x}) d\vec{x}}. \quad (4.72)$$

To obtain the expected (in the adopted formulation the mean) state vector, the state vector \vec{x} is integrated over its phase space weighted with the posterior PDF, i.e.

$$\langle \vec{x} \rangle = \int \vec{x} P_{post}(\vec{x}|\vec{y}_O) d\vec{x}. \quad (4.73)$$

The second moment of the posterior PDF gives an estimation of the retrieval uncertainty, namely the variance around the mean vector $\langle \vec{x} \rangle$

$$\sigma_{\vec{x}}^2 = \int (\vec{x} - \langle \vec{x} \rangle)^2 P_{post}(\vec{x}|\vec{y}_O) d\vec{x} \quad (4.74)$$

Thus in a Bayesian approach a measurement refines previous knowledge of the physical parameters by narrowing their probability distribution function moving from an *a priori* probability P_{pr} to a posterior PDF (eq. 4.72) of the variables that are retrieved. The Bayesian method also allows the determination of the “additional value” added by a measurement via the entropy concept. The entropy of a PDF relative to the *a priori* knowledge of the system (relative entropy) is defined by (Rodgers, C. D., 2000)

$$S(P) \equiv - \int P(\vec{x}) \ln \left[\frac{P(\vec{x})}{P_{pr}} \right] d\vec{x}. \quad (4.75)$$

The additional information provided by a measurement is proportional to the reduction in entropy, i.e. the difference between the entropy before and after taking the measurement, i.e. $H = S_1(P) - S_2(P)$. Since the knowledge about a system before the measurement relies only on the *a priori* PDF its relative entropy is zero ($S_1(P) = 0$). When a measurement is made the information content is augmented by the relative entropy (McFarlane, S., Evans, F., and Ackerman, A., 2002; Rodgers, C. D., 2000)

$$H = \int P_{post}(\vec{x}|\vec{y}_O) \ln \left[\frac{P_{post}(\vec{x}|\vec{y}_O)}{P_{pr}(\vec{x})} \right] d\vec{x} \quad (4.76)$$

When the observation adds information to the retrieval, the posterior PDF occupies a small portion of the *a priori* PDF and the relative entropy H is positive.

In the following it is assumed that (**Assumption 1**) the measurement and model errors are uncorrelated between the different frequencies, thus the covariance matrices become diagonal with variances driven by the instrument and simulation errors.

$$C = \mathcal{I} \sigma_{O+S}^2, \quad (4.77)$$

where \mathcal{I} is the unitary matrix and σ_{O+S} is the instrument noise and the simulation error, nevertheless the latter can be considered as a questionable assumption since the model errors are likely correlated. Thus the term C^{-1} in equations 4.71 becomes a constant value and does not contribute to the minimization of the discriminant function δ .

It is further assumed (**Assumption 2**) that the state profiles in the model database occur roughly with the same relative frequency as those found in the climatological regime where the inversion method is applied. It follows that the probability of occurrence of a given state profile in (4.72) is roughly the same (e.g. $p_{pr}(\vec{x})$) as those naturally occurring (Kummerow, C., Willian, S., and Giglio, L., 1996). In order to satisfy the second assumption, not only a sufficiently large and representative database of atmospheric state profiles is mandatory, but also a proper definition of the *a priori* PDF of the simulations. In the current scheme each **Cloud Resolving Model (CRM)** profile in the data base is used to produce a set of microphysical state and observation geometry configurations (Battaglia, A., Saavedra, P., Rose, T., and Simmer, C., 2010), resulting in $\sim 10^6$ state profiles in the database.

The retrieval state vector \vec{x} contains amongst the detailed profiles the integrated water vapour, the cloud liquid water path, and rain liquid water path, while \vec{y}_O comprises either the three ADMIRARI **TBs** at vertical polarization and the three related **PDs**, i.e. $TB_V - TB_H$ in a pure-radiometer retrieval approach or include also the $Ze(r)$ slant reflectivity profiles in a combined radiometer-radar approach. In the following sections these two definitions of the measurement vector are denoted as RAD when $\vec{y}_O = [TB_V PD_V]^T$ and RADMRR when

$\vec{y}_O = [TB_v PD_v Ze_r]^T$, with v counting for the three ADMIRARI frequencies and r the MRR range.

A more straightforward retrieval technique is the so-called minimum distance, it consists on retrieving the profile which minimize the cost function 4.71:

$$\vec{x}_{min} = \{\vec{x}_i : \min\|\vec{y}_O - \vec{y}_S(\vec{x}_i)\|\}, \quad (4.78)$$

with i running over the whole *a priori* data-set. The disadvantage of this method is that it takes only one profile which may or not be, in fact, close to the real one. On the other hand, the retrieval obtained by equation 4.73 is the result of averaging a set of profiles close to the measurement and its standard deviation gives a hint of the profiles distribution.

As stated in Battaglia, A., Saavedra, P., Rose, T., and Simmer, C. (2010, equation (6)), a quality index (QI) is adopted to assess the closeness between observations and simulations, and it is defined as $QI \equiv \min\{\delta^2\}$ with the minimum determined by a search over the selected *a priori* database and δ^2 given by equation. (4.71). Considering 6 measurable quantities, values of QI equal or lower than 6 indicates that, on average, all six variables are being fitted within the model and measurement standard deviation. On the other hand, values larger than 20 may be considered as an indicator of bad agreement between measurements and simulations.

4.3. The Forward Model

The **Vectorized Radiative Transfer Equation (VRTE)** (chapter 2) is used to describe the interaction of microwave radiation with clouds and precipitation which can be solved with a variety of methodologies (Mishchenko, M., Hovenier, J., and Travis, L., 2000, Chapter 4). The forward model is utilized to perform radiative transfer simulations by the RT4 code (Evans, K. and Stephens, G., 1991) as previously in figure 4.1, section (4.1). Nevertheless the combination of scattering effects, the large spatial variation of precipitation hydrometeors in the atmosphere, and the finite radiometer's FOV require also the inclusion of three dimensional effects. A variety of techniques have been developed to numerically solve the radiative transfer equation for the full Stokes vector in a 3 – D scenario in the presence of dichroic media (Battaglia, A., Davis, C., Emde, C., and Simmer, C., 2007). Thanks to its lower computational cost the backward-forward MonteCarlo technique based on importance sampling (Battaglia, A. and Mantovani, S., 2005), represents the most efficient way to face passive microwave radiative transfer problems related to optically thick structured clouds including non-spherical preferentially oriented hydrometeors (figure 4.5). Therefore the VRTE has been solved by a backward-forward MonteCarlo scheme, which also takes account for a finite antenna beam-width. Thus a significant improvement is achieved in order to obtain realistic synthetic measurements in comparison to RTE simulations that only assumes plane parallel atmospheres with spherical hydrometeors and horizontal homogeneity (Battaglia, A., Saavedra, P., Rose, T., and Simmer, C., 2010, and reference therein).

Box-type Cloud Model

In order to quantify the effects of the 3-D structure of a precipitating cloud on the radiation field sensed by a polarimetric ground-based radiometer, the backward-forward method is applied to a box-type cloud model, as illustrated in figure 4.3. L_x and L_y are the horizontal dimensions of the rain shaft (4km). The point labelled with RAD indicates the position of the

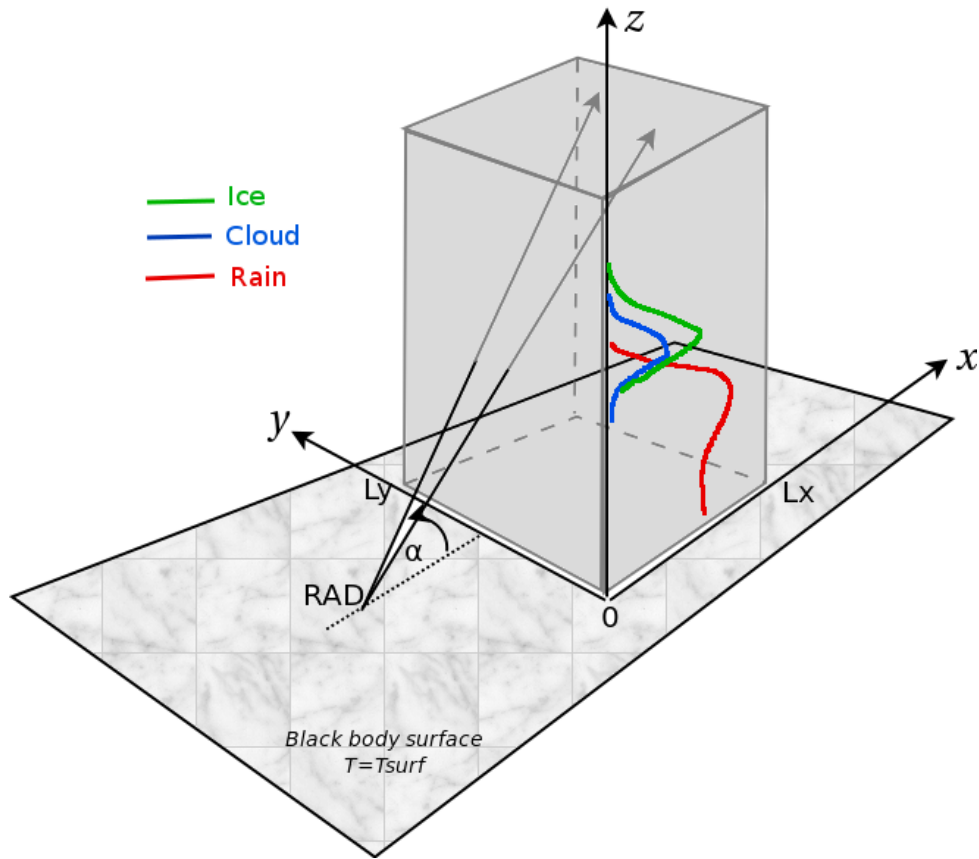


Figure 4.3.: Simplified scheme for the cloud box model. Radiances are computed for the observation point RAD. The hydrometeor atmospheric profile from a Cloud Resolving Model are illustrated by the red, blue and green lines for rain, cloud and ice respectively. Outside the gray box contains only atmospheric gases.

radiometer and the symbol α is the elevation angle of observation. The cone resembles the antenna beam-width.

The cloud box profile is extracted from CRM simulations available from the Goddard Cumulus Ensemble (Tao, W. and Simpson, J., 1993), which are represented by the red, blue and green lines in scheme 4.3. A real example is shown in figure 4.4 for five hydro-meteor types: rain, cloud water, cloud ice, graupel, and snow.

Large atmospheric hydrometeors, e.g. rain drops, tend to have a non-spherical shapes and preferential horizontal orientation. This is illustrated in figure 4.5 that shows the calculated drops shapes of water drops with equi-volume radii range from 0.25 to 3.25mm. For simulations, however, spherical raindrops are replaced by mass-equivalent horizontally oriented oblate spheroids with axial ratios lower than one, parametrized according to Matrosov, S., Clark, K., Martner, B., and Tokay, A. (2002)

$$\mathcal{A} = 1.0 + (0.05 - D_e) b \quad (4.79)$$

with $D_e > 0.05$ cm the equivalent spherical raindrop diameter. The shape factor b is equal to 0.6 for equilibrium drop shapes. The single scattering properties (i.e. the extinction and the phase matrix, and the emission vector) are computed with a T-matrix method according

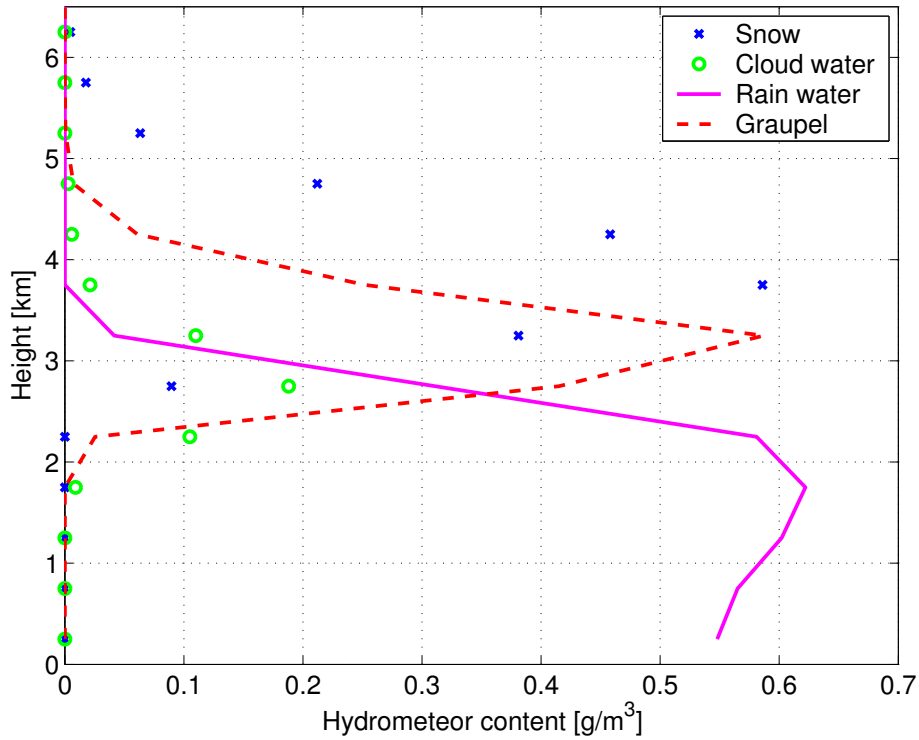


Figure 4.4.: Example of the four hydrometeor profiles (cloud, rain, graupel, and snow) extracted from a Cloud Resolving Model and adopted in the 3 – D radiative transfer simulations (Extracted from Battaglia, A., Saavedra, P., Rose, T., and Simmer, C. (2010)).

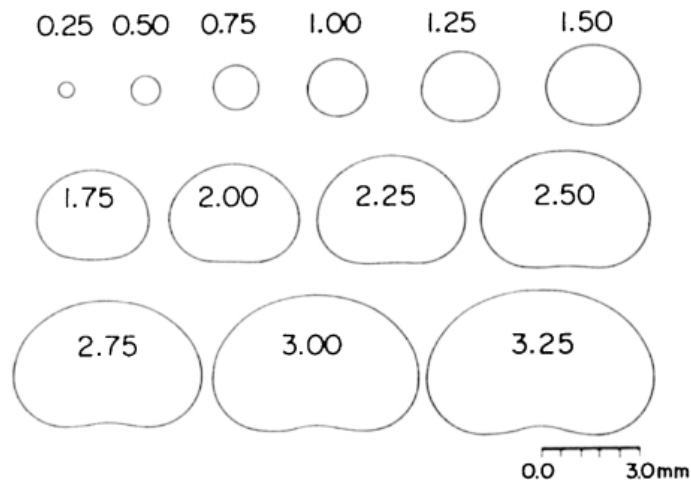


Figure 4.5.: Shapes of drops falling in stagnant air calculated by the procedure in (Pruppacher, H. and Pittler, R., 1971). The number indicates the equi-volume sphere radius. (Extracted from Sokamura, S. and Oguchi, T. (2010))

to Mishchenko, M. (2000). The surface is assumed to be Lambertian with emissivity equal to 0.9. Assumption of surface emissivity equal to one may not be valid, especially for wet surface (e.g. Prigent, C., Jaumouillé, E., Chevallier, F., and Aires, F. (2008)). The emissivity effect is generally negligible for ADMIRARI measurements. In fact, changing surface emissivities from 1.0 to 0.8 (as expected for very wet surfaces) produces TBs (PDs) variation never larger than 0.3K, 0.5K and 1K at 10.7GHz, 21.0GHz and 36.5GHz respectively, as it is shown in Figure 4.6 top panels. For the case of polarization difference the effect is even less with all frequencies being affected by less than 0.2K (Figure 4.6 bottom panels), i.e. within the instrument measurement error. The emissivity impact is larger at intermediate TBs (150-200K) and at higher frequencies, where the scattering signal is significantly contributing to the total radiometer signal. In regimes where the down-welling radiation is dominated by emission processes (e.g. at small rain rates and low frequencies) or by black-body like response (e.g. at very high rain rates) the surface emissivity variability does not play any role. Figure 4.6 shows also the distribution of the differences on TBs and PDs produced by the three emissivity assumptions, it is clearly seen that most of the differences are accumulated close to zero.

In order to include 3-D effects each precipitating profile is embedded in a clear sky atmosphere (gray box in figure 4.3). The radiances are then simulated as sensed by a radiometer with an antenna beam-width of 5° located at different positions either underneath the cloud or at the side of the box-type cloud model, that position (indicated by RAD at figure 4.3) is characterized by different horizontal extents from 250m inside the box relative to L_x to 8km outside the box. Cosmic radiation impinges $TB_{cmb} = 2.73K$ at the top of the atmosphere. The radiative transfer equation is solved according to the backward Monte-Carlo technique (Battaglia, A., Davis, C., Emde, C., and Simmer, C., 2007).

Relevance of 3-D Effects

The relevance and role played by 3-D effects in ground-based polarized radiometer observations were widely discussed by Battaglia, A., Czekala, H., and Simmer, C. (2006). In this work much more realistic profiles are included with vertical variability of hydrometeor profiles, and with the presences of liquid water and ice particles. Three-dimensional effects are caused by geometrical and scattering factors (Battaglia, A. and Mantovani, S., 2005, and references therein). For scenarios with weak scattering, 3D effects are purely geometrical and the leakages from the radiatively warm side of the cloud can be accounted by 1-D slant-path approximation (SPA) (Liu, Q. and Simmer, C., 1996). As in section 5 of Battaglia, A., Czekala, H., and Simmer, C. (2006) the relevance of "3D scattering effects" is evaluated by using as a reference 1D SPA calculations based on the fast RT4 code (Evans, K. and Stephens, G., 1991).

Differences between Monte-Carlo and slant path RT4 computations become noticeable at 21 GHz and even more at 36.5 GHz as demonstrated in figure 4.7. Two striking features are evident: Monte-Carlo produces more negative PDs in the region where the slant optical thickness is roughly one (Battaglia, A., Czekala, H., and Simmer, C., 2006, see discussion of Figure 4) and slightly positive PDs (up to 3.5K at 36.5GHz) when the TB signal is fully saturated (i.e. at large optical thickness). The SPA RT4 cannot reproduce such large positive PDs at all. These discrepancies are attributed to the deficiencies of the 1D SPA model in computing terms with orders of scattering ≥ 1 . Vice-versa at the lowest frequency, absorption represents the dominant process so that the predominant term affecting the total signal is the zeroth order of scattering, which is properly accounted for by the SPA approximation.

Additionally ADMIRARI observations of tropical convective small rain cells have provided

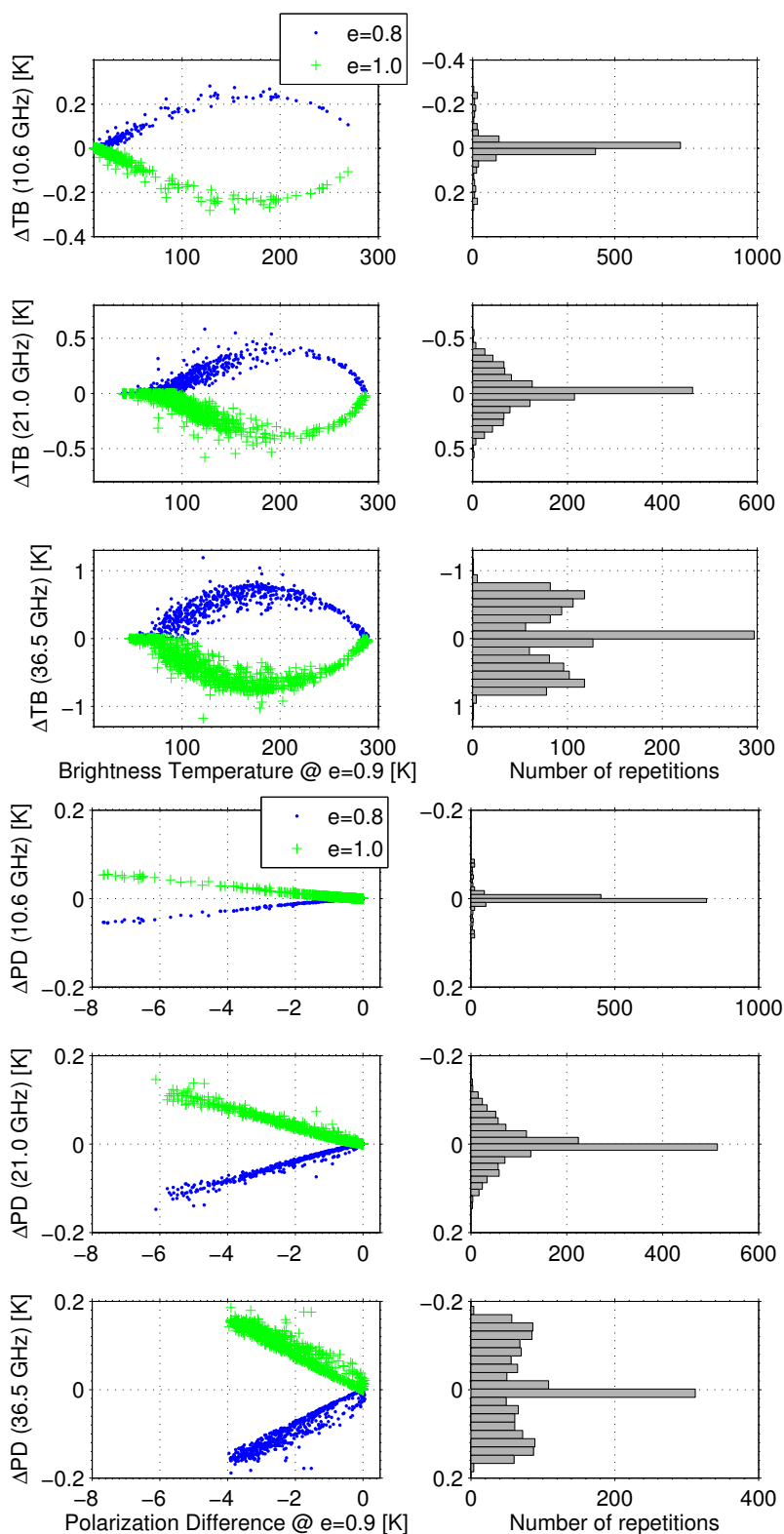


Figure 4.6.: Effect of the emissivity assumption on the down-welling brightness temperature (top) and polarization difference (bottom) for the three ADMIRARI frequencies. The differences on TBs and PDs computed for emissivities of 0.8, 0.9 and 1.0 are compared to the assumed emissivity of 0.9.

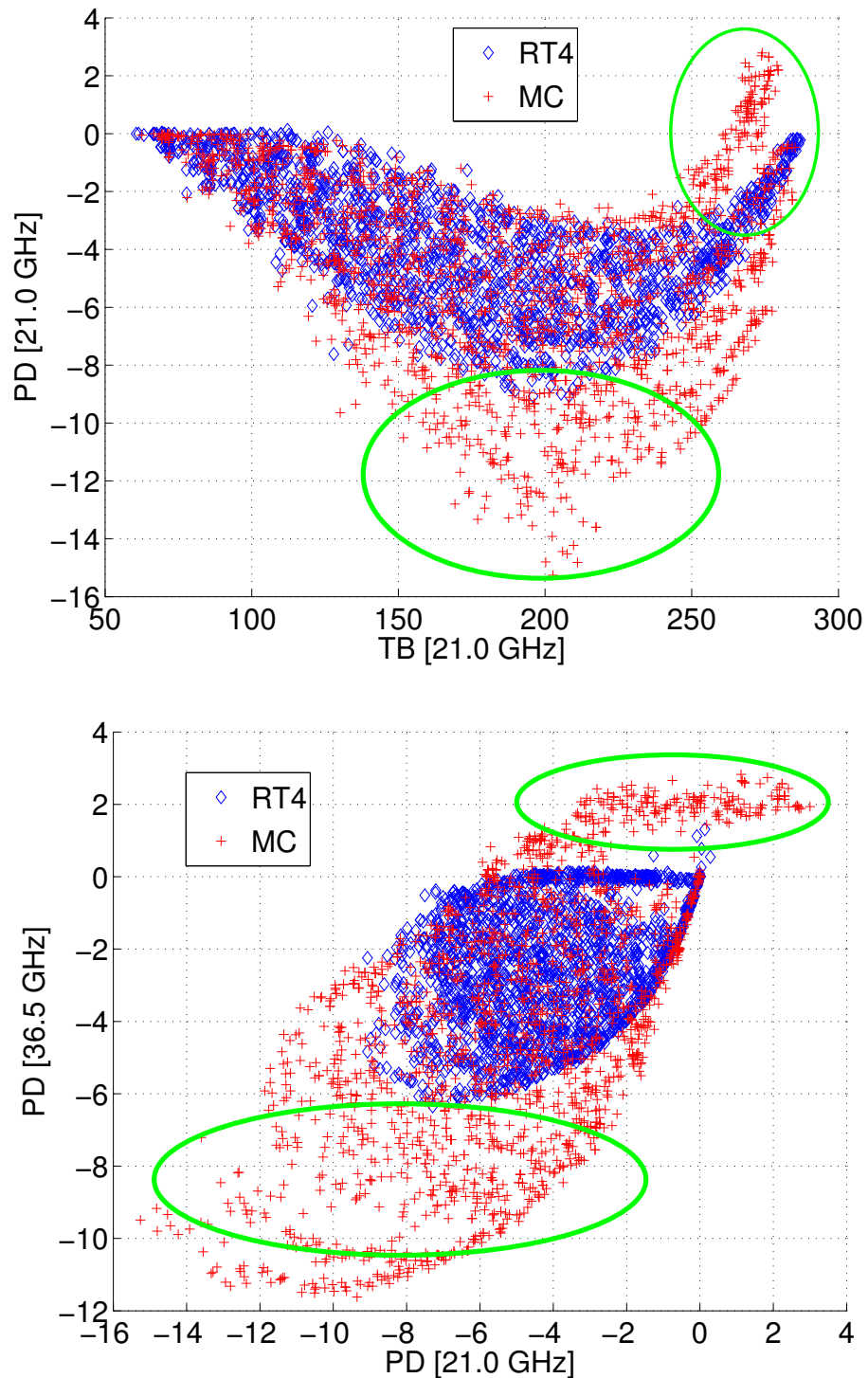


Figure 4.7.: Scatter plots in the TB-PD space for the comparison between SPA RT4 and Monte-Carlo computations to highlight 3-D scattering effects. The geometry of the simulations is the one illustrated in figure 4.3 with an elevation angle of 30° , $L_x = L_y = 4$ km and $P_x = [-3.5, -3.0, -2.5, \dots, 3.5]$ km. About 3000 profiles with freezing level ranging from 2 to 4 km are considered in this example (Extracted from Battaglia, A., Saavedra, P., Rose, T., and Simmer, C. (2010)).

unique information to understand three-dimensional effects in microwave radiative transfer processes. In these cases the above mentioned necessity to account for geometric effects in slant observations is not enough to explain an ubiquitous positive PDs observed values both at 21.0 and 36.5GHz in coincidence with high brightness temperatures. Battaglia, A., Saavedra, P., Morales, C., and Simmer, C. (2011) have found that that signature is a genuine and unique microwave signature of radiation side leakage which cannot be explained in a 1-D radiative transfer frame but it mandates the necessity to include three-dimensional scattering effects. The authors have demonstrated those effects and interdependencies by analysing field campaign case studies and showing that accordance with measurements is only achieved by exploiting a sophisticated 3-D radiative transfer (Battaglia, A., Saavedra, P., Morales, C., and Simmer, C., 2011). That sophisticated method, however, is not yet included in the present work as part of the forward model.

Sensitivity to Axial Ratio Parametrization and DSD Assumptions

Two factors are expected to play a crucial role in modifying the polarization radiometric signal: the axial ratio parametrization and the [Drop Size Distribution \(DSD\)](#) assumptions. Drop size distribution are usually modelled according to the exponential Marshall and Palmer distribution

$$N(D) = N_0 \exp(-\Lambda D) \quad (4.80)$$

with $N_0 = 8.0 \times 10^3 \text{ m}^{-3} \text{ mm}^{-1}$. The median volume diameter D_0 is approximately obtained as $D_0 = 3.67 \left(\frac{R_{LWP}}{\pi \rho_w N_0} \right)^{0.25}$, with $\rho_w = 1.0 \text{ g cm}^{-3}$ the water density. In order to account for the departure from this shape we consider hereafter three other DSDs: Drizzle with $N_0 = 32.0 \times 10^3 \text{ m}^{-3} \text{ mm}^{-1}$, Heavy-rain with $N_0 = 4.0 \times 10^3 \text{ m}^{-3} \text{ mm}^{-1}$ and Thunderstorm with $N_0 = 1.4 \times 10^3 \text{ m}^{-3} \text{ mm}^{-1}$. This terminology follows the original paper by Joss, J. and Waldvogel, A. (1968) although the heavy-rain is a implementation of this work. For the same amount of [R_LWP](#), thunderstorm rain has a low number of raindrops with predominantly large diameter while drizzle is characterized by a large amount of small droplets.

The parametrization of the axial ratio given in equation 4.79 is also modified by allowing variations of the shape factor b from 0.5 to 0.7, which accounts for the observed variability from the equilibrium value Matrosov, S., Clark, K., Martner, B., and Tokay, A. (2002).

Modifications in the [DSD](#) assumptions affect the extinction properties of the medium and hence the TBs. This can be better understood by looking at the single particle extinction cross section of oblate raindrops (at 30° elevation) per unit volume (figure 4.8 top panel). This quantity exhibits a "super-Rayleigh behaviour", i.e. it remains always higher than the corresponding diameter-independent Rayleigh value (which is identical to the value achieved at small diameters). In fact in the Rayleigh approximation (e.g. for the cloud component) this quantity is expected to be equal to $\frac{6\pi}{\lambda} \Im\{K\}$ (about 0.018, 0.070 and 0.205 mm^{-1} for the three frequencies at 10° C), λ being the wavelength, $K = \frac{m^2-1}{m^2+2}$ the dielectric factor, and m the complex refractive index of water. From a direct inspection of the top panel in figure 4.8 it is obvious that such an approximation is valid only for very small droplets with a decreasing range of applicability towards the higher frequencies. Moving out of the Rayleigh region on the left the three frequencies behave differently: while the 10.7GHz the extinction per unit volume almost always increases with size, it reaches a maximum value around a diameter of 4 and 2.3mm, at 21.0 and 36.5GHz respectively. When considering different [DSDs](#) (the amount of rain being the same) we can conclude that at 10.7GHz [DSDs](#) containing large

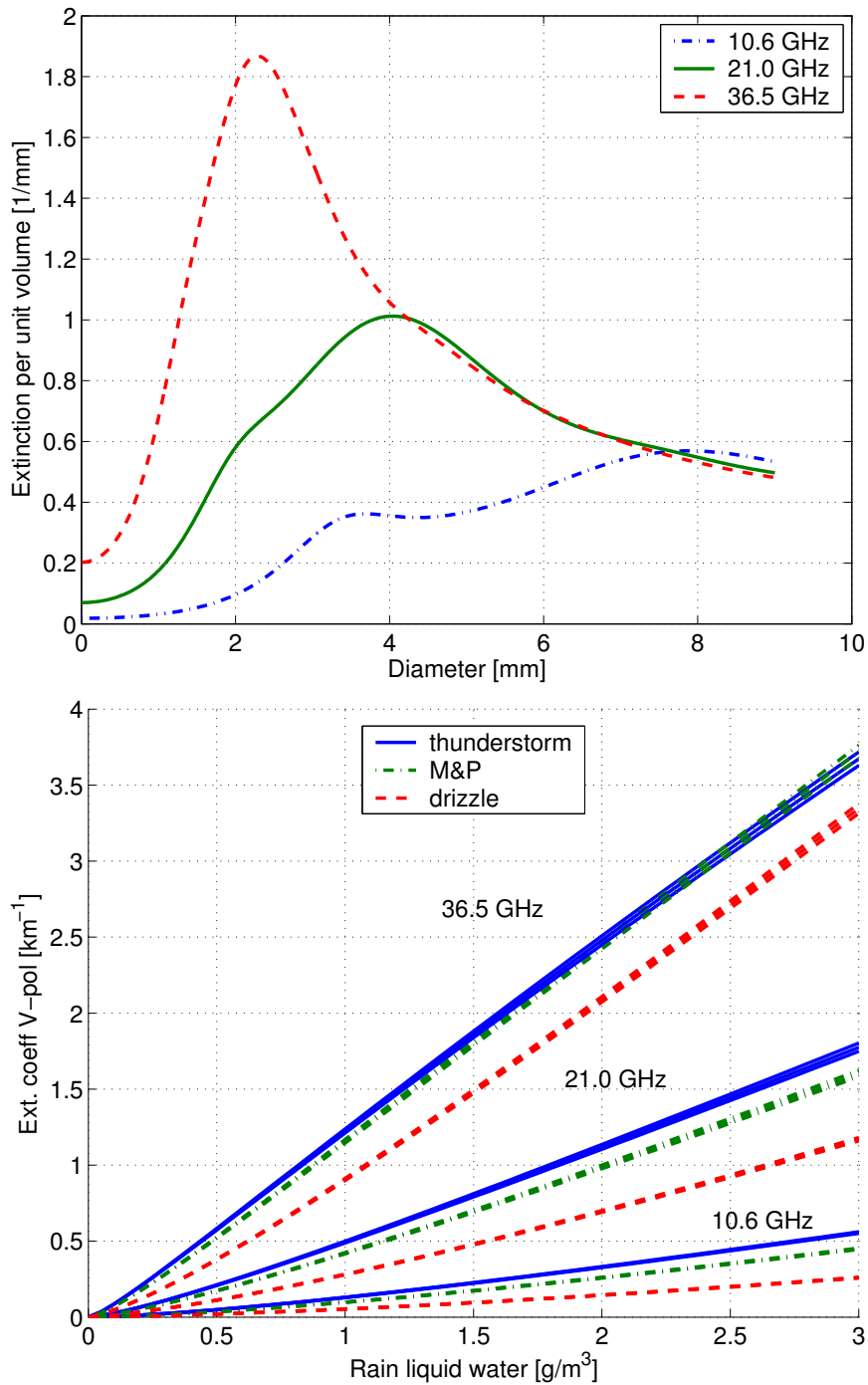


Figure 4.8.: Top panel: extinction cross section per unit volume in $[\text{mm}^2 \text{mm}^{-3}]$ as a function of the raindrop equi-volume diameter for the three ADMIRARI frequencies. Raindrops up to 9 mm diameter are considered. Bottom: vertical polarization extinction coefficient as a function of the rain LWC in g m^{-3} for three different DSDs as indicated in the legend. The line's thickness accounts for the assumed variability in the coefficient b in equation 4.79 from 0.5 to 0.7 (Extracted from Battaglia, A., Saavedra, P., Rose, T., and Simmer, C. (2010)).

particles produce larger absorption and scattering coefficients (already noticed by Viltard, N., Kummerow, C., Olson, W., and Hong, Y. (2000) in their Figure 2). But this is not always true at the other two frequencies (because of the non-monotonic behaviour of the extinction per unit volume curves in figure 4.8). This is highlighted in the bottom panel of figure 4.8 which depicts the vertical polarized extinction coefficients as a function of the rain LWC: the thunderstorm DSDs, which favour large raindrops, produce the largest optical thickness (hence the highest TBs), except at 36.5 GHz for rain LWCs above 2.5 g m^{-3} where the Marshall-Palmer is actually the most efficient of the three DSDs in extinguishing radiation. Due to the large relative spread between the three DSDs visible in the bottom panel in figure 4.8, TBs at 10.7 GHz will be more heavily affected than the 36.5 GHz. Vice-versa the axial ratio parametrization variability (in figure 4.8 indicated by the thickness of the line) is not expected to produce any appreciable variability in TBs. But it will play a key role in affecting the PDs.

When considering polarization effects produced by precipitation, the larger the raindrops the higher the dichroism of the medium, the more negative the values attainable by the PDs will be. The same signal will be produced by more prolate raindrops (larger b values). While TBs are directly related to the extinction profiles, PDs are driven by other combinations of the scattering properties. Battaglia, A., Czekala, H., and Simmer, C. (2006) showed that the following combination of scattering properties (k^{ext} and $\bar{\omega}$ are the angular and polarization-dependent extinction coefficient and single scattering albedo, respectively):

$$\Delta\xi(\theta_{el}) \equiv \frac{k_V^{ext}(\theta_{el})[1 - \bar{\omega}_V(\theta_{el})] - k_H^{ext}(\theta_{el})[1 - \bar{\omega}_H(\theta_{el})]}{0.5[k_V^{ext}(\theta_{el}) + k_H^{ext}(\theta_{el})]} \quad (4.81)$$

is relevant when dealing with polarization difference driven by emission/absorption processes (as mainly happen at the ADMIRARI frequencies). As a rule of thumb, at small optical thickness's, the PDs are obtained by multiplying the parameter $\Delta\xi$ by the TBs. The parameter $\Delta\xi$ is showed for an elevation angle of $\theta_{el} = 30^\circ$ in figure 4.9 as a function of rain LWC for the lowest and highest ADMIRARI frequencies. $\Delta\xi$ is always negative (hence negative PDs) and goes to zero at small rain LWC values (which produce DSDs with mainly spherical particles). The dynamic range attained at 10.7 GHz is much larger than at 36.5 GHz, which suggests the potential for reaching more negative PDs. A strong dependence on the b value is visible (curves with the same symbol are well separated): for instance a thunderstorm rain with an uniform rain LWC of 2.5 g m^{-3} producing a 10.7 GHz equal to 100 K will roughly produce PD equal to -9.5, -11.5, and -14.0 K (see the three red points at the top panel of figure 4.9). The same situation at 36.5 GHz will yield PDs less than a half of these. While at 10.7 GHz DSDs with larger particles (given the same total amount of rain) always produce more negative PDs due to resonance effects, this is not valid any more at 36.5 GHz. At this frequency the most efficient DSDs are the thunderstorm, the Marshall-Palmer and the drizzle roughly for rain LWC $< 0.5 \text{ g m}^{-3}$, $0.5 < \text{rain LWC} < 1.5 \text{ g m}^{-3}$ and LWC $> 1.5 \text{ g m}^{-3}$, respectively (see figure 4.9).

These preliminary considerations have been tested with simulations performed following the methodology described in section 4.3. Profiles with the same total hydrometeor content are hereafter considered; single scattering properties have been computed by assigning the rain content to the three different DSDs and the b parameter to the three values (0.5, 0.6, and 0.7). Results of the corresponding radiative transfer computation are shown in figure 4.10. Considering the Marshall-Palmer DSD with b=0.6 as a reference, it sees that the brightness temperatures are unchanged by a change in the b value (the simulations with b=0.5 and b=0.7 with the same DSD coincide with the diagonal line) while they are significantly modified by the DSD assumption. It has been found that the spread is more marked at 10.7 GHz than at

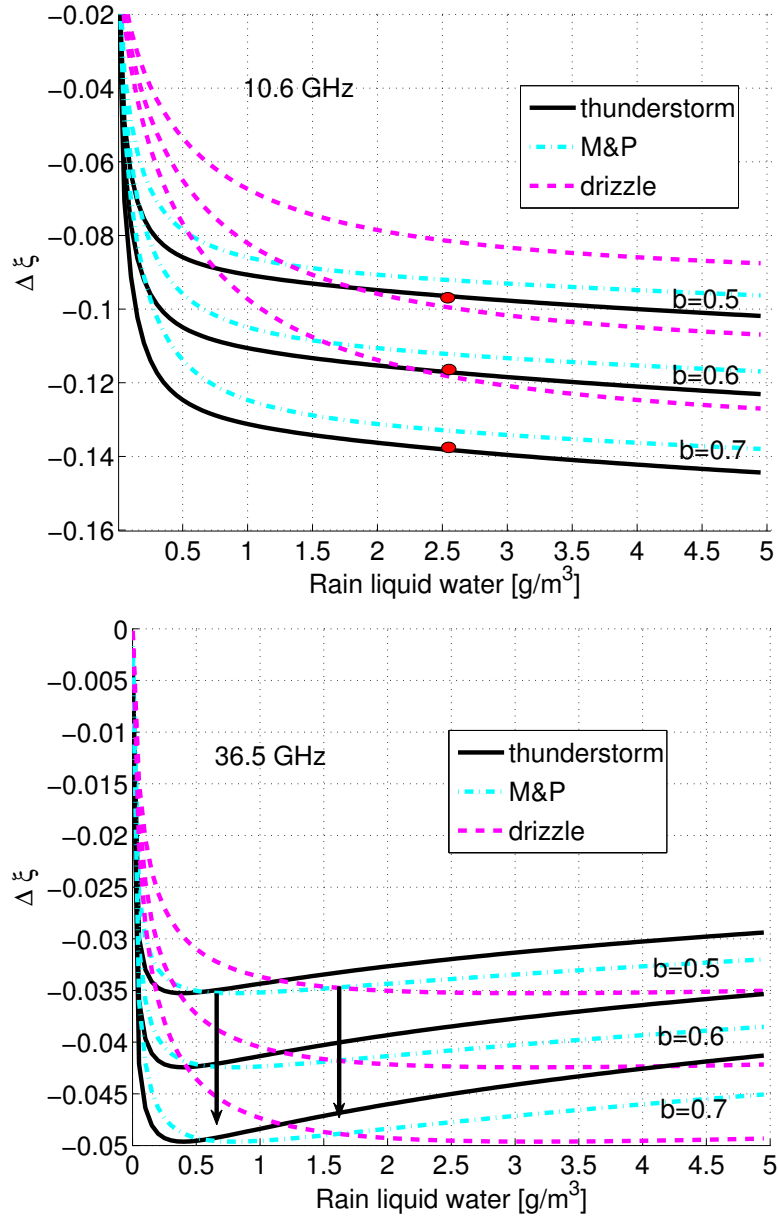


Figure 4.9.: Parameter $\Delta\xi$ as defined in equation 4.81 evaluated at 30° elevation angle for 10.7GHz (top) and 36.5GHz (bottom) for three different DSD as a function of rain LWC. Curves plotted with the same style correspond to different b values: 0.5, 0.6 and 0.7 from the top to bottom (Extracted from Battaglia, A., Saavedra, P., Rose, T., and Simmer, C. (2010)).

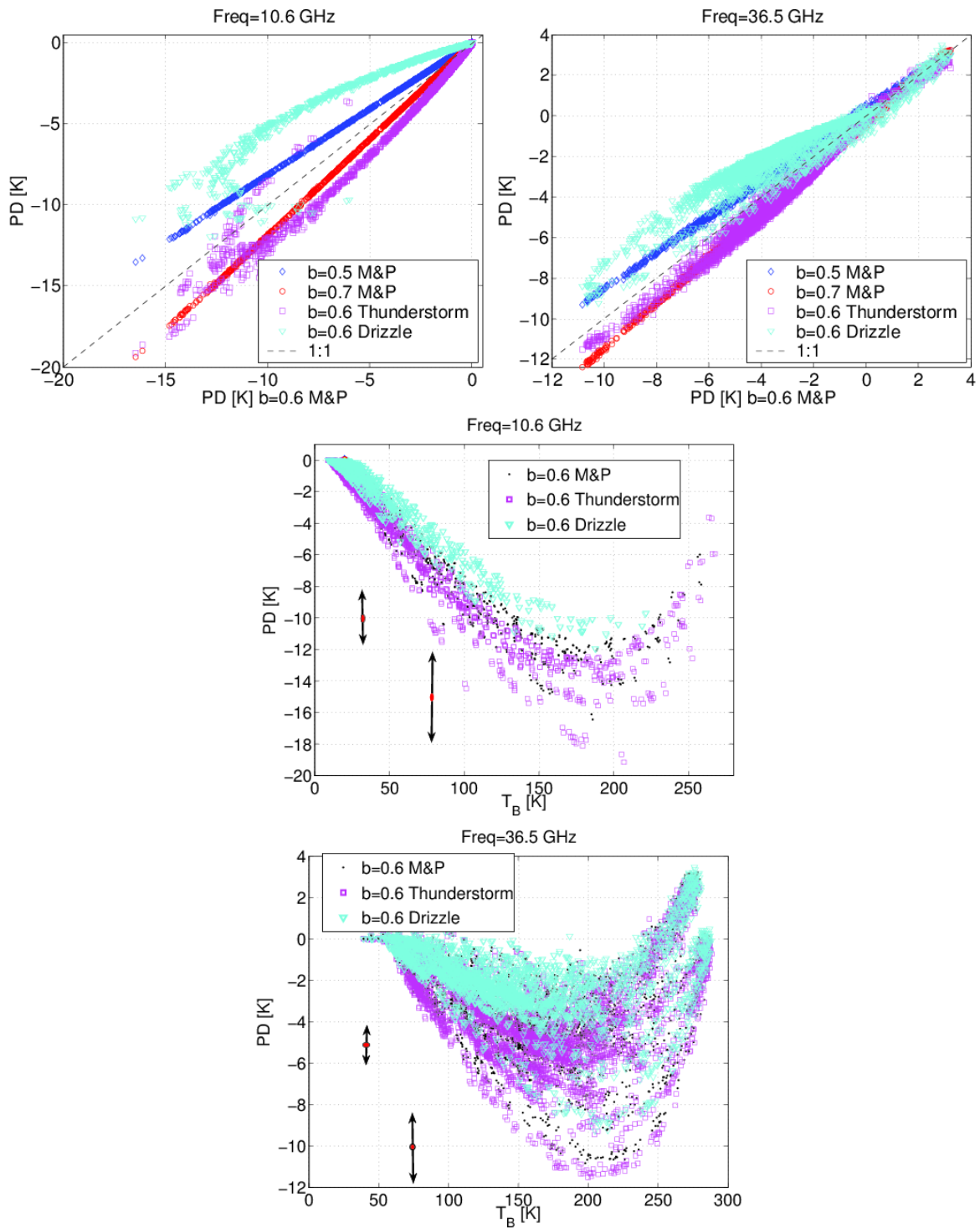


Figure 4.10.: Simulation study for sensitivity of PDs (top panels) to the DSD and the assumed raindrops axial ratio. The equilibrium axial ratio of $b=0.6$ and the Marshall-Palmer DSD is used as a reference. The overall effect in the TB-PD space is shown in the bottom panels (Extracted from Battaglia, A., Saavedra, P., Morales, C., and Simmer, C. (2011))

the two highest frequencies and it can be as large as 70 K. At 10.7 GHz the thunderstorm DSD is always brighter than the other two, while at 36.5 GHz when large TBs (> 260 K) are encountered (and then, plausibly, large rain LWC as well) the drizzle-type of rain becomes the brightest, which is expected from the previous discussion of the bottom panel of figure 4.8.

Polarization differences (figure 4.10 top panel, the Marshall-Palmer DSD with $b=0.6$ is taken again as a reference) are sensitive both to DSD and to the b parameters. The b dependence is roughly linear (compare the curves labelled as Marshall-Palmer and for $b=0.5$ and $b=0.7$ with the diagonal line). A change of ± 0.1 in b yields a decrease/increase in PDs which scales linearly with PD:

$$PD_{[b_{eq}\pm 0.1]} = PD_{[b_{eq}]}(1 \pm \eta_f) \quad (4.82)$$

with the correction factor η_f equal to about 18.5%, 17.5% and 14.5%, respectively, for the three frequencies. For instance at 10.7 GHz a PD = -10 K produced by assuming $b=0.6$ will convert to -8.2 and -11.8 K when adopting $b=0.5$ and $b=0.7$ correspondingly. On the other hand the effect of changing DSD is more subtle because the related change in TBs will alter the PDs themselves. This can be better understood by considering the TB-PD space (bottom panels in figure 4.10). A change in the b factor in the range [0.5-0.7] will basically produce a pure up and down movement, whose intensities are indicated by the double arrows and will depend on the given PD level and on the frequency (see different length of the arrows). On the other hand a change in DSD will also produce a right-left shift, e.g. a right movement when considering larger raindrops. If the absolute minimum of the TB-PD curve is already reached, such a movement will push the solution towards a region where PDs actually decrease and therefore will not produce more negative values in the PDs. The bottom panels of figure 4.10 provide a clear picture about the uncertainties we have to contend with in the retrieval problem.

Relevance of Melting Layer Effects

Melting hydrometeors are known to be brighter in terms of reflectivity and emissivity, i.e. they have higher backscattering and extinction cross sections than equi-volume raindrops. Battaglia, A., Czekala, H., and Simmer, C. (2006) showed that the description of hydrometeors profiles without explicit use of mixed phased hydrometeors generally underestimates the total optical thickness and the TBs. The effect is particularly strong when precipitating systems with low freezing levels are examined, and it is likely to affect more the lower frequency (Battaglia, A., Kummerow, C., Shin, D., and Williams, C., 2003, see Figure 8), i.e. 10.7 GHz in our specific application. The shape of melting snow flakes has been parametrized e.g. by Raynaud, L., Chenerie, I., and Lemorton, J. (2000) and Russchenberg, H. and Lighthart, L. (1996) in terms of oblate spheroids. These parametrization, however, have not been verified in laboratory experiments so far. This represents a major obstacle for the current study since the axis ratio of melting ice particles drives the PD signal.

4.4. Description of the Retrieval Technique

The expected retrieval performance was assessed by a simulation-based sensitivity study. For that purpose a subset of states was identified and removed from the simulations data base. The corresponding simulated radiation temperatures were perturbed by a random Gaussian instrument error with a RMSE of 0.5 K and treated as virtual radiometer measurements. The

range of simulated MRR attenuated reflectivity profiles were interpolated to 300m to match a typical measurement range.

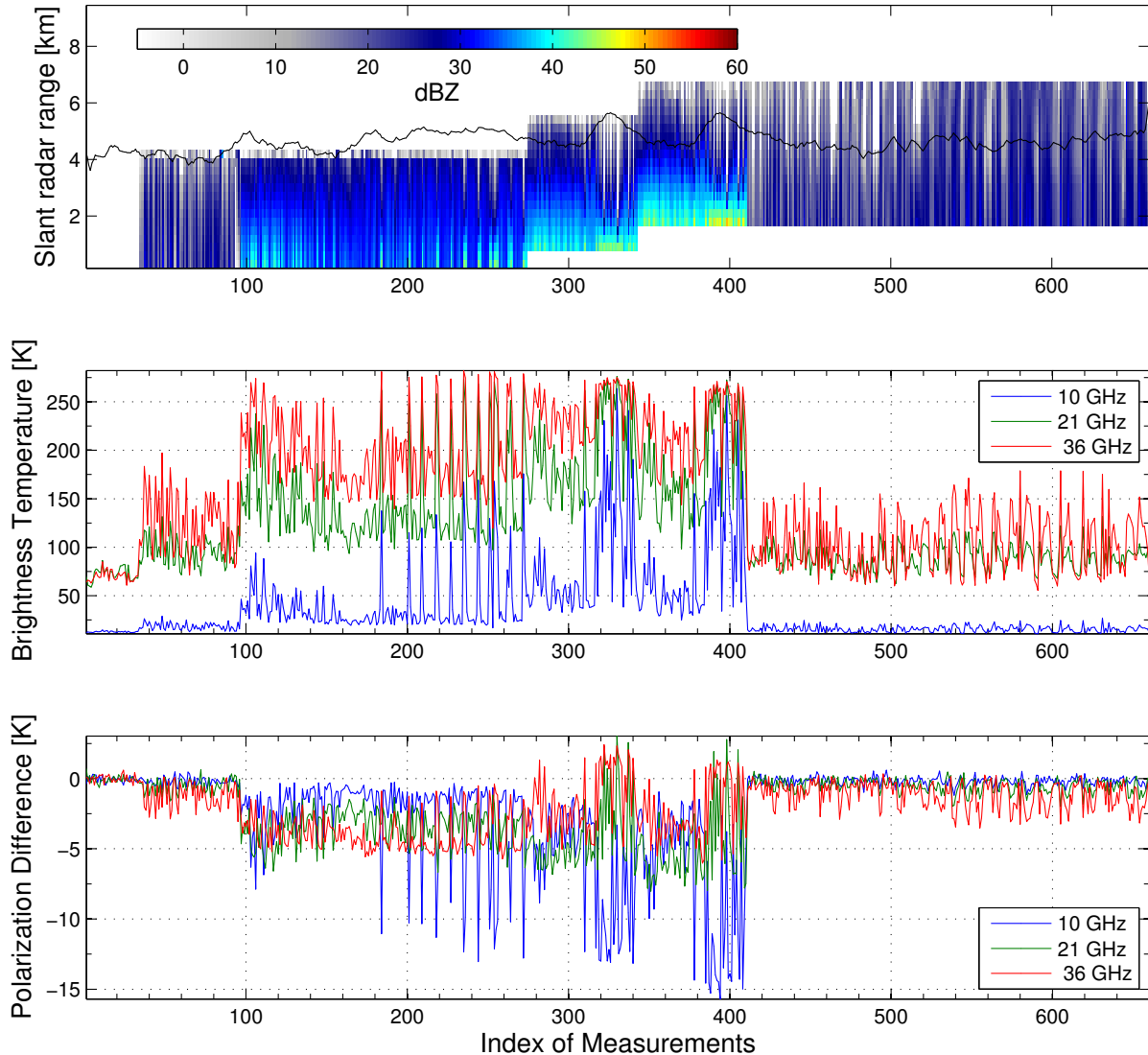


Figure 4.11.: Synthetic measurements selected to test the retrieval technique. Top: Radar attenuated reflectivity, middle: Brightness Temperature and bottom: Polarization Difference at the three ADMIRARI frequencies.

Figure 4.11 depicts 660 samples of synthetic measurements, as they were “observed” at 30° elevation angle. The profiles in Figure 4.11 contain a random selection of simulations sorted according to their DSDs and the positions of the clouds relative to the radiometer. Thus the selection is not intended to represent the development of a natural rain event with time or the full range of possible observations. In this study only states with freezing level between 2.5 and 3.5 km (see black line on top panel in Figure 4.11) are considered in order to confine the actually used states in the simulation database to atmospheric conditions prevailing during a typical mid-latitude autumn rain event (Saavedra, P., Battaglia, A., and Simmer, C., 2012b).

4. Retrieval Methods of Precipitating Clouds

In order to perform an independent retrieval performance evaluation, the states extracted for the generation of measurements were removed from the *a priori* database. The analysis follows several steps. First retrievals are obtained by means of the minimum distance approach as defined in equation 4.78, and compared with the Bayesian retrievals using the radiometric brightness temperature and polarization difference at the three ADMIRARI frequencies as described in section 4.2. Moreover these retrievals are performed for three different values of the diagonal component of the covariance matrix as an attempt to depict the sensitivity to the assumed simulation/measurement errors. Figure 4.12 shows the results of applying the minimum distance and the Bayesian retrievals to the synthetic measurements.

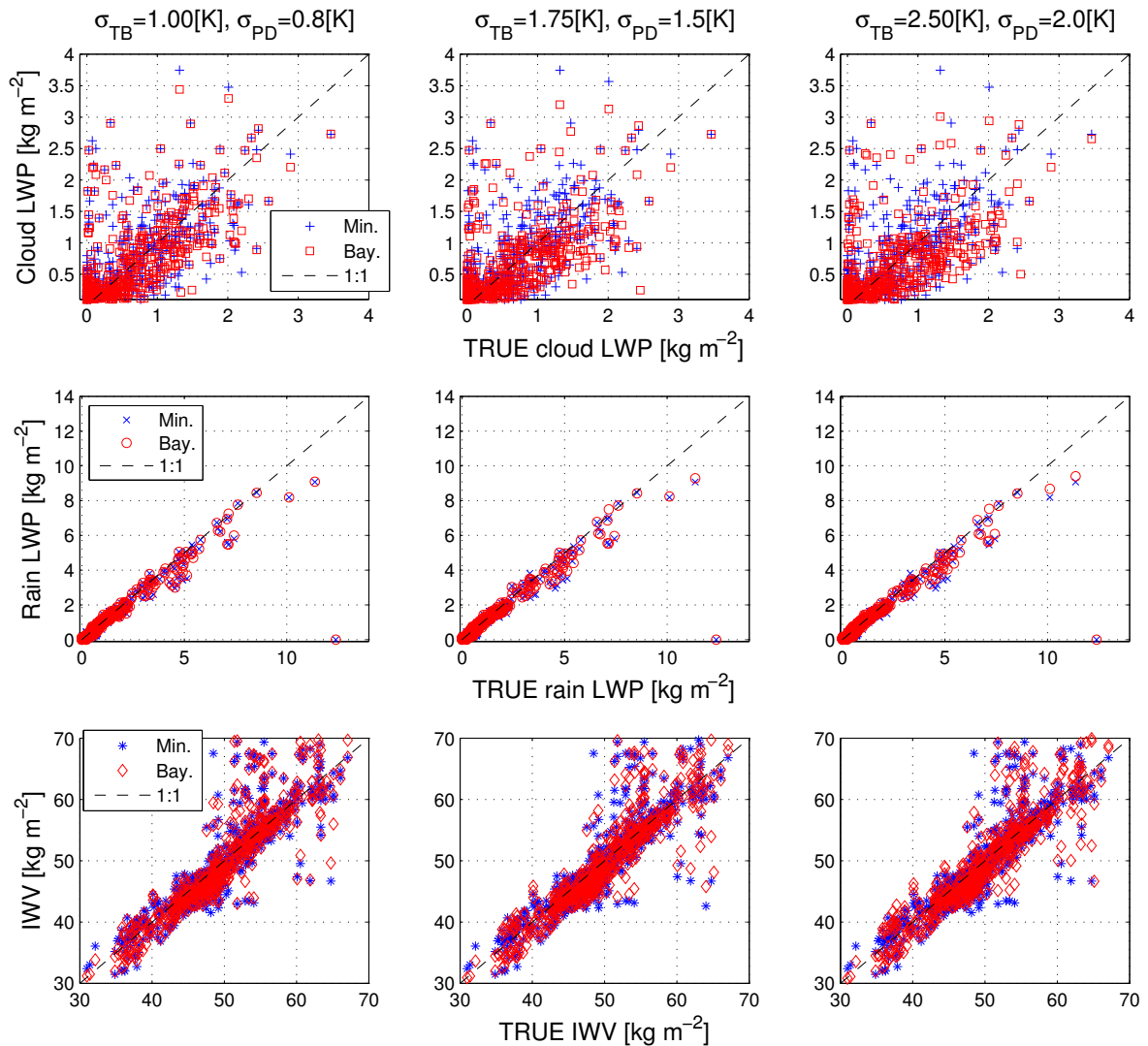


Figure 4.12.: Scatter plot for retrieval versus true values for cloud (first row), rain (middle row) and water vapour (bottom row). The columns correspond to three different elements of the covariance matrix for TBs (from left to right: 1.0, 1.75 and 2.50K) and PDs (from left to right: 0.8, 1.5 and 2.0K). The blue crosses correspond to the minimum distance method and the red-points to the Bayesian retrievals, the black-dashed line indicates the 1:1 relation.

Two main features can be highlighted from Figure 4.12: first, no large difference are found between the retrievals obtained by the minimum distance and the Bayesian method, this specially happens for the rain LWP, followed by the integrated water vapour and finally the cloud LWP showing the last one the most unmatched results. Second, the smaller the assumed errors the tighter the retrieval results relative to the true values. This is specially observed for the cloud LWP whose retrieved-true scattered result spreads larger as a function of the σ_{TB} and σ_{PD} values (from the left to the right in Figure 4.12).

The advantage to use the Bayesian technique instead of the minimum distance is that it can be, in addition, obtained the standard deviation of the expected retrieval value, as indicated by equation 4.74. Thereafter, for the present study it is showed the results using the Bayesian technique and it has been adopted the second pair of (σ_{TB} and σ_{PD}) of 1.75 and 1.5K respectively as a fixed covariance matrix values for the following sensitivity study. The latest because they represent the most realistic error corresponding to the uncertainties related to the instrument and the simulation.

The retrieval algorithm is applied using two variants, namely with passive radiometric information only, i.e. TBs and PDs (hereafter referred to as RAD) and when the MRR reflectivity profile is incorporated to the Bayesian retrieval in a combined radiometer-radar method (referred to as RADMRR). A complementary study assesses the impact of degrading the radiometer from triple to dual-frequency (e.g. 10 & 21, 10 & 36 and 21 & 36GHz, referred to RAD1021 etc.).

Figure 4.13 compares the retrieved cloud and rain LWP and IWV against their corresponding true values for the five retrieval variants. The first column depicts the retrievals without (RAD, blue boxes) and with radar combined (RADMRR, green + markers). The second column presents the results for the dual-frequency degradation approach. Table 4.1 lists the

Table 4.1.: Bias and RMSE for integrated water vapour (IWV), cloud (C_LWP) and rain (R_LWP) liquid water path, resulting from the retrieval sensitivity study normalized to zenith observations. The last column correspond to retrievals obtained by the minimum distance method (eq. 4.78). The last row indicates the Bias and RMSE for retrievals of total LWP below 450g m^{-2} .

		RAD	RADMRR	10&21	10&36	21&36	X_min
IWV [kg m^{-2}]	Bias	0.17	0.14	-0.08	-4.04	-0.09	0.09
	RMSE	1.89	1.63	2.72	6.94	2.38	2.09
C_LWP [g m^{-2}]	Bias	-19.3	-21.6	-6.9	1.5	-4.4	-27.8
	RMSE	235.3	168.5	241.8	250.1	273.9	245.8
R_LWP [g m^{-2}]	Bias	43.3	15.7	59.9	51.6	49.9	39.6
	RMSE	129.1	95.6	152.6	130.0	186.5	133.6
T_LWP < 450g m^{-2}	Bias	-4.6	-2.7	15.7	-6.8	-3.9	-5.8
	RMSE	46.6	13.5	57.8	59.7	45.9	67.3

corresponding bias and root mean square error (RMSE) for all retrieval approaches, while table 4.2 lists the corresponding RMSE separately for the different DSD assumptions. RADMRR leads to retrievals with the least number of outliers in line with the expectation, that geometrical information about the distribution of the rain water reduces ambiguities in radiometric measurements.

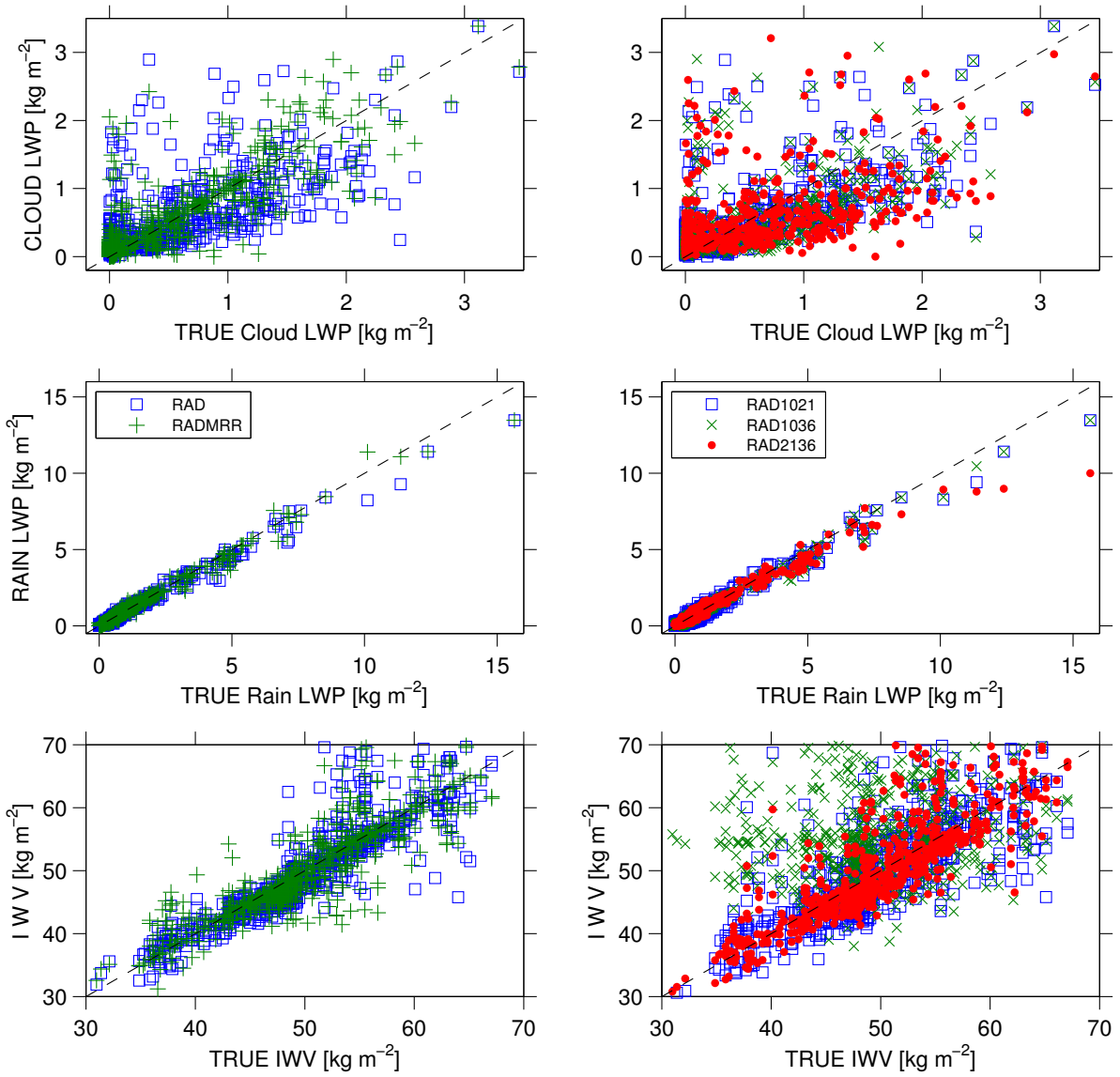


Figure 4.13.: Scatter plot for retrieval versus true values for cloud (first row), rain (middle row) and water vapour (bottom row). The first column corresponds to pure-radiometer (RAD) and radar combined technique (RADMRR), the second column corresponds to the combination of only two frequencies.

Table 4.2.: RMSE for integrated water vapour (IWV [kg m^{-2}]), cloud (C_LWP [g m^{-2}]) and rain (R_LWP [g m^{-2}]) liquid water path, resulting from the retrieval sensitivity study normalized to zenith observations. Every row corresponds to one DSD assumed: Thunderstorm (TS), Heavy-rain (HR), Marshall-Palmer (MP) and Light-rain (LR). The last row indicates the RMSE for retrievals of total LWP [g m^{-2}] below 450 g m^{-2} .

	RAD			RADMRR			RAD 10 & 21			RAD 10 & 36			RAD 21 & 36		
	IWV	CLWP	RLWP	IWV	CLWP	RLWP	IWV	CLWP	RLWP	IWV	CLWP	RLWP	IWV	CLWP	RLWP
TS	0.84	121.5	34.4	0.68	76.5	18.2	1.05	133.6	41.9	1.67	120.8	31.3	1.40	154.9	87.2
HR	1.16	126.5	87.6	0.94	106.4	70.7	1.61	137.6	94.7	2.62	145.9	86.1	1.46	144.7	134.8
MP	1.04	127.5	74.8	0.99	97.8	57.6	1.58	117.9	90.7	3.75	131.7	79.8	1.04	132.7	76.9
LR	0.65	91.2	47.2	0.57	40.5	22.1	1.08	88.1	65.9	4.93	96.3	46.3	0.72	111.8	55.6
Total LWP < 450 g m^{-2}															
	IWV	T_LWP		IWV	T_LWP		IWV	T_LWP		IWV	T_LWP		IWV	T_LWP	
	1.61	45.7		1.59	13.5		2.08	48.4		6.76	53.4		2.22	40.0	

4. Retrieval Methods of Precipitating Clouds

The degradation to dual-frequency retrievals always leads to a lower performance for all frequency combinations. The relevance of the 10GHz channel for rain retrieval is highlighted by the poor performance of the 21-36GHz combination, specially when heavy rain is present. This is also indicated in Table 4.2 by the largest RMSE obtained for the couple 21-36GHz. The worst results for IWV retrieval is found, as expected, when the 21 GHz (close to the weak water vapour rotation line) is absent.

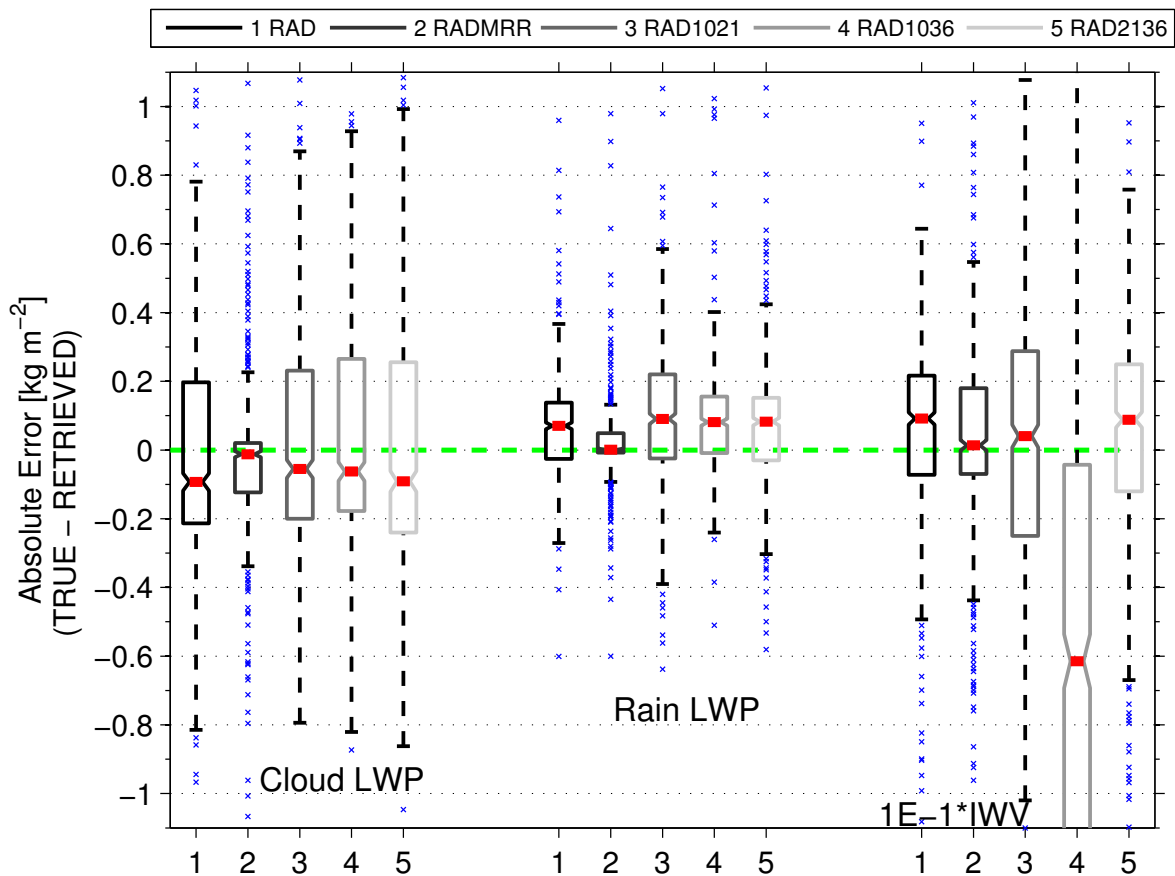


Figure 4.14.: Absolute errors box-plots for cloud, rain and water vapour obtained from the retrieval sensitivity study. The approaches RAD, RADMRR, 10&21, 10&36 and 21&36 are enumerated from 1 to 5 correspondingly. The red mark indicates the median, the first and third quartiles are the bottom and top box's edges and the blue-crosses depicts the outliers.

In figure 4.14 the resulting absolute error for all retrieval schemes are summarized by box plots. Every box plot indicates the distribution of absolute errors by its median (red mark) and its 25th and 75th percentiles (bottom and top box edges); the blue crosses indicate the outliers. In general, the triple and dual-frequency pure-radiometer retrieval approaches differ, predominantly, in the distribution of the absolute error rather than in their median values. Including the radar reflectivity profile to the retrieval leads to a systematic and significant reduction in the variance when comparing the pure-radiometer and the radiometer-radar approaches. The latter is mirrored by a 98%, 86% and 84% reduction on the median absolute error for rain, cloud and water vapour correspondingly. For the retrieval of IWV the MRR incorporation has only a low impact on the spread of the errors distribution compared to the pure-radiometer

mode, and larger errors are found when only two frequencies are used utterly severe when the 21 GHz is absent.

The relative error of the rain/cloud partition $[\frac{LWP_{true}-LWP_{ret}}{LWP_{true}}]$ retrieval from the RAD and RADMRR approaches are presented in Figure 4.15; only results with both cloud and rain components are included (i.e. C_LWP and R_LWP greater than 0). For large cloud or rain water contents, the retrieval performs reasonable (see the accumulation of large square marks scattered around the 0-0 intersection). In general, however, the error distribution shows a clear tendency towards underestimation/overestimation for rain/cloud contents. For RADMRR the improvement compared to RAD in the relative error is accompanied by an increase of points close to the 0-0 intersection, in particular for the rain component; the larger relative errors at low cloud/rain contents are similar for RAD and RADMRR approaches.

The occurrence of extreme relative overestimation errors for the cloud component, in Figure 4.15, suggests that LWP retrievals with relative errors exceeding 50% are much more likely to occur for cloud than for rain (see the spread of the wide relative error histogram for cloud in contrast to the narrower histogram for rain). For cloud (rain) LWP, 65% (13%) of the retrievals lead to errors above 50% for the RAD approach while for RADMRR only 47% (1%) is obtained.

For very low liquid water contents the inversion does not properly reproduce the cloud/rain partition. Simulations show that for light rain, most rain drops are too small to produce significant polarization; e.g. the polarization difference at 30° elevation is not larger than -0.5 K at the most sensitive 36.5 GHz channel for rain water contents up to 120 gm^{-2} . Accordingly the instrument noise level does not allow to distinguish between cloud and rain water contents based on the polarization signal.

For total liquid water contents T_LWP below 450 gm^{-2} the RMSE of the retrieval is on average 45.7 gm^{-2} when only radiometric channels are used (RAD) but decrease to 13.5 gm^{-2} when the MRR is added (RADMRR), see Table 4.2 last row. The 21 and 36.5 GHz dual-frequency approach, however, leads with an RMSE of 40 gm^{-2} to a slightly improved result compared to the RAD. In fact 10.7 GHz is the least sensitive frequency with low LWP, thus the channel contributes no information but noise.

The Figure 4.15 suggests that LWP retrievals with relative errors exceeding 50% are much more likely to occur for cloud than for rain (see the spread relative error histogram for cloud in contrast to the narrower histogram for rain).

The information content introduced by the measurements has been estimated according to equation 4.76. Figure 4.16 depicts the relative entropy as a function of the rain and cloud LWP for the RAD, RADMRR and RAD 10&21 approaches. The relative entropy in Figure 4.16 is expressed in bits of information by dividing the result of equation 4.76 by $\ln(2)$, which is equivalent to changing the natural logarithm in equation 4.75 to \log_2 . Accordingly the narrowing of the *a priori* PDF by increasing the knowledge of the retrieved parameters is given by a factor of 2^{bits} (McFarlane, S., Evans, F., and Ackerman, A., 2002; Rodgers, C. D., 2000).

Figure 4.16 (left panel) clearly highlights, the information added to the retrieval by the MRR reflectivity profiles. Since the MRR is a good rain detector, its measurements improve the retrieval mainly for low rain water contents: in these cases the radiometer polarization signature is negligible or within the instrument noise and the MRR represents the only mean to separate both components. As the rain content increases the relative entropy tends to stay constant for values ranging from 0.5 to 2 kgm^{-2} rain LWP followed by a drop to similar levels as the RAD approach for rain contents above 10 kgm^{-2} . Then the radar signal is basically

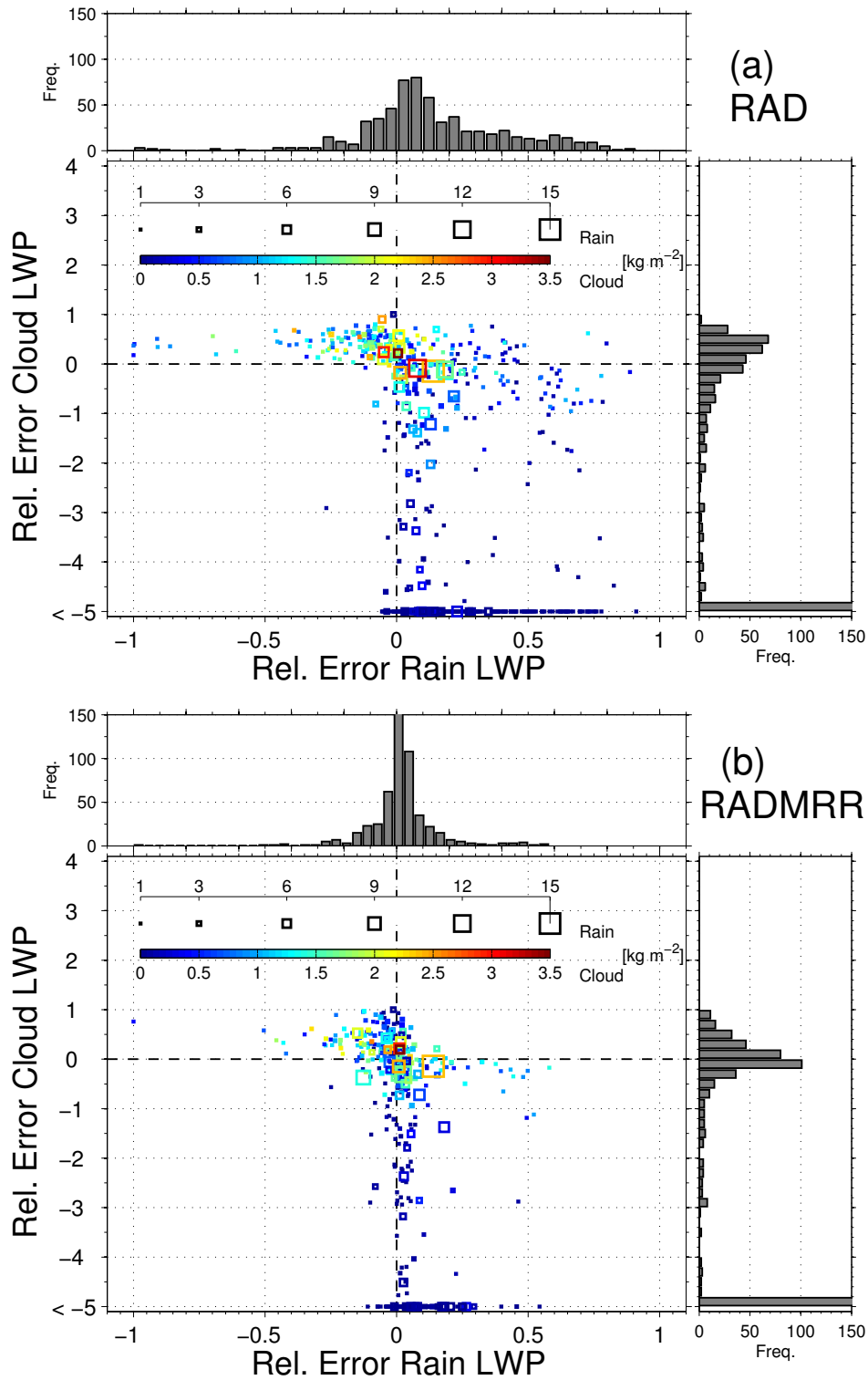


Figure 4.15.: Relative error ($\frac{LWP_{true} - LWP_{ret}}{LWP_{true}}$) for cloud versus rain for: (a) RAD and (b) RADMRR. The color modulates the cloud component, and the square marker size modulates the rain component as it is shown in the inner coloured table. The distribution of relative errors for cloud and rain are shown in the right and top panels respectively.

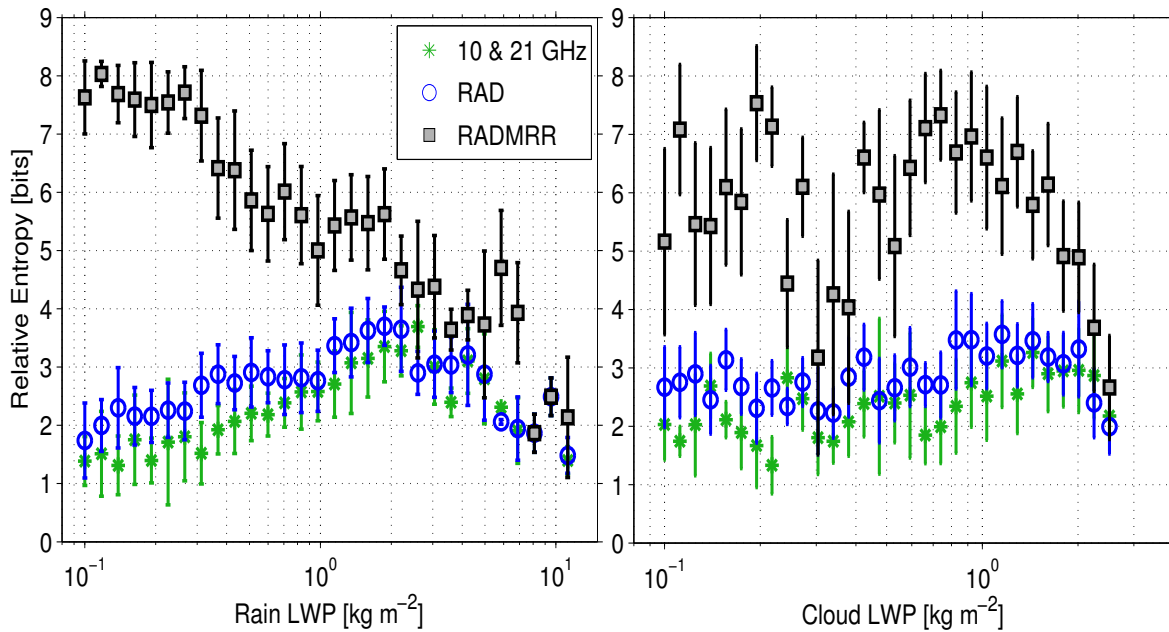


Figure 4.16.: Relative entropy (a quantity indicative of the information content added by the measurement in the sensitivity study) as a function of rain LWP (left panel) and cloud LWP (right panel).

fully attenuated and does not add any information to the retrieval. For the radiometer-only approach measurements add the most information in the range between 0.5 to 4 kg m^{-2} . As a reference when the 36.5 GHz channel is absent the information content remains low until 1 kg m^{-2} .

Figure 4.16 (right panel) indicates no specific range of cloud LWP for the RAD approach where the information stands significantly out, with only a slight increase for values from 0.8 to 2 kg m^{-2} . When the radar measurements are incorporated in the retrieval (RADMRR), a well defined hump is observed between 0.6 to 2 kg m^{-2} LWP, with a fast degradation after and a very dispersed behaviour before that range. At large cloud LWP the MRR is not adding any information to the retrieval process.

In order to look in more detail the effect introduced by the radar geometrical constraint the figure 4.17 depicts the profiles for the synthetic observations and their corresponding retrievals for the RAD and RADMRR approaches. Although the technique presented here does not aim the profiling of neither cloud nor rain, nevertheless by means of finding the minimum distance between measurements and simulations (equation 4.78), it is possible to estimate the most probably observed profiles. In figure 4.17 the first column corresponds to the cloud liquid water content (LWC) profiles for the true (a), RAD retrieval (c) and RADMRR at (e); the same is mirrored in the second column but for rain LWC. By comparing the true profiles (a,b) and the retrievals (c,d,e,f) it is evident the improvement obtained by including the MRR information. For the cloud component the radar profile incorporation not only yields the adequateness of the profile's shape but also improves the integrated values as it has been shown in figures 4.14 and 4.15 (b). The retrieval technique in absence of radar information produce physically inconsistencies from the profiling point of view, i.e. locates cloud and rain where they were not actually observed and shows a large variability on the slant path

extension. Nonetheless it sees that in cases where the rain component holds a large quantity the pure-radiometer approach (RAD) is also able to resolve sporadically the location of the rain cell (see profiles from samples 270 to 410), in that case the rain position is roughly located to approx. 2km range (fig. 4.17 (d)) where the true profiles have the ranges at 2 and 3 km in the same interval. When looking the synthetic measurements (TB and PD at Figure 4.11) for the same interval of samples, it is observed that the 21 and mainly 36.5GHz nearly reach the saturation level and the polarization difference shows even positive values of approximately +3 K in the case of the 36.5GHz, this feature leads to the algorithm to reduce some ambiguity in choosing near-real profiles, since the positive polarization difference is only produced by the backward Monte-Carlo RT code when the radiometer is located outside the rain cell (Battaglia, A., Saavedra, P., Morales, C., and Simmer, C., 2011; Battaglia, A., Saavedra, P., Rose, T., and Simmer, C., 2010, at fig. 8 and fig. 9 respectively). On the other hand when the rain content is not sufficiently large the RAD approach is not able to resolve properly the rain location and comes out with a large variability on the water content profile distribution. Another feature to point out is the fact that when the radar information is not adopted the algorithm includes rain profiles in the first 33 samples where pure cloud conditions were imposed. In that case the RADMR algorithm set zero rain component when the radar has not detected any rain.

Finally, it is worth to emphasize the fact that a good performance of the RADMR approach in figure 4.17 is achieved mainly because the true profiles are geometrically well defined and they have exactly the same geometry as the *a-priori* database. A real rain layer shows certainly more spatial variability rather than the well-defined rain cells in figure 4.17 (a) and (b), but the retrievals are confined to discrete geometries (1 km slant resolution at 30°) as the cases shown here.

4.4.1. Non-precipitating LWP Retrievals

Although the main aim for the radiometer ADMIRARI is the cloud/rain LWP partition, the radiometer also has good performance for cases where no liquid precipitation is observed. The present section gives an overview on the retrievals for total LWP in case of non-precipitation clouds as a complement to the retrievals technique.

The last section has shown that in cases with total LWP below the 450 gm⁻² threshold at a slant elevation angle of 30° the inversion method is prone to produce large errors in the rain-cloud partition, therefore below the above mentioned threshold only total LWP might be retrieved. Furthermore ADMIRARI's Bayesian retrieval has been originally developed focused on mid-latitude convective precipitation, therefore in case of winter precipitation the *a priori* becomes inappropriate for observations alike the [Light Precipitation and Verification Experiment \(LPVEx\)](#) extended observation period (EOP). For that reason a new database has been built up from radiosonde launches from the two nearest WMO sites, i.e. Jokioinen and Tallinn. A total of 5520 profiles have been collected from 30 years of radiosonde for the period October to February, available twice daily (00 and 12 UTC). [Liquid Water Content \(LWC\)](#) profiles are estimated from those radiosonde measurements using the relative humidity (RH), where cloud layers are assumed to exist in a profile when RH exceeds a threshold value as it is presented by Löhnert, U. and Crewell, S., 2003. Once the cloud layer is determined the calculated lwc from a modified adiabatic assumption, along with water vapour, temperature and pressure profiles are used as input variables for the 1-D radiative transfer calculation to compute a set of synthetic brightness temperatures for the corresponding ADMIRARI frequencies. That training data set is used to find out a relationship between TBs and LWP which

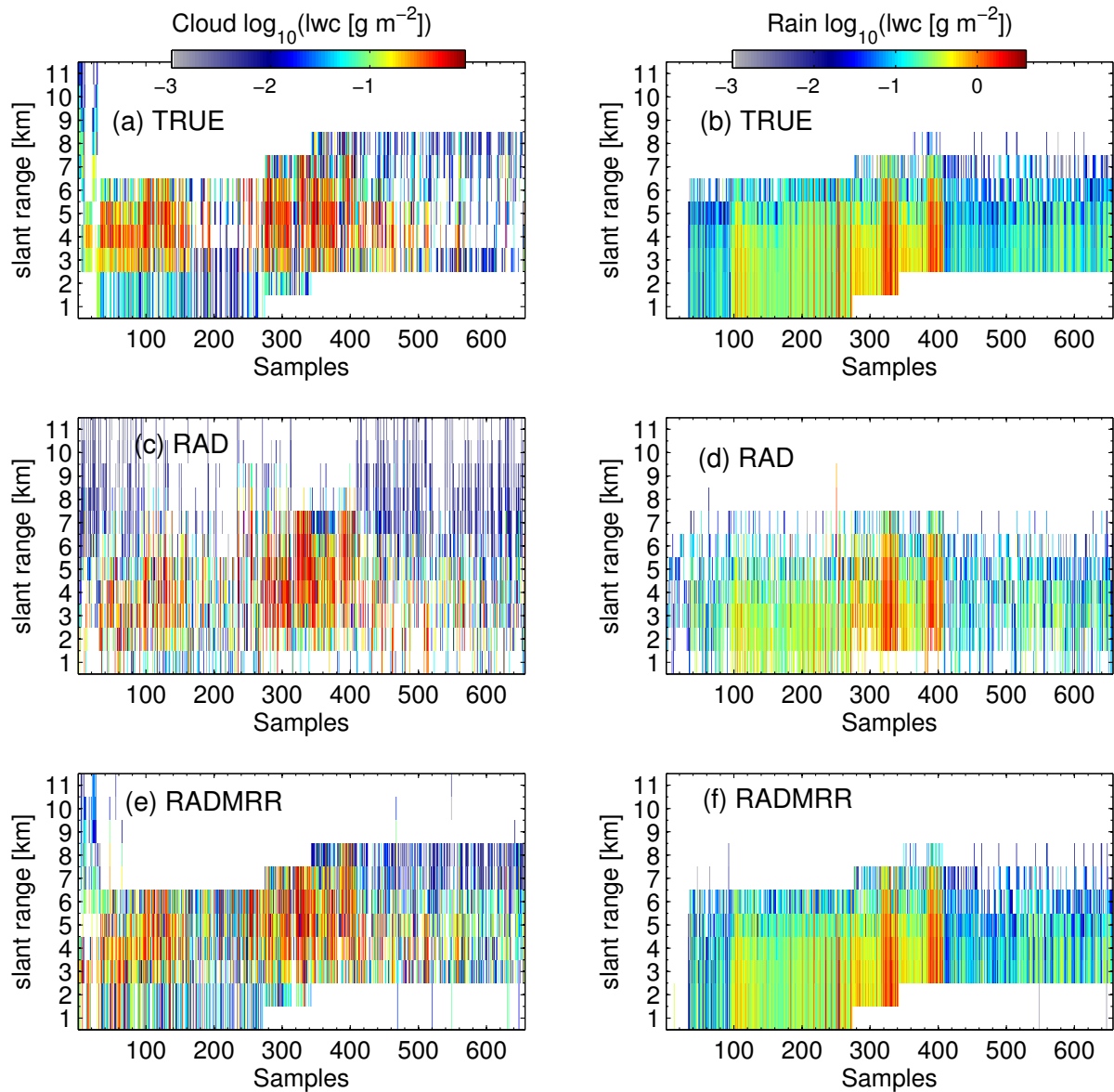


Figure 4.17.: Cloud and rain profiles for the 660 samples retrieval sensitivity study: a) True cloud lwc in logarithm scale, c) the cloud lwc retrieved using the NSI approach, e) NSI approach for cloud but including the MRR geometrical constrain. The second column's panels b), d) and f) same as the first column but for the rain lwc.

is assumed to be a quadratic equation in order to account for possible non-linearities. The quadratic regression follows the expression

$$f_k = a_{0k} + \vec{a}_{1k} \cdot \vec{T\bar{B}} + \vec{a}_{2k} \cdot \vec{T\bar{B}}^2 \quad (4.83)$$

where f_k corresponds to the variable to be retrieved (k being either columnar [LWP](#) or [IWV](#)). The vectors $\vec{T\bar{B}}$, \vec{a}_{1k} and \vec{a}_{2k} are the brightness temperature and the frequency dependent regression coefficients.

As a result of the retrieval sensitivity study in section 4.4, table 4.2 (Saavedra, P., Battaglia, A., and Simmer, C. (2012b, Table 1)), the accuracy for T_LWP retrievals depend on the selected set of frequencies with the largest RMSE obtained when the pair 10.7 and 36.5 GHz are used and the lowest RMSE is obtained with the pair 21.0 and 36.5 GHz. For the case of non-precipitating total LWP retrievals from the regression technique, two sets of frequencies ({21.0, 36.5} and {10.7,21.0, 36.5} GHz) have been used in order to study a RMSE frequency dependence.

To assess the retrieval quality, a subset of synthetic brightness temperatures has been extracted from the database and treated as actual measurements by adding Gaussian noise corresponding to the instrument characteristics i.e. 0.5 K for all the channels. Since the corresponding [LWP](#) values for this subset is exactly know, they are treated as true LWP and being compared to the retrieved LWP obtained applying equation 4.83, for the two set of frequencies. The results are shown in figure 4.18 where the true LWP is compared with the retrieved values for the two-(three) frequency approach represented by the blue circles (red squares). It is noticeable the difference on retrievals' performance mainly for low amounts of liquid water content with large scattering below approximately 50 g m^{-2} (200 g m^{-2}) LWP for the two (three)-frequency retrieval approaches, with a 79% increase on RMS associated to the presence of the 10.7 GHz channel. On the contrary, for large LWP quantities the regression technique has a good performance independent with either two or three frequencies.

The distribution of retrievals' relative errors have been calculated as a function of minimum LWP threshold and is summarized in a sequence of box-plots for the two (three)-frequency retrieval approaches at the top (bottom) panel in figure 4.19. In case of the two-frequency retrievals most of the results have a median error ranging from 4 to 7% , while for the 75% quantile only beginning from 30 g m^{-2} LWP the errors are clearly below 10% error. On the other hand, the three-frequency approach (bottom panel in Fig 4.19) reveals the fact that the inclusion of the 10.7 GHz channel degrades the retrievals by spreading largely the errors. This is due to the poor sensitivity of 10.7 GHz to cloud liquid water; this frequency plays an important role mainly for LWP retrievals in cases of moderate to heavy rain.

The instrumental noise is the only source of error assumed in the previous study, however other source of uncertainties might diminish the good retrieval performance e.g. observation slant geometry, beam-width effects or radiometer calibration drifts. For instance for cloud-free cases (as it is detected by the ceilometer) the regression technique could produce a bias with slightly negative values up to -20 g m^{-2} . Therefore based on the relative error distribution (figure 4.19) a nominal value of 30 g m^{-2} is assumed as minimum detectable LWP, which is in accordance with reports regarding detection limit for two channel radiometer LWP retrievals by Löhnert, U. and Crewell, S., 2003.

As alternative, the ADMIRARI's retrieval Bayesian technique has been extended with the same synthetic database used for the regression technique, the results (figure 4.20) are comparable in terms of minimum detectable value with only two main differences: first, the Bayesian

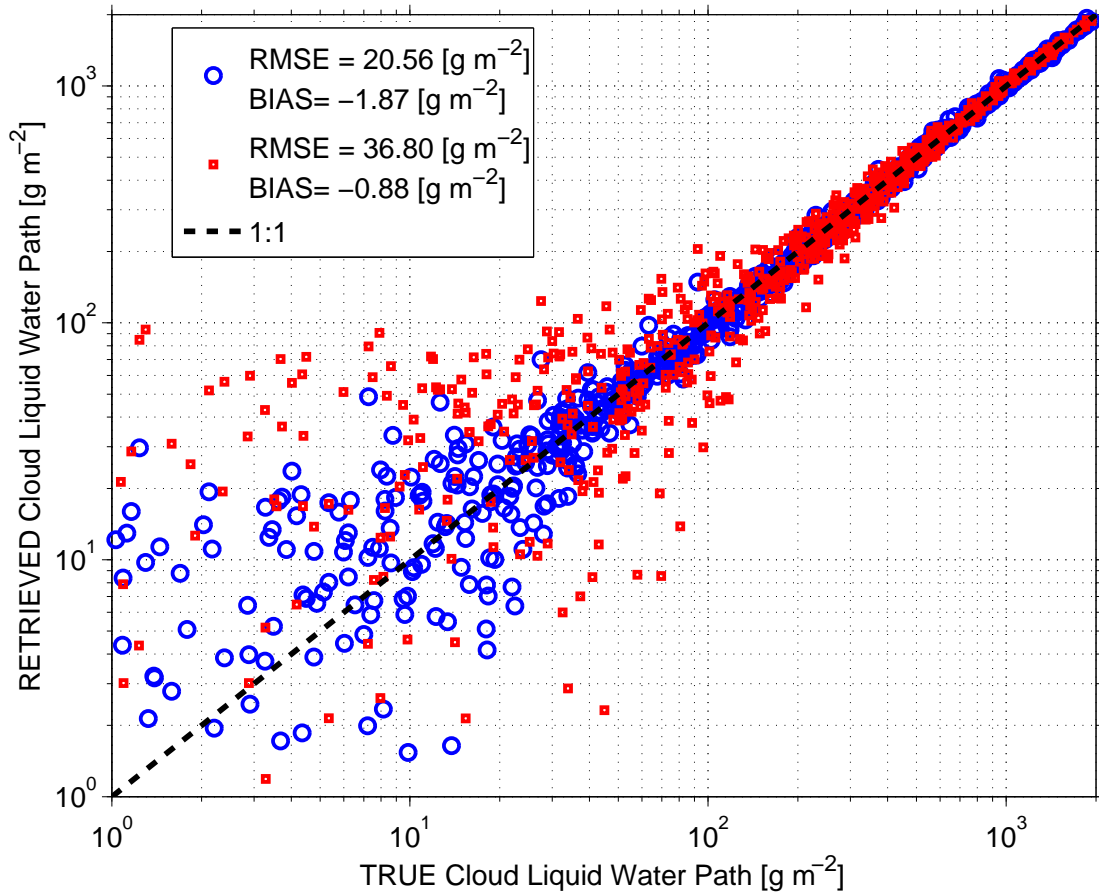


Figure 4.18.: Retrieval performance based on the comparison between the true and the retrieved LWP. Results from the tree-frequencies 10.7, 21.0 and 36.5 GHz (red squares), and two-frequencies 21.0 and 36.5 GHz (blue circles) approaches. The black dashed line represents the one to one line.

technique clearly underestimate LWP below approximately 40 g m^{-2} , and second, there is not significantly difference between the two or three-frequency retrieval approaches as the regression technique shows. Hereafter, the LWP values in the case of non-precipitating clouds might be obtained by the regression technique with similar or better accuracy than the Bayesian technique.

4. Retrieval Methods of Precipitating Clouds

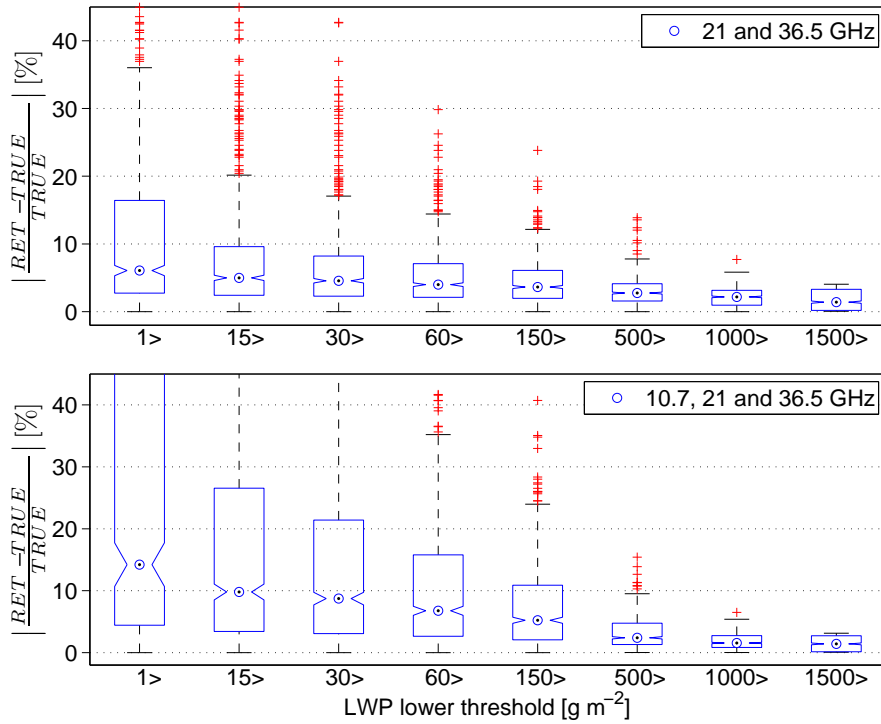


Figure 4.19.: Relative errors as a function of minimum LWP. The dot-circle represents the median, the 25th (75th) quantile are the lower (upper) box limit. The whiskers corresponds to $\pm 2.7\sigma$ and the red crosses are outliers.

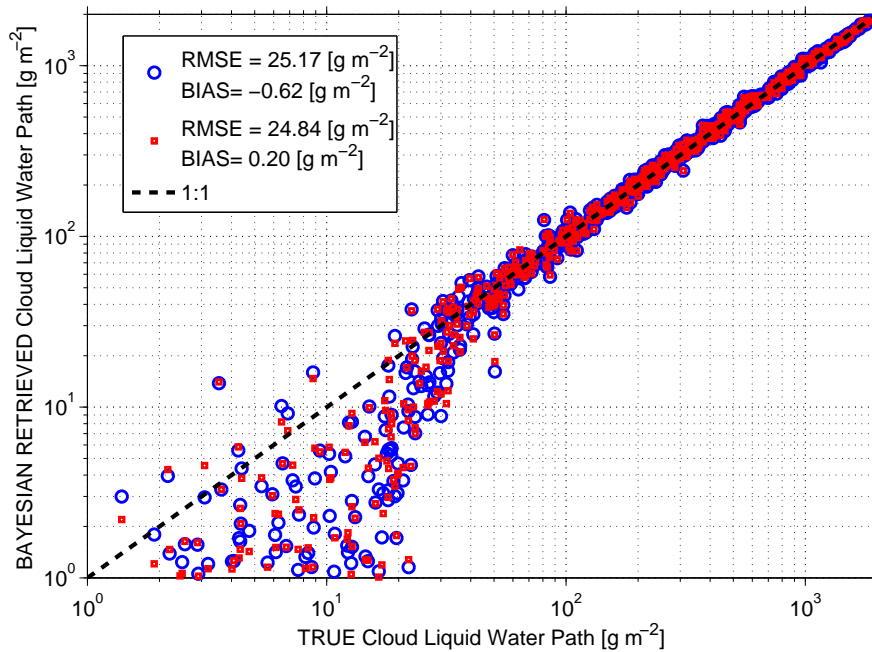


Figure 4.20.: Same as figure 4.18 but using Bayesian technique. Results from the tree-frequencies 10.7, 21.0 and 36.5 GHz (red squares), and two-frequencies 21.0 and 36.5 GHz (blue circles) approaches. The black dashed line represents the one to one line.

5. Observations of Precipitating Clouds

Abstract

This chapter gives a short introduction regarding the set of observations performed by the radiometer, and the features that precipitating clouds produce in the microwave polarization signature. Measurements collected with the radiometer ADMIRARI at different field campaigns are presented and discussed, along with the data treatment to achieve a quality controlled database is also discussed.

5.1. The COPS Field Campaign

The [Convective and Orographic-ally Induced Precipitation Study \(COPS\)](#), was an international field campaign that took place in the black forest, Germany in 2007. The main motivation was the attempt to improve the quantitative precipitation forecast, specifically with respect to orographic precipitation. In that frame COPS aimed at collecting high quality data sets usable for model validation as well as at data assimilation in order to improve initial fields in numerical models. COPS gathered a large number of measurement systems able to build data set with unprecedented accuracy and resolution from intensive observational periods. Four super-sites along the Black Forest were utilized for that goal. These super-sites were located at the Hornisgrinde mountain (H-site), Stuttgart (S-site), at the Murg Valley (M-site) and at Achern (R-site). For a full description see Wulfmeyer, V. et al., [2008](#).

The [ADMIRARI](#) radiometer was first deployed at the H-site. However due to microwave frequency interference produced by a nearby Ka-band vertical pointing radar (see section [3.1.2](#) for more information), ADMIRARI needed to be relocated at the [ARM](#) Mobile Facility in the Murg Valley, M-site. This offered the opportunity to integrate the ADMIRARI measurements with the large suit of instrumentation present at the [ARM Mobile Facility \(AMF\)](#) (e.g. the AMF meteorological station including a rain gauge, radiosondes, and the vertically pointing W-band radar).

At the M-site, ADMIRARI has been continuously measuring from the 8th of August to the 19th December. Rain events occurred at the M-site (Murg Valley) during that period are summarized in figure [5.1](#) where the cumulative rain is shown together with the temperature evolution and corresponding freezing level. The basic scanning strategy adopted during the campaign consisted of a 15 minutes cycle subdivided into a 8 minutes-long [PPI](#) scan at 30° elevation, a 4 minutes [Range Height Indicator \(RHI\)](#) scan at a fixed azimuth direction plus a zenith mode for the remaining 2 minutes.

Important to note that during COPS the radiometer did not operate together with any of the auxiliary instruments presented in chapter [3](#), and the measurements collected by ADMIRARI comprised of only the passive radiometer.

An example of a time series of PPI scans during a whole day is provided in Figure [5.2](#). This case highlights the standalone feasibility of ADMIRARI to obtain information about the precipitation by means of the polarization difference. The case from 18th of September was

5. Observations of Precipitating Clouds

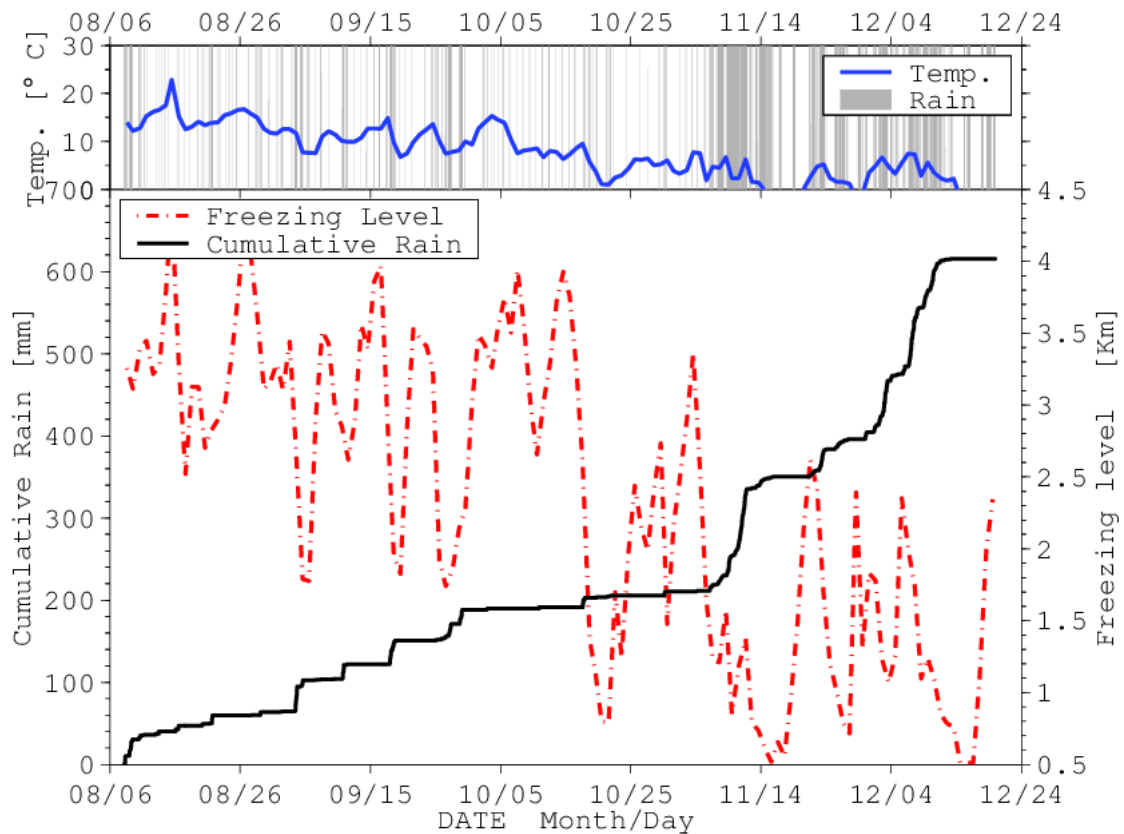


Figure 5.1.: Precipitation regime and temperature registered during the whole COPS campaign.

characterized by a series of rain events with the first part of the day dominated by stratiform events with different convective events occurred during the afternoon.

The TBs show a strong correlation with the rain rate (as expected) but with a frequency dependent dynamic range: the 10.7GHz channel is basically never exceeding 110K with a clear-sky baseline around 8K while 21.0GHz (36.5GHz) TBs range between 45 and 240K (277K). This is obviously due to the larger opacity of the atmosphere at higher frequencies. The polarization differences show negative values only in presence of rain in agreement with theoretical studies. However the amplitude of this signal does not follow in general the TB. For instance although having similar TBs at 21.0 and 36.5 GHz, the two peaks at 11:00 AM and at 11:30 AM present different PDs. According to the theory (Czekala, H., Crewell, S., Hornbostel, A., et al., 2001b), this should be a sign of the presence of a higher fraction of rain versus cloud water in the scanned volume at 11:30 AM. At 36.5GHz the PD signal is generally lower, with the largest negative values not achieved in parallel with the highest TBs. This is a result of the saturation effect when large optical thicknesses (≥ 4) are sensed, i.e. of the counterbalancing between emission (due to their preferential horizontal alignment raindrops tend to emit more H than V-polarized radiation, thus producing negative PDs) and propagation effects (raindrops attenuate more horizontal radiation, thus letting more vertical radiation reach the receiver). In some cases for very high TBs (like at 4:00 AM) PDs become even positive. This effect has been predicted in the frame of 3D effects (Battaglia, A., Czekala, H., and Simmer, C., 2006).

The whole COPS dataset have been quality checked. Cases identified as rainy by the gauge

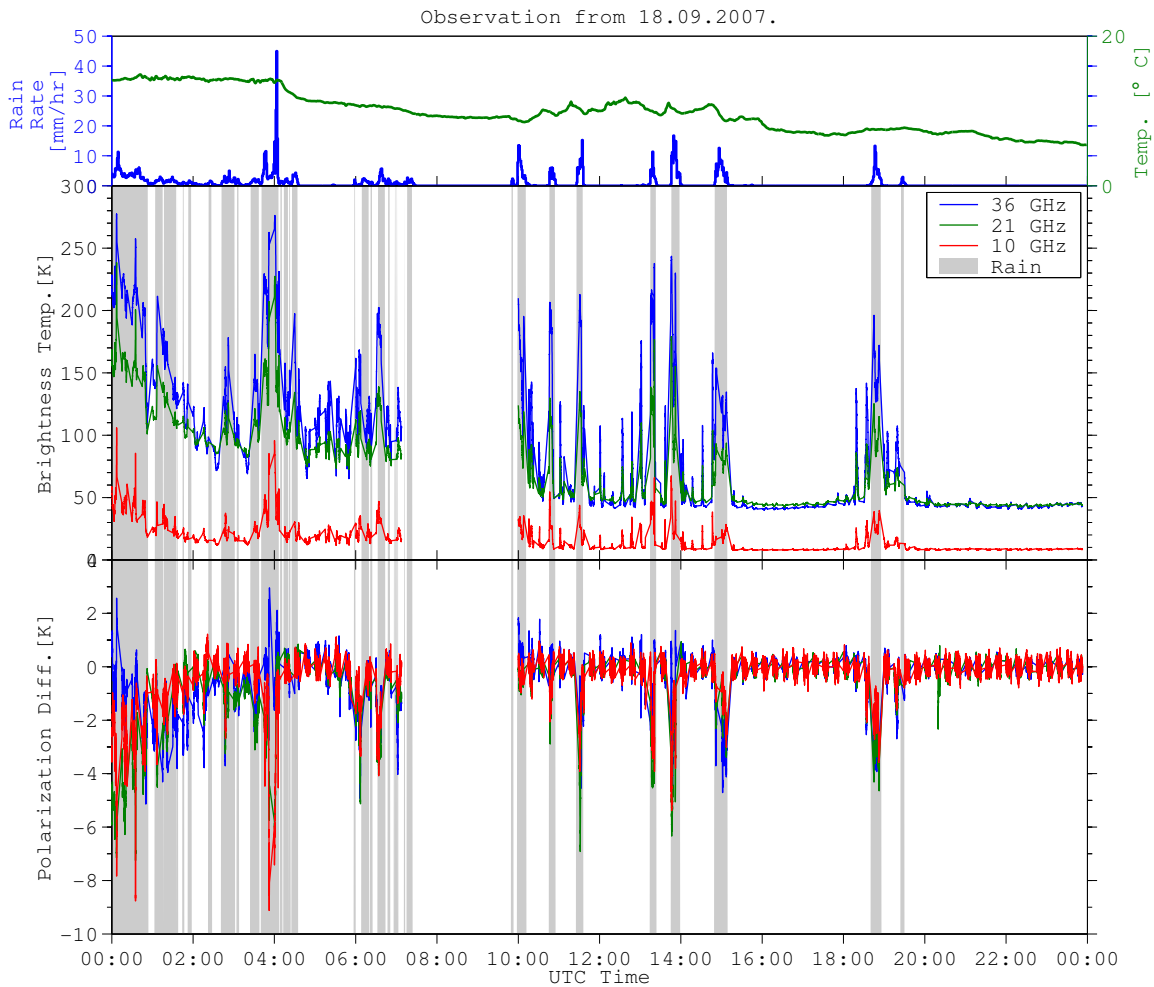


Figure 5.2.: Examples of measurements for 18/9/2007. From top to bottom: gauge rain rate and 2 meter temperature, 10.7, 21.0 and 36.5GHz brightness temperature and polarization difference. Grey intervals indicate rainy periods as sensed by the gauge at the [ARM](#) site.

have been further analysed: for each frequency, (TB, PD) occurrence plots are presented in figure 5.3. When looking at each frequency separately, the results appear to be in agreement with theoretical expectations and with figures 2 and 3 by Czekala, H., Crewell, S., Hornbostel, A., et al., 2001b. At 10.7GHz TBs never exceed 130K which roughly corresponds to a slant optical thickness of 0.65. On the other hand at 36.5GHz values close to ambient ground temperature are reached, typical signatures of very thick atmospheres. For any given TB the variability of PDs is related to the relative presence of rain/cloud particles in the slant column under observation. When a large fraction of raindrops (cloud particles) is present the observation points are likely to be located in the lower (upper) branch of the coloured contour.

COPS campaign was important in order to collect the first ADMIRARI data set, thereon have a complete picture of the kind of signature produced by a large range of rain intensities. That ensemble of measurements was a reference to compare with simulations in an attempt to develop a retrieval scheme for ADMIRARI.

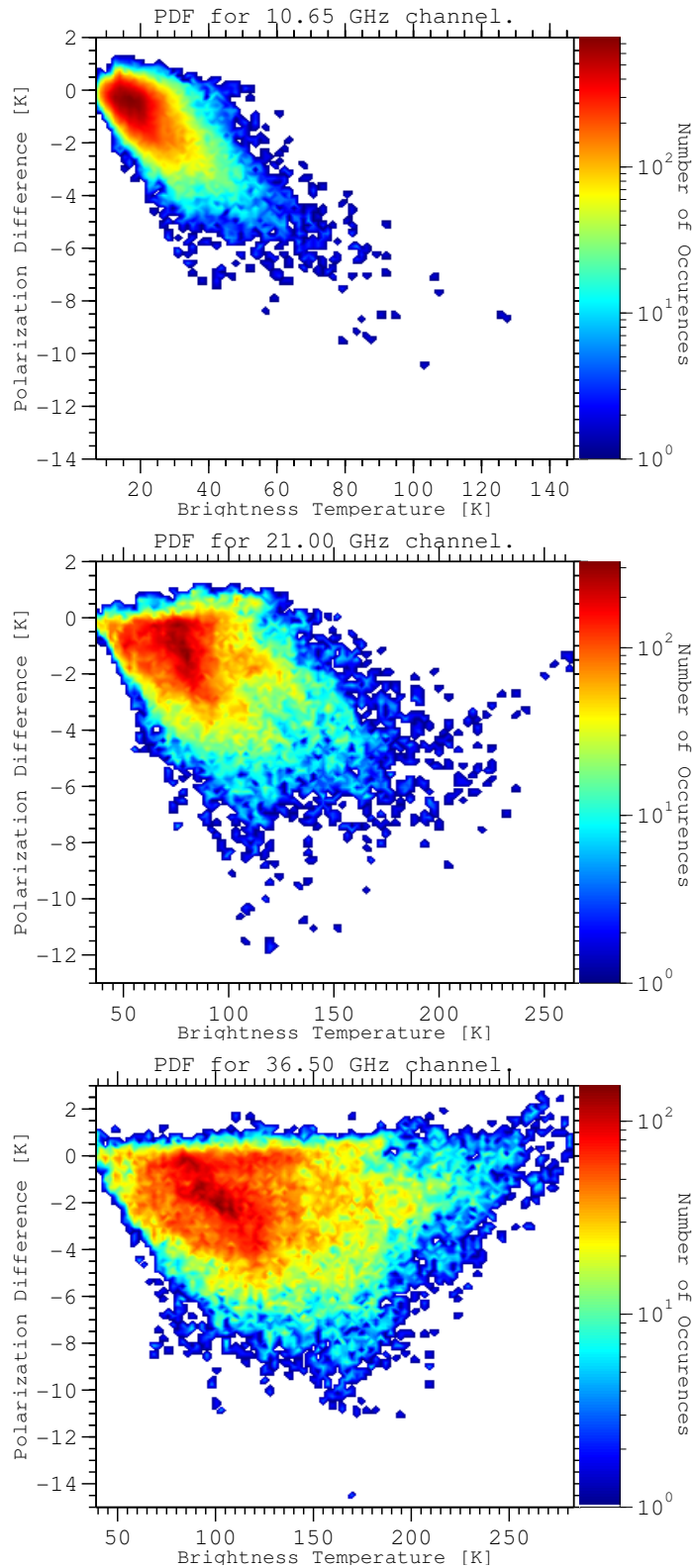


Figure 5.3.: Distribution of occurrences for long term measurements (TB, PD) in rainy conditions for the whole COPS campaign. The three ADMIRARI frequencies are shown (10.7GHz top, 21.0GHz center, 36.5GHz bottom).

5.2. CABA UW Measurements

The [Cabauw Experimental Site for Atmospheric Research \(CESAR\)](#) in the Netherlands provides an optimal platform for microwave radiometry for cloud investigations, activity which was initiated in 2001 in the framework of the first BALTEX Bridge Campaign (BBC, see (Crewell, S., Simmer, C., et al., 2004)). In 2008 the European integrated project on aerosol, cloud, climate, and air quality interactions (EUCAARI) campaign has been taken place in [CESAR](#) (<http://www.knmi.nl/eucaari/>), this campaign was used as a test-bed for ADMIRARI's measuring from May 5th to December 12th 2008. For those measurements ADMIRARI was up-graded with the co-located [MRR](#) as discussed in section 3.2.1, chapter 3. The new ADMIRARI-MRR configuration, enriched the data set by having a range resolved insight of the precipitation profile. Figure 6.1 depicts a typical data set from EUCAARI with the new incorporated active sensor.

From the whole radiometer observations at CESAR, the data set was quality-checked and cases of obvious radio interferences and direct Sun overpasses within the instrument field of view were discarded. In order to avoid measurements with likely wet antennas, the CESAR's continuous wind direction observations were used to remove cases when the radiometer was pointing to down-stream directions. ADMIRARI's data was flagged by means of the MRR detection of rain within the same line of sight, due to the unequal time resolution of both instruments (1 and 10 seconds for ADMIRARI and MRR respectively) it has been given a window of ± 10 seconds before and after a MRR profile has been measured. Thereby the MRR's rain flag is extended to two consecutive measurements to cover the radiometer data. In addition, this procedure has been cross checked with the radiometer's *in-situ* rain sensor in order to avoid false flagging.

The radiometer was kept measuring at a fixed azimuth due to problems of interference produced by the scanning MRR over other passive radiometers in the K-band. Moreover, most of the analysis was performed at a elevation angle of 30° in order to avoid signal variability due to change of observational geometry. Results presented in chapter 4 are based mainly on observations made at CESAR

6. Retrieval Results

Abstract

The results obtained by applying the retrieval technique described in 4.2 to the measurements are the main subject in this chapter. The retrievals are discussed for a case study and a long-term basis, the corresponding statistics is also put into consideration. A special section is dedicated for the discussion regarding the partition of Rain and Cloud LWP according the findings in the present work and the reports from other authors mainly for space-borne instruments. A brief analysis on the differences arose from retrieving slant observation with respect to the corresponding columnar atmospheric state is presented. Finally a validation approach is proposed for the case of Rain LWP obtained from two different sensors and techniques.

6.1. Mid-Latitude Rain Regime Retrieval

In this section retrievals from the data collected at the CABA UW observatory, as described in section 5.2, are applied first to a single case study and then to the entire dataset. In this context the retrieval methodology, with the MRR as a tool to select *a priori* profiles according the geometrical position and thickness of the rain layer, is applied to the case study of 10 November 2008, between 04:00 and 07:00 UTC (Figure 6.1). The wind is blowing from azimuthal directions between 210° and 250° , while the radiometer is pointing at 170° . This set-up ensures that the radiometer antennas were not affected by wetting. The MRR slant path reflectivity time series (top panel in Figure 6.1) nicely depicts a sequence of rain cells, each with its own peculiar temporal duration and spatial variability. The rain duration as detected by the rain sensor located at the radiometer (indicated by the shaded areas in Figure 6.1) ranges from 2 min (e.g. at 04:45 UTC) to ~ 30 min (from 04:00 to 04:33 UTC). Slanted paths through rain range from ~ 4 km at 04:07 UTC to ~ 300 m at 05:42 UTC. The estimated freezing level from the surface temperature is also drawn as a dashed-black line in the MRR reflectivity time-height cross section.

This case study epitomizes several observational scenarios that the radiometer can sense, ranging from pure cloud atmosphere to liquid and solid precipitation with different geometrical radiometer sensing positions, e.g. radiometer situated under the precipitating cloud (until 6:00 UTC) or away from it (e.g. at about 3 km distance after 6:00 UTC). Figure 6.2 shows the corresponding retrieval results for IWV, cloud and rain LWP together with the retrieval standard error. Hereafter all retrieval results are re-normalized to equivalent vertical column values by scaling the 30° slant observations to zenith.

From measurements in Figure 6.1 and their respective retrievals in Figure 6.2, the following features can be highlighted.

- Measurements shows an uneven variability for both TBs and PDs, with several PD minima of ~ -6 K at 36.5 GHz which do not correspond to minimum PDs at the other frequencies. The MRR also depicts dissimilar reflectivity profiles at these PD minimums. On the other hand, when the minimum PD of ~ -8 K at 10.7 GHz is observed (04:06 UTC), the

6. Retrieval Results

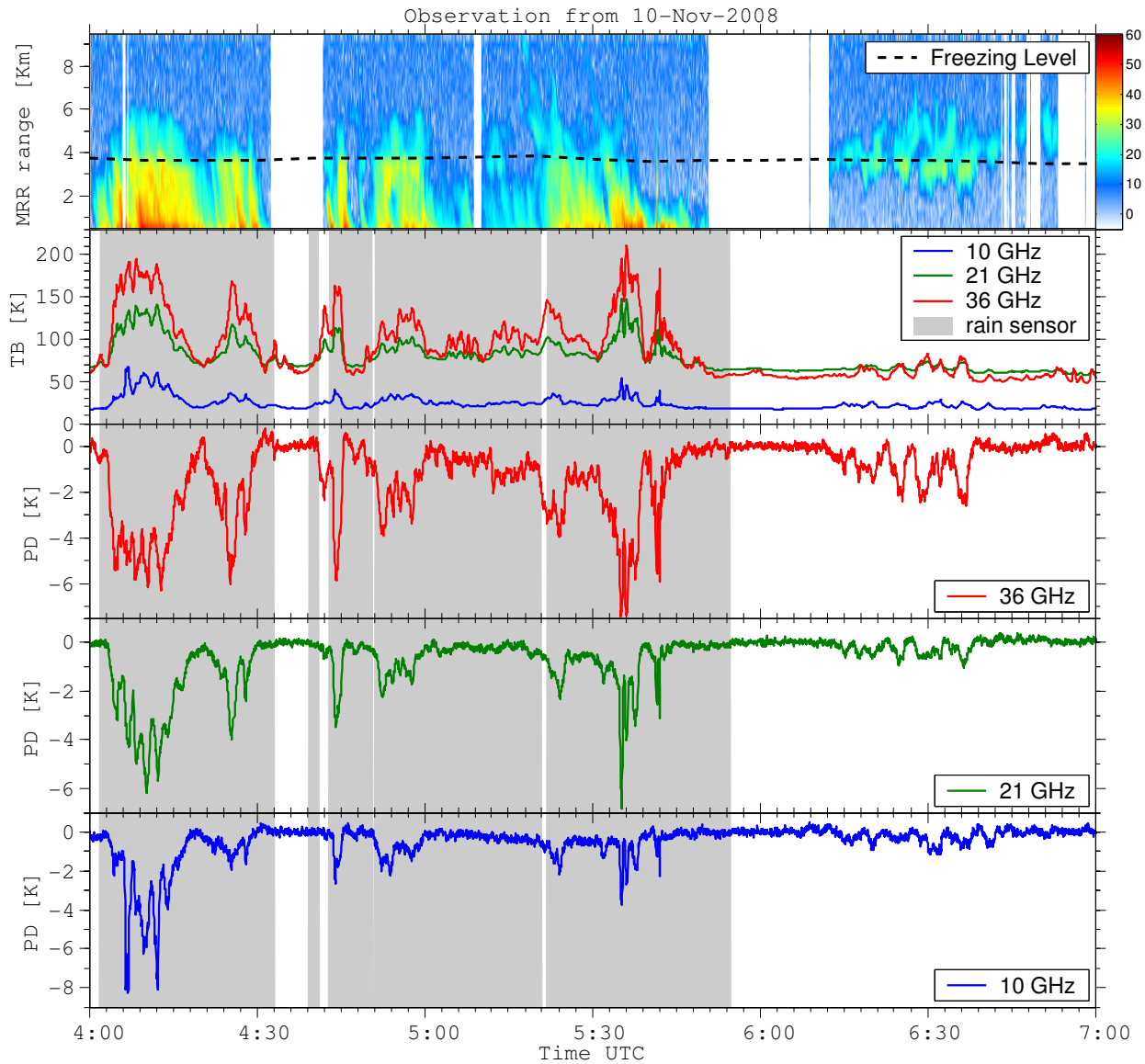


Figure 6.1.: Measurements from 10 November 2008, at 30° elevation angle and fixed azimuth. Top panel: MRR slant path reflectivity in dBZ, the estimated freezing level is shown in dashed black line; second panel: brightness temperatures for the three frequencies; third, fourth and bottom panels: polarization difference at 36, 21 and 10GHz respectively. Gray areas indicate rainy periods flagged by the rain sensor.

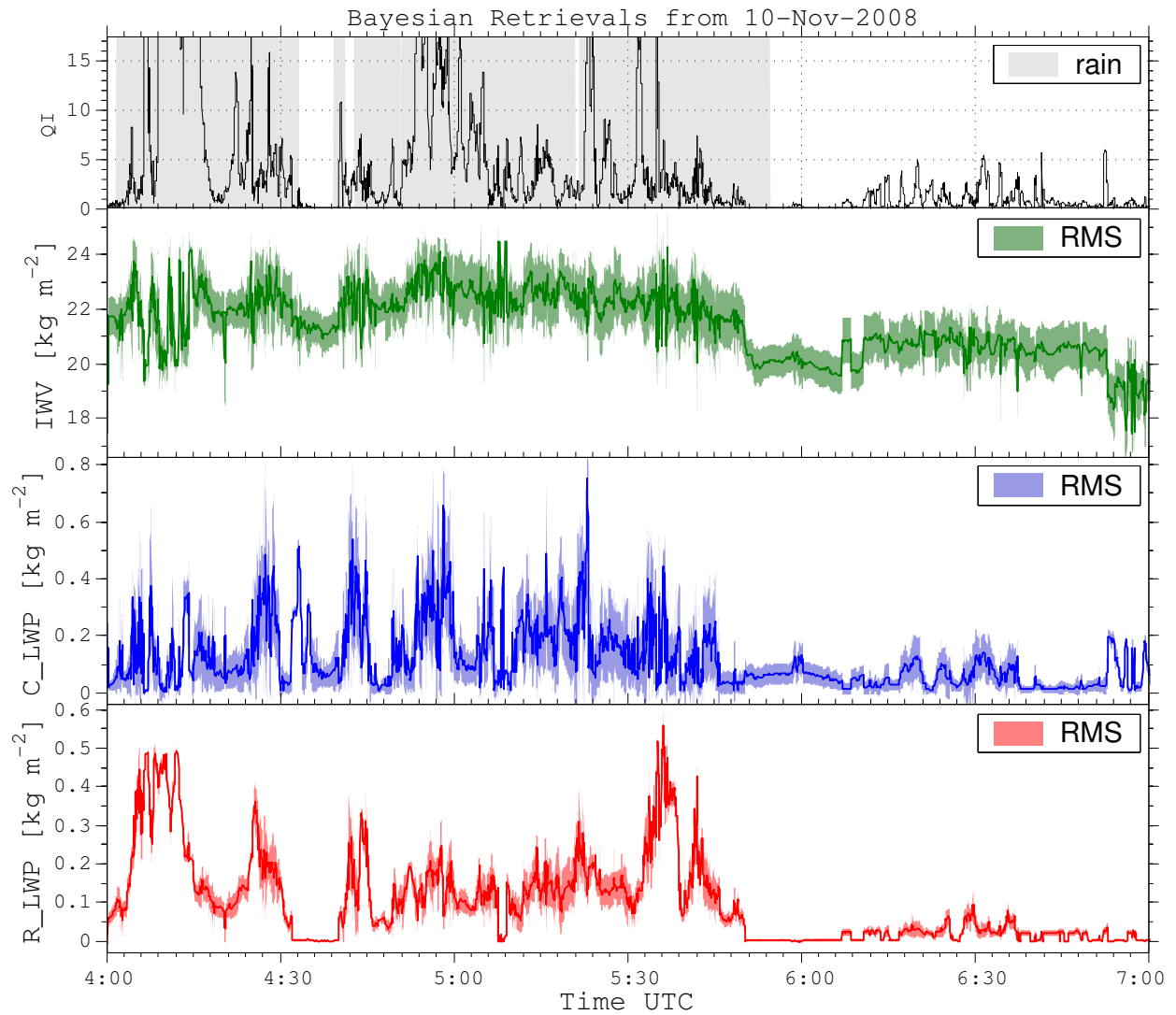


Figure 6.2.: Retrieval results for the case illustrated in Figure 6.1. Top panel: quality index (QI); second panel: integrated water vapour; third panel: cloud LWP; bottom panel: rain LWP. The gray area in the top panel indicates precipitation sensed by the rain sensor; colored areas shade the one-standard-deviation interval for the retrieved quantities.

21 and 36.5 GHz depict PDs only of about ~ -4.2 and ~ -4 K, respectively. This stresses the importance of a multi-frequency approach, since every frequency reacts differently to several atmospheric regimes.

- ADMIRARI has unique capability in distinguishing the signal from cloud and rain even when it is located far away from the radiometer (see Figure 6.1 from 06:12 to 06:40 UTC). In fact when the radiometer rain sensor did not flag such events as rainy, the negative PDs suggest the presence of rain as confirmed by the MRR reflectivity. This aspect cannot be featured by a standard single-polarized radiometer whose TBs would have been misinterpreted as coming from a pure cloud scenario, leading to inappropriate LWP values.
- The radiometer polarization signature responds mainly to liquid precipitation composed by raindrops with horizontally oriented shapes. For instance, from 06:42 to 06:55 UTC, the radiometer PDs are negligible while the MRR detects some targets with reflectivity around 20 dBz. Such targets are however located above the 0° C isotherm and, therefore, they likely involve solid precipitation (ice phase). The radiometer has low or marginal sensitivity at solid precipitation and only can sense the absorption from super-cooled liquid water as it has been reported by Lautaportti, S., Moisseev, D., Saavedra, P., Battaglia, A., and Chandrasekar, V., 2012; Petersen, W., L'Ecuyer, T., and Moisseev, D., 2011; Saavedra, P., Battaglia, A., and Simmer, C., 2012a for LPVEx and GPM Cold Precipitation Experiment (GCPEX) field campaigns.
- ADMIRARI is capable to resolve very short rain showers like the events at 04:43 UTC and 04:45 UTC in Figure 6.2, with duration of only 1 and 2 minutes respectively. Light rain observations from 05:06 to 05:21 UTC, where only the 36.5 GHz polarization signature is detectable, can be resolved with R_LWP around $\sim 0.15 \text{ kg m}^{-2}$. Even low rain water content like 0.05 kg m^{-2} (from 06:06 to 07:00 UTC) with coincident cloud water below 0.1 kg m^{-2} can be retrieved. However, as discussed in section 4.4, for low water contents the partition cloud/rain LWP may be affected by large uncertainties.
- Similar retrieval rain contents are obtained from completely different radiometric signatures. This is the case of the two peaks of 0.55 kg m^{-2} retrieved at 04:12 UTC and 05:36 UTC in Figure 6.2. While the TBs in the two events are similar in magnitude at their corresponding frequencies, the PDs, which are more strongly raindrops shape and DSD dependent, are not. This pinpoints at a commonality in the macro physical property of the system under observation (i.e. same R_LWP) but at disparity in the cloud microphysics (i.e. different DSDs). On the other hand, while in the first case the radar reflectivity profile ranges from ~ 50 dBz to 30 dBz in a rain layer of approximately 4 km, for the second case the same reflectivity range values are spread in approximately only 2 km, meaning that using a pure radar rain liquid water content retrieval, the obtained R_LWP would be larger for the first case than for the second, because their integration paths are different, arising thereof a disagreement with the radiometer retrievals.
- ADMIRARI retrieval provides information about temporal evolution of IWV during rain events. For instance, Figure 6.2 reveals a rapid variation of the water vapour during the rain period followed by a reduction by about 2 kg m^{-2} when the rain ceased, and by a relatively steady period even during the following rain events from 06:12 to 06:51 UTC.

Rapid fluctuations of total water vapour content during rain events were already reported by Knupp, K. et al. (2009) from a vertical observation of deep convective showers with a microwave radiometer profiler.

- The MRR is extremely useful as a “rain detector” within the slant volume observed by ADMIRARI. Nevertheless it must be mentioned that because its noise level corresponds to rain rates in the range $0.04 - 0.08 \text{ mm hr}^{-1}$, it can lead to discontinuities at the transition from no-rain to rain conditions in the retrieved C_LWP . In addition, its sensitivity to solid precipitation can mislead the radiometer-based retrieval and cause it to mistake liquid for solid precipitation as for the case shown in Figure 6.1 from 06:45 to 07:00 UTC.

6.2. Long-term Statistical Analysis

This section presents a statistical analysis of the measurements between 23 August and 12 November 2008. The observations are first filtered by a rigorous quality control procedure, which also rejects possible antenna wetting and occurrences of signal interference. Periods with high probability for antenna wetting are detected during rainy periods by analysing the angular difference between the wind direction and the ADMIRARI observing azimuth: periods with angular differences below $\pm 20^\circ$ are filtered out. A bias correction procedure for PDs is deemed necessary despite the radiometer internal calibration systems. The procedure first isolates periods with very low R_LWP , which are expected to have negligible PD values. The corrections are then made mimicking the method used by Gaussiat, N., Hogan, R., and Illingworth, A. (2007) who took advantage of vertically pointing Lidar observations to discriminate between clouds and clear sky in order to avoid a bias in the cloud LWP retrieval. Here instead, the MRR observations are used to flag rain-free periods to avoid a R_LWP bias during dry spells. During such periods the PDs are set to zero, and adjacent rain-free periods are used to interpolate the bias during the rainy periods in between.

The time series of retrieved parameters during rainy spells is presented in Figure 6.3 together with observations of rain-rate from a co-located gauge to enable the characterization of precipitation conditions during the measuring period. A correlation between rainfall and R_LWP is apparent, but the difference between the radiometer and the gauge sampling volume makes a direct inter-comparison not very meaningful, as already noted by Marzano, F. S., Cimini, D., and Ware, R. (2005b). C_LWP exhibits a large variability with values sometimes exceeding 1.2 kg m^{-2} . R_LWP can be even higher with values up to 2.4 kg m^{-2} (e.g. at the end of September and on 11 November 2008). IWV is less variable during long rainy spells (e.g. the second half of September or in October) but reveals some abrupt changes during few short periods. Those jumps are not artefacts from the retrieval algorithm but rather indicate boundaries between rain periods since rain-free periods have been taken out. Air temperatures measured at 2 m (Figure 6.3 (a)) are well correlated with IWV, as expected.

The occurrence distribution of retrieved parameters (derived for all cases with $QI < 20$) is displayed in Figure 6.4 separately for non-precipitating clouds (class 1), precipitating clouds sensed from underneath the rain (class 2) and sensed from outside the rain (class 3). The quality criterion reduces the database by only 12%. A mean QI of 5.4 for class 2 indicates an overall good match between observations and simulations, but the large tail with values even above 15 indicates also that cases like the period from 04:06 to 04:36 UTC in Figure 6.1 are

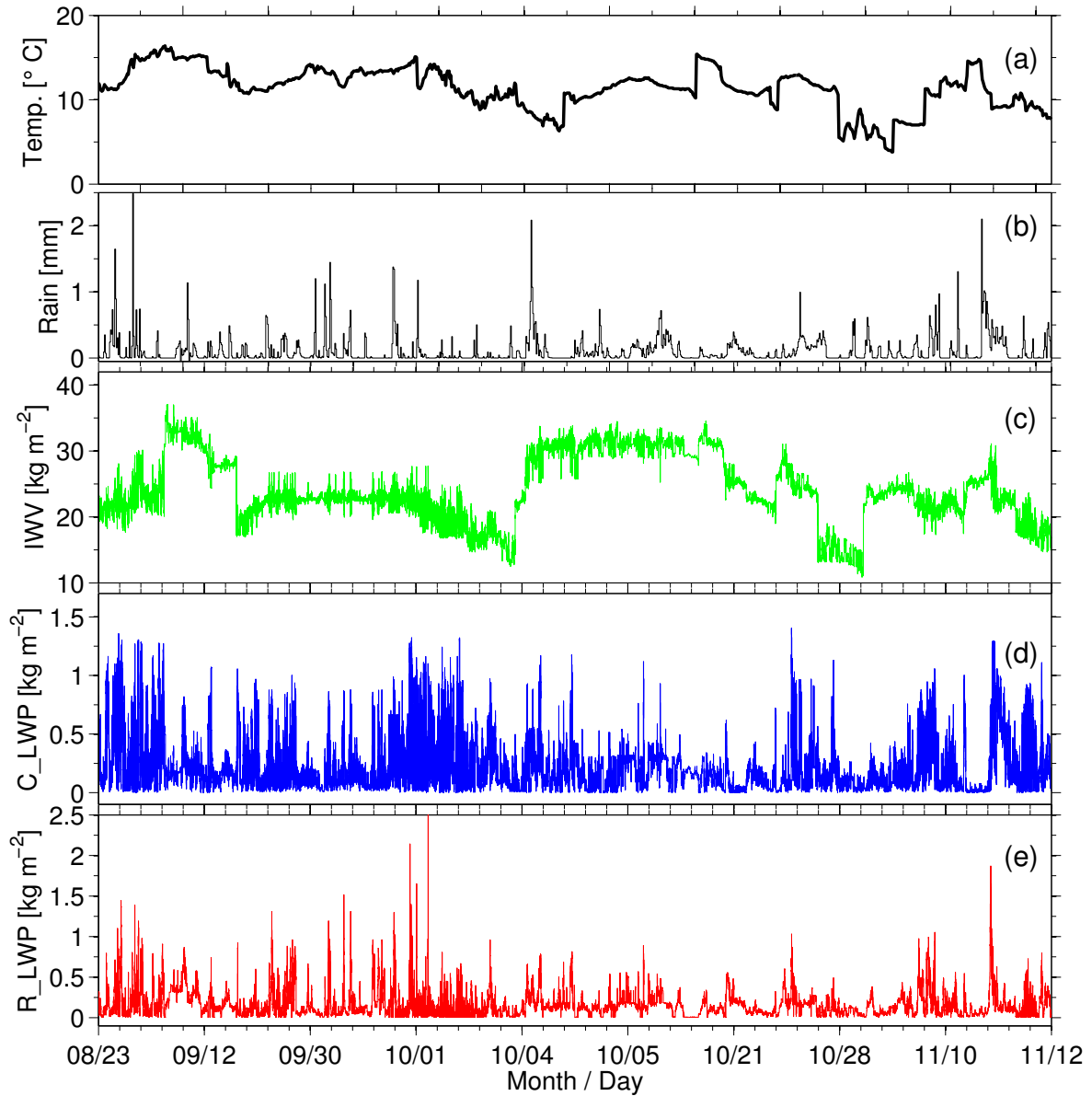


Figure 6.3.: Time series of (a) 2 m temperature and (b) rain amount accumulated at ten minute intervals from a rain gauge at CESAR; (c) retrieved IWV, (d) C_LWP and (e) R_LWP, from 23 August to 12 November 2008. Only rainy periods are shown.

rather frequent. Although $QI < 20$ indicates already a good match, the existence of retrievals with QI larger than 20 gives a clue on the limitations of this retrieval scheme. Sources of mismatching, which are not being taken into account in the forward model, are for instance the presence of a melting layer or non-uniform beam filling as it was shown by Battaglia, A., Saavedra, P., Morales, C., and Simmer, C. (2011). It is important, however, to note that poor retrieval performance (large QI) like the period 04:09 to 04:15 UTC in Figure 6.2 could also be explained by a $\sim 7^\circ$ antenna misalignment of the 10.7 GHz channels relative to the others, a shortcoming already noted by Battaglia, A., Saavedra, P., Simmer, C., and Rose, T. (2009). The current retrieval scheme takes this misalignment into account to some degree, by including in the database simulations of this proper misalignment (section 5 in Battaglia, A., Saavedra, P., Rose, T., and Simmer, C., 2010).

The IWV shows clearly a bimodal distribution for the three classes, with the peculiarity that for pure cloud retrievals (class 1) the lowest peak is shifted approximately 8 kg m^{-2} below the corresponding first peak at class 2. Since the pure cloud observations were selected either before or after the rain periods, this shift can be associated with an increase on water vapour caused by rain events. The PDFs for C_LWP and R_LWP are heavily skewed, as expected, with C_LWP holding a more populated tail than its rainy counterpart, especially for class 2, with an accumulation around 1.3 kg m^{-2} . On the other hand the cloud distribution for class 3 depicts fewer observations with low C_LWP values, which can be due to the slant observational geometry since when dealing with finite cloud structure, the radiometer is likely to sense a larger cloud volume from a certain distance (class 3) than from underneath the cloud (class 2). The PDF of R_LWP shows a more monotonically decreasing distribution with values ranging even till 1.3 kg m^{-2} for class 2, but only around 1.0 kg m^{-2} for the class 3.

Table 6.1 summarizes the mean of the Bayesian's standard deviation for the retrieved parameters of the three classes shown in Figure 6.4 at the three classes. The mean RMSE for cloud LWP is 43 g m^{-2} for rain-free cases; the accuracy is degraded to 144.5 g m^{-2} when cloud and rain LWP are retrieved simultaneously. It is observed that the RMSE presents a decrease of approximately 10% from class 2 to class 3 for both cloud and rain LWP, corroborated also by a reduction in QI . The RMSE for IWV increases from class 1 to class 3 only in the order of 20%.

Table 6.1.: Mean of the standard deviation for the retrieved variables according to three classifications: 1) non-precipitating clouds, 2) radiometer inside the rain cloud, and 3) radiometer outside the rain cloud. The last two rows indicate the mean QI and the number of observations for every class.

RMSE	Class 1: Pure Cloud	Class 2: Inside rain	Class 3: Outside rain
IWV [kg m^{-2}]	1.31	1.54	1.58
C_LWP [g m^{-2}]	43.9	144.5	132.4
R_LWP [g m^{-2}]	–	52.1	46.5
QI	2.5	5.4	3.9
Numb. Obs.	78393	153400	28768

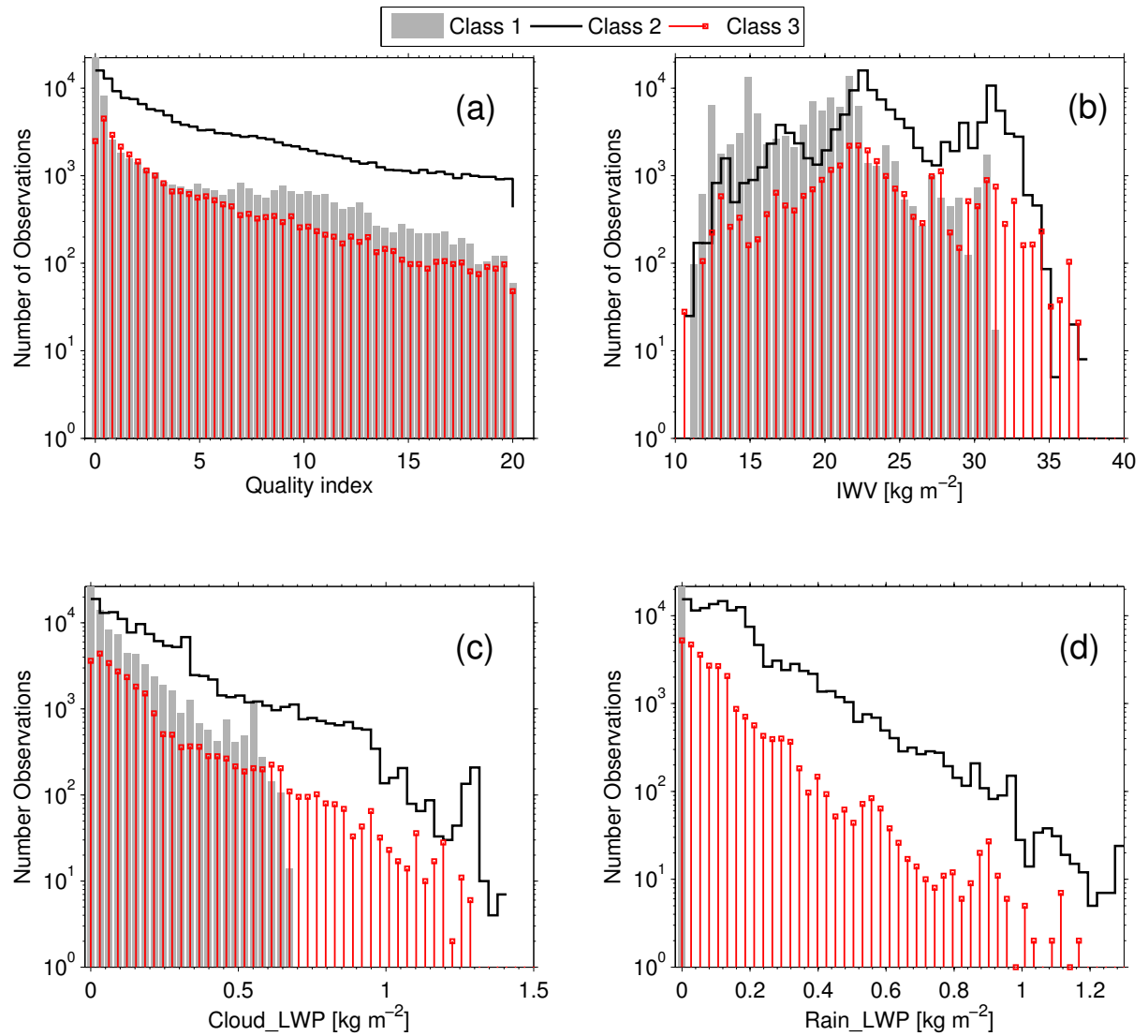


Figure 6.4.: Histograms of (a) quality index QI , retrieved (b) IWV , (c) C_LWP and (d) R_LWP from 23 August to 12 November 2008. Statistics for pure cloud (class 1: gray area), radiometer inside the rain cell (class 2: solid black line) and outside the rain cell (class 3: red line-dot columns) are presented separately as described in the text.

From Figure 6.2 and from the whole analysed period it is observed that, during rainy periods, the C_LWP is retrieved with lower accuracy compared with its rain counterpart. The retrieved cloud RMSE by ADMIRARI are, however, smaller than the uncertainties values quoted by Matrosov, S. (2009a, Fig. 14) as typical for stratiform rain systems retrieved from a dual-frequency radar approach (i.e. cloud LWP uncertainties ranging from $\sim 100 \text{ g m}^{-2}$ to $\sim 600 \text{ g m}^{-2}$ for rain rates in the interval from 1 to 10 mm h^{-1} , respectively).

7. Discussion on LWP Partition

Abstract

In this chapter the results regarding the retrieved cloud and rain LWP partition are discussed in contrast with other works based on retrievals from space-borne instruments. Moreover a largely scattered distribution of cloud versus rain LWP is reported as a first result of this kind of observations from a ground-based instrument, along with their main characteristics. Finally, the effect of the slant observational geometry on the retrieved quantities is studied by tracing back the corresponding columnar rain and cloud LWP to every slant retrieval.

7.1. Observed Cloud/Rain Partition

The first cloud water/rain water partition obtained by ADMIRARI has been reported by Saavedra, P., Battaglia, A., and Simmer, C. (2012b) and it is presented in figure 7.1 (re-normalized to vertical column) for precipitating clouds (class 2 and class 3 merged together). A large range of C_LWP for low rain contents is observed, with C_LWP ranging from 0 to $\sim 1 \text{ kg m}^{-2}$ while the R_LWP stays $< 0.06 \text{ kg m}^{-2}$ (every pixel represents a bin of $\sim 0.02 \text{ kg m}^{-2}$), which can be attributed to observations corresponding to start/cease of precipitation as well as observation from outside the rain cell (class 3) since the slant radiometer FOV favours the sensing of the higher part of the precipitating cloud and catching only a small part of the rain component. In addition it sees a clear tendency on the cloud versus rain distribution to follow the 2:1 line until approximately 0.4 kg m^{-2} for either cloud and rain LWP, then the distribution spreads out with C_LWP reaching as high as 1.4 kg m^{-2} , but that feature is not equally followed by the R_LWP.

The C_LWP seems to level off at very high rain water contents. No cloud LWP above 1 kg m^{-2} is observed with rain counterparts less than 0.10 kg m^{-2} . On the contrary it is feasible to find tens of observations with very large R_LWP ($> 1.5 \text{ kg m}^{-2}$) but low C_LWP ($< 0.2 \text{ kg m}^{-2}$) counterparts. This however can be an artefact of the *a priori* database which might not contain events with high cloud and low rain LWP.

Figure 7.1 provides a first overview of the statistics of cloud versus rain water for precipitating clouds attainable by a ground-based instrument, a product potentially extremely useful in the physical validation of passive microwave satellite rainfall retrievals, which inherently assume a cloud/rain partitioning. Different algorithms attributes different weights to the cloud and rain component and this is the cause of large discrepancies in the different precipitation product. For instance, Hilburn, K. and Wentz, F. (2008) compared the Unified Microwave Ocean Retrieval Algorithm (UMORA) results with the cloud water/rain water relationship obtained from the Goddard Profiling Algorithm (GPROF, Kummerow, C., Hong, Y., et al. (2001)) on a pixel-to-pixel basis (see their Fig. 11). The squared correlation coefficient between UMORA and GPROF for total liquid water is $R^2 = 0.62$, and for surface rain rate 0.56. GPROF attributes more water to precipitation and less to cloud water compared to UMORA. Typically GPROF partitions $0.5 - 1.0 \text{ kg m}^{-2}$ less cloud water for a given precipitation water

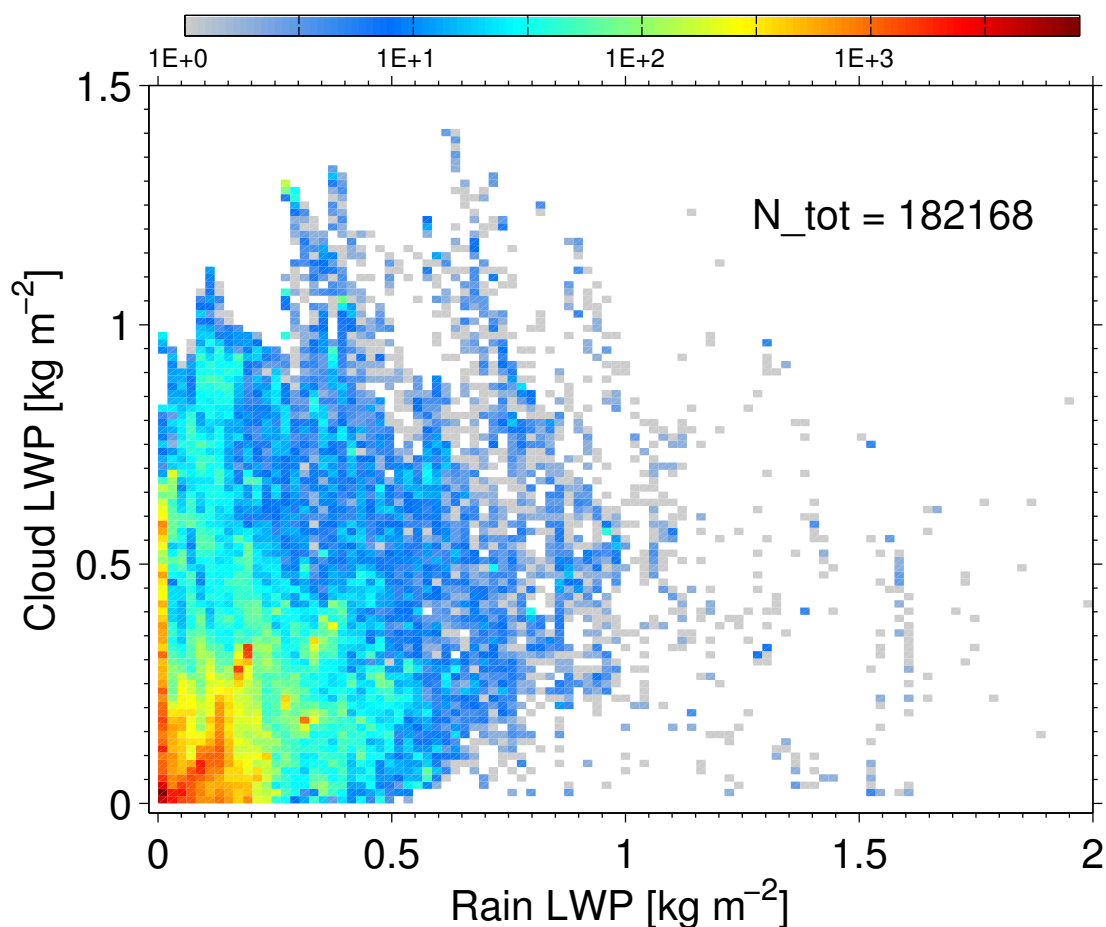


Figure 7.1.: Retrieved partition for Cloud and Rain LWP during the whole observation period (class 2). The color bar indicates the number of observations in logarithmic scale.

than UMORA.

It is obvious that our retrieved dataset corresponds to ground-based observations for a specific location and a limited period (representative of a Mid-latitude Autumn precipitation) with high temporal and spatial resolution, while satellite products are related to vastly different sensed volumes and are applicable to the global scale over ocean. Despite these preliminary remarks, it is here interesting to briefly discuss how to establish a paradigm in ground validation field campaigns for validating the physical assumptions underpinning satellite retrievals.

Hilburn, K. and Wentz, F. (2008) reported satellite derived relationships between columnar cloud and rain water over oceans for tropical observation relying on UMORA. Based on the work by Wentz, F. and Spencer, R. (1998) on northeaster Pacific extra-tropical cyclones the following assumptions are made:

- 1.) Rain is initiated at $C_LWP=0.180\text{kg m}^{-2}$.
- 2.) C_LWP increases with R_LWP .
- 3.) The cloud versus rain relationship levels off at high R_LWP , with C_LWP reaching a maximum value between 1 and 2kg m^{-2} .

The following are our respective findings.

- 1.) For the EUCAARI ADMIRARI dataset, clouds can support a C_LWP (re-normalized to vertical observations) larger than 0.55 kg m^{-2} before a rain components develops (see Figure 6.4, panel c, class 1). Our findings are in line with other ground-based microwave observations like those documented by Karstens, U., Simmer, C., and Ruprecht, E. (1994) who deduced a threshold C_LWP of about 0.5 kg m^{-2} over the North Sea or those reported by Crewell, S., Simmer, C., et al. (2004) over the same CESAR site. On the other hand rain is observed even at cloud LWPs below 0.55 kg m^{-2} (see e.g. Figure 6.2, period from 06:39 to 06:51 UTC). A large population of the cloud versus rain distribution depicts a tendency to follow the 2:1 line, interestingly similar observation is reported by Lebsock, M., L'Ecuyer, T., and Stephens, G. (2011) for precipitating shallow marine clouds with occurrence of rain at very low cloud water paths even below 200 g m^{-2} .
- 2.) ADMIRARI results do not seem to favour a well defined functional relationship between C_LWP and R_LWP as obtained by UMORA; they resemble more the GPROF distribution. The GPROF cloud/rain partitioning displays a branch of cloud LWP with maximum values of $\sim 1.0 \text{ kg m}^{-2}$ starting at very low rain contents e.g. $R_LWP < 0.3 \text{ kg m}^{-2}$, which agrees quite well with the ADMIRARI results; here maximum cloud values of $\sim 1.1 \text{ kg m}^{-2}$ are observed for R_LWP below 0.3 kg m^{-2} . This however may simple be due to the fact of using similar CRM simulations to build up the *a priori* database.
- 3.) The maximum C_LWP for a given R_LWP tends to level-off at $\sim 1.4 \text{ kg m}^{-2}$ while the rain LWP still increases.

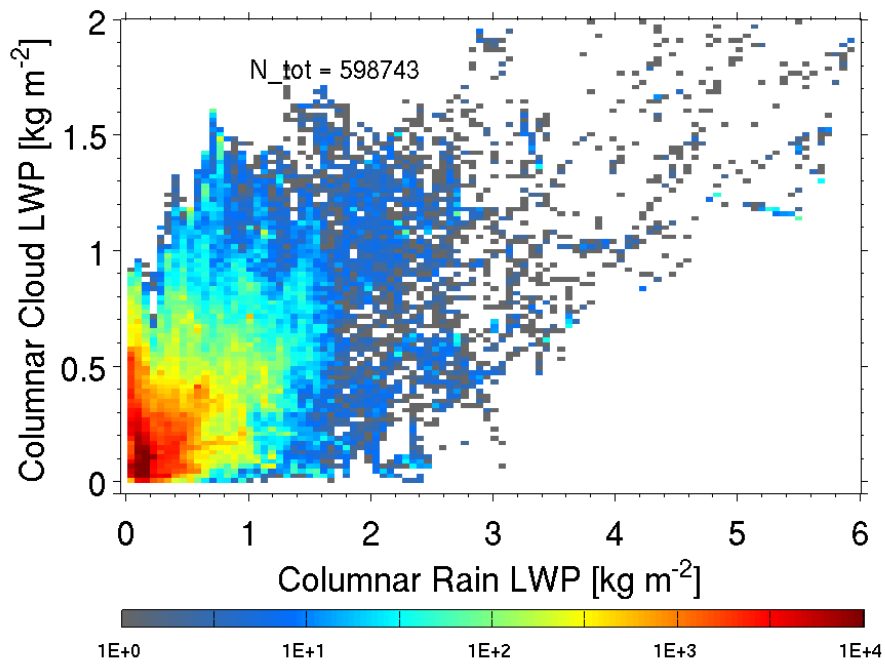
More conclusive assessments of the satellite inherent assumptions could be drawn only by adopting long term field campaign strategies involving ADMIRARI-like measurements and targeting specific precipitation regimes. The effect of the mismatch between space and ground-based sensed volumes could be reduced by properly temporally averaging the ground-based retrieved products.

7.2. Effects on the Retrievals Due to the Geometry of Observation

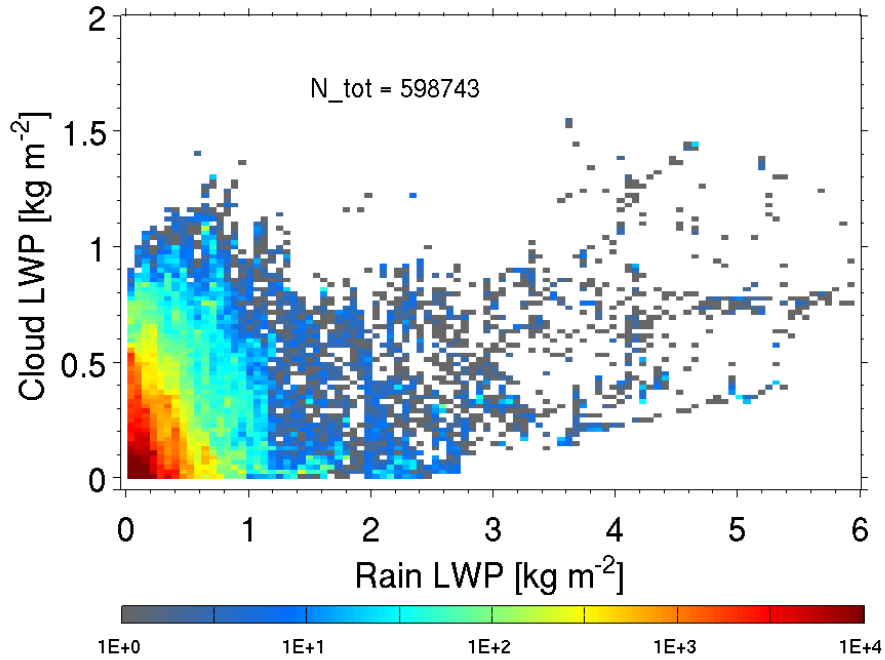
Traditionally ground-based radiometers mainly perform vertical observations, nevertheless in the last decade their scanning capabilities have been improved e.g. (Kneifel, S., Crewell, S., Löhnert, U., and Schween, J., 2009; Mätzler, C. and Morland, J., 2008, 2009; Morland, J., 2002). However standard radiometers which only retrieve [Integrated Water Vapour \(IWV\)](#) and [Cloud Liquid Water Path \(C_LWP\)](#) might still have certain representativeness by reporting the results as projected to the vertical column. This is particularly applied to water vapour which has not large spatial variability.

In the case of ADMIRARI its slant retrievals cannot be expected to have a representativeness for the vertical column, since cloud and mainly rain present significant spatial variability. For reference reasons the results in previous sections have been normalized to vertical (see 7), however it is important to keep in mind that the retrievals are only representative of the slant observations.

To highlight this, in addition to slant retrievals for slant cloud, rain LWP and IWV, their corresponding vertical counterparts are traced back from the synthetic brightness temperature following the same Bayesian technique as in chapter 4. In fact within the Bayesian framework



(a) Vertical



(b) Slant

Figure 7.2.: Cloud versus Rain LWP distribution for vertical (top) and slant (bottom) retrievals.

it is possible to compare the retrieved slant parameters with their vertical counterpart to whom the retrievals come from. Figure 7.2 is the same as figure 7.1, but for a larger dataset (from May 29th to December 9th, 2009) at MIUB in Bonn and at 30° slant. In this case however the retrievals are separated in two sets shown in figure 7.2(a) and 7.2(b) for the cloud versus rain distribution for vertical and slant retrievals respectively.

The results depict some interesting features, for instance for the slant cloud versus rain LWP distribution (figure 7.2(b)) most of the points seem to be clustered in a region shaped as a right-triangle with 1 kg m^{-2} rain LWP base and $\sim 0.6 \text{ kg m}^{-2}$ altitude (red-orange region), with the hypotenuse showing a displacement as the number of observation drops (from red, yellow, clear-green, to blue and gray in the color table) driven by the increase of cloud and rain water content. That triangular shape is absolutely absent in the columnar retrievals (figure 7.2(a)), rather a branch-shape distribution is found.

The slant cloud component is confined basically below 1.3 kg m^{-2} while the rain component extends largely to same magnitudes as its columnar counterpart (figure 7.2(a)). Regarding the departure of cloud water content from the zero level respect to the increasing of rain water content, for slant retrievals the clouds present near zero values till even 2.3 kg m^{-2} rain LWP, while its columnar counterpart shows already a significant departure at 1 kg m^{-2} , with almost no cloud LWP observed for 2.3 kg m^{-2} rain LWP or larger.

It is interesting to note that the cloud-rain columnar retrievals resembles better the distribution for the slant retrievals from Cabauw Experimental Site for Atmospheric Research (CESAR) observations discussed in previous section (7) and summarized in figure 7.1. In other words, the distribution of cloud-rain slant retrievals from CESAR does not mimic the triangular shape of the slant retrievals from Bonn in figure 7.2(b). That may be due to the different climatologies and the fact that the MIUB retrievals include measurements ranging from middle spring, through summer till early winter, which also explain the extreme values on rain water content in figure 7.2. It might be stressed the fact that those datasets comes from dissimilar measurement locations: while CESAR is a countryside flat open area, MIUB is located in an urban environment with obvious differences in the boundary layer-affected processes which may change the wind conditions in the lowest layers.

From figures 7.2 it is obvious that the distribution of rain/cloud partition as retrieved from the slant observations presents large differences respect to its corresponding vertical (columnar) retrievals, both in magnitude and shape. However in order to look at the relationship between rain and cloud more accurately, the ratio R_LWP/C_LWP is compared for both datasets. This is done based in a quantile-quantile plot (qq-plot) which has the following advantages: qq-plot can easily highlight if both datasets come from the same distribution independently of the magnitude of the variables; and the rain/cloud ratio shows if both variables are equally affected by the geometrical effect of the observational configuration.

Figure 7.3 shows the qq-plot of the rain/cloud ratios for slant versus columnar, the 1:1 dashed black line is a reference for an exact match of both ratios. The columnar ratio ranges from approximately 0.3×10^{-2} to 10^2 while the slant ratio does from 0.3×10^{-2} to 3×10^2 . The two red circles indicate the position for the 1st and 3rd quantiles, and the points laying between them comprise the 50% of the dataset. The red-dashed line indicates whether or not the two datasets follow the same distribution, in this case the blue-crosses lay almost parallel to the red-dashed line. For low ratios (until ~ 1) both shows the same values, then the slant ratio starts to depart from the 1 to 1 relationship. Above the the second quantile (median) the slant ratio clearly develops higher values with respect to the columnar ratios.

Thus 50% of the dataset have the same distribution but with different magnitudes mainly

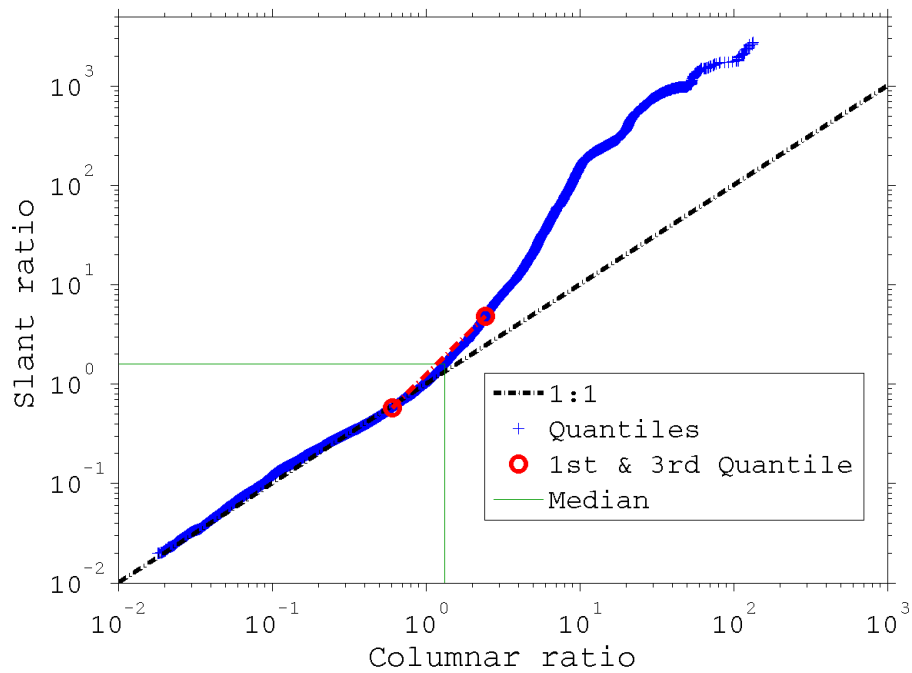


Figure 7.3.: Quantile-Quantile plot for the rain/cloud ratio to compare the distribution of columnar (x-axis) versus slant (y-axis) retrievals.

above the median. The columnar ratio has 0.6068, 1.3313 and 2.4338 as 1st, 2nd and 3rd quantiles respectively, while the slant ratio has 0.5798, 1.5904 and 4.7926 for its 1st, 2nd and 3rd quantile. In summary the rain/cloud ratio is larger when large amounts of rain water is observed while for cases with low rain water and/or large amounts of cloud water the ratios are similar.

8. Validation for Rain Water Content

Abstract

The present chapter summarize the effort to validate one of ADMIRARI's retrieved parameters i.e. the rain LWP. Two independent sensors have been utilized for validation, namely a co-located micro-rain-radar and a dual-polarized weather radar. Moreover different methods have been applied to each sensor in order to estimate the rain LWP. In the case of the micro-rain-radar a DSD needs to be assumed and the obtained retrievals depends strongly on this assumption, giving the best correlation with ADMIRARI retrievals when thunderstorm DSD is considered. On the case of the dual-pol radar, it has been found a good correlation between both instruments, specially for large LWP values, but with a slight bias towards the ADMIRARI retrievals.

8.1. Retrievals by Two Active Sensors

Validation is pursued in order to verify the accuracy of retrievals. However in case of a novel instrument as [ADMIRARI](#) it becomes a difficult task since there is not any other instrument or technique that allows to estimate the rain, cloud LWP and integrated water vapour simultaneously during precipitation.

In this section the results from two approaches to validate the [Rain Liquid Water Path \(R_LWP\)](#) are discussed. Rain LWP has been estimated by distinct instruments, namely the [Micro Rain Radar \(MRR\)](#) and the [Jülich X-band Polarimetric Weather Radar \(JuXPOL\)](#). The procedures for both approaches have been presented in extended detail by Saavedra, P., Battaglia, A., and Simmer, C., [2012b](#) and Saavedra, P., Battaglia, A., Ryzhkov, A., and Simmer, C., [2013](#) respectively, and it is summarized in appendix [A](#).

8.1.1. MRR Approach

For the first approach the co-located [MRR](#) has been used, which has the advantage of measuring with an optimal radar-radiometer co-location set-up and good temporal resolution (see section [3.2.1](#), chapter [3](#) for the instrument description). On the other hand the MRR measures only reflectivity and therefore parameters for the [DSD](#) must be assumed. In that sense four exponential DSD parameters have been used and the retrieved [R_LWP](#) results depends strongly on these assumptions (Saavedra, P., Battaglia, A., and Simmer, C., [2012b](#)).

Table [8.1](#) and figure [A.1](#) shows the results for the MRR's rain LWP, as a function of the four DSDs, compared against the ADMIRARI retrievals. According to those results, it seems that the radiometer retrievals trend to favour the results with DSDs assumed for heavy rain and thunderstorm with [RMSEs](#) of 187.6 and 167.2 gm^{-2} respectively. While DSDs representing to a Marshall-Palmer distribution and light-rain produce larger biases. This is specially stressed when light-rain is assumed with a -268.0 gm^{-2} bias indicating an overestimation by the MRR retrieval (see table [8.1](#)). Important to note is the fact that the unmatched beam-widths of

radiometer and radar has not been taken into account, this could explain the biases as it will be shown in the following for the second approach.

Table 8.1.: Results for R_LWP Radiometer-MRR comparison assuming four different intercept parameter for an exponential DSD: Light rain (L-R), Marshall-Palmer (M-P), Heavy rain (H-R) and Thunderstorm (TH-S). Results normalized to zenith.

	L-R	M-P	H-R	TH-S
$N_0 \times 10^3 \text{ [m}^{-3}\text{mm}^{-1}\text{]}$	32.0	8.0	4.0	1.4
RMSE [g m^{-2}]	484.9	241.5	187.6	167.2
BIAS [g m^{-2}]	-268.0	-85.4	-30.7	22.7

8.1.2. Dual-Polarization Approach

For the second approach the [Jülich X-band Polarimetric Weather Radar \(JuXPoI\)](#) has been used in synergy with ADMIRARI at the [Jülich Forschung Zentrum \(JFZ\)](#) in Germany during spring 2013. The employed technique to estimate R_LWP is based on the ZPHI method (Testud, J., Le Bouar, E., Obligis, E., and Ali-Mehenni, M., 2000) for [Quantitative Precipitation Estimation \(QPE\)](#). The method corrects the radar reflectivity from attenuation due to rain, and thereof calculates rain rates from low elevation [PPI](#) radar scans.

This approach has the advantage of exploiting the polarimetry capabilities of [JuXPoI](#) and therefore reduce uncertainties, but on the contrary an important disadvantage is the poor synergy in temporal resolution and instruments co-location.

The observation's set up and the retrieval technique is explained in detail by Saavedra, P., Battaglia, A., Ryzhkov, A., and Simmer, C. (2013) and summarized in appendix A, section A.3. There the parameters and equations have been developed and adapted from the classical ZPHI method to the requirements for the specific ADMIRARI-RADAR synergy.

A first point to point comparison (RADAR-RADIOMETER) R_LWP is shown in figure A.7 for slant observations made at 30° elevation. From A.3, after normalized to zenith, a reasonable [RMSE](#) of 0.6 kg m^{-2} and a bias of -0.150 kg m^{-2} has been found. Two features to note: first, widespread scattered points for retrievals below $\sim 0.5 \text{ kg m}^{-2}$, and second a clear overestimation of ADMIRARI's retrievals for high liquid water content. The first was explained mainly because the ZPHI method performs better when rain produces significant attenuation and polarization. The second, it was thought to be attributed to the contribution of the melting layer on the radiometer's columnar observation.

Recently, improvements have been incorporated on the radar's retrieval and the matching of radiometer's [FOV](#) (Saavedra, P., Battaglia, A., Ryzhkov, A., and Simmer, C., 2014b). Mainly a problem related to the unequal instruments' beam-width has been found to be responsible for artificial biases. The experiment's configuration allowed the radar ($\sim 0.5^\circ$ beam-width) to scan over the radiometer's position with only one [RHI](#), which is inefficient to cover the complete radiometer's [FOV](#) ($\sim 6^\circ$). Thus, there is a sector which is not being swept by the radar's scan, in consequence the reconstruction of the radiometer's sight from the radar observation is intrinsically underestimated. That issue has not been taken into account in figure 8.1 and may explain the bias favourable to the radiometer's retrievals.

In the present work, in order to account for the issue mentioned in the previous paragraph, the following procedure has been implemented. Based on geometrical considerations a factor

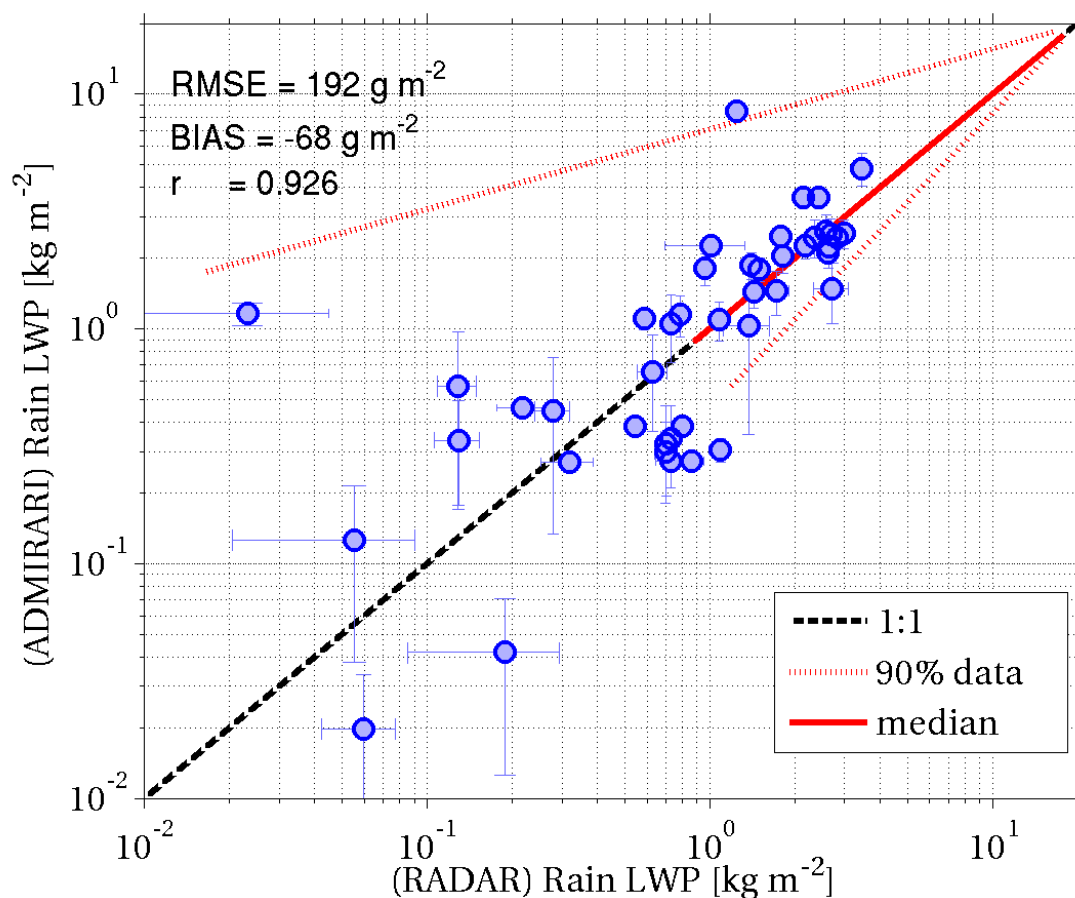


Figure 8.1.: Independent retrievals for Rain LWP as observed by ADMIRARI and a X-band Radar. The vertical errorbars indicate the Bayesian 2σ , while the horizontal errorbars represent the variance of radar observations along the radiometer's FOV. The black-dashed line represents a 1:1 relationship, the solid red line the median of the distribution of the point-to-point difference, while the upper and lower dashed-dotted-red lines holds the 90% of the data.

has been defined for every radar's RHI elevation angle. The factor comprises of the volume percentage of radiometer's FOV which is not being covered by the radar scan. The average and standard deviation of radar range resolved observations, that intersect the radiometer's sight, are calculated and multiplied by this geometrical factor. Note that the factor can represent either an over or underestimation depending on the geometry of observation.

Figure 8.1 summarizes the new results based on the consideration for a geometrical factor (as described in previous paragraph) to take into account the radiometer's larger beam-width. Moreover the results have been normalized to zenith and outliers have been dismissed in the computation of RMSE and bias by rejecting points outside the 95% confidence level. Thus, the following can be noted:

1. clearly the bias has been reduced significantly with a new value of -0.068 kg m^{-2} and RMSE of 0.192 kg m^{-2} ,
2. the scattered points below $\sim 0.5 \text{ kg m}^{-2}$ R_LWP is significantly reduced,

3. the possible bias effect due to melting layer becomes less evident or very subtle.

The last point seems to agree with similar conclusions found by Saavedra, P., Battaglia, A., and Simmer, C. (2012a, figure 2) regarding the contribution of melting layer to the radiometer’s signature at the three ADMIRARI’s frequencies, with the 10.7GHz frequency found to be the least affected.

Additionally figure 8.1 includes landmarks for the distribution of R_LWP difference i.e. RADAR-ADMIRARI, with dashed-dotted red lines to highlight the region where 90% of the data is constrained. The median (solid red line), with a value of 0.002kg m^{-2} , is practically on the 1:1 relationship (dashed black line).

Note that in figure 8.1 the largest dispersion of points occurs at low rain water contents, therefore in order to quantify its effects on the statistics for $RMSE$, $BIAS$ and correlation coefficient r , sub-sets of R_LWP minimum threshold are treated separately. The results are summarized in table 8.2 with sub-sets selected for $R_LWP \geq 0.0\text{kg m}^{-2}$ and thereafter increasing the minimum R_LWP in intervals of 0.5kg m^{-2} . The results show that the $BIAS$ has a increase of $\sim 55\%$ after extracting R_LWP below 0.5kg m^{-2} , thereafter it basically stays constant and negative (overestimation by ADMIRARI) for all sub-sets. The $RMSE$ presents a moderate increase as the minimum R_LWP is incremented from 0.0 to 1.5kg m^{-2} .

Table 8.2.: Results for the radar-radiometer comparison as a function of the minimum rain LWP considered. Values are normalized to zenith.

R_LWP_{\min} [kg m^{-2}]	0.0	0.50	1.00	1.50
$RMSE$ [g m^{-2}]	192	249	256	260
$BIAS$ [g m^{-2}]	-68	-105	-104	-100
Corr. coeff. r	0.926	0.853	0.817	0.616

Although this comparison highlights the feasibility of retrieving [Rain Liquid Water Path \(\$R_LWP\$ \)](#) by two totally different methods and independent observations by distinct sensors, it must be noted that the statistics are certainly not significant. The analysis discussed in this section is based only on a case study with 168 synergistic observations by both instruments. In order to improve this validation approach more cases must be included and thereafter have more reliable results. That implies a carefully selection of cases which are free of artefacts for both instruments that usually affect the analysis e.g. antenna wetting, clutter contamination, temporal synchronization or spatial matching among others.

9. Conclusions

The present document summarizes a collection of experimental work, data analysis, simulation studies and mainly the development of a retrieval technique featured with the [ADvanced MICrowave RAdiometer for Rain Identification \(ADMIRARI\)](#), a novel triple-frequency (10.7, 21.0 and 36.5GHz) dual-polarized (H & V) passive radiometer from the [Meteorological Institute, University of Bonn \(MIUB\)](#). From the present work the following remarks and conclusions can be listed:

Instrumentation: In chapter 3 all features of the microwave radiometer has been introduced. As it was theorized by Czekala, H., Crewell, S., Simmer, C., and Thiele, A., 2001 it has been shown the radiometer's unique capabilities to make the instrument able to sense the polarization signature produced by oblate raindrops as well as the un-polarized signal from cloud droplets. Moreover the multi-frequency attribute has led to a deeper understanding in the interpretation of the polarization signal.

The radiometer's performance quality has been analysed and shown that its calibration procedures and the system stability ensures the reliability of brightness temperature measurements in a short as well as long-term basis (chapter 3, section 3.1.1.1). Issues related with some of the radiometer original specifications have been identified and corrected/mitigated, amongst them the beam-width, band-width, channels alignment, calibration, polarization biases, antenna wetting, etc. were properly worked out and summarized in chapter 3, sections 3.1.2.

The benefits of adding ancillary active instrumentation, in addition to the passive radiometer, is put into consideration. With the inclusion of a [Micro Rain Radar \(MRR\)](#) (chapter 3, section 3.2.1) the observation of precipitation is extended to range resolving features to the same radiometer's sight after an adaptation to slant configuration, (chapter 3, section 3.2.1.2). Similarly a cloud [LIDAR](#) has been utilized to provide an estimation of the cloud base height in cases with no precipitation and, under certain conditions, even during light rain or snow cases (chapter 3, section 3.2.2). Thus the standard ADMIRARI's dataset, which comprises of radiometer's brightness temperatures and polarization difference, has been enriched with radar reflectivity profiles, cloud base height and [LIDAR](#) backscattering factor with time resolutions of 2, 10 and 15 seconds respectively. An example of the synergistic measurements provided by the suit of instruments is depicted in figure 3.20.

Retrievals: The radiometer ADMIRARI was conceived to simultaneously retrieve integrated water vapour and [Liquid Water Path \(LWP\)](#). Being the partition of [LWP](#) into its rain and cloud components the main objective of the apparatus. Due to its multi-frequency feature, the radiometer has the potential to separate the effects introduced by the influences of different drop size distributions ([DSD](#)), and the non-Rayleigh scattering signature exhibited by large raindrops, which are discussed in detail in chapter 4 and by Battaglia, A., Saavedra, P., Rose, T., and Simmer, C. (2010).

The first observations obtained by ADMIRARI and their subsequent interpretation based on simulations were published by Battaglia, A., Saavedra, P., Simmer, C., and Rose, T. (2009), and extended to a first retrieval approach by Battaglia, A., Saavedra, P., Rose, T., and Simmer, C. (2010).

As already noticed by Czekala, H., Crewell, S., Hornbostel, A., et al., 2001b our observations have shown that for convective precipitation the corresponding microwave signature cannot be simulated with only one-dimensional radiative transfer models. Simulations obtained by solving the 3-D radiative transfer equation according to the backward Monte Carlo technique (Battaglia, A., Davis, C., Emde, C., and Simmer, C., 2007) were found to be in good correspondence with a wide range of observations at the three ADMIRARI frequencies (chapter 4, section 4.3). The study published by 2011, based on ADMIRARI observations of tropical rain, also pinpointed at the necessity to include three dimensional effects in the radiometric simulation scheme in order to explain the whole dynamics of polarization signature. This is specially true with strong convective rain that enhances issues like non-uniform beam filling effect, side leakage and position of the observing system relative to the rain cell.

The above mentioned 3-D effects hamper the application of a straightforward retrieval approach as suggested by (Czekala, H., Crewell, S., Simmer, C., and Thiele, A., 2001) based only on mono-frequency system (chapter 4, section 4.1). Therefore an inversion method based on Bayesian theory was adopted to take advantage of many realizations of the Goddard Cumulus Ensemble (GCE) CRM to establish a prior probability density function of rainfall profiles. Chapter 4 presents the fundamentals for the Bayesian technique to estimated of C_{LWP} , R_{LWP} and IWV simultaneously.

A pure-simulation-based retrieval sensitivity study (presented in chapter 4 section 4.4) confirms the suitability of retrieving integrated cloud water, rain water content and water vapour from ADMIRARI's synthetic measurements. The additional constrain for the rain water content's distribution along the line of sight provided by the co-located MRR improves the accuracy of the retrieval by confining the number of profiles entering the Bayesian average to structurally comparable profiles. It has been found that for cases with very low water content the ADMIRARI approach can produce large uncertainties when distinguishing the cloud and rain components from the total water content. The incorporation of the radar reflectivity profiles into the retrieval technique has been evaluated in the sensitivity study, showing large improvement in the retrieval uncertainties, specially for the cases with low rain/cloud LWP. This approach has shown the way towards a synergistic retrieval technique combining active and passive measurements, but an incorporation of the MRR reflectivity profiles needs more detailed studies mainly due to FOV mismatching, attenuation due to rain and MRR calibration. Those are the reasons why only geometrical constraints have been included in the present work.

The forward modelling used to construct the retrieval database is capable of reproducing the observed brightness temperatures and polarization differences within the model and instrument errors (chapter 4, section 4.3). The database in conjunction with the Bayesian technique, when applied to the measurements, retrieves the rain, cloud and water vapour integrated parameters with average errors of about 50 g m^{-2} , 150 g m^{-2} and 1.6 kg m^{-2} , respectively. Clearly the main uncertainties lay on the cloud component with its RMSE significantly higher than typical values obtained by passive microwave retrievals for non-precipitating clouds ($\sim 20\text{--}40 \text{ g m}^{-2}$, Löhnert, U. and Crewell, S. (2003)). However no reference on typical cloud retrieval uncertainties for precipitating cases are reported so far.

Rain and cloud partition: In presence of low [Liquid Water Path \(LWP\)](#) the partitioning between cloud and rain is prone to large errors. Below 450 gm^{-2} only the total LWP can be retrieved properly with RMSE around 40 gm^{-2} . This mirrors the obvious fact that small rain contents are associated with almost spherical raindrops which do not produce polarized signals and diminish the ADMIRARI potential. When the radar reflectivity information is utilized the RMSE for total LWP can be reduced to even 13 gm^{-2} (chapter 6, section 7).

According to the observations by ADMIRARI, no trivial relationship has been established regarding the partitioning of [LWP](#) into its rain and cloud components (chapter 6, section 7). This contrasting with studies by Hilburn, K. and Wentz, F., 2008; O'Dell, C., Wentz, F., and Bennartz, R., 2008 who present a well defined relationship between cloud and rain water content retrieved from space-borne observations. Nevertheless the rain/cloud LWP distribution obtained in the present work resembles better the results obtained by the GPROF algorithm (Kummerow, C., Hong, Y., et al., 2001). Besides, it has been found that the ADMIRARI's set-up (slant observations) produces retrievals that might significantly depart from their equivalent columnar values (figure 7.2(a) versus 7.2(b)), noting that the columnar values are the variables that standard ground-based and space-borne radiometers retrieve. Yet, interestingly the distribution for slant and columnar rain/cloud-LWP ratio presents similar behaviour for values between approximately 0.7 to 3 kg m^{-2} (chapter 6, section 7.2, figure 7.3).

Validation: As an attempt on the validation for the ADMIRARI retrievals, two independent methods to obtain the rain LWP from two different radars have been developed:

- The first involves the co-located [MRR](#), and the method minimizes the measured-simulated reflectivity to estimate the rain LWP. Results from the radar-radiometer comparison present a typical RMSE of 484.9, 241.5, 187.6 and 167.2 gm^{-2} as function of assumed [DSD](#) for light-rain, Marshall-Palmer, heavy-rain and thunderstorm respectively (chapter 6, section 8, table 8.1).
- The second approach takes advantage of the [JuXPoI](#) polarimetry capabilities. The ZPHI method for [QPE](#) has been extended and adapted to estimate rain water content from rain attenuation (Saavedra, P., Battaglia, A., Ryzhkov, A., and Simmer, C., 2013). Based on one case study, a radar-radiometer correlation of $r = 0.926$ has been found with a [RMSE](#) and [BIAS](#) of 192 and -68 gm^{-2} respectively within a 95% confidence level (chapter 6, section 8, figure 8.1).

This however permits only the validation for the [R_LWP](#), since no other technique or instrument is currently available to validate the cloud component during precipitation.

Outlook for future studies: Out of the long-term data collection and posterior analysis, only 12% of the data are dismissed due to high residuals. This indicates that there is still room for improving the forward model, e.g. by accounting for non-uniform beam-filling effects, by including full horizontal spatial variability of the cloud structure and by considering a realistic melting layer. In order to address the latter issue, an approach to estimate the attenuation due to melting layer at ADMIRARI's frequencies has been attempted by Saavedra, P., Battaglia, A., and Simmer, C. (2012a). Based on measurements from the [Light Precipitation and Verification Experiment \(LPVEx\)](#) (Petersen, W., L'Ecuyer, T., and Moisseev, D., 2011), results suggest that the 36.5GHz channel is the most affected by attenuation by melting particles, followed in

magnitude by the 21.0GHz channel and with a subtle effect on the 10.7GHz channel. Further studies, however, needs to be done on precipitating systems with very low freezing levels since they are ideal to isolate the multi-frequency microwave signatures of melting particles and use that information for electromagnetic and microphysical models (Szyrmer, W. and Zawadzki, I., 1999).

In addition, the construction of better physically constrained *a priori* data set needs to be pursued by mimicking the work of Kummerow, C., Ringerud, S., Crook, J., Randel, D., and Berg, W., 2001 for the passive microwave retrievals over ocean using the operational TRMM precipitation radar. That could allow to reduce the uncertainties in the assumptions about the *a priori* introduced by the climatological CRM simulations. In terms of the instrumentation, a mandatory step is the improvement regarding the rapid scan capabilities, thereof fine synergy of active-passive observations may be achieved. Hence retrievals with a high temporal/spatial resolution would significantly enrich the validation or assimilation of NWP models, alike weather radars are used nowadays.

Final remarks: The results of the present work represent the first continuous long-term retrievals of parameters for precipitating clouds derived by ground-based microwave observations. While these results are representative for the specific climatological regime and observational configuration, they certainly reveal the potential of ground-based passive microwave polarimetric observations to constrain the microphysical assumptions regarding the cloud/rain partition underpinning space-borne microwave-based LWP retrievals and reduce their errors as stressed by O'Dell, C., Wentz, F., and Bennartz, R. (2008).

The Global Precipitation Measurement - Ground Validation (GPM/GV) experiments provide a potential test bed to extend ADMIRARI's studies to tropical, high latitudes and solid precipitation. As such, ADMIRARI will continuously contribute to a deeper understanding of precipitating cloud parameters and offer unprecedented information for cloud modelling and for the validation of GPM space-based rain retrieval algorithms (Hou, A. et al., 2014). The present work set certainly a milestone in such research avenue.

Appendix

Table of appendices

A. Rain Liquid Water Path Retrieved by Two Independent Method	135
A.1. Introduction	135
A.2. Rain LWP retrieval from pure MRR data	135
A.2.1. Results for R_LWP as a function of DSD	137
A.3. The ZPHI Method Applied to RHI observations	139
A.3.1. Instrumentation and strategy	140
A.3.2. ZPHI application for LWC retrievals	140
A.3.3. Results for rain liquid water content	142
A.4. Conclusions	144
B. Publications	147
Acronyms	149
List of Symbols	153
List of Constants	155
Bibliography	157
Acknowledgements	167

A. Rain Liquid Water Path Retrieved by Two Independent Method

Abstract

Rain liquid water path is estimated from two independent instruments i.e. a [MRR](#) and a dual-polarized X-band radar. Different methods are used according to each instrument's features. The MRR case uses a best matching method, the matching is performed on reflectivity measurements and simulated attenuated. The liquid water content is traced back and when compared with ADMIRARI results it is found a systematic underestimation by the radiometer.

The second case (dual-pol X-band radar) is a more robust method and takes advantage of the radar's polarimetry capabilities. It uses the ZPHI algorithm to estimate first the specific attenuation. The method has been extended to use on radar RHI scans which are in synergy with the radiometer ADMIRARI. It is shown that the ZPHI algorithm can be applied for RHI scans when proper detection of the top of the rain layer is achieved. Liquid water content is estimated from the specific attenuation based on a power-law relationship and compared with independent retrievals by ADMIRARI.

A.1. Introduction

In order to take advantage of the multi-sensor observations, a development of a radiometer-radar retrieval scheme for precipitating cloud parameters is being pursued. Nevertheless before to attempt a combined algorithm, independent estimations of liquid precipitating parameters are first developed to have an overview on the retrieval's performance of the active and passive sensors when observing the same precipitating system.

The present study summarize two approaches to estimate liquid water content from active sensors and thereafter obtain the radiometer's retrievals independently. One approach is a straightforward retrieval based on best matching with MRR observations and synthetic measurements, work published by Saavedra, P., Battaglia, A., and Simmer, C. ([2012b](#)). While the second approach is an extension of the well known ZPHI method (Bringi, V. and Chandrasekar, V., [2001](#); Testud, J., Le Bouar, E., Obligis, E., and Ali-Mehenni, M., [2000](#)) applied to RHI scans. This approach is explained in squeeze details by Saavedra, P., Battaglia, A., Ryzhkov, A., and Simmer, C. ([2013](#)) presented at the American Meteorological Society 36th Radar Conference 2013, and the 14th Cloud Physics and Atmospheric Radiation 2014 described by Saavedra, P., Battaglia, A., Ryzhkov, A., and Simmer, C. ([2014b](#)).

A.2. Rain LWP retrieval from pure MRR data

Since the MRR was sensing exactly at the same elevation angle as ADMIRARI, a pure MRR-based [R_LWP](#) estimation can be treated as an independent retrieval. In that sense, a procedure

has been developed to obtain liquid water content by matching MRR synthetic and measured reflectivity profiles.

Although the MRR reflectivity data is susceptible to be affected by mis-calibration and attenuation, rain LWP can be estimated from the synthetic measured reflectivity Z_m if treated properly. To simulate the slant profile of Z_m it is used the same hydrometeors profile inputs as for the synthetic brightness temperatures described in section 4.3. Hence attenuated reflectivity as measured by a MRR-like radar has been computed via Mie theory and imposing the DSD described by equation 4.80. The radar position relative to the rain cell, the finite thickness of the rain layer (figure 4.3) and the attenuation modulated by the cloud structure have been accounted for.

Then the simulated reflectivity is given by

$$Z_m(s) = Z(s) - 2 \int_0^s A_{tot}(r) dr, \quad (\text{A.1})$$

with $Z(s)$ the radar reflectivity factor at range s and expressed in dBz and $A_{tot}(r)$ [dB km^{-1}] the specific attenuation.

The equivalent reflectivity per unit volume $Z(s)$ in equation A.1 is given by (Bringi, V. and Chandrasekar, V., 2001)

$$Z = \frac{\lambda^4}{\pi^5 |\kappa|^2} \int_0^\infty \sigma_b^{MIE} N(D) dD \quad (\text{A.2})$$

in linear units [$\text{mm}^6 \text{m}^{-3}$], where σ_b^{MIE} is the backscattering cross-section computed according to Mie theory, λ the MRR wavelength (12.4mm), $\kappa = \frac{m^2 - 1}{m^2 + 2}$ the dielectric factor with $m(\lambda)$ the complex index of refraction of the hydrometeor and $N(D)$ the inverse exponential DSD $N(D) = N_0 \exp(-\Lambda D)$ modulated by its slope parameter Λ which depends on the liquid water content following:

$$\Lambda = \left(\frac{N_0 \pi \rho_w}{\text{LWC}} \right)^{\frac{1}{4}} \quad (\text{A.3})$$

with the rain liquid water content LWC in [g m^{-3}] and $\rho_w = 1.0 \text{ g cm}^{-3}$ is the water density and N_0 is the exponential DSD intercept parameter which for this case takes the four representative values of 1.4, 4.0, 8.0 and $32.0 \times 10^3 \text{ m}^{-3} \text{ mm}^{-1}$ for Thunderstorm, Heavy-rain, Marshall-Palmer and Light-rain, respectively.

The total specific attenuation $A_{tot}(r)$ in equation A.1 is expressed as (Bringi, V. and Chandrasekar, V., 2001; Janssen, M. A., 1993)

$$A_{tot}(r) = 10 \log_{10}(e) \left[A_{gases}(r) + 6 \pi \nu q_c(r) \frac{\Im m\{\epsilon_w\}}{|\epsilon_w + 2|^2} + \int_0^\infty N_{rain}(D, r) \sigma_{ext}^{MIE}(D) dD \right] \quad (\text{A.4})$$

decomposed into the attenuation due to gases (oxygen, dry air and water vapour), cloud and rain respectively. With σ_{ext}^{MIE} being the extinction coefficient and ϵ_w the dielectric constant of water at the given frequency and temperature.

The backscattering and extinction cross-section coefficients, σ_b^{MIE} and σ_{ext}^{MIE} in equations A.2 and A.4 respectively, are calculated following the exact Mie solution for absorption and

scattering of an incident plane wave by homogeneous dielectric spheres (Mishchenko, M., Hovenier, J., and Travis, L., 2000). According to Mie's formulation the backscattering cross-section coefficient is given by Bringi, V. and Chandrasekar, V., 2001, pp. 81-83

$$\sigma_b = \frac{\pi}{k_0^2} \left| \sum_{n=1}^{\infty} (-1)^n (2n+1) (\alpha_{o1n} - \beta_{e1n}) \right|^2 \quad (\text{A.5})$$

and the extinction coefficient by

$$\sigma_{ext} = -\frac{2\pi}{k_0^2} \sum_{n=1}^{\infty} (2n+1) \Re\{(\alpha_{o1n} + \beta_{e1n})\} \quad (\text{A.6})$$

in m^2 , where k_0 is the angular wavenumber and α_{o1n} and β_{e1n} are the scattered field expansion coefficients (also know as Lorenz-Mie coefficients) and are expressed as

$$\alpha_{o1n} = -\frac{j_n(mx_0)[x_0 j_n(x_0)]' - j_n(x_0)[mx_0 j_n(mx_0)]'}{j_n(mx_0)[x_0 h_n^{(2)}(x_0)]' - h_n^{(2)}(x_0)[mx_0 j_n(mx_0)]'} \quad (\text{A.7})$$

$$\beta_{e1n} = -\frac{j_n(x_0)[mx_0 j_n(mx_0)]' - m^2 j_n(mx_0)[x_0 j_n(x_0)]'}{h_n^{(2)}(x_0)[mx_0 j_n(mx_0)]' - m^2 j_n(mx_0)[x_0 h_n^{(2)}(x_0)]'} \quad (\text{A.8})$$

where $m(\lambda) = \sqrt{\epsilon_w}$ is the complex refractive index, $x_0 = \frac{2\pi}{\lambda}$ the size parameter and $j_n(\cdot)$ is the spherical Bessel function of the first kind and $h_n^{(2)}(\cdot)$ the spherical Hankel function of the second kind. The number of elements in the summation in equations A.5 and A.6 is of the order x_0 , and based on extensive calculation is commonly estimated using the criterion (Mishchenko, M., Hovenier, J., and Travis, L., 2000, p. 231)

$$n_{max} = x_0 + 4.05 x_0^{\frac{1}{3}} + 2 \quad (\text{A.9})$$

Finally the radar rain liquid water path is obtained by mapping back the reflectivity obtained after combining equations A.3 and A.2, given a certain LWC, by

$$R_LWP_{(N_0)} = \int LWC(s, N_0) ds, \quad (\text{A.10})$$

with the integral evaluated over the slant MRR range s .

A.2.1. Results for R_LWP as a function of DSD

The MRR R_LWP has been calculated for the same long-term database as in section 6.1. It is shown against the ADMIRARI counterpart in figure A.1 for the four N_0 values. Figure A.1 depicts a large dispersion of R_LWP when the ADMIRARI and the independent MRR retrievals are compared pixel to pixel. A general feature is that the MRR tends to accumulate large range of retrievals for certain ADMIRARI values (see for instance the large populated vertical strips at the four DSD panels). For the thunderstorm or heavy rain cases, the distribution maxima follow the one to one line, with the lowest bias and a RMSE of 167.2 g m^{-2} (figure A.1 a). The opposite is obtained for the light-rain case (figure A.1 d) showing a large overestimation in the MRR retrievals, with the ADMIRARI results practically completely overestimated for R_LWP above $\sim 0.4 \text{ kg m}^{-2}$, with MRR counterpart reaching values as high as 3 kg m^{-2} . The Marshall

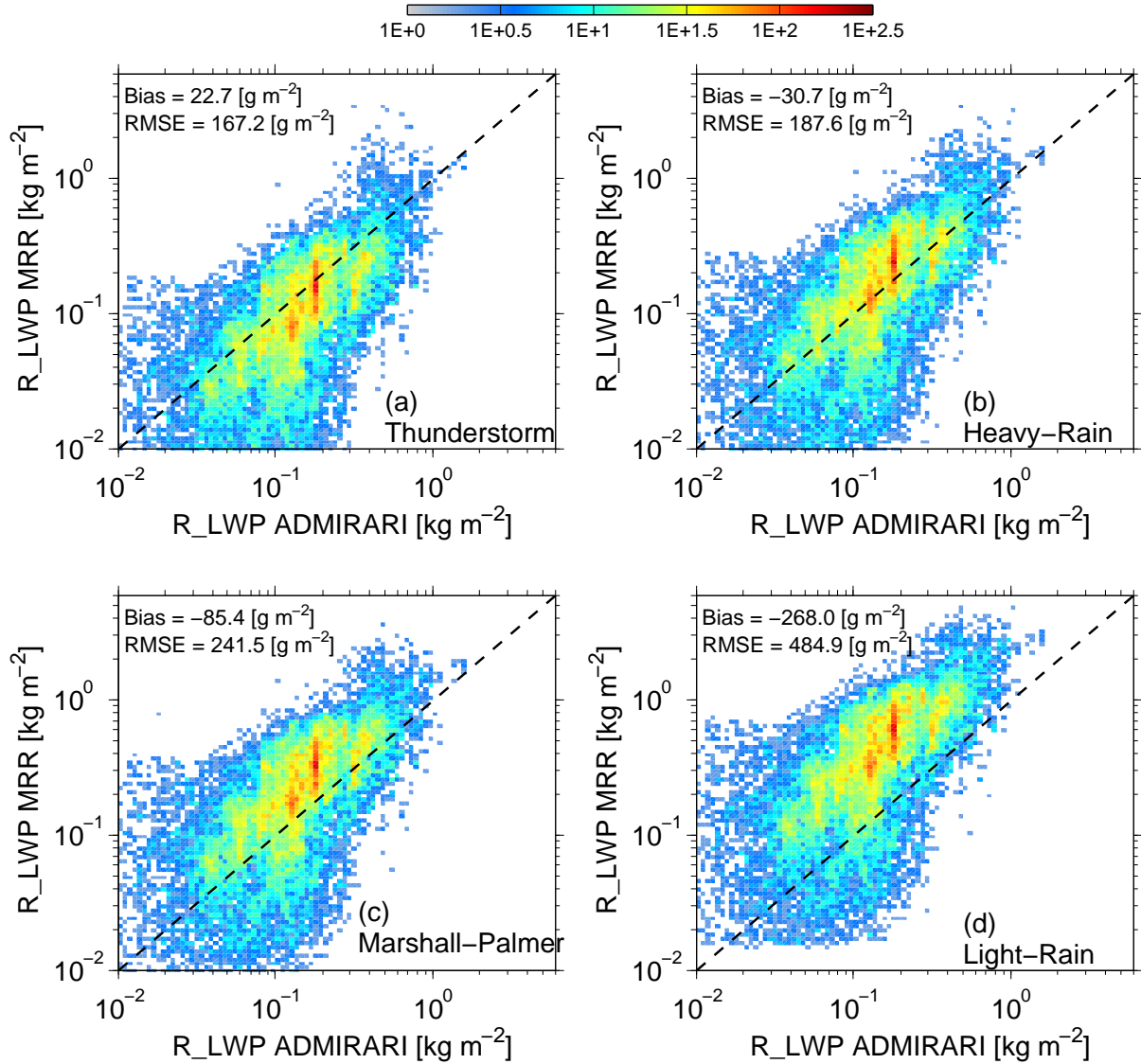


Figure A.1.: Distribution of Rain LWP retrieved by ADMIRARI versus the estimation from MRR by using equation A.10, for $N_0 = 1.4, 4.0, 8.0$ and $32.0 \times 10^3 \text{ m}^{-3} \text{ mm}^{-1}$ at a) thunderstorm, b) heavy-rain, c) M-P and d) Light-rain respectively. The black-dashed-line indicates the 1:1 relation, the color-bar indicates the number of repetitions. (Extracted from Saavedra, P., Battaglia, A., and Simmer, C. (2012b))

and Palmer DSD already shows a slight tendency to overestimate the rain water path respect to the ADMIRARI. In summary figure A.1 indicates that in the pure MRR based retrieval, it is necessary to favour large DSDs for practically all the retrieval cases in order to reproduce the ADMIRARI Bayesian retrievals (Saavedra, P., Battaglia, A., and Simmer, C., 2012b).

One source of mismatching, however, is the different FOV of both instruments i.e. 2° and $\sim 6^\circ$ for the MRR and ADMIRARI respectively. Therefore ADMIRARI's results are averaged over a larger volume which may be the reason they have a systematic bias when compared with any of the MRR's DSD retrievals.

A.3. The ZPHI Method Applied to RHI observations

The Algorithm to correct measured reflectivity from attenuation (ZPHI) method is widely used in QPE applied to radar PPI scans. The technique couples the profiles of attenuated $Z_h(r)$ and the differential phase shift $\Phi_{dp}(r)$. It assumes that attenuation $A(r)$ is related to reflectivity as $A(r) = a(r) [Z(r)]^{b(r)}$, where $Z(r)$ is the intrinsic reflectivity factor, and the coefficients a and b are frequency and temperature dependent. Following the power law equation which relates attenuation and reflectivity and the relationship between attenuation with the specific differential phase K_{dp}

$$A(r) = \alpha(r) K_{dp}, \text{ where } K_{dp} = \frac{\Delta\Phi}{2\Delta r}$$

the following equation can be derived (for the detailed derivation, see Bringi, V. and Chandrasekar, V., 2001; Testud, J., Le Bouar, E., Obligis, E., and Ali-Mehenni, M., 2000):

$$A(r) = \frac{a(r) [Z_h(r)]^{b(r)} [\exp(0.23 b(r) PIA) - 1]}{I_a(r_0, r_{top}) + [\exp(0.23 b(r) PIA) - 1] I_a(r, r_{top})}, \quad (\text{A.11})$$

in $[\text{dB km}^{-1}]$ units and with

$$I_a(r, r_{top}) = 0.46 \int_r^{r_{top}} b(s) a(s) [Z_h(s)]^{b(s)} ds \quad (\text{A.12})$$

Here Z_h is the measured radar reflectivity and the integration must be performed till the top of the rain layer r_{top} . The Path Integrated Attenuation (PIA) in equation A.11 is given as a function of the gradient on differential phase shift $\Delta\Phi$ as follow (Bringi, V. and Chandrasekar, V., 2001; Ryzhkov, A., Diederich, M., Zhang, P., and Simmer, C., 2014; Testud, J., Le Bouar, E., Obligis, E., and Ali-Mehenni, M., 2000):

$$PIA = \alpha(r) \Delta\Phi \quad (\text{A.13})$$

with

$$\Delta\Phi = \Phi_{dp}(r_{top}) - \Phi_{dp}(r_0) \quad (\text{A.14})$$

Equation A.11 is expressed in its most general form. A common practice is to assume the coefficients a and b to be constant along the path. This leads to the following simplification in equation A.11: the coefficient a can be cancelled out from numerator and denominator, and coefficient b can be set outside the integration as an invariant (Ryzhkov, A., Diederich, M., Zhang, P., and Simmer, C., 2014). These two assumptions are acceptable since the ZPHI method is typically applied to PPI scans at low elevation angles e.g. 0.5 to 1.5° .

Once $A(r)$ is computed, the rain liquid water content is estimated according to the power law relationship

$$\text{LWC}(r) = c(r) [A(r)]^{d(r)} \quad (\text{A.15})$$

with LWC in $[\text{gm}^{-3}]$ and the coefficients c and d are temperature and frequency dependent with typical values given in table A.1.

A.3.1. Instrumentation and strategy

The [Jülich Forschung Zentrum \(JFZ\)](#) is a research facility near the city of Jülich in Germany which possess a large instrument suite to make studies on the environment, clouds and precipitation. The main instrument for this study is the 9.3GHz [JuXPoL](#) which is one of the twin X-band systems in Bonn and Jülich, Germany. The radiometer ADMIRARI has been installed at JFZ and set up for measurements at fixed 30° elevation and RHI mode since end of April 2013. JuXPoL performed RHI scans every 5 minutes towards ADMIRARI position (234° azimuth). The radiometer was located at a distance of 3.8 km south-west from JuXPoL. The radar's RHI scans have typically 150 meters range resolution with a maximum range of 50km, and 0.2° elevation steps sweeping from 0 to 90° which ensures a good spatial resolution.

For the present study, observations from June 20th 2013 at [JFZ](#) are utilized as test bed to apply the ZPHI method. Figures A.2 and A.3 give an overview to the data collected by ADMIRARI and JuxPol respectively.

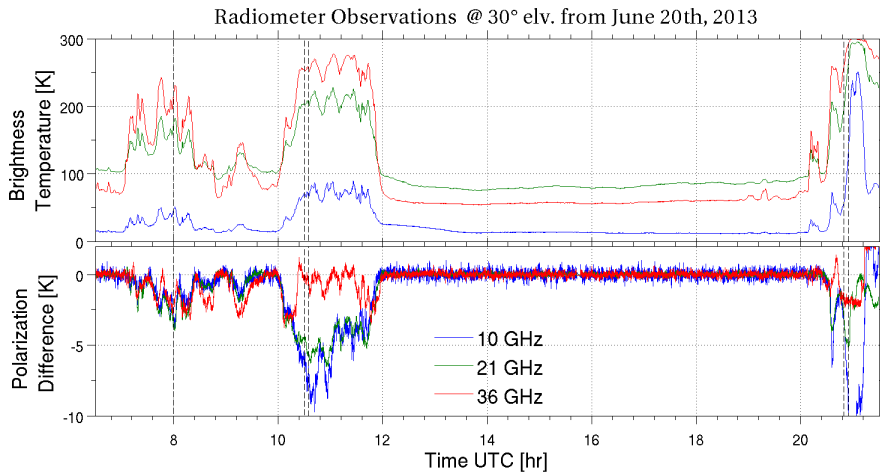


Figure A.2.: ADMIRARI time series of Brightness Temperatures and Polarization Difference at 10.7 (blue), 21.0 (green) and 36.5 (red) GHz. Case study from June 20th, 2013. Gray area represent rain periods.

A.3.2. ZPHI application for LWC retrievals

For our purposes the ZPHI method needed to be extended to the following cases:

- [RHI](#) radar scans in order to cover the radiometer's slant observations,
- capability to detect the melting layer bottom in order to apply the method only to the liquid layer,

- from the attenuation estimation, calculate liquid water content instead of the most common rain rate.
- reconstruction of the radiometer's FOV out of radar scans for all variables, e.g. reflectivity, attenuation, liquid water content.

An important issue is that for the case when elevation scans (RHI) sweep the radiometer's FOV the assumptions regarding the constant coefficients a and b along the path (see section A.3) are not valid since the temperature gradients –from the nearest to the furthest radar ranges– become significant. The same is true for the coefficients c and d in equation A.15.

Thus, the coefficients a , b , c and d were estimated at specific temperatures by T-matrix simulations applied to representative DSD for continental precipitation. Their values are summarized in table A.1.

In order to assign a set of coefficients at each radar range bin, a quadratic and linear relationships have been fitted to the values in table A.1 with the temperature as independent variable. Hence every single range is first mapped to a temperature profile and then the corresponding

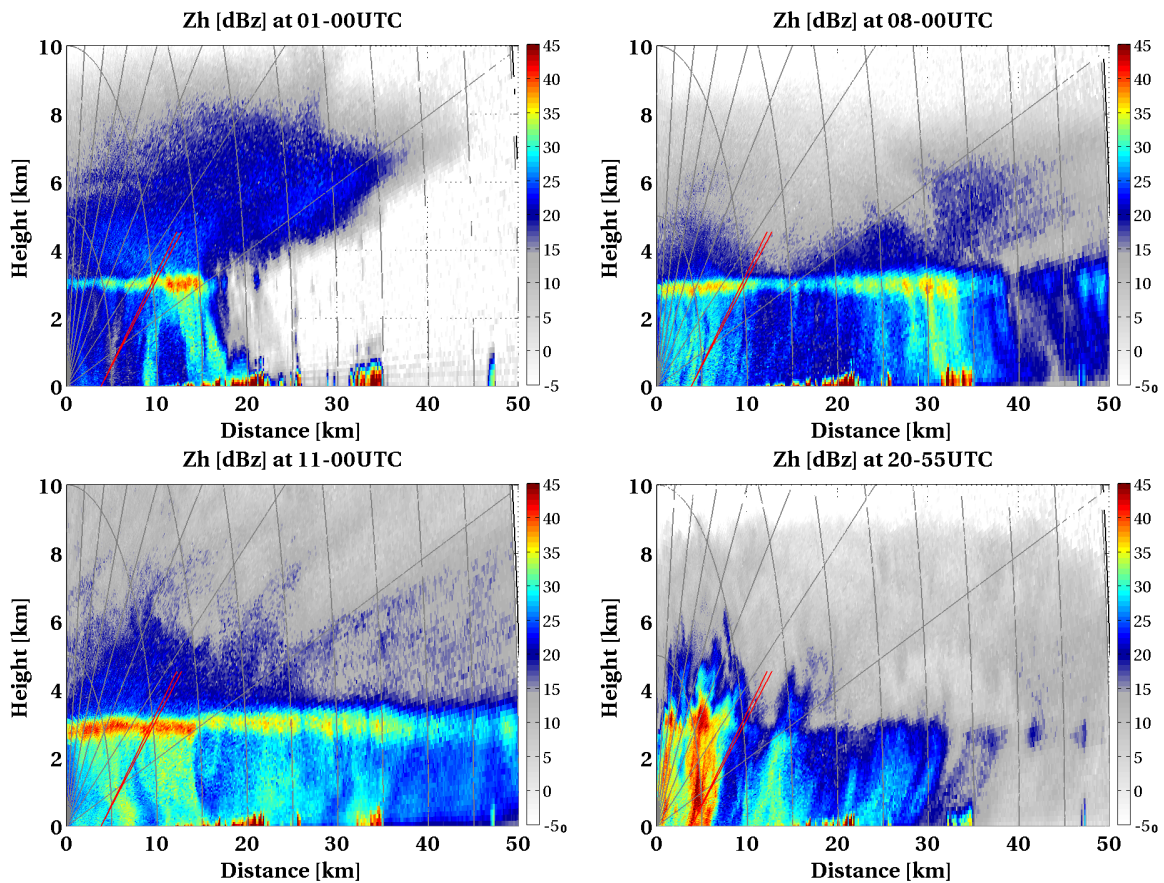


Figure A.3.: JuXPoL radar reflectivity RHI scans at same ADMIRARI's azimuth. Red cone at 3.8km represents the instantaneous radiometer FOV.

Table A.1.: Coefficients c and d in equation A.15 for different temperatures.

T [° C]	a	b	c	d
	$\times 1E - 5$			
0	16.2	0.74	2.04	0.765
10	11.5	0.78	1.88	0.724
15	–	–	1.81	0.705
20	7.99	0.82	1.78	0.689
30	5.50	0.86	1.75	0.661

coefficients are assigned by applying the equations A.16.

$$\begin{aligned}
a(T) &= [16.19 - 0.52T + 0.01T^2] 10^{-5}, & 0 \leq T \leq 30^\circ C \\
\alpha(T) &= [38 - 0.53T] 10^{-2} \\
c(T) &= 2.0410 - 0.0201T + 0.0003T^2 \\
d(T) &= 0.7651 - 0.0045T
\end{aligned} \tag{A.16}$$

The method must only be applied to the rain layer, therefore the location corresponding to the top of pure-liquid layer (i.e. the radar's range r_{top} in previous equations) needs to be accurately determined. By taking advantage from a set of radar polarimetric variables the following conditions determine the melting layer's position: increase in reflectivity, drop on ρ_{hv} , increase of Z_{dr} texture. The range that fulfils these conditions is located inside the melting layer and taken as first point to start an iterative procedure which discards the ranges till the following threshold is achieved:

$$\left| \frac{1}{N} \sum_{i=r_0}^{r_{top}-1} \rho_{hv}(i) - \rho_{hv}(r_{top}) \right| < 0.05 \tag{A.17}$$

thus it is ensured that the ranges from r_0 to r_{top} contains only the rain layer and thereon avoiding any possible contamination from bright-band. Alternatively, in cases where the signal from the polarimetric variables are not strong enough to apply the method, then the ambient temperature is used to estimate the range corresponding to the 0° iso-thermal.

The ZPHI algorithm applied to QPE (low elevation PPI scans) normally requires a $\Delta\Phi$ minimum of 5° to ensure a significant Φ_{dp} departure from the noise level Testud, J., Le Bouar, E., Obligis, E., and Ali-Mehenni, M., 2000. That constrain might, however, jeopardize the feasibility of the ZPHI algorithm for our purposes since at high elevation angles e.g. 25°, $\Delta\Phi$ may be around or less than 5° even in presence of strong precipitation (figure A.4), therefore that minimum threshold must be flexible in order to pursue the applicability of the ZPHI for elevation scans.

A.3.3. Results for rain liquid water content

The ZPHI method with its main equation A.11 is applied to the radar RHI scans that sweep the radiometer's FOV typically from 0 to 35° elevation and at the azimuth of 234°. The results for specific attenuation corresponding only to the liquid layer sensed by RHI scans are shown in figure A.5. Once the specific attenuation is estimated, the liquid water content LWC is

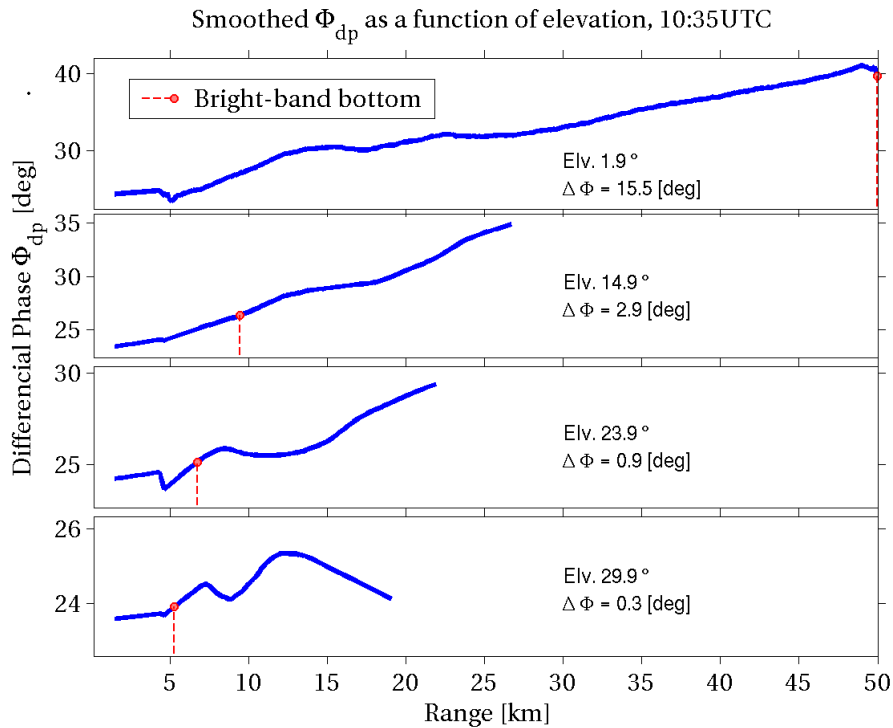


Figure A.4.: Φ_{dp} range profile for different elevation angles. The red circle denotes the bottom of the bright-band i.e. the maximum range for the integration.

calculated using A.15 to all elevation angles where the method is applicable e.g. significant Φ_{dp} signal. Radar moments i.e. reflectivity Z_h , specific attenuation, cross-correlation coefficient, liquid water content; for the ADMIRAR sight are extracted considering the instrument's beam-width.

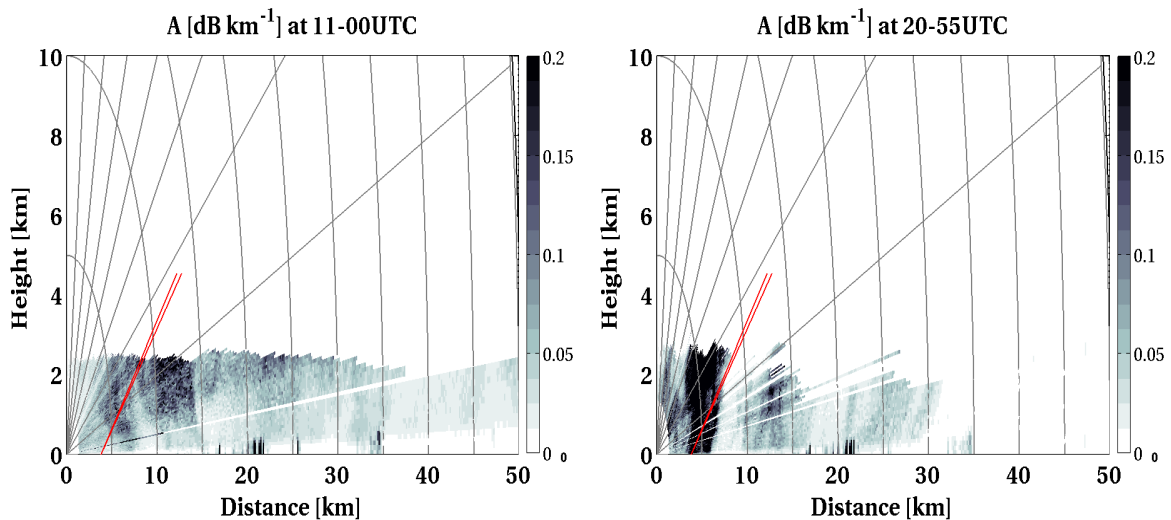


Figure A.5.: X-band specific attenuation for RHI sequences. The red cone at 3.8km represents the instantaneous radiometer FOV.

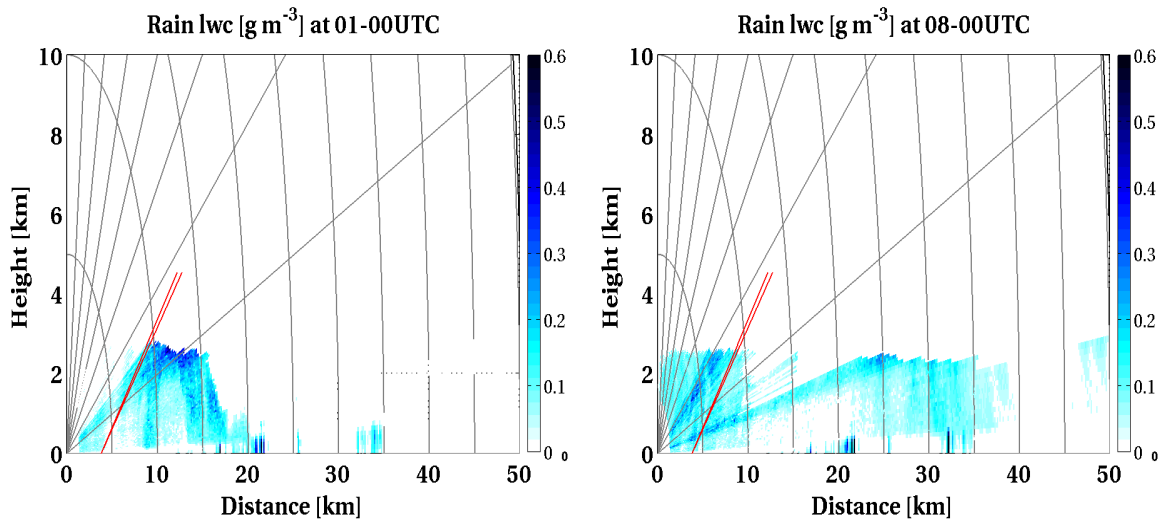


Figure A.6.: Liquid water content for RHI sequences. Red cone represent the instantaneous radiometer's FOV.

In order too have two comparable magnitudes, the estimations for radar LWC along ADMIRARI's slant path must be first integrated (red cone in figure A.6). The result for slant observations (red cone in figures A.3) is shown in figure A.7. The ADMIRARI's Bayesian retrieval scheme allows to estimate also the standard deviation for every point, that is shown as an error-bar corresponding to 2σ of the *posteriori* distribution from which the Bayesian technique estimates the expected value (see section 4.2 and Saavedra, P., Battaglia, A., and Simmer, C. (2012b)).

A.4. Conclusions

A reasonable correlation is found specially for rain LWP values above $\sim 0.5 \text{ kg m}^{-2}$. That might be seen as an obvious consequence of the fact that the ZPHI method performs better when significant attenuation is observed i.e. large quantities of rainwater. In general a RMSE of 1.2 kg m^{-2} is found, this however is largely affected by the widespread dispersion of points at low LWP values. On the other hand the bias (RADAR-ADMIRARI) is slightly negative and suggests an overestimation of ADMIRARI retrievals (figure A.7). That may be explained from the fact that the radiometer's observations include the effect of the bright-band while the radar estimation come only due to the rain layer.

The origin for the large scattered points at low LWP, shown in figure A.7, which depart from the 1:1 line are more complicated to interpret. They can be attributed to weaknesses on the radar and radiometer algorithms, errors corresponding to the set-up and instrumentation synergy, namely minimum detectable values, radar-radiometer collocation, beam mismatching, uneven beam-widths, etc.

The number of points shown in figure A.7 are largely reduced due to the uneven temporal resolution of both instruments, and the fact that for some cases the retrievals are not possible, either by the radiometer or the radar or both. Extending this study to larger data sets will lead to improvements on the statistics and finding out whether the results are a case specific behaviour or they highlight a more general pattern.

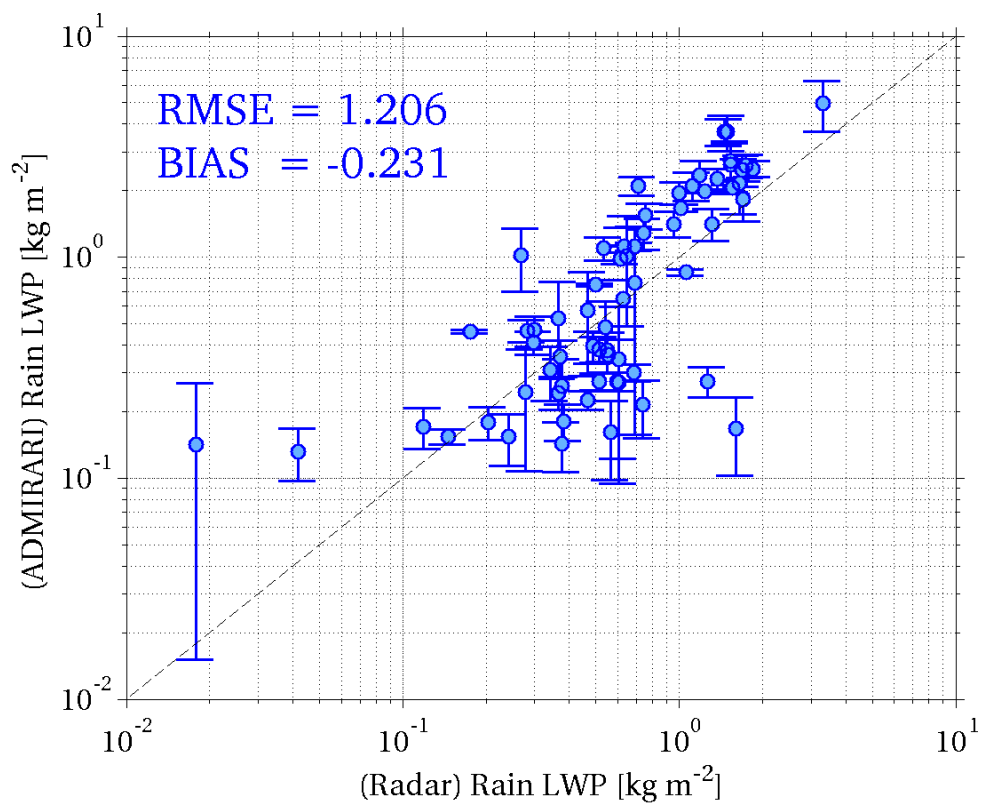


Figure A.7.: Scatter plot for LWP as retrieved from ADMIRARI versus the ZPHI algorithm from RHI radar data. Note that ADMIRARI's retrievals are shown with error-bars corresponding to 2σ . The black-dashed line represent a 1:1 relation. The data as well as RMSE and BIAS corresponds to slant 30° elevation angle. (Extracted from Saavedra, P., Battaglia, A., Ryzhkov, A., and Simmer, C. (2013))

B. Publications

Peer-reviewed Articles

- 1.) P. Saavedra, A. Battaglia, and C. Simmer (2012b). “Partitioning of cloud water and rain water content by ground-based observations with the radiometer ADMIRARI in synergy with a micro rain radar.” In: *J. Geophys. Res.* D05203.177. doi:10.1029/2011JD016382
- 2.) A. Battaglia, P. Saavedra, C.A. Morales, and C. Simmer (2011). “Understanding three-dimensional effects in polarized observations with the ground-based ADMIRARI radiometer during the CHUVA campaign.” In: *J. Geophys. Res.* 116. doi:10.1029/2010JD015335, p. D09204
- 3.) A. Battaglia, P. Saavedra, T. Rose, and C. Simmer (2010). “Characterization of precipitating clouds by ground-based measurements with the triple-frequency polarized microwave radiometer ADMIRARI.” in: *J. Appl. Meteorol.* 43.3, pp. 394–414
- 4.) A. Battaglia, P. Saavedra, C. Simmer, and T. Rose (2009). “Rain Observation by a Multifrequency Dual-Polarized Radiometer.” In: *Geosci. Rem. Sens. Lett. IEEE* 6.2. doi:10.1109/LGRS.2009.2013484, pp. 354–358

Conference Proceedings

- 1.) P. Saavedra, A. Battaglia, A. Ryzhkov, and C. Simmer (Sept. 2014a). “Melting layer attenuation as observed by polarimetric radar-radiometer synergistic approach.” In: 8th European Conference on Radar in Meteorology and Hydrology. (Garmisch-Patenkirchen, Germany, Sept. 1–5, 2014). Deutsches Zentrum fuer Luft- und Raumfahrt (DLR). URL: http://www.pa.op.dlr.de/erad2014/programme/ExtendedAbstracts/374_Saavedra.pdf
- 2.) P. Saavedra, A. Battaglia, A. Ryzhkov, and C. Simmer (July 2014b). “On the multi-frequency signature of precipitation water content as observed by passive and active sensors.” In: 14th Conference on Cloud Physics, Atmospheric Radiation, American Meteorological Society (AMS). (Boston, USA, July 7–11, 2014). American Meteorological Society (AMS). URL: <https://ams.confex.com/ams/14CLOUD14ATRAD/webprogram/Paper250912.html>
- 3.) P. Saavedra, A. Battaglia, A. Ryzhkov, and C. Simmer (Sept. 2013). “Synergy between polarimetric radar and radiometer ADMIRARI for estimation of precipitating parameters.” In: 36th Conference of Radar Meteorology, American Meteorological Society (AMS). (Breckenridge CO., USA, Sept. 16–20, 2013). American Meteorological Society (AMS). URL: <https://ams.confex.com/ams/36Radar/webprogram/Paper229168.html>

- 4.) S. Lautaportti, D. Moisseev, P. Saavedra, A. Battaglia, and V. Chandrasekar (June 2012). “Dual polarization radar and microwave radiometer observations of winter precipitation during LPVEX.” in: *Proceedings of the European Radar Conference*. European Radar Conference. (Toulouse, France, June 25–29, 2012). Meteo France. URL: http://www.meteo.uni-bonn.de/mitarbeiter/pablo-saavedra-garfias/procee/MIC_201_ext_abs.pdf
- 5.) P. Saavedra, A. Battaglia, C. Simmer, M. Vega, and V. Chandrasekar (Aug. 2012). “On the feasibility to combine observations from multi-wavelength radar and the multi-frequency radiometer ADMIRARI to retrieve precipitating clouds parameters.” In: *Proceedings of the International Radiation Symposium*. International Radiation Symposium. (Berlin, Germany, Aug. 6–10, 2012). American Institute of Physics (AIP), pp. 260–263. DOI: [doi:http://dx.doi.org/10.1063/1.4804756](http://dx.doi.org/10.1063/1.4804756). URL: http://proceedings.aip.org/resource/2/apcpcs/1531/1/260_1
- 6.) P. Saavedra, A. Battaglia, and C. Simmer (Aug. 2012a). “The contribution of the microwave radiometer ADMIRARI to the NASA GPM ground validation field experiments.” In: *Proceedings of the International Radiation Symposium*. International Radiation Symposium. (Berlin, Germany, Aug. 6–10, 2012). American Institute of Physics (AIP), pp. 592–595. DOI: [doi:http://dx.doi.org/10.1063/1.4804839](http://dx.doi.org/10.1063/1.4804839). URL: http://proceedings.aip.org/resource/2/apcpcs/1531/1/592_1
- 7.) P. Saavedra, A. Battaglia, and C. Simmer (Oct. 2009). “Partitioning of cloud and rain water content by ground-based observations with a multi-frequency microwave radiometer in synergy with a micro rain radar.” In: *Proceedings of the 8th International Symposium on Tropospheric Profiling*. 8th International Symposium on Tropospheric Profiling. (Delft, The Netherlands, Oct. 18–23, 2009). URL: <http://cerberus.rivm.nl/ISTP/data/1660768.pdf>

Acronyms

ADMIRARI

ADvanced MICrowave RAdiometer for Rain Identification. [6](#), [55](#), [62](#), [69](#), [103](#), [123](#), [127](#), [139](#)

AMF

ARM Mobile Facility. [103](#)

ARM

Atmospheric Radiation Measurement. [50](#), [103](#), [105](#)

C_LWP

Cloud Liquid Water Path. [4](#), [7](#), [69](#), [91](#), [92](#), [94](#), [119](#), [128](#)

CESAR

Cabauw Experimental Site for Atmospheric Research. [107](#), [121](#)

COPS

Convective and Orographic-ally Induced Precipitation Study. [103](#), [104](#)

CRM

Cloud Resolving Model. [74](#), [75](#), [119](#), [128](#), [130](#)

D3R

Dual-frequency, Dual-polarization, Doppler Radar. [Web site](#). [50](#)

DSD

Drop Size Distribution. [5](#), [53](#), [54](#), [56](#), [73](#), [81–84](#), [86–88](#), [92](#), [123](#), [127](#), [129](#), [136](#), [141](#)

EC

Environment Canada. [50](#)

FM-CW

Frequency Modulated-Continues Wave. [53](#), [58](#)

FOV

Field of View. [33](#), [50](#), [63](#), [75](#), [124](#), [128](#), [139](#), [140](#)

GCPEX

GPM Cold Precipitation Experiment. [112](#)

GPM

Global Precipitation Measurement. [5](#), [130](#)

GPM/GV

Global Precipitation Measurement - Ground Validation. [130](#)

HPBW

Half-Power Beamwidth. [31](#)

IWV

Integrated Water Vapour. [7](#), [88](#), [91–93](#), [99](#), [119](#), [128](#)

JFZ

Jülich Forschung Zentrum. [124](#), [140](#)

JuXPol

Jülich X-band Polarimetric Weather Radar. [123](#), [124](#), [129](#), [140](#)

KASACR

Ka-band Scanning ARM Cloud Radar. [Web site](#). [50](#)

LIDAR

Light Detection And Ranging. [58](#), [61](#), [62](#), [127](#)

LN2

Liquid Nitrogen. [34](#), [38](#), [39](#)

LPVEx

Light Precipitation and Verification Experiment. [97](#), [112](#), [129](#)

LWC

Liquid Water Content. [3](#), [15](#), [16](#), [82–84](#), [86](#), [97](#), [136](#), [137](#), [139](#), [143](#)

LWP

Liquid Water Path. [3–6](#), [69](#), [71](#), [88](#), [91](#), [92](#), [94](#), [96](#), [97](#), [99](#), [100](#), [109](#), [125](#), [127](#), [129](#), [136](#), [143](#)

METEK

Meteorologische Messtechnik GmbH. [53](#), [55](#)

MIUB

Meteorological Institute, University of Bonn. [62](#), [121](#), [127](#)

MRR

Micro Rain Radar. [53–55](#), [58](#), [62](#), [74](#), [87](#), [88](#), [93](#), [96](#), [98](#), [107](#), [123](#), [127](#), [129](#), [135](#), [139](#)

NWP

Numerical Weather Prediction. [2](#), [130](#)

PD

Polarization Difference. [6](#), [74](#), [83](#), [86](#), [88](#), [89](#), [105](#)

PIA

Path Integrated Attenuation. [5](#), [139](#)

PPI

Plane Position Indicator. [41](#), [103](#), [124](#)

QPE

Quantitative Precipitation Estimation. [124](#), [129](#), [139](#), [143](#)

R_LWP

Rain Liquid Water Path. [7](#), [69](#), [71](#), [81](#), [91](#), [92](#), [94](#), [123–126](#), [128](#), [129](#), [135](#)

RADAR

RAdio Detection And Ranging. [50](#), [53](#), [61](#), [62](#)

RF

Radio-Frequency. [27](#)

RHI

Range Height Indicator. [103](#), [124](#), [140](#)

RMSE

Root Mean Square Error. [6](#), [28](#), [87](#), [88](#), [91–94](#), [115](#), [123–126](#), [129](#)

RPG

Radiometer Physics GmbH. [30](#), [34](#), [38](#), [42](#), [43](#), [46](#)

RT4

Radiative Transfer, version 4. [24](#), [69](#), [75](#), [78](#)

RTE

Radiative Transfer Equation. [9](#), [14](#), [19](#), [21–23](#), [75](#)

T_LWP

Total LWP i.e. Rain plus Cloud. [69](#), [94](#)

TB

Brightness temperature. [6](#), [11](#), [74](#), [83](#), [86](#), [88](#), [89](#), [105](#)

TRMM

Tropical Rainfall Measurement Mission. [5](#)

VRTE

Vectorized Radiative Transfer Equation. [21](#), [22](#), [75](#)

ZPHI

Algorithm to correct measured reflectivity from attenuation. [139](#), [143](#)

List of Symbols

$B_\nu(T)$	Surface brightness of a black-body emitter depending on frequency ν , and temperature T , [$W m^{-2} sr^{-1} Hz^{-1}$]. 10, 13, 22
G	Radiometer's receiver gain factor, [$mV K^{-1}$]. 34, 38, 39, 41
I_ν	Instantaneous radiant power in the medium, per unit area, per unit frequency ν , in a given direction per unit solid angle, , [$W m^{-2} sr^{-1} Hz^{-1}$]. 9–11, 14
K_{dp}	Specific differential phase, [$^\circ km^{-1}$]. 139
N_0	Intercept parameter for an exponential DSD, [$m^{-3} mm^{-1}$]. 136
Q_a	Absorption efficiency for spherical particles. 19
Q_e	Extinction efficiency for spherical particles. 19
T_n	Noise injector temperature, [K]. 34, 39
T_{mr}	Atmospheric mean radiating temperature, [K]. 38, 39
T_{sys}	Radiometer system temperature, [K]. 34, 39
Z_h	Radar reflectivity, horizontally polarized, [dBz]. 139, 143
Z_{dr}	Differential reflectivity Z_h - Z_v , [dB]. 142
$\Im m$	Imaginary part of a complex number. 16, 18, 136
Λ	Slope parameter for an exponential DSD, [L^{-1}]. 136
Φ_{dp}	Differential phase shift, [$^\circ$]. 139, 143
$\Re e$	Real part of a complex number. 18, 137
β	Lidar backscattering coefficient, [$m^{-1} sr^{-1}$]. 61, 62, 65
$\alpha_{e\nu}$	Extinction matrix at frequency ν , [L^{-1}]. 13, 18, 22
$\delta(\cdot)$	Dirac delta function, with $\delta = 0$ when the function's argument $\neq 0$. 20
ϵ_w	Dielectric constant of liquid water. 16, 136
κ	Dielectric factor. 136
λ	Electromagnetic wavelength, [L]. 136
M	The 4×4 scattering (Mueller) matrix proportional to the phase matrix Z . 22
R_d	Bidirectional reflectance matrix for diffuse reflection. 20
R_s	Bidirectional reflectance matrix for specular reflection. 20
Z_v	Phase matrix at frequency ν , [L^{-1}]. 13
μ	The cosine of the incident angle. 21, 22
ν	Frequency of an electromagnetic wave, [Hz]. 10, 16
ω	$= 2\pi\nu$ Circular frequency of an electromagnetic wave, [Hz]. 11
ρ_{hv}	Cross correlation coefficient between H and V polarization. 142
τ	Atmospheric optical thickness. 10, 14, 22, 38
\vec{I}	$(I, Q, U, V)^T$, Stokes vector of the monochromatic orthogonal electromagnetic wave, [$W m^{-2} sr^{-1} Hz^{-1}$]. 12
$\vec{\alpha}_{a\nu}$	Absorbption vector at frequency ν , [L^{-1}]. 13, 16, 18
$\vec{\Psi}$	Surface emission vector. 20, 21

$\tilde{\omega}$	Single scattering albedo, equal to the ratio of the scattering and extinction cross sections. 22
$h_n^{(2)}$	Spherical Hankel function of the second kind. 137
j_n	Spherical Bessel function of the first kind. 137
k_0	$= \frac{2\pi}{\lambda}$ Angular wave-number, [L^{-1}]. 17 , 137
$m(\lambda)$	$= \sqrt{\epsilon_w}$ Complex refractive index. 136 , 137
m_A	Atmospheric airmass. 38
x_0	$= k_0 a$ Size parameter for particle radius a and wavelength λ . 137

List of Constants

$$R = 8.3144621 \text{ JK}^{-1} \text{ mol}^{-1}$$

Universal gas constant. [36](#)

$$T_{\text{cmb}} = 2.73\text{K}$$

Cosmic Microwave Background radiation. [19](#), [28](#), [38](#), [78](#)

$$\Delta H = 199.1 \text{ kJkg}^{-1}$$

Nitrogen latent heat. [36](#)

$$\rho_w = 1.0 \text{ g cm}^{-3}$$

Liquid water density. [81](#), [136](#)

$$c = 2.997925 \times 10^8 \text{ ms}^{-1}$$

Speed of light in vacuum. [10](#), [61](#)

$$h = 6.62606957 \times 10^{-34} \text{ m}^2 \text{ kg s}^{-1}$$

Planck's constant. [10](#), [34](#)

$$k_B = 1.3806488 \times 10^{-23} \text{ m}^2 \text{ kg s}^{-2} \text{ K}^{-1}$$

Boltzmann constant. [10](#), [34](#)

Bibliography

Adler, R.F. et al. (2003).

“The Version-2 Global Precipitation Climatology Project (GPCP) Monthly Precipitation Analysis (1979–Present).”

In: *J. Hydrometeor.* 4. doi:[http://dx.doi.org/10.1175/1525-7541\(2003\)004<1147:TVGPCP>2.0.CO;2](http://dx.doi.org/10.1175/1525-7541(2003)004<1147:TVGPCP>2.0.CO;2), pp. 1147–1167.

Rose, Th. and H. Czekala (2007).

RPG-XCH-DP X Frequency, Dual Polarized Radiometer, Operational Manual.

Radiometer Physics GmbH. Meckenheim, Germany.

Allan, R.P. and B.J. Soden (2007).

“Large discrepancy between observed and simulated precipitation trends in the ascending and descending branches of the tropical circulation.”

In: *Geophys. Res. Lett.* 34.L18705. doi:10.1029/2007GL031460.

Battaglia, A., H. Czekala, and C. Simmer (2006).

“Three dimensional effects in polarization signatures as observed from precipitating clouds by low frequency microwave radiometer.”

In: *Atmos. Chem. Phys.* 6, pp. 4383–4394.

Battaglia, A., C. Davis, C. Emde, and C. Simmer (2007).

“Microwave radiative transfer intercomparison study for 3-D dichroic media.”

In: *J. Quant. Spectrosc. Radiat. Transfer* 105.1, pp. 55–67.

Battaglia, A., C. Kummerow, D.B. Shin, and C. Williams (2003).

“Toward characterizing the effect of radar bright bands on microwave brightness temperatures.”

In: *J. Atmos. Ocean Technol.* 20.6, pp. 856–871.

Battaglia, A. and S. Mantovani (2005).

“Forward Monte Carlo computations of fully polarized microwave radiation in non isotropic media.”

In: *J. Quant. Spectrosc. Radiat. Transfer* 95.3, pp. 285–308.

Battaglia, A., P. Saavedra, C.A. Morales, and C. Simmer (2011).

“Understanding three-dimensional effects in polarized observations with the ground-based ADMIRARI radiometer during the CHUVA campaign.”

In: *J. Geophys. Res.* 116. doi:10.1029/2010JD015335, p. D09204.

Battaglia, A., P. Saavedra, T. Rose, and C. Simmer (2010).

“Characterization of precipitating clouds by ground-based measurements with the triple-frequency polarized microwave radiometer ADMIRARI.”

In: *J. Appl. Meteorol.* 43.3, pp. 394–414.

Battaglia, A., P. Saavedra, C. Simmer, and T. Rose (2009).

“Rain Observation by a Multifrequency Dual-Polarized Radiometer.”

In: *Geosci. Rem. Sens. Lett. IEEE* 6.2. doi:10.1109/LGRS.2009.2013484, pp. 354–358.

- Bringi, V.N. and V. Chandrasekar, eds. (2001).
Polarimetric Doppler Weather Radar, Principles and applications.
ISBN 0-521-01955-9.
Cambridge University Press.
- Crewell, S., H. Czekala, et al. (2001).
“Microwave Radiometer for Cloud Cartography: A 22-channel ground-based microwave radiometer for atmospheric research.”
In: *Radio Sci.* 36.4, pp. 621–638.
- Crewell, S., K. Ebell, U. Loehnert, and D.D. Turner (2009).
“Can liquid water profiles be retrieved from passive microwave zenith observations?”
In: *Geophys. Res. Lett.* 36. doi: 10.1029/2008GL036934, p. L06803.
- Crewell, S. and U. Löhnert (2003).
“Accuracy of cloud liquid water path from ground-based microwave radiometry. Part II. Sensor accuracy and synergy.”
In: *Radio Sci.* 38.3. doi: 10.1029/2002RS002634.
- Crewell, S., C. Simmer, et al. (2004).
“The BALTEX Bridge Campaign: An integrated approach for a better understanding of clouds,”
In: *Bull. Amer. Met. Soc.* 85.10. doi: 10.1175/BAMS-85-10-1565, pp. 1565–1584.
- Czekala, H. (1999).
“Microwave radiative transfer calculations with multiple scattering effects by nonspherical hydrometeors.”
PhD thesis. Auf dem Hügel 20, 53121 Bonn: Rheinische Friedrich-Wilhelms-Universität Bonn.
- Czekala, H., S. Crewell, A. Hornbostel, et al. (2001b).
“Interpretation of polarization features in ground based microwave observations as caused by horizontally aligned oblate rain drops.”
In: *J. Appl. Meteorol.* 40, pp. 1918–1932.
- Czekala, H., S. Crewell, C. Simmer, and A. Thiele (2001).
“Discrimination of cloud and rain liquid water path by groundbased polarized microwave radiometry.”
In: *Geophys. Res. Lett.* 28.2, pp. 267–270.
- Czekala, H. and C. Simmer (1998).
“Microwave radiative transfer with non-spherical precipitating hydrometeors.”
In: *J. Quant. Spectrosc. Radiat. Transfer* 60.3, pp. 365–374.
- Dicke, R.H (1946).
“The measurement of thermal radiation at microwave frequencies.”
In: *Rev. Sci. Instr.* 17, pp. 268–275.
- Evans, K.F. and G.L. Stephens (1991).
“A new polarized atmospheric radiative transfer model.”
In: *J. Quant. Spectrosc. Radiat. Transfer* 46, pp. 413–423.
- Gaussiat, N., R.J. Hogan, and A.J. Illingworth (2007).
“Accurate liquid water path retrieval from low-cost microwave radiometers using additional information from lidar and operational forecast models.”
In: *J. Atmos. Ocean Technol.* 24, pp. 1562–1575.
- Han, Y. and Ed R. Westwater (May 2000).
“Analysis and Improvement of Tipping Calibration for Ground-Based Microwave Radiometer.”
In: *IEEE Trans. Geosci. Remote Sensing* 38.3, pp. 1260–1276.

- Hilburn, K.A. and F.J. Wentz (2008).
“Intercalibrated Passive Microwave Rain Products from the Unified Microwave Ocean Retrieval Algorithm (UMORA).”
In: *J. Appl. Meteorol.* 47. doi:10.1175/2007JAMC1635.1, pp. 778–794.
- Hildebran, P.H. and R.S. Sekhon (1974).
“Objective determination of the noise level in Doppler spectra.”
In: *J. Appl. Meteorol.* 13. doi:10.1175/1520-0450(1974)013<0808:ODOTNL>2.0.CO;2, pp. 808–811.
- Hogan, R., N. Gaussiat, and A. Illingworth (2005).
“Stratocumulus Liquid Water Content from Dual-Wavelength Radar.”
In: *J. Atmos. Ocean Technol.* 22, pp. 1207–1218.
- Hou, A.Y. et al. (May 2014).
“The Global Precipitation Measurement Mission.”
In: *Bull. Amer. Met. Soc.* DOI:10.1175/BAMS-D-13-00164.1, pp. 701–722.
- Janssen, M. A., ed. (1993).
Atmospheric Remote Sensing by Microwave Radiometry.
Wiley Series in Remote Sensing.
Wiley-Interscience.
- Joss, J. and A. Waldvogel (1968).
“Raindrop size distribution and sampling size errors.”
In: *J. Atmos. Sci.* 26.566–569.
- Karstens, U., C. Simmer, and E. Ruprecht (1994).
“Remote sensing of cloud liquid water.”
In: *Meteorol. Atmos. Phys.* 54, pp. 157–171.
- Kneifel, S., S. Crewell, U. Löhnert, and J. Schween (Feb. 2009).
“Investigating water vapor variability by ground-based microwave radiometry: evaluation using airborne observations.”
In: *Geosci. Rem. Sens. Lett. IEEE.* DOI:10.1109/LGRS.2008.2007659.
- Kneifel, S., M. Maahn, G. Peters, and C. Simmer (2011).
“Observation of snowfall with a low-power FM-CW K-band radar Micro Rain Radar.”
In: *Meteorol. Atmos. Phys.* 113, pp. 75–87.
- Knupp, K.R. et al. (2009).
“Ground-based passive microwave profiling during dynamic weather conditions.”
In: *J. Atmos. Ocean Technol.* 26, pp. 1057–1073.
- Kummerow, C., Y. Hong, et al. (2001).
“The evolution of the Goddard Profiling Algorithm (GPROF) for rainfall estimation from passive microwave sensors.”
In: *J. Appl. Meteorol.* 40, pp. 1801–1820.
- Kummerow, C., S. Ringerud, J. Crook, D. Randel, and W. Berg (2001).
“An Observationally Generated A Priori Database for Microwave Rainfall Retrievals.”
In: *J. Atmos. Ocean Technol.* 28. doi:10.1175/2010JTECHA1468.1., pp. 113–130.
- Kummerow, C., S.O. Willian, and L. Giglio (1996).
“A Simplified Scheme for Obtaining Precipitation and Vertical Hydrometeor Profiles from Passive Microwave Sensor.”
In: *IEEE Trans. Geosci. Remote Sensing* 35(5), pp. 1213–1232.

- Lautaportti, S., D. Moisseev, P. Saavedra, A. Battaglia, and V. Chandrasekar (June 2012).
“Dual polarization radar and microwave radiometer observations of winter precipitation during LPVEX.”
In: *Proceedings of the European Radar Conference*.
European Radar Conference. (Toulouse, France, June 25–29, 2012).
Meteo France.
URL: http://www.meteo.uni-bonn.de/mitarbeiter/pablo-saavedra-garfias/procee/MIC_201_ext_abs.pdf.
- Lebsack, M.D., T. L'Ecuyer, and G.L. Stephens (2011).
“Detecting the Ratio of Rain and Cloud Water in Low-Latitude Shallow Marine Clouds.”
In: *J. Appl. Meteorol.* 50. doi:10.1175/2010JAMC2494.1, pp. 419–432.
- Liebe, H. J., G. A. Hufford, and M. G. Cotton (1993).
“Propagation modelling of moist air and suspended water/ice particles at frequencies below 1000 GHz.”
In: *Proceedings AGARD 52nd Specialist Meeting of the Electromagnetic Wave Propagation Panel*.
Palma de Mallorca, Spain.
AGARD,
pages.
- Liljegren, J.C., E.E. Clothiaux, G.G. Mace, S. Kato, and X. Dong (2001).
“A New Retrieval for Cloud Liquid Water Path Using a Ground-Based Microwave Radiometer and Measurements of Cloud Temperature.”
In: *J. Geophys. Res.* 106.D13, pp. 14, 485–14, 500.
- Liu, Q. and C. Simmer (1996).
“Polarization and intensity in microwave radiative transfer.”
In: *Beitr. Phys. Atmosph.* 69, pp. 535–545.
- Löhnert, U. (2002).
“Derivation of cloud liquid water from ground-based active and passive microwave remote sensors.”
PhD thesis. Auf dem Hügel 20, 53121 Bonn: Rheinische Friedrich-Wilhelms-Universität Bonn.
- Löhnert, U. and S. Crewell (2003).
“Accuracy of cloud liquid water path from ground-based microwave radiometry Part I: Dependency on cloud model statistics.”
In: *Radio Sci.* 38. doi:10.1029/2002RS002654, p. 8041.
- Maahn, M. and P. Kollias (2012).
“Improving Micro Rain Radar snow measurements using Doppler spectra post-processing.”
In: *Atmos. Meas. Tech.* 5. doi:10.5194/amt-5-2661-2012, pp. 2661–2673.
- Marshak, A. and A.B. Davis, eds. (2005).
3D Radiative Transfer in Cloudy Atmospheres.
Physics of Earth and Space Environment.
ISBN 3-540-23958-8.
Springer.
- Marzano, F. S., D. Cimini, P. Ciotti, and R. Ware (2005a).
“Modeling and measurements of rainfall by ground-based multispectral microwave radiometry.”
In: *IEEE Trans. Geosci. Remote Sensing* 43, pp. 1000–1011.

- Marzano, F. S., D. Cimini, and R. Ware (2005b).
“Monitoring of rainfall by ground-based passive microwave systems: Models, measurements and applications.”
In: *Adv. Geosci.* 2, pp. 259–265.
- Marzano, F. S., A. Mugnai, et al. (1999).
“Bayesian estimation of precipitating cloud parameters from combined measurements of spaceborne microwave radiometer and radar.”
In: *IEEE Trans. Geosci. Remote Sensing* 37, pp. 596–613.
- Marzano, F.S. and G. Visconti, eds. (2002).
Remote Sensing of Atmosphere and Ocean from Space: Models, Instruments and Techniques.
Vol. 13.
Advances in Global Change Research.
ISBN 1-4020-0943-7.
Kluwer Academic Publishers.
- Matrosov, S., K. Clark, B. Martner, and A. Tokay (2002).
“X-Band Polarimetric Radar Measurements of Rainfall.”
In: *J. Appl. Meteorol.* 41.9, pp. 941–952.
- Matrosov, S.Y. (2009a).
“A Method to Estimate Vertically Integrated Amounts of Cloud Ice and Liquid and Mean Rain Rate in Stratiform Precipitation from Radar and Auxiliary Data.”
In: *J. Appl. Meteorol.* 48. doi:10.1175/2009JAMC2196.1, pp. 1398–1410.
- (2009b).
“Simultaneous estimates of cloud and rainfall parameters in the atmospheric vertical column above the Atmospheric Radiation Measurement Program southern Great Plains site.”
In: *J. Geophys. Res.* 144. doi:10.1029/2009JD012004, p. D22201.
- Mätzler, C. and J. Morland (2008).
Advances in surface-based radiometry of atmospheric water.
Tech. Rep.
2008-02-MW.
Bern, Switzerland: Inst. Angewandte Physik, Univ. Bern.
- (2009).
“Refined physical retrieval of integrated water vapor and cloud liquid for microwave radiometer data.”
In: *IEEE Trans. Geosci. Remote Sensing* 47.6, pp. 1585–1594.
- McFarlane, S.A., F.K. Evans, and A.S. Ackerman (2002).
“A Bayesian algorithm for the retrieval of liquid water cloud properties from microwave radiometer and millimeter radar data.”
In: *J. Geophys. Res.* 107(D15), p. 4271.
- Meneghini, R. (2005).
“A Broadband Microwave Radiometer Technique at X-band for Rain and Drop Size Distribution Estimation.”
In: *IEEE Trans. Geosci. Remote Sensing* 43.5. doi:10.1109/TGRS.2004.839590, pp. 990–999.
- METEK-GmbH (2010).
Micro Rain Radar Physical Basics Version 5.2.0.9.
MRR manual.
Meteorologische Messtechnik GmbH.

- Mishchenko, M.I. (2000).
“Calculation of the amplitude matrix for a nonspherical particle in a fixed orientation.”
In: *Appl. Opt.* 39.6, pp. 1026–1031.
- Mishchenko, M.I., J.W. Hovenier, and L.D. Travis, eds. (2000).
Light Scattering by Nonspherical Particles.
Academic Press.
- Morland, J. (2002).
TROWARA-Tropospheric Water Vapour Radiometer. Radiometer Review and new calibration model.
Tech. Rep.
2002-15.
Bern, Switzerland: Inst. Angewandte Physik, Univ. Bern.
- O’Connor, E.J., A.J. Illingworth, and R.J. Hogan (Mar. 2004).
“A technique for autocalibration of Cloud lidars.”
In: *J. Atmos. Ocean Technol.* 21.5. doi:10.1175/1520-0426(2004)021<0777:ATFAOC>2.0.CO;2,
pp. 777–786.
- O’Dell, C.W., F. Wentz, and R. Bennartz (2008).
“Cloud Liquid Water Path from Satellite-Based Passive Microwave Observations: A New Climatology over the Global Ocean.”
In: *J. Climate* 1.8. doi:10.1175/2007JCLI1958.1, pp. 1721–1739.
- Petersen, W., T. L’Ecuyer, and D. Moisseev (July 2011).
“The NASA CloudSat/GPM Light Precipitation Validation Experiment (LPVEx).”
In: *The Earth Observer* 23.4, pp. 4–8.
- Platt, C.M.R. (1973).
“Lidar and radiometric observations of cirrus clouds.”
In: *J. Atmos. Sci.* 30, pp. 1191–1204.
- Pospichal, B. (2009).
“Diurnal to annual variability of the Atmospheric Boundary Layer over West Africa: A comprehensive view by remote sensing observations.”
PhD thesis. Cologne, Germany: University of Cologne.
- Prigent, C., E. Jaumouillé, F. Chevallier, and F. Aires (2008).
“A parameterization of the microwave land surface emissivity between 19 and 100 GHz anchored to satellite-derived estimates.”
In: *IEEE Trans. Geosci. Remote Sensing* 46.2.
- Pruppacher, H.R. and R.L. Pitter (1971).
“A Semi-empirical Determination of the Shape of Cloud and Rain Drops.”
In: *J. Atmos. Sci.* 28. [http://dx.doi.org/10.1175/1520-0469\(1971\)028<0086:ASEDOT>2.0.CO;2](http://dx.doi.org/10.1175/1520-0469(1971)028<0086:ASEDOT>2.0.CO;2),
pp. 86–94.
- Randall, D. et al. (2003).
“Confronting models with data: The GEWEX cloud systems study.”
In: *Bull. Amer. Met. Soc.* 84.4, pp. 455–469.
- Raynaud, L., I. Chenerie, and J. Lemorton (2000).
“Modeling of radiowave scattering in the melting layer of precipitation.”
In: *IEEE Trans. Geosci. Remote Sensing* 38.4. doi:10.1109/36.851957, pp. 1574–1584.
- Rodgers, C. D. (2000).
Inverse Methods for Atmospheric Sounding, Theory and Practice.
World Scientific.

- Rose, T., S. Crewell, U. Löhnert, and C. Simmer (2009).
“A network suitable microwave radiometer for operational monitoring of the cloudy atmosphere.”
In: *Atmos. Res.* 75. doi:10.1016/j.atmosres.2004.12.2005, pp. 183–200.
- Russchenberg, H. and L. Ligthart (1996).
“Backscattering by and propagation through the melting layer of precipitation: A new polarimetric model.”
In: *IEEE Trans. Geosci. Remote Sensing* 34, pp. 3–14.
- Ryzhkov, A., M. Diederich, P. Zhang, and C. Simmer (Mar. 2014).
“Potential Utilization of Specific Attenuation for Rainfall Estimation, Mitigation of Partial Beam Blockage, and Radar Networking.”
In: *J. Atmos. Ocean Technol.* 31.3. doi: <http://dx.doi.org/10.1175/JTECH-D-13-00038.1>, pp. 599–619.
- Saavedra, P., A. Battaglia, A. Ryzhkov, and C. Simmer (Sept. 2013).
“Synergy between polarimetric radar and radiometer ADMIRARI for estimation of precipitating parameters.”
In:
36th Conference of Radar Meteorology, American Meteorological Society (AMS). (Breckenridge CO., USA, Sept. 16–20, 2013).
American Meteorological Society (AMS).
URL: <https://ams.confex.com/ams/36Radar/webprogram/Paper229168.html>.
– (Sept. 2014a).
“Melting layer attenuation as observed by polarimetric radar-radiometer synergistic approach.”
In:
8th European Conference on Radar in Meteorology and Hydrology. (Garmisch-Patenkirchen, Germany, Sept. 1–5, 2014).
Deutsches Zentrum fuer Luft- und Raumfahrt (DLR).
URL: http://www.pa.op.dlr.de/erad2014/programme/ExtendedAbstracts/374_Saavedra.pdf.
– (July 2014b).
“On the multi-frequency signature of precipitation water content as observed by passive and active sensors.”
In:
14th Conference on Cloud Physics, Atmospheric Radiation, American Meteorological Society (AMS). (Boston, USA, July 7–11, 2014).
American Meteorological Society (AMS).
URL: <https://ams.confex.com/ams/14CLOUD14ATRAD/webprogram/Paper250912.html>.
- Saavedra, P., A. Battaglia, and C. Simmer (Oct. 2009).
“Partitioning of cloud and rain water content by ground-based observations with a multi-frequency microwave radiometer in synergy with a micro rain radar.”
In: *Proceedings of the 8th International Symposium on Tropospheric Profiling*.
8th International Symposium on Tropospheric Profiling. (Delft, The Netherlands, Oct. 18–23, 2009).
URL: <http://cerberus.rivm.nl/ISTP/data/1660768.pdf>.

- Saavedra, P., A. Battaglia, and C. Simmer (Aug. 2012a).
“The contribution of the microwave radiometer ADMIRARI to the NASA GPM ground validation field experiments.”
In: *Proceedings of the International Radiation Symposium*.
International Radiation Symposium. (Berlin, Germany, Aug. 6–10, 2012).
American Institute of Physics (AIP),
Pp. 592–595.
DOI: [doi:http://dx.doi.org/10.1063/1.4804839](http://dx.doi.org/10.1063/1.4804839).
URL: http://proceedings.aip.org/resource/2/apcpcs/1531/1/592_1.
- (2012b).
“Partitioning of cloud water and rain water content by ground-based observations with the radiometer ADMIRARI in synergy with a micro rain radar.”
In: *J. Geophys. Res.* D05203.177. doi:10.1029/2011JD016382.
- Saavedra, P., A. Battaglia, C. Simmer, M. Vega, and V. Chandrasekar (Aug. 2012).
“On the feasibility to combine observations from multi-wavelength radar and the multi-frequency radiometer ADMIRARI to retrieve precipitating clouds parameters.”
In: *Proceedings of the International Radiation Symposium*.
International Radiation Symposium. (Berlin, Germany, Aug. 6–10, 2012).
American Institute of Physics (AIP),
Pp. 260–263.
DOI: [doi:http://dx.doi.org/10.1063/1.4804756](http://dx.doi.org/10.1063/1.4804756).
URL: http://proceedings.aip.org/resource/2/apcpcs/1531/1/260_1.
- Salby, Murry L. (1996).
Fundamentals of Atmospheric Physics.
Academic Press.
International Geophysics Series.
- Sokamura, S. and T. Oguchi (2010).
“Electromagnetic wave propagation in rain and polarization effects.”
In: *Proc. Jpn. Acad., Ser. B* 86.6. doi: 10.2183/pjab.86.539, pp. 539–563.
- Sundqvist, H (1978).
“A parameterization scheme for non-convective condensation including prediction of cloud water content.”
In: *Q. J. R. Meteorol. Soc.* 104, pp. 677–690.
- Sundqvist, H, E. Berge, and J. E. Kristjánsson (1989).
“Condensation and cloud studies with a mesoscale numerical weather prediction model.”
In: *Mon. Wea. Rev.* 117, pp. 1641–1657.
- Szyrmer, W. and I. Zawadzki (1999).
“Modeling of the melting layer. Part I: Dynamics and microphysics.”
In: *J. Atmos. Sci.* 56, pp. 3573–3592.
- Tao, W.K. and J. Simpson (1993).
“Goddard cumulus ensemble model. Part I: Model description.”
In: *Terrest. Atmos. Oceanic Sci.* 4, pp. 35–72.
- Testud, J., E. Le Bouar, E. Oblis, and M. Ali-Mehenni (2000).
“The Rain Profiling Algorithm Applied to Polarimetric Weather Radar.”
In: *J. Atmos. Ocean Technol.* 17, pp. 332–356.

- Tridon, F., J. Van Baelen, and Y. Pointin (2011).
“Aliasing in Micor Rain Radar data due to strong vertical winds.”
In: *Geophys. Res. Lett.* 38.L02804. doi:10.1029/2010GL046018.
- VAISALA (1999).
Ceilometer CT25K User’s Guide.
CT25K-U059en-2.1.
Version 2.1.
- Viltard, N., C.D. Kummerow, W.S. Olson, and Y. Hong (2000).
“Combined use of the radar and radiometer of TRMM to estimate the influence of drop size distribution on rain retrievals.”
In: *J. Appl. Meteorol.* 39.12, pp. 2103–2114.
- Weitkamp, Claus (2004).
Lidar, Range-Resolved Optical Remote Sensing of the Atmosphere.
Vol. 102.
Optical Sciences.
Springer.
- Wentz, F.J., L. Ricciardulli, K. Hilburn, and C. Mears (2007).
“How Much More Rain Will Global Warming Bring?”
In: *Science* 317.5835. DOI:10.1126/science.1140746, pp. 233–235.
- Wentz, F.J. and R.W. Spencer (1998).
“SSM/I Rain Retrievals within a Unified All-Weather Ocean Algorithm.”
In: *J. Atmos. Sci.* 55, pp. 1613–1627.
- Wulfmeyer, V. et al. (2008).
“The Convective and Orographically-induced Precipitation Study: A Research and Development Project of the World Weather Research Program for improving quantitative precipitation forecasting in low-mountain regions.”
In: *Bull. Amer. Met. Soc.* DOI 10.1175/2008BAMS2367.1.
- Zhao, Q. and F.H. Carr (Aug. 1995).
“A prognostic Cloud Scheme for Operational NWP Models.”
In: *Mon. Wea. Rev.* 125, pp. 1931–1953.

Acknowledgements

The project and the radiometer ADMIRARI have been funded by the *Deutsche Forschungsgemeinschaft* (DFG) under grant BA 3485/1-1. Therefore special thanks to DFG for making possible my research.

I am very grateful to Priv.Doiz. Dr. Alessandro Battaglia from University of Leicester, who gave me the opportunity to work for the ADMIRARI project. To enlighten me on the field of microwave remote sensing in general and the doctoral thesis in particular. His continuous support, advisement, and fruitful discussions as well as his patient review of publications and the dissertation have enriched my research and the quality of the present work.

Special thanks to Prof. Dr. Clemens Simmer who gave me the special opportunity to work at the Meteorological Institute, for the support and advise in my doctoral thesis as well as his guidance in the management of the ADMIRARI project, for his suggestions and corrections while writing the publications, project proposal and the dissertation.

This research work has been possible only due to the efforts of numerous colleagues. Particularly Mr. Martin Lennefer, who expended large number of hours in the improvement and/or reparation of the different apparatus, supporting me in the installation and proper functioning of the instrumentation, as well as for transporting the radiometer to several locations in two continents. His hard work was decisive for the successful participation of the radiometer ADMIRARI in every field experiment.

I want to express my gratitude to the NASA Global Precipitation Measurement/Ground Validation (GPM/GV) community. Specially to Dr. Matthew Schwaller from NASA Goddard Space Flight Center first for making possible taking part at the Brazilian CHUVA campaign and second for the ADMIRARI deployment to the CHILL Radar National Laboratory in Colorado, USA.

Special thanks to all the staff of the CHUVA field campaign in Brazil, their friendly help and hospitality made a successful and unforgettable stay in Brazil.

To Prof. Dmitri Moisseev from University of Helsinki for making possible my and ADMIRARI's participation at the LPVEx experiment and his collaboration during the experiment.

My acknowledgements to Dr. Walter A. Petersen from NASA Wallops Flight Facility for his support in all GPM/GV campaigns.

I am also thankful to the staff of the Department of Energy's Atmospheric Radiation Measurement program in Oklahoma, their assistance was decisive in tough moments I experienced dealing with instrument technical problems during the MC3E campaign.

Gratitudes also go to Dr. David Hudak and Mr. Steve Brady from Environment Canada for their collaboration with logistic and participation in the GCPEX experiment in Canada.

Finally acknowledgements to Mr. Marcel Brinkenbergh from CABAW observatory in the Netherlands and Dr. Birger Bohn from *Forschungszentrum Jülich GmbH* in Germany for making possible the ADMIRARI measurements at EUCAARI and HOPE campaigns respectively.

To Prof. V. Chandrasekar from Colorado State University for hosting the radiometer at CHILL radar facility and to Mr. Manuel A. Vega from NASA Goddard Space Flight Center for his work with the radiometer's antenna band-width and his friendly help during my stay at the Colorado State University's CHILL facility.

I want to acknowledge the support of Dr. Thomas Rose from Radiometer-Physics GmbH, who was keen to discuss issues related to the radiometer and its eventual reparations, as well as for giving me the opportunity of a short working experience at Radiometer-Physics GmbH.

To Prof. Susanne Crewell from Institute for Geophysics and Meteorology, University of Cologne, and to Prof. Frank Bertoldi from Argelander-Institute for Astronomy, University of Bonn. I thank them for accepting being part of my thesis committee as third and fourth referees, receptively.

I am also very thankful to my friends, colleagues and administrative staff at the University of Bonn in general and the Meteorological Institute in particular. They always were keen to help me specially at the beginning of my stay when the language was a huge limitation. A pleasant stance in Bonn has only been possible due to all of them.

Finally I am very much thankful to my family that even being in distant countries was not an impediment for their continuous support, I am very sorry for the time I could not shared with you all. To my mother who despite her affliction has always been giving me the encouragement to continue my work and teaching me how to persist even in adverse situations. My efforts are dedicated to my love ones.

BONNER METEOROLOGISCHE ABHANDLUNGEN

Herausgegeben vom Meteorologischen Institut der Universität Bonn durch Prof. Dr. H. FLOHN (Hefte 1-25), Prof. Dr. M. HANTEL (Hefte 26-35), Prof. Dr. H.-D. SCHILLING (Hefte 36-39), Prof. Dr. H. KRAUS (Hefte 40-49), ab Heft 50 durch Prof. Dr. A. HENSE.

Heft 1-39: siehe <http://www2.meteo.uni-bonn.de/bibliothek/bma.html>

- Heft 40: **Hermann Flohn**: Meteorologie im Übergang Erfahrungen und Erinnerungen (1931-1991). 1992, 81 S. + XII. € 23
- Heft 41: **Adnan Alkhalaf and Helmut Kraus**: Energy Balance Equivalents to the Köppen-Geiger Climatic Regions. 1993, 69 S. + IX. € 19
- Heft 42: **Axel Gabriel**: Analyse stark nichtlinearer Dynamik am Beispiel einer reibungs-freien 2D-Bodenkaltfront. 1993, 127 S. + XIV. € 30
- Heft 43: **Annette Münzenberg-St.Denis**: Quasilineare Instabilitätsanalyse und ihre Anwendung auf die Strukturaufklärung von Mesozyklonen im östlichen Weddellmeergebiet. 1994, 131 S. + XIII. € 33
- Heft 44: **Hermann Mächel**: Variabilität der Aktionszentren der bodennahen Zirkulation über dem Atlantik im Zeitraum 1881-1989. 1995, 188 S. + XX. € 48
- Heft 45: **Günther Heinemann**: Polare Mesozyklonen. 1995, 157 S. + XVI. € 46
- Heft 46: **Joachim Klaußen**: Wechselwirkung der Klima-Subsysteme Atmosphäre, Meereis und Ozean im Bereich einer Weddellmeer-Polynia. 1996, 146 S. + XVI. € 43
- Heft 47: **Kai Born**: Seewindzirkulationen: Numerische Simulationen der Seewind-front. 1996, 170 S. + XVI. € 48
- Heft 48: **Michael Lambrecht**: Numerische Untersuchungen zur tropischen 30-60-tägigen Oszillation mit einem konzeptionellen Modell. 1996, 48 S. + XII. € 15
- Heft 49: **Cäcilia Ewenz**: Seewindfronten in Australien: flugzeuggestützte Messungen und Modellergebnisse. 1999, 93 S. + X. € 30
- Heft 50: **Petra Friederichs**: Interannuelle und dekadische Variabilität der atmosphärischen Zirkulation in gekoppelten und SST-getriebenen GCM-Experimenten. 2000, 133 S. + VIII. € 25
- Heft 51: **Heiko Paeth**: Anthropogene Klimaänderungen auf der Nordhemisphäre und die Rolle der Nordatlantik-Oszillation. 2000, 168 S. + XVIII. € 28
- Heft 52: **Hildegard Steinhorst**: Statistisch-dynamische Verbundsanalyse von zeitlich und räumlich hoch aufgelösten Niederschlagsmustern: eine Untersuchung am Beispiel der Gebiete von Köln und Bonn. 2000, 146 S. + XIV. € 25
- Heft 53: **Thomas Klein**: Katabatic winds over Greenland and Antarctica and their interaction with mesoscale and synoptic-scale weather systems: three-dimensional numerical models. 2000, 146 S. + XIV. € 25
- Heft 54: **Clemens Drüe**: Experimentelle Untersuchung arktischer Grenzschichtfronten an der Meereisgrenze in der Davis-Straße. 2001, 165 S. + VIII. €
- Heft 55: **Gisela Seuffert**: Two approaches to improve the simulation of near surface processes in numerical weather prediction models. 2001, 128 S. + VI. € 25

- Heft 56: **Jochen Stuck**: Die simulierte axiale atmosphärische Drehimpulsbilanz des ECHAM3-T21 GCM. 2002, 202 S. + VII. € 30
- Heft 57: **Günther Haase**: A physical initialization algorithm for non-hydrostatic weather prediction models using radar derived rain rates. 2002, 106S. + IV. € 25
- Heft 58: **Judith Berner**: Detection and Stochastic Modeling of Nonlinear Signatures in the Geopotential Height Field of an Atmospheric General Circulation Model. 2003, 157 S. + VIII. € 28
- Heft 59: **Bernd Maurer**: Messungen in der atmosphärischen Grenzschicht und Validation eines mesoskaligen Atmosphärenmodells über heterogenen Landoberflächen. 2003, 182 S. + IX. € 30
- Heft 60: **Christoph Gebhardt**: Variational reconstruction of Quaternary temperature fields using mixture models as botanical – climatological transfer functions. 2003, 204 S. + VIII. € 30
- Heft 61: **Heiko Paeth**: The climate of tropical and northern Africa – A statistical-dynamical analysis of the key factors in climate variability and the role of human activity in future climate change. 2005, 316 S. + XVI. € 15
- Heft 62: **Christian Schölzel**: Palaeoenvironmental transfer functions in a Bayesian framework with application to Holocene climate variability in the Near East. 2006, 104 S. + VI. € 15
- Heft 63: **Susanne Bachner**: Daily precipitation characteristics simulated by a regional climate model, including their sensitivity to model physics, 2008, 161 S. € 15
- Heft 64: **Michael Weniger**: Stochastic parameterization: a rigorous approach to stochastic three-dimensional primitive equations, 2014, 148 S. + XV. open access¹
- Heft 65: **Andreas Röpnack**: Bayesian model verification: predictability of convective conditions based on EPS forecasts and observations, 2014, 152 S. + VI. open access¹
- Heft 66: **Thorsten Simon**: Statistical and Dynamical Downscaling of Numerical Climate Simulations: Enhancement and evaluation for east Asia, 2014, 48 S. + LXXVII. open access¹
- Heft 67: **Elham Rahmani**: The Effect of Climate Variability on Wheat in Iran, 2015, 96 S. + XIII. open access¹
- Heft 68: **Pablo A. Saavedra Garfias**: Retrieval of Cloud and Rainwater from Ground-Based Passive Microwave Observations with the Multi-frequency Dual-polarized Radiometer ADMIRARI, 2015, 168 S. + XIII. open access¹

¹Available at <http://hss.ulb.uni-bonn.de/fakultaet/math-nat/>



METEOROLOGISCHES INSTITUT
MATHEMATISCH NATURWISSENSCHAFTLICHE FAKULTÄT
UNIVERSITÄT BONN

